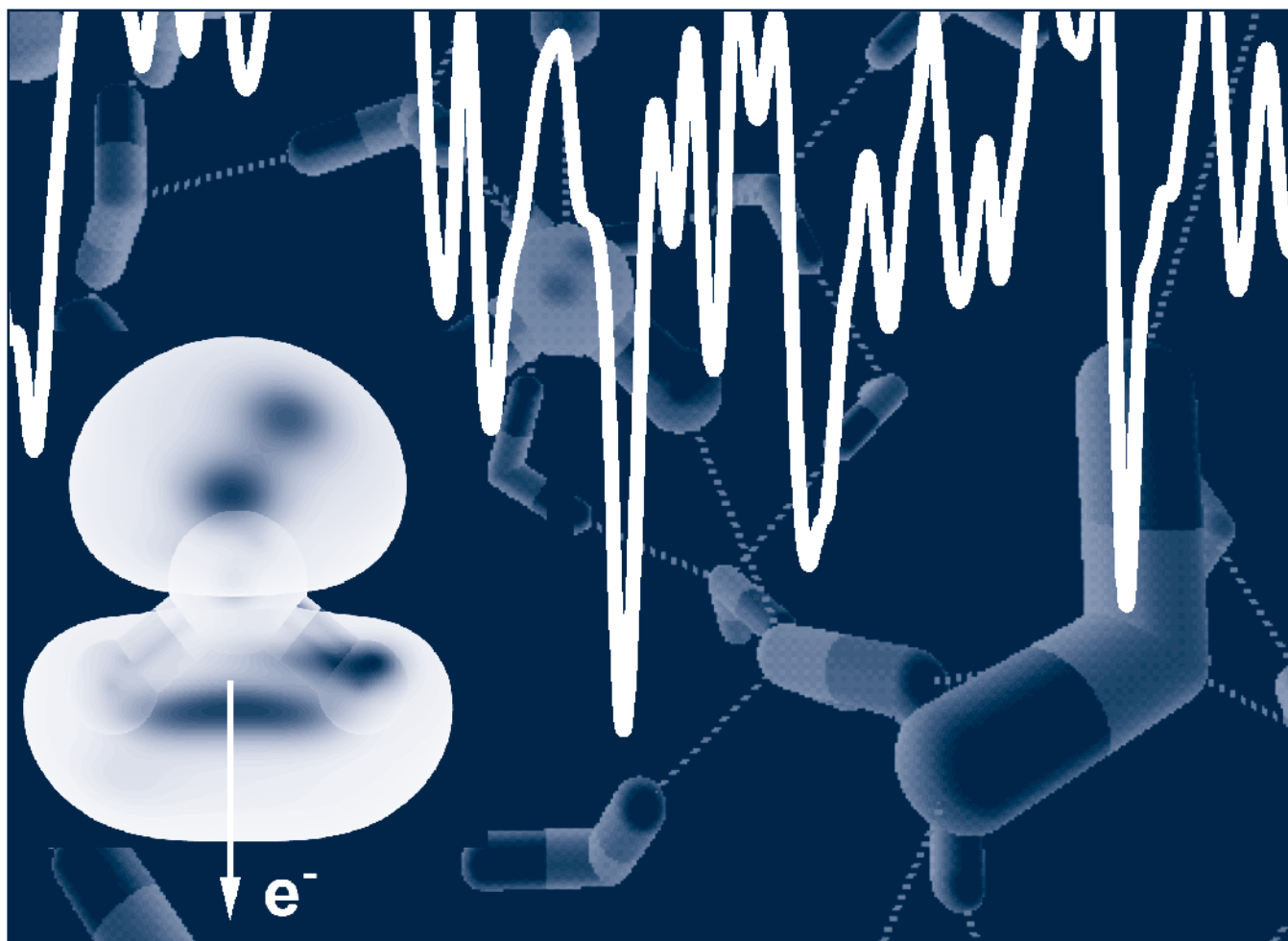




Max-Born-Institut  
für Nichtlineare Optik  
und Kurzzeitspektroskopie  
im Forschungsverbund Berlin e.V.

# Annual Report 2020



**Max-Born-Institut**

für Nichtlineare Optik  
und Kurzeitspektroskopie  
im Forschungsverbund Berlin e.V.



# Annual Report 2020



Annual Report 2020

Max-Born-Institut  
für Nichtlineare Optik  
und Kurzzeitspektroskopie  
im Forschungsverbund Berlin e.V.

Max-Born-Straße 2 A  
12489 Berlin  
Germany  
Phone: (+49 30) 63 92 - 15 05  
Fax: (+49 30) 63 92 - 15 19  
[mbi@mbi-berlin.de](mailto:mbi@mbi-berlin.de)  
[www.mbi-berlin.de](http://www.mbi-berlin.de)

## Preface

5

## Scientific Highlights

Light from inside the tunnel	11
Photon-recoil imaging: a new route to study nonlinear x-ray physics	13
Twisting magnetization with light – Ultrafast creation of skyrmions after optical excitation	15
Strong electric fields and ultrafast molecular motions – how to generate and steer electrons in liquid water	17
A novel high-flux femtosecond hard x-ray source driven by a mid-infrared OPCPA system	19
Lightwave topology for strong-field valleytronics	21
Extending solid-state calculations to ultra long-range length scales	23

## Short Description of Research Projects

### 1 – Laser Research

1.1: Fundamentals of Extreme Photonics	29
1.2: Ultrafast Laser Physics and Nonlinear Optics	38

### 2 – Ultrafast and Nonlinear Phenomena: Atoms, Molecules, and Clusters

2.1: Time-resolved XUV-science	49
2.2: Strong-field Few-body Physics	55

### 3 – Ultrafast and Nonlinear Phenomena: Condensed Phase

3.1: Dynamics of Condensed Phase Molecular Systems	61
3.2: Solids and Nanostructures: Electrons, Spins, and Phonons	67
3.3: Transient Structures and Imaging with X-rays	76

### 4 – Laser Infrastructure and Knowledge Transfer

4.1: Implementation of Lasers and Measuring Techniques	80
4.2: Application Laboratories and Technology Transfer	85
NanoMovie – Application Laboratory for nanoscopic spectroscopy and imaging	85
Berlin Laboratory for innovative X-ray Technologies (BLiX)	88
4.3: Nanoscale Samples and Optics	91

## Appendices

Appendix 1: Publications	94
Appendix 2: External Talks, Teaching	106
Appendix 3: Ongoing Bachelor, Master, and PhD theses	110
Appendix 4: Guest Lectures at the MBI	112
Appendix 5: Grants and Contracts	113
Appendix 6: Activities in Scientific Organizations	114



## Preface

This Annual Report provides an overview of the research pursued at the Max-Born-Institut (MBI) in 2020. A presentation of scientific highlights is followed by progress reports of all projects which are part of the scientific program of the institute. A complete record of publications and invited talks is given in the appendix, together with information on academic teaching and training, guest lectures, activities in scientific organizations, and third-party funding. More detailed up-to-date information is available on the MBI website (<http://www.mbi-berlin.de>).

Following the start of the COVID-19 pandemic in the beginning of the year, 2020 has been an exceptional year in the history of the institute. Over prolonged periods of time, the operation of MBI's laboratories was only possible on a reduced scale. Instead, MBI scientists and support divisions adapted to the pandemic by significantly reducing their presence at the institute and by extensively working from home. It is a credit to MBI's members high motivation and effort, that this transition into working from home for the most part went very smoothly, and that a significant number of excellent results were achieved also under these difficult circumstances.

The following key results are representative of the extensive scientific output of MBI in 2020:

- A new mechanism for harmonic generation in amorphous quartz was revealed, relying on nonlinearities associated with the injection of electrons into the conduction band. Close to the damage threshold, these nonlinearities dominate over intraband and interband contributions. Remarkably, the nonlinear response emerging from the sub-cycle injection dynamics of electrons into the conduction band had previously been almost completely overlooked in solids and only partially considered in the gas phase. The sensitivity of the harmonic emission to the sub-cycle ionization dynamics offers an original approach to characterize the evolution of laser-induced plasma formation in optical micro-processing.
- Extreme-ultraviolet (XUV) sources including high-harmonic generation (HHG), free-electron lasers (FELs), soft-X-ray lasers and laser-driven plasmas are widely used for applications ranging from femtochemistry and attosecond science to coherent diffractive imaging and EUV (or XUV) lithography. The bandwidth of the XUV light emitted by these sources reflects the XUV generation process used. A concept was demonstrated for efficient spectral compression by four-wave mixing (FWM), exploiting a phase-matching scheme based on closely-spaced resonances. Compression of few-eV bandwidth radiation in the 145–130 nm wavelength range was demonstrated into a few-meV bandwidth XUV pulses at 100.3 nm wavelength.
- Photon Recoil Imaging has been established as a new method to investigate nonlinear light-matter interaction in the x-ray regime. In experiments at the European XFEL the approach was introduced to study x-ray Raman scattering on the single atom level, which in spite of its fundamental importance has been elusive so far. The key element was to exploit the significant transfer of momentum to an atom that can occur when interacting with an x-ray photon, allowing to distinguish the weak stimulated x-ray Raman scattering from the spontaneous process. The method is an important stepping stone to transfer concepts of nonlinear optics into the x-ray spectral range in order to investigate and control coherent wave function evolution and intramolecular charge transfer with elemental specificity.
- Magnetic skyrmions are magnetization textures which have particle-like properties. They can be generated via laser pulses in suitably tailored thin magnetic films, necessitating a change of local topology of the magnetization pattern. Via time-resolved resonant x-ray scattering experiments the nucleation and growth of the skyrmions was observed, demonstrating that the associated change in topology occurs unexpectedly fast, within 300 ps. Combining the experimental results with atomistic spin simulations it was possible to clarify that this transition is mediated by a transient topology-fluctuation state never observed before, lowering the energy barrier for a local change of topology. This mechanism may well be relevant in completely different areas beyond magnetism, suggesting a path towards ultrafast topological switching in a wide variety of materials.
- The electric dipole moment of water molecules gives rise to strong fluctuating electric fields in the liquid. Such fields induce spontaneous tunneling ionization of water molecules which, however,

is fully reversible under equilibrium conditions. New experiments provided the first evidence for field-induced ionization by making it irreversible through imposing an external directed terahertz (THz) field on the liquid. Time-resolved nonlinear THz spectroscopy allows for mapping charge separation, transport, and localization of the released electron on a few-picosecond time scale. A THz-supported persistent charge separation requires a minimum THz field on the order of 250 kV/cm which is determined by the ionization potential. The solvated electrons display pronounced polaronic properties, due to the many-body Coulomb interactions in the liquid.

- The frequency of lattice vibrations or phonons in a crystal is determined by its electronic structure. Excitation of the prototypical semiconductor GaAs by a pair of femtosecond near-infrared pulses generates a transient shift of electronic charge which alters the frequency of transverse optical (TO) phonons. A highly sensitive phase-resolved detection of the nonlinear THz emission of TO phonons allowed for the first observation of an up-shift in TO phonon frequency by some 100 GHz. The frequency shift is caused by transverse electronic shift currents, which modify the dielectric function of the crystal. The results establish the coherent emission of TO phonons as a most sensitive probe of subtle changes in the electronic charge distribution and Coulomb correlations among carriers.

More than 170 articles have been published in peer-reviewed journals and books, including a substantial number of papers in high-impact journals. The number of invited talks at international conferences naturally was lower than in previous years, due to cancellation of a large number of conferences.

#### Honors and Awards:

- B. P. Fingerhut: Coblenz Award, Coblenz Society
- J. Mikosch: Consolidator Grant, The European Research Council (ERC)
- D. Reiche: The Best Poster Award, together with K. Busch, and F. Intravaia, METANANO 2020 ONLINE, V International Conference on Metamaterials and Nanophotonics
- A. Rouzee: JCP Editor's Choice Award, Atomic-resolution imaging of carbonyl sulfide by laser-induced electron diffraction (Denver, USA)
- O. Smirnova: Ahmed Zewail Award in Ultrafast Science & Technology (ACS, San Francisco, CA, USA)

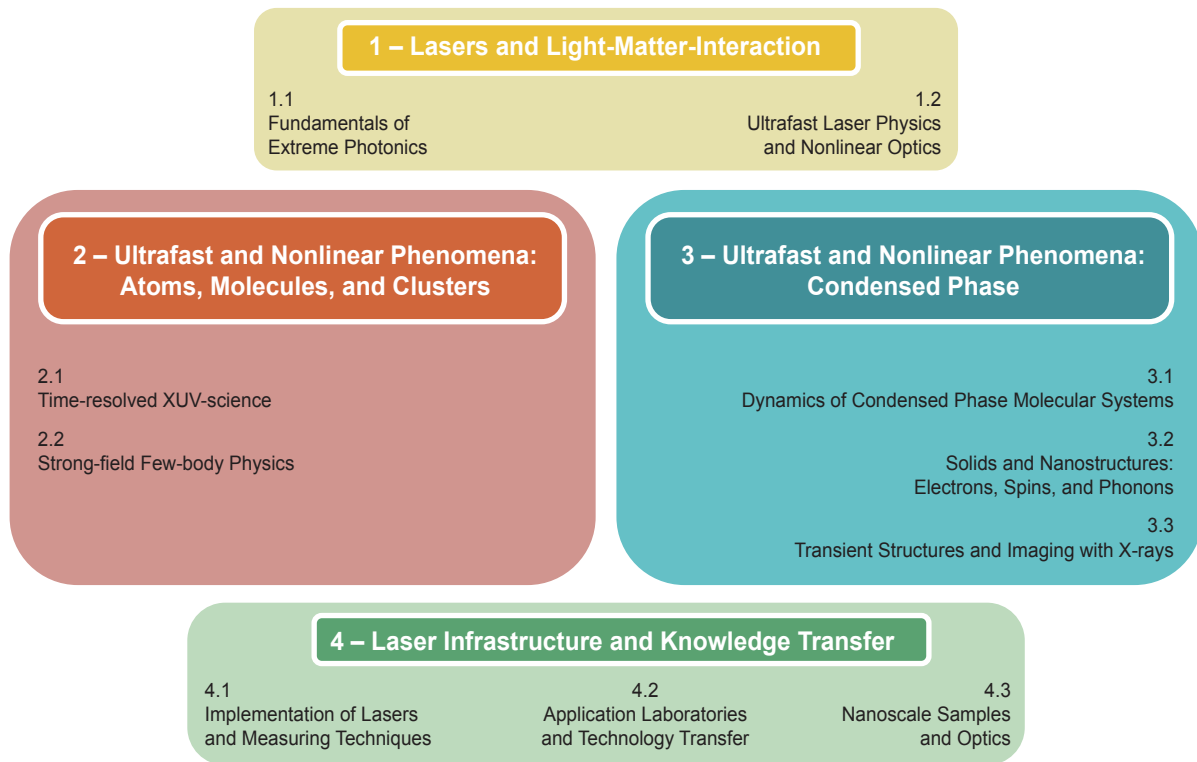
Berlin, March 2021

Stefan Eisebitt

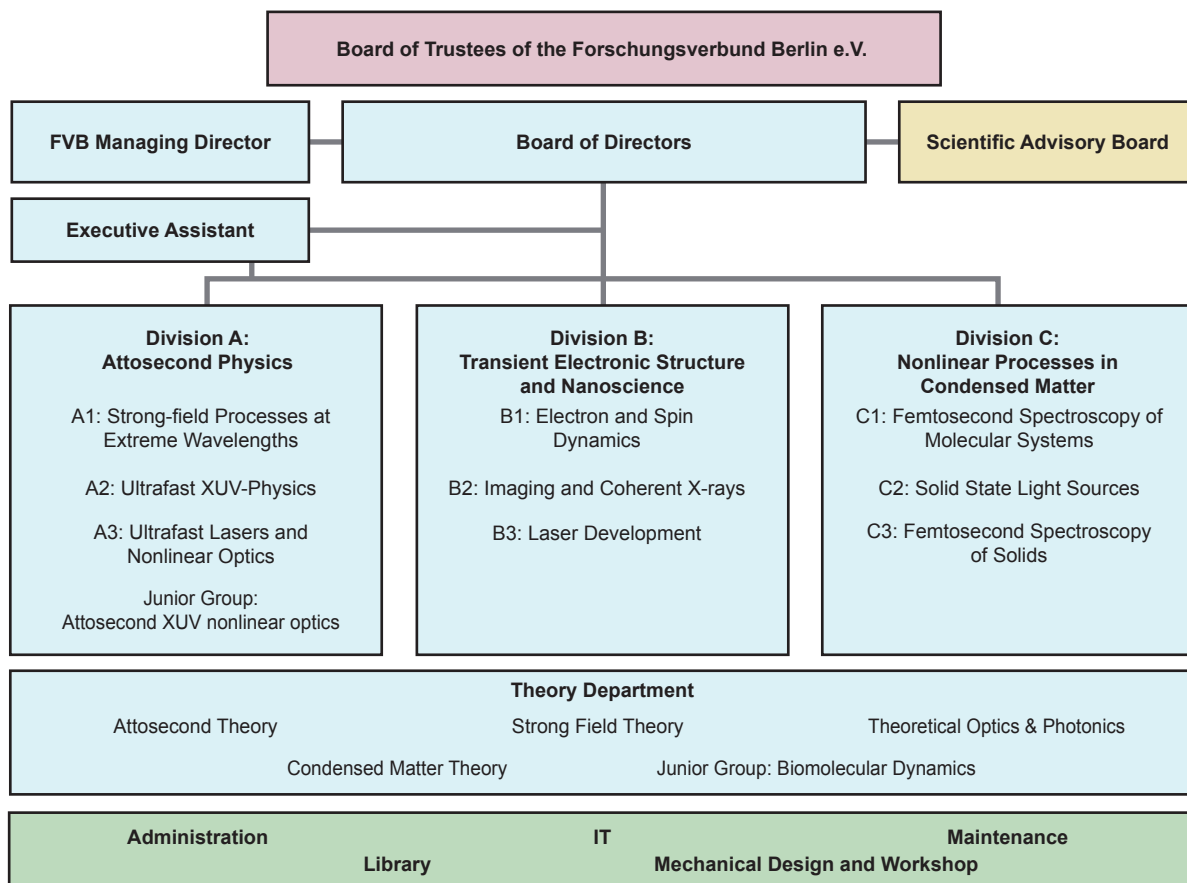
Thomas Elsaesser

Marc Vrakking

## Research Structure of the Max-Born-Institut



## Organizational Structure of the Max-Born-Institut



## **Members of the Scientific Advisory Board**

*Prof. Dr. Giulio Cerullo*  
Politecnico de Milano, Dipartimento di Fisica, Italy

*Prof. Dr. Majed Chergui (Chair)*  
École Polytechnique Fédérale de Lausanne (EPFL), Institute of Chemical Sciences and Engineering, Switzerland

*Prof. Tony Heinz*  
Stanford University, Department of Applied Physics, USA

*Prof. Dr. Jon Marangos*  
Imperial College London, Department of Physics, UK

*Prof. Dr. Christoph Quitmann*  
Lund University, Max IV Laboratory, Sweden

*Prof. Dr. Ursula Roethlisberger*  
École Polytechnique Fédérale de Lausanne (EPFL), Institute of Chemical Sciences and Engineering, Switzerland

*Prof. Dr. Regina de Vivie Riedle*  
Ludwig-Maximilians-Universität München (LMU), Department Chemie, Germany

*Prof. Dr. Jan Michael Rost*  
Max-Planck-Institut für Physik komplexer Systeme, Dresden, Germany

## **Representatives of the Cooperating Universities**

*Prof. Dr. Christoph Koch*  
Humboldt-Universität zu Berlin, Institut für Physik, Germany

*Prof. Dr. Andreas Knorr*  
Technische Universität Berlin, Institut für Optik und Atomare Physik, Germany

*Prof. Dr. Martin Weinelt*  
Freie Universität Berlin, Fachbereich Physik, Germany

## **Representatives of the Federal Republic and the State of Berlin**

*Jan Neitzke*  
Bundesministerium für Bildung und Forschung, Ref. 711, Bonn, Germany

*Dr. Heike Mewis*  
Senatskanzlei, Wirtschaft und Forschung, Ref. VI D, Berlin, Germany

MBI is a member of the Leibniz Association



# Scientific Highlights



# Light from inside the tunnel

P. Jürgens<sup>1</sup>, B. Liewehr<sup>2</sup>, B. Kruse<sup>2</sup>, C. Peltz<sup>2</sup>, D. Engel<sup>1</sup>, A. Husakou<sup>1</sup>, T. Witting<sup>1</sup>, M. Ivanov<sup>1</sup>, M.J.J. Vrakking<sup>1</sup>, T. Fennel<sup>2</sup> and A. Mermillod-Blondin

<sup>1</sup> Max-Born-Institute for Nonlinear Optics and Short Pulse Spectroscopy, Berlin, Germany

<sup>2</sup> Institute for Physics, University of Rostock, Rostock, Germany

Whenever an oscillating laser field interacts with matter, charge carriers are accelerated within their respective potentials. The associated movement of the carriers results in a polarization of the material. For sufficiently strong fields the induced polarization forms the basis for perturbative nonlinear optics leading to a multitude of nonlinear effects such as self-focusing, wave-mixing and solitary waves. At even higher laser intensities higher order nonlinear effects (e.g. strong-field ionization) tend to dominate the nonlinear response, potentially leading to the generation of new frequencies that are multiples of the incident laser frequency [high harmonic generation (HHG)]. HHG in solids has evolved to an established research field since the first experimental demonstration in 2011 [1] and is currently interpreted as a combined effect of intraband carrier dynamics [2] and interband recollisions [3].

In collaboration with researchers from the University of Rostock we have demonstrated that the nonlinear response emerging from the transfer of electrons from the valence to the conduction band – that has so far been overlooked in the context of HHG in solids – constitutes the dominant source of low-order harmonic emission from SiO<sub>2</sub> at near-threshold intensities.

We have performed time-resolved, two-color wave-mixing experiments using a close-to-collinear pump-probe geometry in amorphous and crystalline quartz (see Figs. 1 & 2). A transient delay-dependent wave-

mixing signal was detected around the pump-probe overlap (Fig. 1). In crystalline quartz the orientation-dependent yield of this harmonic signal evolved from an anisotropic response at low laser intensity (Fig. 2(a)) to an isotropic response at an intensity close to the damage threshold of the used samples (Fig. 2(b)). Based on our experimental observations we excluded all traditional mechanisms (Kerr-type wave-mixing, interband recollisions and intraband currents) as the dominant source of the observed harmonics.

In order to compare our experimental data to numerical predictions and to unequivocally identify the microscopic origin of the detected harmonic emission we introduced the effective nonlinearity  $m$  that is defined as the ratio of the harmonic signal obtained with parallel and perpendicular pump and probe polarizations. Based on the excellent agreement between the theoretical and the experimental results (Fig. 3) we identified the injection current as the leading source of low-order harmonic generation under our experimental conditions. This time-dependent injection current is directly associated with the spatial displacement of the electrons during the strong-field ionization process.

Our findings not only advance the understanding of ultrafast light-matter interaction on sub-cycle timescales but also open up a promising route to monitor the strong-field-induced plasma formation during laser micromachining in real time.

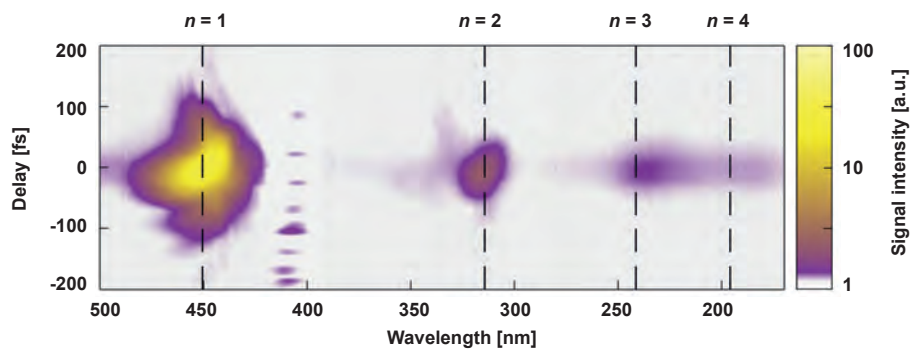


**Fig. 1:**

Spectrally resolved low-order harmonic emission from the a-SiO<sub>2</sub> sample measured as a function of the delay between the strong pump laser pulse with 2.1- $\mu\text{m}$  central wavelength focused to an intensity of 12 TWcm<sup>-2</sup> and the weak probe laser pulse at 0.8- $\mu\text{m}$  central wavelength focused to an intensity of 0.015 TWcm<sup>-2</sup>. The pump and probe laser pulses were used with parallel polarizations and have durations of 140 fs and 45 fs, respectively. We verified that only a single probe photon participated in the underlying wave-mixing processes by demonstrating the linear dependence of all observed signals on the intensity of the probe beam.

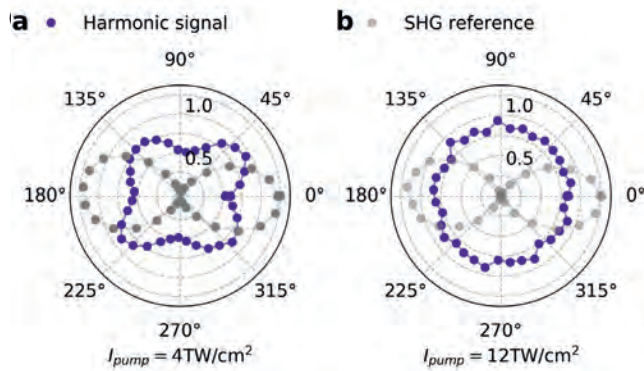


**Fig. 2:**

Dependence of the  $n=1$  harmonic emission yield from  $c\text{-SiO}_2$  on the angle between the principal axis of the crystal and the polarization axis of the pump laser pulse, measured at a pump laser intensity of  $4\text{ TWcm}^{-2}$  (a) and  $12\text{ TWcm}^{-2}$  (b). The pump and probe beams were orthogonally polarized. The probe pulse intensity was  $I_{\text{probe}} \approx 0.05\text{ TWcm}^{-2}$ . The angular dependence of second-harmonic generation (SHG) of the probe laser pulse provides a reference orientation.

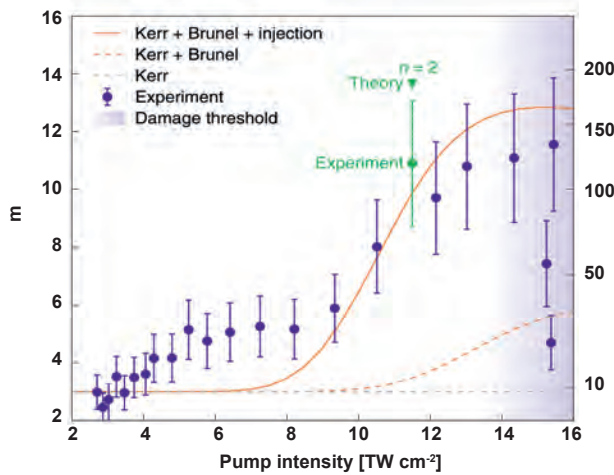


**Fig. 3:**

Comparison of the measured effective nonlinearity with the values predicted by our model. The error bars represent 20% of the measurand, corresponding to the maximum intensity fluctuations when measuring 10 times the harmonic yield with parallel polarizations of pump and probe fields at a pump intensity of  $12\text{ TWcm}^{-2}$ . The green symbols show the effective nonlinearity for  $n=2$ . The numerical predictions for  $m$  are shown when considering Kerr-type nonlinearities only ( $m=3$ ), the joint contribution of Kerr-type and Brunel-type nonlinearities and the sum of Kerr, Brunel and injection-induced nonlinearities for a bandgap of  $7.7\text{ eV}$ .

## Publication

JLK20: P. Jürgens *et al.*; Origin of strong-field-induced low-order harmonic generation in amorphous quartz, *Nat. Phys.* 16 (2020) 1035-1039

## References

- [1] S. Ghimire, A.D. DiChiara, E. Sistrunk, P. Agostini, L.F. DiMauro, and D.A. Reis; *Nat. Phys.* 7, (2011) **138-141**
- [2] O. Schubert, M. Hohenleutner, F. Langer, B. Urbanek, C. Lange, U. Huttner, D. Golder, T. Meier, M. Kira, S. W. Koch, and R. Huber; *Nat. Phot.* 8, (2014) **119-123**
- [3] G. Vampa, T.J. Hammond, N. Thiré, B.E. Schmidt, F. Légaré, C.R. McDonald, T. Brabec, D.D. Klug, and P.B. Corkum; *Phys. Rev. Lett.* **115** (2015) 193603

# Photon-recoil imaging: a new route to study nonlinear x-ray physics

U. Eichmann, H. Rottke, S. Eisebitt

One of the key scientific drivers for the development of intense x-ray free-electron lasers (XFELs) has been the prospect to transfer the concepts of nonlinear optics into the x-ray spectral range. One of the building blocks is the stimulated Raman scattering, which is a well-established and important process in the optical domain.

In one of the first user experiments at the SQS instrument at the European XFEL in Hamburg we have established photon-recoil imaging as a novel approach to study x-ray Raman scattering. Rather than detecting the scattered x-ray radiation from dense (gaseous) media as it is usually pursued in related studies we have measured individual scattered atoms subjected to the photon recoil.

To understand the new technique it is helpful to recall that a photon, i.e., the quantized energy portion of electromagnetic radiation, also carries momentum; a fact that is well-known since the early days of quantum physics at the times of Einstein. As a consequence, absorption of a photon inevitably pushes the atom very much like a billiard ball gets a push when hit by another one. In the spontaneous Raman scattering process, transient absorption of a photon is rapidly followed by spontaneous emission of a photon with less energy. The photons' energy difference remains in the atom lifting an electron to a bound excited state. While the absorption

pushes the atom in the direction of the incoming photon, the spontaneous emission of a photon, which happens into a random direction, scatters the atom accordingly to a corresponding opposite random direction.

To detect the scattered excited atoms in the experiment we used a collimated supersonic beam of neon atoms, which travel towards a position-sensitive detector. The detector is set to be sensitive to impinging excited atoms only. Well in front of the detector the atomic beam is crossed perpendicularly by the XFEL beam defining a sharp elongated interaction volume. If the x-ray photon energy is tuned close to an inner-shell resonance of the Ne atom, about 2% of the transiently excited atoms undergo spontaneous x-ray Raman scattering leaving the atom intact in finally a long lived bound excited state (the overwhelming portion of transiently excited atoms ionizes through a fast Auger process since the transient excitation energy exceeds the first ionization threshold by a factor of about 40). The photon momentum transfer slightly deflects the excited atoms from the collimated atomic beam. Accumulating the resulting detector signal over many XFEL pulses a characteristic pattern on the detector is produced, as shown in Fig. 1(a). The pattern has an extended elliptical shape due to the deflections in random directions experienced by the atoms in the interaction volume during spontaneous Raman scattering.

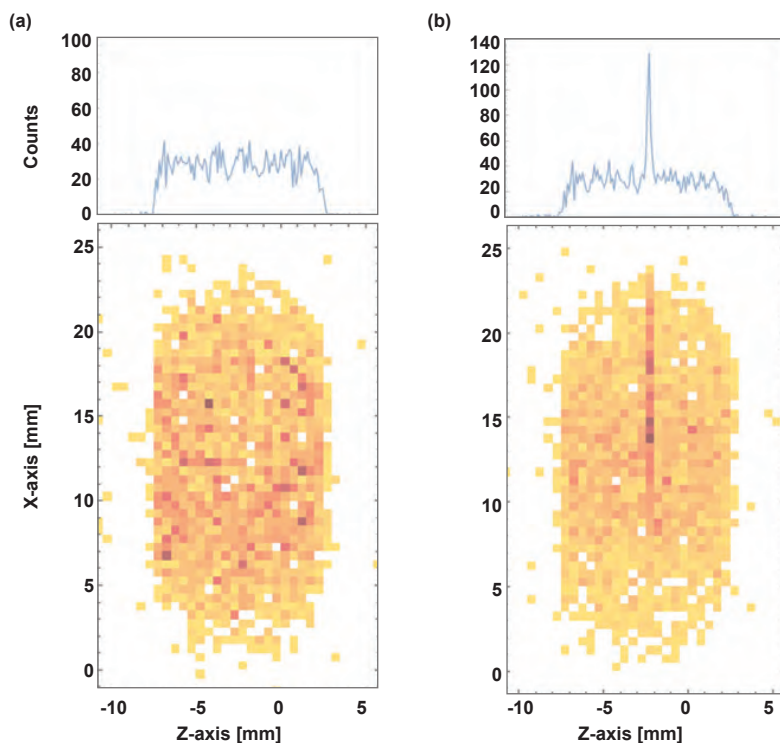


**Fig. 1:**  
(a) Distribution of excited atoms on the detector after spontaneous x-ray Raman scattering.  
(b) Same as (a) plus excited atoms after stimulated x-ray Raman scattering (narrow stripe).

Optimizing the XFEL intensity and the photon energy of the x-ray beam, which has a photon energy bandwidth in the range of the atomic excitation energy, we were able to increase the probability for the transiently excited atom to get hit by a second photon with suitable energy, before it actually has a chance to emit a photon spontaneously. In this case the transiently excited atom will be stimulated to emit a photon along the direction of the incoming photon. Since this process depends on two photons of the x-ray pulse, the process is called nonlinear. The net momentum transfer by the incoming and stimulated photon is almost zero due to the low final excitation energy of the atom compared with the x-ray photon energies. Excited atoms from stimulated Raman scattering are thus basically not deflected and appear on the detector as a sharp straight line mapping the interaction volume. They can be clearly distinguished from the spontaneously Raman scattered atoms, as shown in Fig. 1(b). The measured excited Ne\* atom yield is amenable to a quantitative theoretical analysis as presented in the study.

Photon-recoil imaging enables the investigation of x-ray stimulated Raman scattering on a single atom level almost background free. In combination with short, time-delayed controlled pairs of x-ray pulses with different photon energies – which have already been demonstrated at seeded XFELs – it establishes a highly promising nonlinear x-ray spectroscopy method. We envisage photon-recoil imaging to unravel fundamental features in x-ray photon interaction with atoms and molecules, even allowing to adopt coherent optical control methods.

## Publication

ERM20: U. Eichmann, H. Rottke, S. Meise, J.-E. Rubensson, J. Söderström, M. Agåker, C. Sätze, M. Meyer, T. M. Baumann, R. Boll, A. D. Fanis, P. Grychtol, M. Ilchen, T. Mazza, J. Montano, V. Music, Y. Ovcharenko, D. E. Rivas, S. Serkez, R. Wagner, and S. Eisebitt; Photon-recoil imaging: expanding the view of nonlinear X-ray physics; *Science* **369** (2020) 1630-1633

# Twisting magnetization with light – Ultrafast creation of skyrmions after optical excitation

B. Pfau, S. Eisebitt

Magnetic skyrmions are chiral topological spin textures with solitonic character which can exist, e.g., in ferromagnetic multilayers with out-of-plane magnetic anisotropy. In these magnetic thin films, skyrmions are stable at room temperature and emerge as confined, isolated textures with nanometer-scale dimensions. For these reasons, the use of skyrmions has been discussed for data memory, storage, and processing applications. Shifting, writing, and deleting operations were already efficiently realized using spin-polarized currents with nanosecond pulse duration. Femtosecond laser pulses offer an alternative approach to manipulate magnetization at accordingly shorter time scale. In our work, we have demonstrated that magnetic skyrmions can be created in a ferromagnetic material with single, suitably intense femtosecond laser pulses. In a time-resolved X-ray scattering experiment, we revealed that the formation of the skyrmions is mediated by a previously unobserved transient fluctuation phase on a timescale of 300 ps.

In our study, we first confirmed laser-induced formation of skyrmions in the thin-film multilayer material using static X-ray holographic imaging at the PETRA III synchrotron-radiation source. As shown in Fig. 1b, the multilayer film is initially prepared in a uniformly magnetized state via an external magnetic field. After exposure to a single laser pulse (1030 nm, linear polarization) of suitable fluence, this state transforms into a skyrmion state in the presence of a symmetry-breaking magnetic field. In our images, the individual skyrmions appear as circular, black domains. They are homogeneously distributed over the circular microscopic field of view in a dense, disordered arrangement. The skyrmion creation changes

the net magnetization of the material, but also – fundamentally even more important – the system's topology from the topologically trivial uniform magnetization state to a state where each skyrmion carries nonzero topological charge. Each skyrmion is a tiny whirl of magnetization directions with a topological charge of one, as we could confirm via Lorentz electron microscopy and tracing the skyrmion Hall effect when moving skyrmions with current pulses. To answer the question how the topological transition microscopically proceeds, we carried out time-resolved small-angle x-ray scattering (SAXS) experiments on Co/Pt multilayer-based samples at the European XFEL. Sensitivity to the magnetization is provided by x-ray magnetic circular dichroism via resonant scattering at the Cobalt 2p absorption edge.

As shown in Fig. 1(a), we followed the magnetization dynamics using a pump-probe scheme, which has to include magnetic field cycling. In each cycle, the sample is first reset to the magnetically uniform state and probed via resonant SAXS in this initial state (Fig. 1(c)). Then a femtosecond laser pulse excites the magnetic thin film and the transient magnetic state of the sample is probed with a certain time delay (see Fig. 1(d) where SAXS at 125 ps delay is shown). The next X-ray pulse (60  $\mu$ s later) probes the sample in its final state (Fig. 1(e)). The scattering of this final state is characterized by a distinct ring-like intensity pattern reflecting the correlation length of the equilibrium skyrmion distribution as shown in Fig. 1(b). In contrast, the transient scattering signal is broadly distributed to much higher scattering angles pointing to very disordered magnetic textures with much shorter correlation length, indicative of a hitherto unknown fluctuation phase.

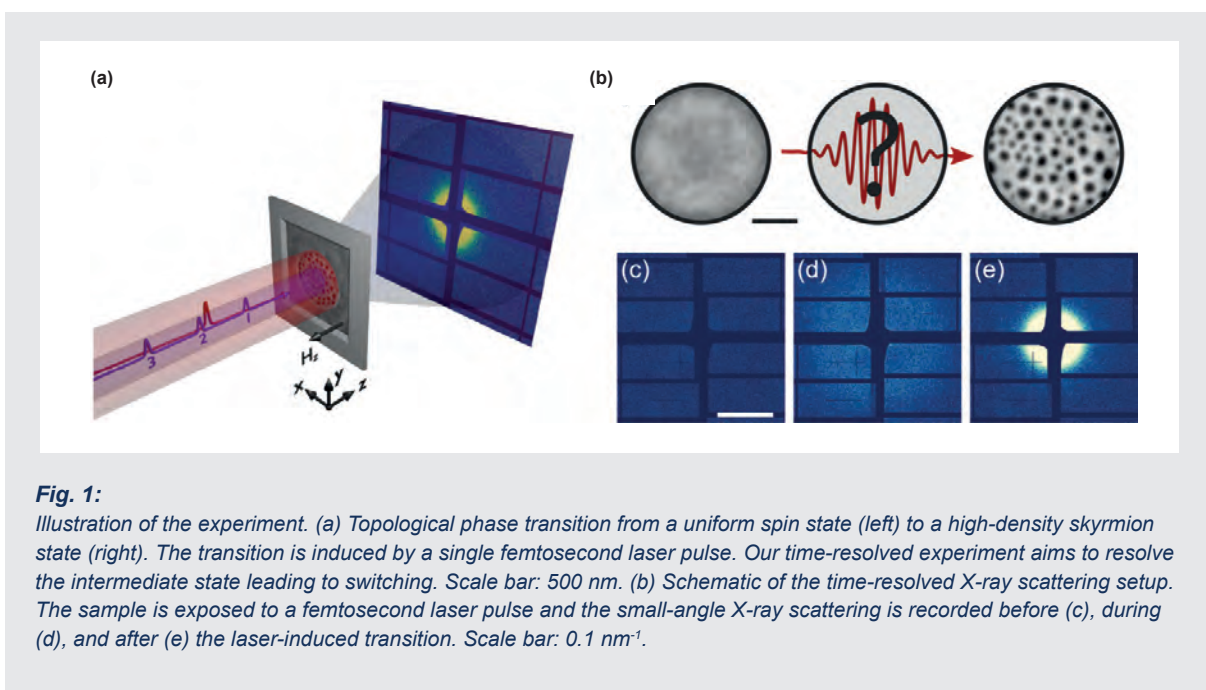
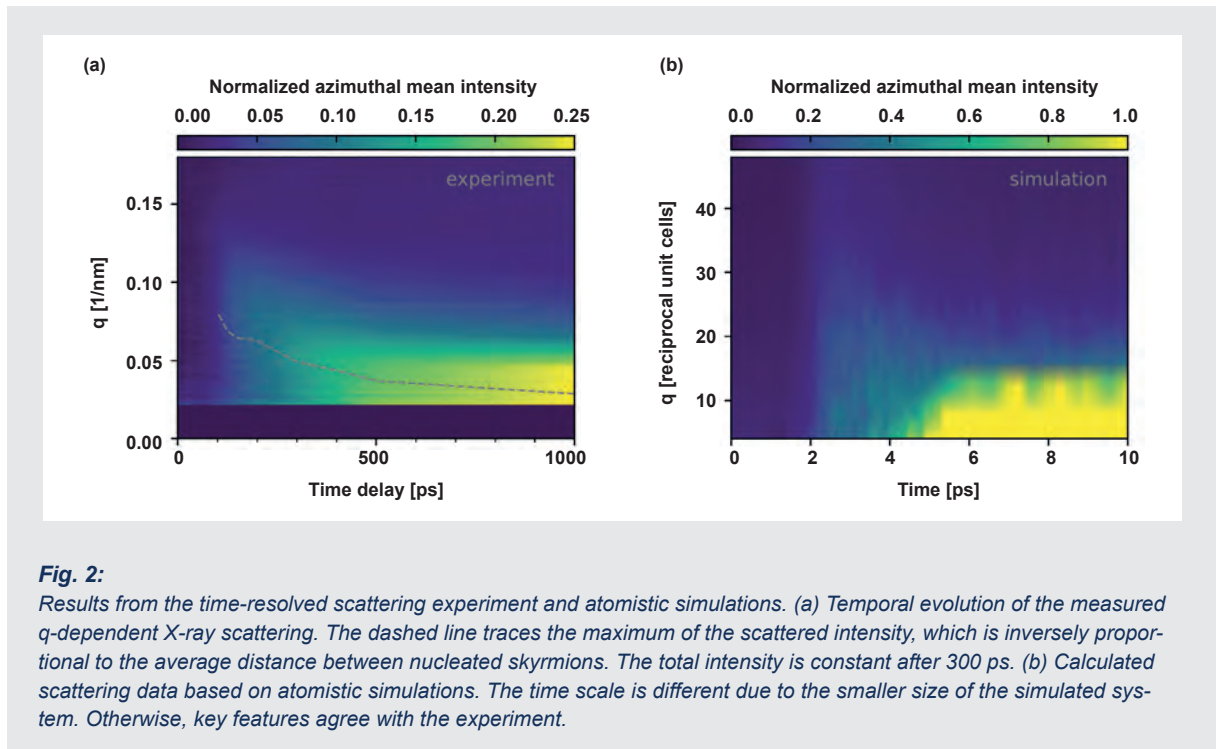


**Fig. 1:**

*Illustration of the experiment. (a) Topological phase transition from a uniform spin state (left) to a high-density skyrmion state (right). The transition is induced by a single femtosecond laser pulse. Our time-resolved experiment aims to resolve the intermediate state leading to switching. Scale bar: 500 nm. (b) Schematic of the time-resolved X-ray scattering setup. The sample is exposed to a femtosecond laser pulse and the small-angle X-ray scattering is recorded before (c), during (d), and after (e) the laser-induced transition. Scale bar: 0.1 nm<sup>-1</sup>.*



The temporal evolution of this fluctuation state, shown in Fig. 2(a), is governed by two dynamic processes, partly overlapping in time in different parts of the sample: A nucleation phase, indicated by a temporal increase of the integrated scattered intensity, is followed by a coarsening of the magnetic texture, represented by the progressive shift of scattering intensity towards smaller scattering angle, i.e., lower momentum transfer  $q$ . The fact that the total scattering intensity reaches 80 % of the final-state intensity within the first 300 ps indicates that both the reversal of perpendicular magnetic moments and the ferromagnetic coupling of these moments across the whole film thickness are completed within this time.

We infer the microscopic mechanism of skyrmion nucleation from comparing the experimental results to atomistic simulations. The simulations predict the existence of a phase with fluctuations of the local magnetization and associated local topological charge. SAXS calculated on the basis of the atomistic spin simulations agree with the observed scattering signal (Fig. 2(b)). The high-temperature fluctuation phase is characterized by lack of long-range coupling, rapid spin fluctuations, and in particular a significant reduction of the topological energy barrier, thus enabling topological fluctuations leading to the generation of net topological charge. In contrast to a paramagnetic phase, persisting short-range order promotes the formation of skyrmion seeds that freeze out and later coarsen during cooldown of the magnetic film to the equilibrium skyrmion size and density. As our experimental data indicate that the topological energy barrier must be reestablished 300 ps after the laser excitation, we conclude that the change of topology has been completed during that time.

The timescale of laser-induced creation of skyrmions is significantly faster than any formation of *ferromagnet-*

ic order observed so far. Sub-nanosecond magnetic switching in response to a single laser pulse was, so far, only known from *ferrimagnetic* systems where the net magnetization is low and the reversal is driven by the inherently different dynamics of the magnetic sublattices. The mechanism of topological switching via a topological fluctuation phase may be of relevance beyond the physics of magnetic skyrmions as it provides fundamental insight into the nature of topological phase transitions in general.

## Publication

BPB: F. Büttner, B. Pfau, M. Böttcher, M. Schneider, G. Mercurio, C. M. Günther, P. Helsing, C. Klose, A. Witmann, K. Gerlinger, L.-M. Kern, C. Strüber, von Korff Schmising, C., J. Fuchs, D. Engel, A. Churikova, S. Huang, D. Suzuki, I. Lemesch, M. Huang, L. Caretta, D. Weder, S. Zayko, K. Bagschik, R. Carley, L. Mercadier, J. Schlappa, A. Yaroslavtsev, L. Le Guyarder, N. Gerasimova, A. Scherz, C. Deiter, R. Gort, D. Hickin, J. Zhu, M. Turcato, D. Lomidze, F. Erdinger, A. Castoldi, S. Maffessanti, M. Porro, A. Samartsev, M. Kuster, C. Ropers, J. Sinova, J. H. Mentink, B. Dupé, G. S. D. Beach, and S. Eisebitt; *Observation of fluctuation-mediated picosecond nucleation of a topological phase*; Nat. Materials (in press)

# Strong electric fields and ultrafast molecular motions – how to generate and steer electrons in liquid water

A. Ghalgaoui, L.-M. Koll, B. Schütte, B. P. Fingerhut, K. Reimann, M. Woerner, T. Elsaesser

Electrons solvated in liquid water are one of the elementary charged species in soft condensed matter and have raised strong interest in physics and chemistry. They are generated by optical pulse radiolysis or irradiation of water samples with electrons, both resulting in the ionization of water molecules in the liquid. The detached electron undergoes a subpicosecond localization process and eventually resides in the liquid far from its parent cation. The solvated electron has been described as a particle locally bound in a self-consistent potential originating from a reorientation of dipolar water molecules and a concomitant minimization of the electric interaction energy.

On the other hand, there is a very strong fluctuating electric field in the liquid. The water molecule displays an electric dipole moment due to the different electron densities on the oxygen and hydrogen atoms (Fig. 1(a)). Such molecular dipoles generate an electric field of up to 200 MV/cm which fluctuates on a femto- to picosecond time scale due to thermally activated motions of water molecules (Fig. 1(b)). While the strength of this field is sufficient to induce tunneling ionization of water molecules, the macroscopic rate of successful ionization events is extremely small due to the high efficient charge recombination.

This behavior changes dramatically in the presence of an external THz field. In a series of experiments with strong THz transients, we have demonstrated that a THz field of an amplitude above 250 kV/cm makes the separation of the electron from the parent ion and electron transport along the external field direction

feasible. For an irreversible charge separation, the electron needs to acquire an amount of energy in the THz field that is on the order of the ionization potential of the water molecule.

The experiments were based on time-resolved nonlinear two-dimensional terahertz (2D-THz) spectroscopy with a pair of phase-locked THz pulses separated by a delay time  $\tau$ . In this way, nonlinear changes of the THz dielectric function of the liquid are measured. The sample was a 50  $\mu\text{m}$ -thick driven gravity jet of liquid water at ambient temperature. In the experiment, the time-dependent electric field of the pulses after interaction with the sample is measured with electro-optic sampling as a function of real time  $t$ . Fig. 2(a) shows a contour plot of the nonlinear signal field, displaying a high amplitude of up to 100 kV/cm which corresponds to one third of the maximum field of the probe pulse (Fig. 2(a),(c)). The 2D Fourier transform of the nonlinear signal (Fig. 2(b)), is dominated by the pump-probe signal. Other nonlinear signals, in particular third-order photon echoes, are absent. Measurements with a different peak field strength of the pump pulse reveal a sharp threshold, the nonlinear THz response occurs only for an electric-field amplitude above 250 kV/cm.

In Fig. 2(c), the nonlinear signal is plotted as a function of the real time  $t$  (blue line) for a delay time  $\tau=7$  ps together with the probe field (orange line) and the total THz probe field transmitted through the excited sample (black dashed line) as a function of the real time  $t$  for a pump peak field of 500 kV/cm. One observes an increase of transmission and a phase shift of the nonlinear signal to earlier time  $t$ . Both arise from a

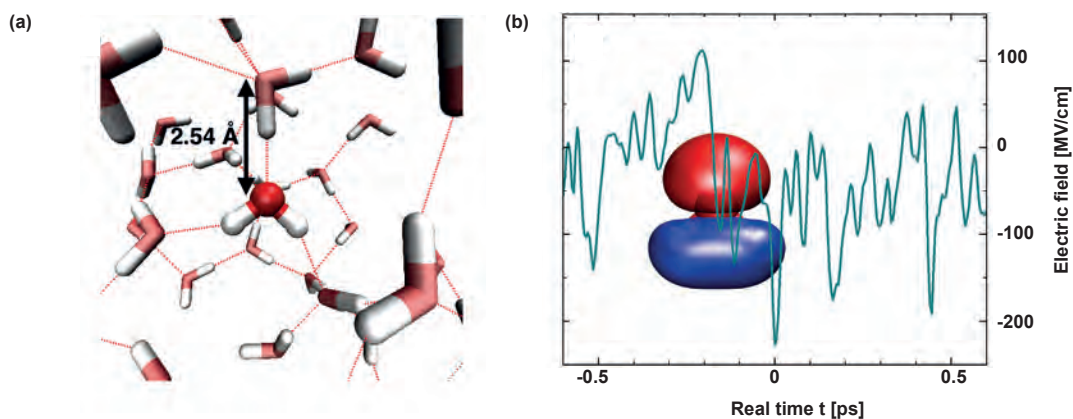


**Fig. 1:**

(a) Snapshot of the arrangement of water molecules in the liquid (red: oxygen atoms, grey; hydrogen atoms).

(b) Fluctuating electric fields in liquid water as calculated from a molecular dynamics simulation for electrons at the position of the highest orbital  $3a_1(\text{HOMO}-1)$ .

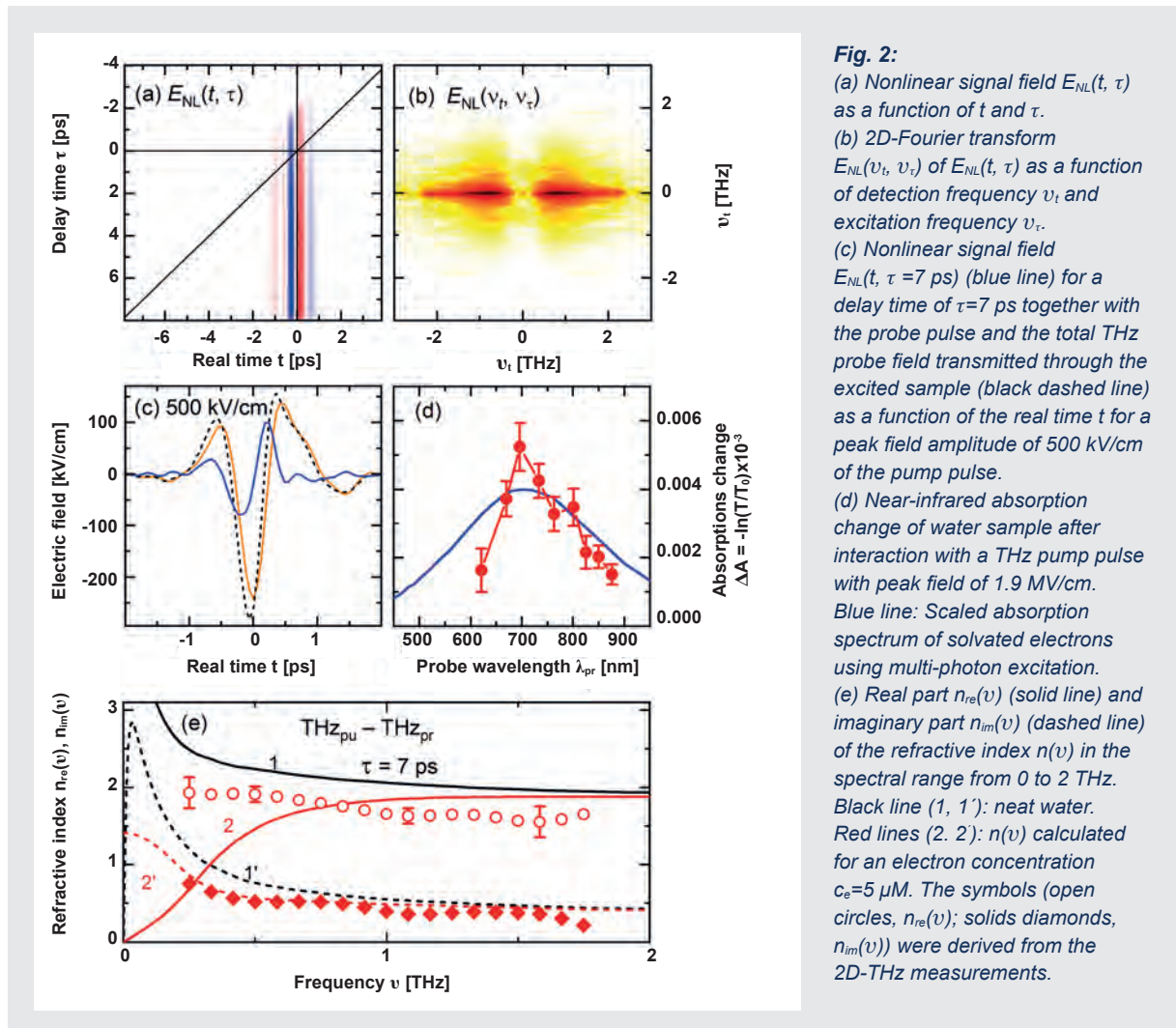


**Fig. 2:**

(a) Nonlinear signal field  $E_{NL}(t, \tau)$  as a function of  $t$  and  $\tau$ .  
 (b) 2D-Fourier transform  $E_{NL}(\nu_t, \nu_\tau)$  of  $E_{NL}(t, \tau)$  as a function of detection frequency  $\nu_t$  and excitation frequency  $\nu_\tau$ .  
 (c) Nonlinear signal field  $E_{NL}(t, \tau = 7 \text{ ps})$  (blue line) for a delay time of  $\tau = 7 \text{ ps}$  together with the probe pulse and the total THz probe field transmitted through the excited sample (black dashed line) as a function of the real time  $t$  for a peak field amplitude of  $500 \text{ kV/cm}$  of the pump pulse.  
 (d) Near-infrared absorption change of water sample after interaction with a THz pump pulse with peak field of  $1.9 \text{ MV/cm}$ . Blue line: Scaled absorption spectrum of solvated electrons using multi-photon excitation.  
 (e) Real part  $n_{re}(\nu)$  (solid line) and imaginary part  $n_{im}(\nu)$  (dashed line) of the refractive index  $n(\nu)$  in the spectral range from 0 to 2 THz. Black line (1, 1'): neat water. Red lines (2, 2'):  $n(\nu)$  calculated for an electron concentration  $c_e = 5 \mu\text{M}$ . The symbols (open circles,  $n_{re}(\nu)$ ; solids diamonds,  $n_{im}(\nu)$ ) were derived from the 2D-THz measurements.

pronounced decrease in the real and imaginary part of the complex refractive index of the water sample.

To clarify the origin of the strong changes in the index of refraction, the 2D-THz experiments were complemented by THz pump/near-infrared probe experiments. After excitation by a THz pulse with a peak amplitude of  $1.9 \text{ MV/cm}$ , one observes a transient absorption band in the near-infrared (Fig.1(d)), which matches the electronic absorption spectrum of solvated electrons generated via multi-photon excitation (blue line). These results demonstrate that strong-field THz excitation leads to the creation of electrons solvated in the water environment.

Thus, the strong changes in both the real and imaginary parts of the refractive index upon THz excitation are a hallmark of solvated electrons.

To gain quantitative insight, the nonlinear response is described as a pump-induced change in the The present work shows for the first time how the interplay of strong fluctuating intermolecular electric fields and a much weaker directed external THz field induces tunneling ionization of water molecules. The latter could play an important role in the self-dissociation of  $\text{H}_2\text{O}$  molecules into  $\text{OH}^-$  and  $\text{H}_3\text{O}^+$ -ions. Beyond the insight into the

nonlinear THz response of water, the present work establishes a concept for enhanced charge separation and manipulation in aqueous systems with strong THz fields. complex refractive index. The real and the imaginary parts of  $n'(\nu)$  exhibit a marked decrease by  $\sim 10 \%$  compared to the stationary equilibrium  $n(\nu)$  (Fig. 1(e)). Theoretical calculations based on a local-field account for the observed changes of refractive index, in good agreement with our experimental observation.

## Publications

GFR20: A. Ghalgaoui, B. P. Fingerhut, K. Reimann, M. Woerner, and T. Elsaesser; Nonlinear terahertz response of solvated electrons in liquid water; in *The 22nd International Conference on Ultrafast Phenomena 2020*, F. Kärtner, M. Khalil, R. Li, F. Légaré, and T. Tahara (eds.) (OSA Publishing, Washington, D.C., USA, 2020); doi.org/10.1364/UP.2020.Th4A.4

GKS20: A. Ghalgaoui, L.-M. Koll, B. Schütte, B. P. Fingerhut, K. Reimann, M. Woerner, and T. Elsaesser; Field-induced tunneling ionization and terahertz-driven electron dynamics in liquid water; *J. Phys. Chem. Lett.* **11** (2020) 7717-7722

# A novel high-flux femtosecond hard x-ray source driven by a mid-infrared OPCPA system

A. Koç, C. Hauf, M. Woerner, L. v. Grafenstein, D. Ueberschaer, M. Bock, U. Griebner, and T. Elsaesser

Femtosecond X-ray diffraction experiments allow for studying structure changes of crystalline materials on atomic length and time scales. Such “movies” give direct insight in both the relocation of electronic charge and structural changes in the lattice, occurring after excitation of the material with femtosecond optical pulses. This technique has been implemented both with accelerator-based and laser-driven hard X-ray sources. So far, the table-top hard X-ray source developed at MBI has been driven by 35 fs pulses at 0.8  $\mu\text{m}$  central wavelength from an amplified Ti:sapphire laser system working at a 1 kHz repetition rate. It provides 100-fs long copper  $K\alpha$  pulses with an X-ray photon flux of  $5 \times 10^{10}$  photons per second emitted into the full solid angle. This source has been widely used in pioneering studies of transient charge densities and coupled nuclear-electronic motions in crystals. There is an increasing demand to determine more subtle changes of diffracted intensity on a multitude of Bragg reflections and to conduct the experiments faster, requiring a higher X-ray flux. Very recently, we have completed a new compact high-flux table-top femtosecond hard X-ray source with an unprecedented photon yield at a 1 kHz repetition rate,

driven by a four-stage mid-infrared optical parametric chirped pulse amplifier (OPCPA) system [GBU20b]. This driver system has been developed in project 1.2.

The generation of characteristic X-ray pulses in laser-driven table-top sources is based on the interaction of the strong electric field of a sub-100 femtosecond optical pulse with a thin metallic target in a three-step process: (i) Electron extraction from target into vacuum occurs via tunnel ionization by the in-plane electric component of the pulse  $E_{\perp}$  perpendicular to the target surface. (ii) Vacuum electrons are accelerated for a period given by optical cycle, and (iii) the accelerated electrons with a kinetic energy up to 100 keV re-enter the target which leads to the generation of characteristic  $K\alpha$  X-ray pulses with a femtosecond time structure. In parallel, spectrally broad bremsstrahlung is emitted in the full solid angle of  $4\pi$ . The maximum kinetic energy of the vacuum electrons scales with  $I_{\text{peak}}\lambda^2$ , where  $I_{\text{peak}}$  and  $\lambda$  denote the peak intensity and the central wavelength of the optical driver. Hence, the acceleration of the electrons is enhanced with longer wavelengths which results in a strong increase of the X-ray yield.

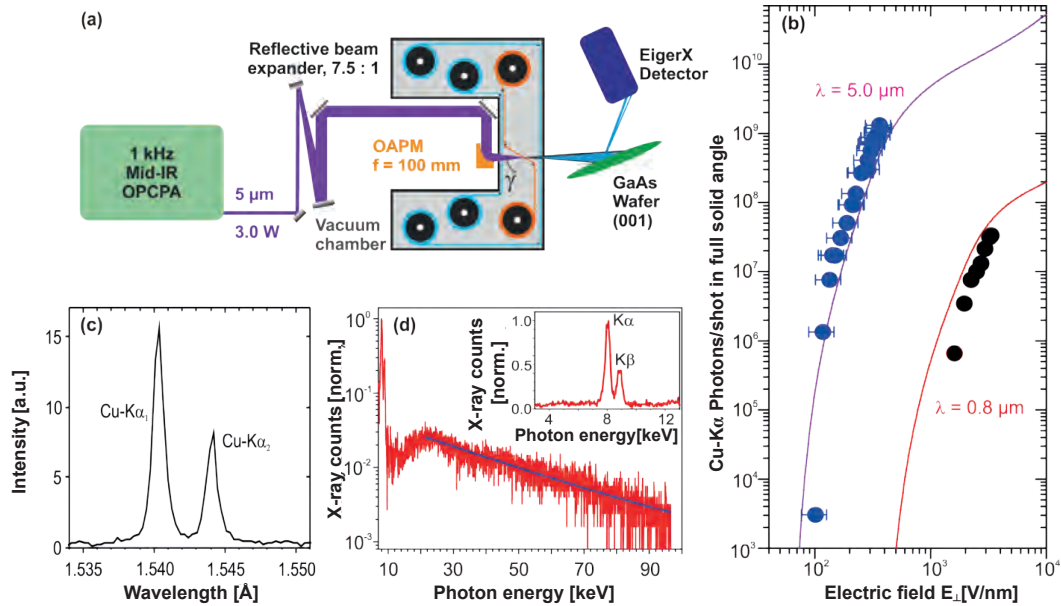


**Fig. 1:**

(a) Schematic of the experimental setup: four-stage optical parametric chirped-pulse amplifier laser system and laser-target interaction chamber (OAPM, off-axis parabolic mirror). (b) Cu- $K\alpha$  photons per pulse in full solid angle of  $4\pi$  as function of the in-plane electric field component  $E_{\perp}$  of the driving optical pulse perpendicular to the target surface. Blue and black symbols are the experimental data for the 5  $\mu\text{m}$  and 0.8  $\mu\text{m}$  optical drivers. The solid lines are the theoretical calculations. (c) The X-ray spectrum on the characteristic Cu- $K\alpha_1$  and Cu- $K\alpha_2$  emission. (d) Full X-ray spectrum of the source. The inset shows a magnified view of characteristic  $K\alpha$  and  $K\beta$  emission. The blue line is an exponential fit of the high-energy tail of bremsstrahlung giving a photon temperature of 29 keV.

Exploiting this concept, the four-stage OPCPA system pumped by a high performance chirped pulse amplifier at 2.0  $\mu\text{m}$  serves as optical driver for the new X-ray source. The OPCPA system provides an idler output at wavelengths around 5  $\mu\text{m}$  with an energy of up to 3.5 mJ per pulse and an 80 fs pulse duration at a 1 kHz repetition rate. The mid-infrared pulses display a nearly diffraction-limited beam profile and very low fluctuation in pulse energy (1.2% rms). For reaching a strong electric field on the target, the in-plane polarized 5  $\mu\text{m}$  pulses are focused onto a 20  $\mu\text{m}$  thick Cu target with a focal spot size of 19  $\mu\text{m}$ . The setup is schematically shown in Fig. 1(a). The Cu target (red lines/spools in Fig. 1(a) and two plastic tapes (blue lines/spools) are continuously moved during the laser excitation in order to provide a fresh target volume for each driver pulse and to remove the Cu debris. For a quantitative analysis, the characteristic  $K\alpha$  emission generated in transmission through the target is reflected from a GaAs single crystal and the (002) Bragg reflections of the  $K\alpha_1$  and  $K\alpha_2$  emission are detected with an area detector. The spectrum of the characteristic X-ray emission is shown in Fig. 1(c) with the clearly separated  $K\alpha_1$  and  $K\alpha_2$  components (photon energies 8047 eV and 8027 eV).

The measured total number of Cu- $K\alpha$  photons per pulse in the full solid angle  $4\pi$  is derived from the detected X-ray photon flux and plotted in Fig. 1(b) as a function of the electric-field component  $E_{\perp}$  perpendicular to the Cu target. We achieved the record value of  $1.5 \times 10^9$  Cu- $K\alpha$  photons in a single femtosecond X-ray pulse corresponding to a total flux of  $1.5 \times 10^{12}$  X-ray photons per second. Such an average flux is 30 times higher than that of the best femtosecond hard X-ray sources driven by Ti:sapphire lasers with kHz repetition rates (black symbols in Fig. 1(b)). Most important, there is a marked difference between the driving electric fields of both sources. The much smaller driving field required for pumping at 5  $\mu\text{m}$  is a consequence of the  $I_{\text{peak}}\lambda^2$  scaling of the electron kinetic energy. The magenta and red lines in Fig. 1(b) are the result of theoretical calculations for 5  $\mu\text{m}$  and 0.8  $\mu\text{m}$  optical drivers. The full X-ray spectrum as measured with an energy resolving CdTe detector in the single photon regime (energy resolution 500 eV) is shown in Fig. 1(d). From the high-energy tail of the broad spectrum of bremsstrahlung one estimates a photon temperature of 29 keV for the 5  $\mu\text{m}$  driving wavelength. Consistent with the theoretical predictions, this photon temperature is much higher than the photon temperature 19 keV achieved for a 0.8  $\mu\text{m}$  driver. A duration of the hard X-ray pulses of approximately 120 fs is estimated from the theoretical analysis of the generation process.

In summary, the present results establish a highly versatile technology for ultrafast time-resolved X-ray diffraction studies. First experiments are currently underway.

## Publications

GBU20b L. v. Grafenstein, M. Bock, D. Ueberschaer, E. Escoto, A. Koç, K. Zawilski, P. Schunemann, U. Griebner, and T. Elsaesser; Multi-millijoule, few-cycle 5  $\mu\text{m}$  OPCPA at 1 kHz repetition rate; *Opt. Lett.* **45** (2020) 5998-6001

KHW A. Koç, C. Hauf, M. Woerner, L. v. Grafenstein, D. Ueberschaer, M. Bock, U. Griebner, and T. Elsaesser; Compact high-flux hard X-ray source driven by femtosecond mid-infrared pulses at a 1 kHz repetition rate; *Opt. Lett.* (in press)

# Lightwave topology for strong-field valleytronics

Á. Jiménez-Galán, O. Smirnova, M. Ivanov

Intense light fields shaped at the femtosecond and sub-femtosecond timescale of individual oscillations provide unique opportunities for imaging and steering the coherent electronic response at timescales of 0.1 fs-10 fs. These capabilities are at the core of lightwave electronics – ultrafast optical control of the electron dynamics in solids, aiming at information processing at petahertz rates. When a material is dressed by a strong laser field, it acquires additional dimensions associated to the number of photons absorbed in the Floquet formalism. This allows to manipulate the parameters of the materials in the laser-dressed sample, which are otherwise fixed. One of the most attractive possibilities of Floquet engineering of materials is to induce topological phase transitions, i.e., Floquet topological insulators, which was proposed and realized experimentally 10 years ago. It is known that a gap can be opened in graphene by using circular fields with frequencies larger than the bandwidth, while the gap can be closed in gapped graphene systems by using resonant circular fields. Yet, in the cycle-average, resonant (or above-resonant) regime in which the Floquet formalism works, the timescale of control for these processes is given by the full duration of the laser pulse. In our work, we bring the frequency-domain concept of topological Floquet

systems to the few-femtosecond time-domain by manipulating the topological properties of two-dimensional materials with fields well below resonance that are tailored on the sub-laser-cycle timescale to the symmetry of the lattice. Using these concepts, we show that we can modify the band structure of 2D materials to create valley-selective excitation without relying on the optical valley selection rule and on time-scales given by the individual light oscillations, orders of magnitude faster than valley lifetimes, which is crucial for the implementation of valleytronic devices.

In our theoretical study, we consider gapped graphene systems, e.g., hexagonal boron nitride, or transition metal dichalcogenide TMD-like systems, as shown in Fig.1(a). To a first approximation, these materials can be described by two bands with different on-site energies  $M$  at each atom, opening a gap  $2M$  at  $K$  and  $K'$ , a first neighbour hopping  $t_1$ , a real second neighbour hopping  $t_2$  and negligible higher-order hoppings. The second neighbour hopping must be real in order to preserve the time-reversal invariance of the system. A complex second neighbour hopping breaks this symmetry and lifts the degeneracy between the  $K$  and  $K'$  valleys. If this symmetry is strongly broken, one of the valleys will

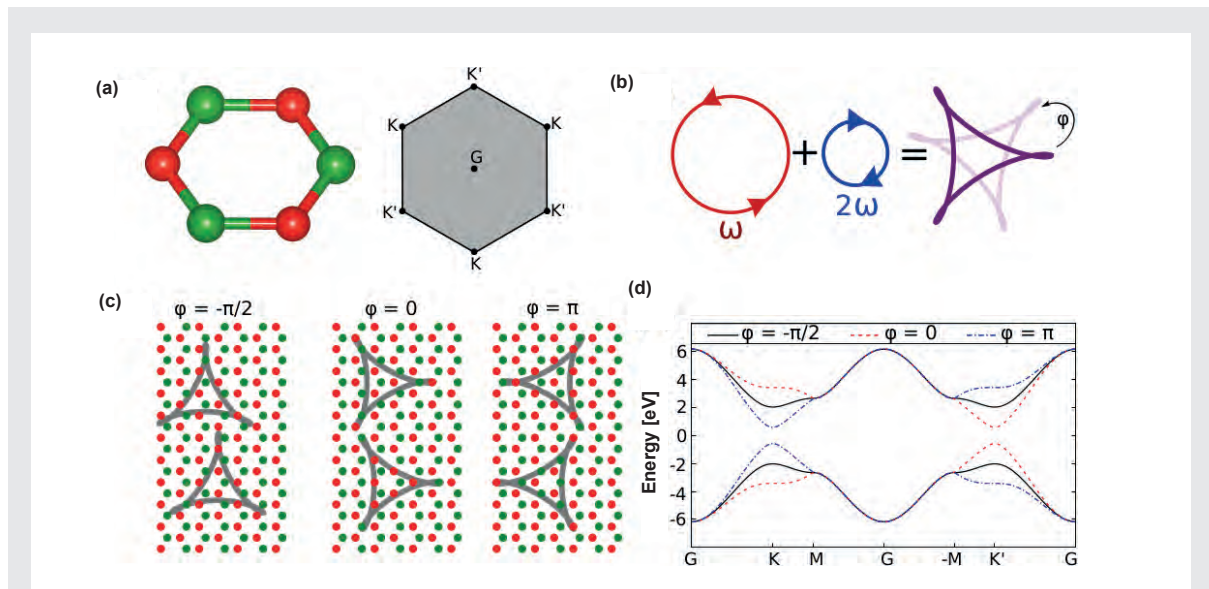


**Fig. 1:**

(a) A 2D hexagonal lattice with broken inversion symmetry in real space (left), with red and green representing two different atoms, and reciprocal space (right), with the valleys  $K$  and  $K'$  at the vertices.

(b) The Lissajous figure generated by the field (purple trefoil) has the symmetry of the sublattice and can be rotated by changing the relative phase,  $\phi$ , between the two colours.

(c) Depending on the field orientation (grey trefoil), the two atomic sites are addressed differently.

(d) For  $\phi = -\pi/2$ , the field interacts with both atoms equally and the bands show valley degeneracy (black solid line). For  $\phi = 0$ , the field interacts with the two types of atom differently (note how the two atoms inside the trefoil are now not interchangeable, irrespective of where the field is placed in the lattice). This lifts the valley degeneracy (red dashed line). For  $\phi = \pi$ , the situation is reversed (blue dash-dotted line).

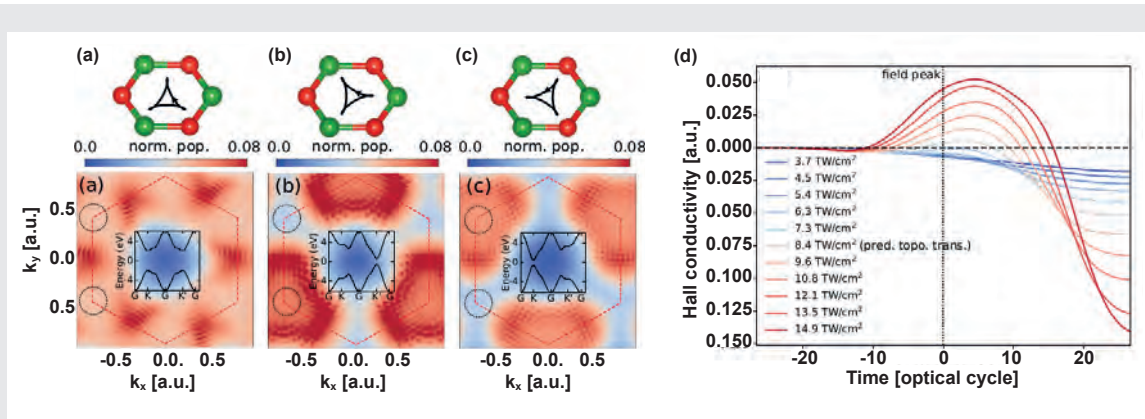


**Fig. 2:**

(a-c) Normalized electron populations (colour scale) in the lowest conduction band of hBN after applying a bicircular field with  $\lambda = 3\mu\text{m}$  and a two-color phase delay of  $\varphi = -\pi/2$  (a),  $\varphi = 0$  (b) and  $\varphi = \pi$  (c). The insets in a-c show the modified, cycle-averaged band structures for hBN at each  $\varphi$ . The red hexagon shows the first Brillouin zone, with the K and K' valleys at the vertices. (d) Curves showing the time-dependent Hall conductivity in hBN induced by bicircular fields with fixed carrier  $\lambda = 3\mu\text{m}$  and different total electric field amplitudes (low intensity with cold colours, high intensity with warm colours). The grey line corresponds to the analytical prediction of the topological phase transition, which coincides with a change of sign in the Hall conductivity at the peak of the field ( $t=0$ ).

close the band gap, changing the topology of the system from a trivial insulator into a quantum anomalous Hall or Chern insulator. The condition for this to occur was given by Haldane in his seminal paper, where he proposed to break time-reversal symmetry with a staggered magnetic field that has vanishing flux through the unit cell. This gives the second neighbour hopping a complex value and chiral direction such that when  $\text{Im}(t_2) > M/(3\sqrt{3})$ , the system undergoes a topological phase transition. This proposal has so far escaped realization in condensed matter systems.

In order to achieve a breaking of the time-reversal symmetry, we investigated the use of a field tailored to the symmetry of the sub-lattice (Fig.1(b)). Such trefoil field is made of a superposition of a circularly-polarized fundamental field and its counter-rotating second harmonic. The dressed system then breaks temporal symmetry depending on the orientation of the trefoil in space with respect to the sample, as shown in Fig.1(c). This orientation is controlled by the phase delay between the two colours, and can therefore be controlled on a sub-laser cycle timescale with current ultrafast laser technology. Using lowest order perturbation theory, we predict that the second neighbour hopping will acquire an imaginary component that is dependent on the phase-delay between the two pulses, i.e., the orientation of the pulse in space, which is stronger for low-frequency and high-intense fields. As the field is rotated, the second neighbour hopping is modified and therefore the valley degeneracy is lifted, see Fig.1(d).

To test this prediction, we performed ab-initio simulations on hexagonal boron nitride and MoS<sub>2</sub>. The field-free band structures were obtained from first principles using open-source density functional theory codes. The field-free system was then propagated in the presence of the bicircular field in the length gauge and in the dipole approximation using a basis of maximally-localized Wannier functions, which allows a consistent phase re-

lation between couplings at different crystal momenta. We computed the electron populations in the conduction band at the end of the pulse, for different phase-delays between the two pulses, as shown in Fig. 2(a-c). We observe no valley polarization for a phase-delay  $\varphi = -\pi/2$  (panel a), a maximum of population localized at the K' valley for  $\varphi = 0$  (panel b), that switches to the K valley for  $\varphi = \pi$ . The mechanism for valley polarization here is completely different from that of conventional, resonant valleytronics with circular light: valley population switches only when the trefoil is rotated, i.e., for different phase delays, irrespective of the field helicity. The band structure modification induced by the tailored field, in combination with the exponential sensitivity of tunneling ionization to the band gap, leads to an increase of population injection at the valley with the minimum band gap. The same was found for MoS<sub>2</sub>. Rotation of the trefoil on the sub-laser-cycle scale allows control over the band structure properties and valley physics on the timescale of individual light oscillations, not the full pulse duration.

We additionally performed simulations for various field strengths and frequencies, scanning through the threshold values that lead to the predicted topological phase transition (Fig.2(d)). We observe that the cycle-averaged Hall conductivity during the pulse, defined as the Chern number but for time-dependent populations, precisely changes sign at these values, hinting the closing of the band gap in the laser-dressed system. In this way, our work may open the way to a new, non-resonant, ultrafast regime of valleytronics and light-induced control of topological properties.

## Publication

JSS20: Á. Jiménez-Galán, R.E.F. Silva, O. Smirnova and M. Ivanov; *Lightwave control of topological properties in 2D materials for sub-cycle and non-resonant valley manipulation*; Nat. Photonics **14** 728-732 (2020).

# Extending solid-state calculations to ultra long-range length scales

S. Sharma

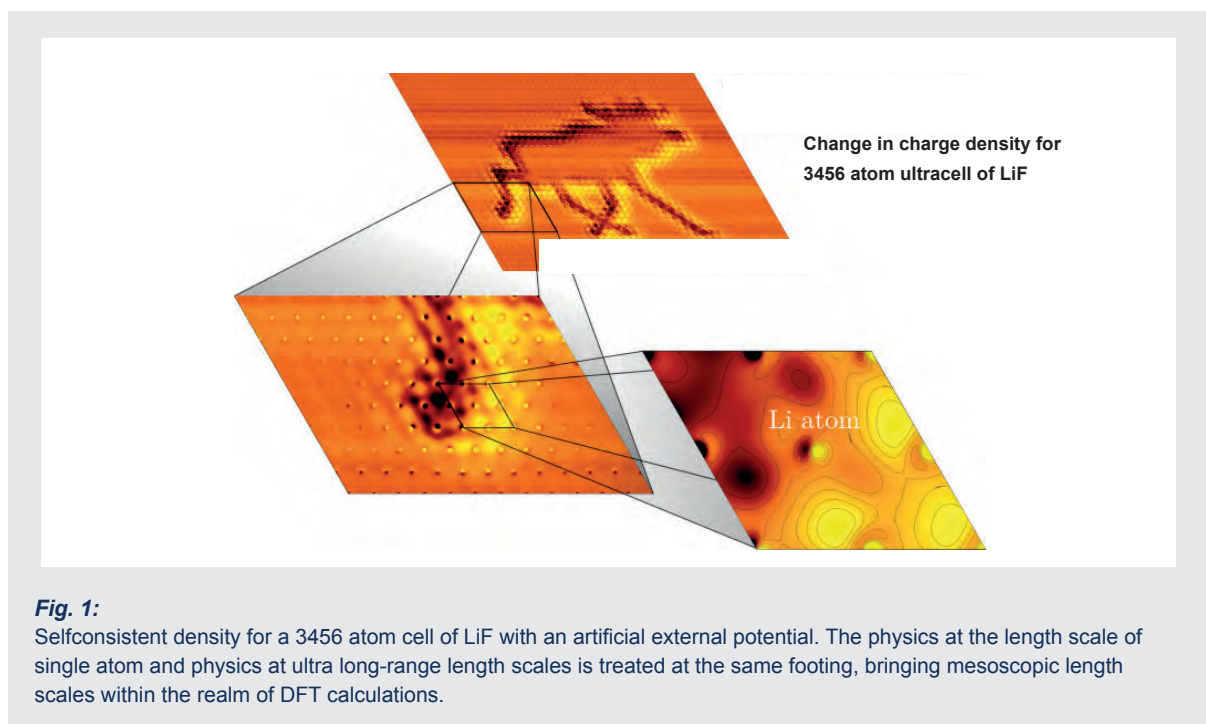
Density functional theory (DFT) has had a tremendous impact on solid-state physics and is, due to its computational efficiency, at the heart of modern computer based material research. While DFT offers in-depth understanding of microscopic properties, so far it cannot tell anything about physics on larger, mesoscopic length scales. Such effects include long-ranged quasiparticles, magnons, skyrmions, magnetic domains, or spatially dependent electric fields. As DFT is a formally exact theory, the underlying physics for such phenomena is readily at hand, yet actual calculations remain the very difficult. While it is, in principle, possible to use ever larger super-cells, in practice one quickly reaches the limit of computational viability.

We have now developed a fundamentally different approach to drastically extend the length scale of DFT calculations without significantly increasing the computational cost. As reported in our recent work, the approach relies on altered Bloch states by introducing an additional sum in the Bloch states over a finer grid in reciprocal space around each k-point. The resulting densities then become a Fourier series with a controllable periodicity, which may extend to nanometers. To demonstrate the power of the new method, the scientists have performed a calculation which is too large for a conventional super-cell. Calculations were performed for 3456 LiF units under a random potential – for demonstration purposes in the shape of an Elk. The calculation was performed on 480 CPU cores and each iteration took about 40 minutes. The convergence was achieved in 24 iterations. This level of performance for

an all-electron calculation indicates that physical phenomena involving modulations of the electronic state over hundreds or thousands of unit cells are within reach of this approach, paving the way to calculations of mesoscopic systems, such as magnetic domain walls or skyrmions, which have so far been too “computationally expensive” and hence out of reach for ab-initio methods.

## Publication

MSG20: T. Müller, S. Sharma, E.K.U. Gross, and J.K. Dewhurst; Extending solid-state calculations to ultra-long-range length scales; Phys. Rev. Lett. **125** (2020) 256402/1-5





# **Short Description of Research Projects**



# 1.1: Fundamentals of Extreme Photonics

*O. Smirnova, B. Fingerhut (project coordinators)*

*and M. Ivanov, K. Busch, M. Kück, A. Perez-Leija, K. Tschernig, D. Reiche, F. Loth, T. Bredtmann, S. Patchkovskii, Á. Jiménez-Galán, S. Carlstroem, W. Becker, D. Milosevic, H. Reiss, F. Morales, I. Babushkin, D. Ayuso, A. Ordonez, M. Richter, A. Harvey, J. Kaushal, A. Andreev, J. Herrmann, A. Gusakov, M. Osswald, E. Palacino-González, N. Acharyya, R. Ovcharenko, S. Sharma, N. Singh, S. Shallcross, P. Elliott, Q. Li, P. Scheid, P. Stammer, S. Solovjev*

## 1. Overview

The main objective of the project 1.1 in 2020 has remained to be the development of analytical and numerical methods for the description of light-matter interactions in extreme conditions. The number of photons in a light field incident on a system can range from zero (vacuum fluctuations), to just a few (quantum electrodynamics and quantum optics regime), to hundreds and thousands of absorbed or emitted photons during the interaction with very intense light fields. When a low number of photons are involved, the quantum properties of matter and light play very important role in the description of the interaction. At high intensities, the description of light as a classical electromagnetic wave is adequate, but a precise description of the (often highly nonlinear) quantum response of matter is needed. Non-perturbative theoretical models and methods are developed and applied, focusing on adequate description of system's optical properties and geometrical structure, as well as on many-body effects such as electron-electron correlation, coupled electronic and nuclear dynamics, optically induced and controlled spin dynamics, including laser-driven and laser-controlled ultrafast spin and magnetization dynamics in solids, and the role of quantum coherence in these dynamics. The range of material systems involves atoms, molecules, and solids – from dielectrics to semiconductors to magnetic materials, and photonic structures such as waveguides.

## 2. Topics and collaborations

In 2020 the project was organized around five general directions:

**T1: Theory of attosecond and few-femtosecond electron dynamics**

**T2: Theory of matter in intense laser fields**

**T3: Theoretical optics and photonics in structured media (Joint HU-MBI Group)**

**T4: Bio-molecular dynamics in condensed phase**

**T5: Condensed matter theory**

In-house collaborations with Projects 1.2, 2.1, 2.2, 2.3, 3.1, and 3.2.

External collaborations: IC London (UK), HU Berlin, TU Berlin, The Weizmann Institute, CEA Saclay (France), CELIA and University Bordeaux (France), University of Ottawa (Canada), UCLA (USA), RQC Moscow (Russia), UA Madrid (Spain), University Trieste (Italy), XLIM Limoges (France), University Sherbrook (Canada), University of Central Florida, (USA), University Sarajevo (Bosnia-Herzegovina), University Geneva (Switzerland), MPI Halle (Germany), Hebrew University of Jerusalem (Israel), University of Colorado and JILA (USA), University of Zurich (Switzerland).

## 3. Results in 2020

Representative results are given below for a range of general research direction.

### T1-T2: Sub-cycle valleytronics

The isolation of single-layer 2D materials signaled a breakthrough in modern condensed matter physics. One of the most exciting prospects of these materials is the possibility to harness an additional electronic degree of freedom, known as the valley pseudospin, for efficient information processing, known as valleytronics. Valleys are energy-degenerate extrema of the crystal band structure. In hexagonal 2D materials, there are two valleys, located at the  $\mathbf{K}$  and  $\mathbf{K}'$  points of the hexagonal Brillouin zone (BZ). The localization of the electrons in one or the other valley is labeled by the valley pseudospin that takes the values of  $\mathbf{K}$ ,  $\mathbf{K}'$ , or their coherent superposition.

Development of methods to selectively excite a desired valley in 2D materials has emerged as one of important research topics. So far, valley polarization, i.e., selective electron population injection into one of the valleys, has been achieved using circularly-polarized light with frequency tuned to the transition energy between the valence and the conduction bands of the BZ at the  $\mathbf{K}$ ,  $\mathbf{K}'$  points. The resonance ensures that conduction electrons are injected into one of the two valleys. The selection between the two degenerate valleys is done by taking advantage of the valley selection rules: resonant light couples to one or the other valley depending on its helicity, so that clockwise-rotating resonant field couples to only one valley while the counter-clockwise rotating field couples to the other. However, such resonant fields: i) are material specific, ii) offer temporal control limited by their envelope duration, iii) rely on the optical valley selection rule outlined above, which is not applicable in many non-inversion symmetric systems.

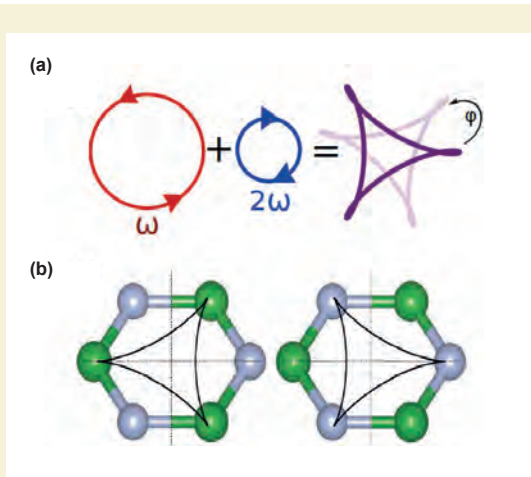


**Fig. 1:** Valleytronics with polarization-shaped non-resonant light field. (a) The trefoil Lissajous figure generated by the field. Its orientation is controlled by the relative two-color phase. (b) Hexagonal structure with two different atoms, e.g. hBN. Changing  $f$  rotates the trefoil relative to the crystal structure and selects the valley.

Development of robust and non-material-specific methods of selective valley excitation in 2D quantum materials has emerged as one of the key current research top-

ics. Following the successful work on topological strong field physics on sub-cycle time scale in 2019 [SJA19], which in turn extended our work on high harmonic spectroscopy of phase transitions [SBR18], we have developed a new protocol for selective valley excitation in gapped hexagonal 2D materials [JSS20].

In this work we have considered application of the bi-circular light field generated by the combination of the counter-rotating circularly polarized fundamental field with frequency  $\omega$  and its second harmonic  $2\omega$  to a hexagonal 2D material. The Lissajous figure of such field forms a tre-foil structure symmetric with respect to 120 degrees rotation in the polarization plane, see Fig. 1. We have shown that the valley is selected by changing the two-color time-delay between the two pulses on the sub-cycle time-scale. This controls the orientation of the Lissajous figure generated by the two-color field relative to the geometry of the lattice, see Fig.1 (b). Crucially, there is no requirement for resonance in this scheme.

It is also widely accepted that linearly-polarized light, which couples equally to both valleys, is not suitable to generate valley polarization. In our work [JSS21], we demonstrate that this is not always true and introduce a non-material-specific, single-pulse method to control the valley excitation and read the valley pseudospin on timescales shorter than valley polarization, using linearly polarized nearly single-cycle pulses with controlled

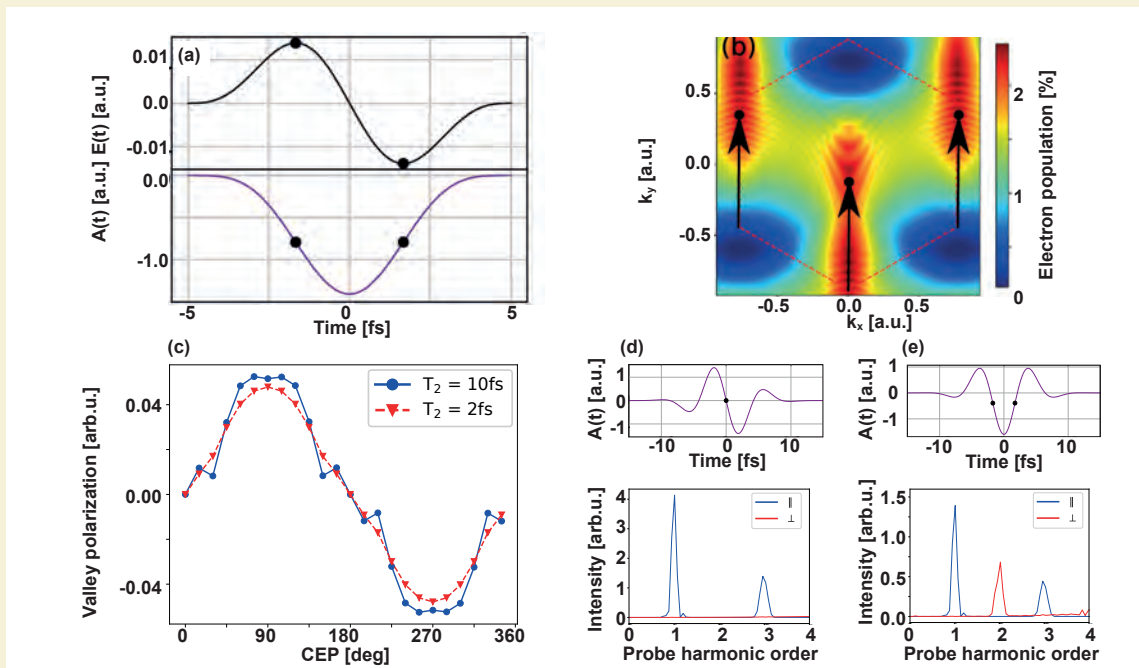


**Fig. 2:** Sub-laser-cycle valleytronics with linearly polarized fields. (a) Electric field (top) and vector potential (bottom) showing the field peaks (black dots), where the electron injection mostly occurs, corresponding to a non-zero vector potential amplitude. (b) Conduction band electron populations in the Brillouin zone after the pulse. Arrows indicate the streaking from the minimum band gap crystal momenta  $k_0$  to  $k_0 - AL(0)$ , see text. (c) CEP control of valley polarization for two dephasing times (10fs and 2fs). (d,e) Lower panels show the HHG spectrum of a probe field that comes after the single-cycle pulses shown in the upper panels. Second harmonic is absent for the case of no valley polarization (panel d) and strongly present for the case of maximum valley polarization (panel e). Blue and red indicate the components parallel and perpendicular to the probe field, respectively, which is polarized along  $x$ . (Adapted from [JSS21]).

carrier envelope phase (CEP) and with a carrier frequency well below the bandgap of the material. In this regime, electrons are injected into the conduction band near the instantaneous maxima of the electric field, marked with black dots in Fig.2(a). Also, the injection occurs near the minima of the bandgap, hence initiating the population in both K and K' valleys. There is no preference between the two valleys during the injection. Charge injection is followed by light-driven acceleration of electrons and holes inside the bands. The electron crystal momenta at the end of the pulse depends on the strength of the vector potential at the injection time as  $k=k_0-A_L(t_0)$ , where  $k_0$  and  $A_L(t_0)$  are the crystal momenta and laser vector potential at the time of injection  $t_0$ . The final electron distributions are thus not located at K,K', but are shifted by  $-A_L(t_0)$  (see Fig.2(b)). Changing the CEP of the field changes the magnitude of  $A_L(t_0)$ , allowing to control where the final electron population resides in the Brillouin zone. In this way, one can control the valley polarization with few-cycle pulses by changing the CEP (Fig.2(c)). When valley polarization is present, the hexagonal system breaks the inversion symmetry along the y-direction (see Fig.2(b)), leading to the appearance of even harmonics in the high harmonic spectrum driven by a posterior probe pulse. Thus, the strength of the even harmonics in the high harmonic spectrum serves as an all-optical probe of the valley pseudospin (see Fig.2(d),(e)).

### T1-T2: Air lasing inside laser filaments

In 2020, we have continued our research on the “air lasing” effect, where 391 nm radiation is generated very efficiently during propagation of intense femtosecond laser pulses in air, under standard conditions where laser filamentation leads to self-guiding of light. The 391 nm line corresponds to the transition between the two ground vibrational levels  $v'',v' \neq 0$  of the ground and

second excited electronic states  $X^2\Sigma_g^+$  and  $B^2\Sigma_u^+$  in  $N_2^+$ . Identifying the mechanism responsible for the coherent emission at this line has been a long-standing puzzle, as it is unclear how population inversion between the X and B states is created by the fs laser pulse, whose intensity is clamped around  $10^{14}$  W/cm<sup>2</sup> during filamentation. We have shown in [RLM20] that neither electronic, nor vibrational, nor rotational population inversion is necessary. Amplification is possible without inversion thanks to the combination of molecular ionization and molecular alignment, both unavoidable in intense light fields.

In a medium prepared in a specific superposition state, quantum interference may fully suppress absorption while leaving stimulated emission intact, opening the possibility of lasing without inversion (LWI). Conventional LWI schemes generally strive to maintain a specific phase relationship between the lower-lying states that carry most of the population. In [RLM20] we identified a scheme that does not follow this tradition. It uses only the natural dynamics of a multi-level quantum system and requires no coherence between the excited and the lower electronic states; effectively, LWI comes “for free”.

We have focused on the pump-probe scheme typically employed to study the lasing effect in  $N_2^+$ : an intense pump pulse prepares the gas and transient absorption (or gain) of a delayed probe pulse is measured. The short pump pulse impulsively aligns the neutral  $N_2$  molecules, generating rotational dynamics. It also ionizes some of the  $N_2$  molecules, producing molecular ions mostly in the ground X, but also in the excited  $A^2\Pi_u$  and B states, and continues to align them. After the end of the pulse, the ions continue to rotate, soon reaching maximum alignment, followed by periodic revivals of alignment and anti-alignment with the revival periods of the ions controlled by their different, state-dependent rotational constants.

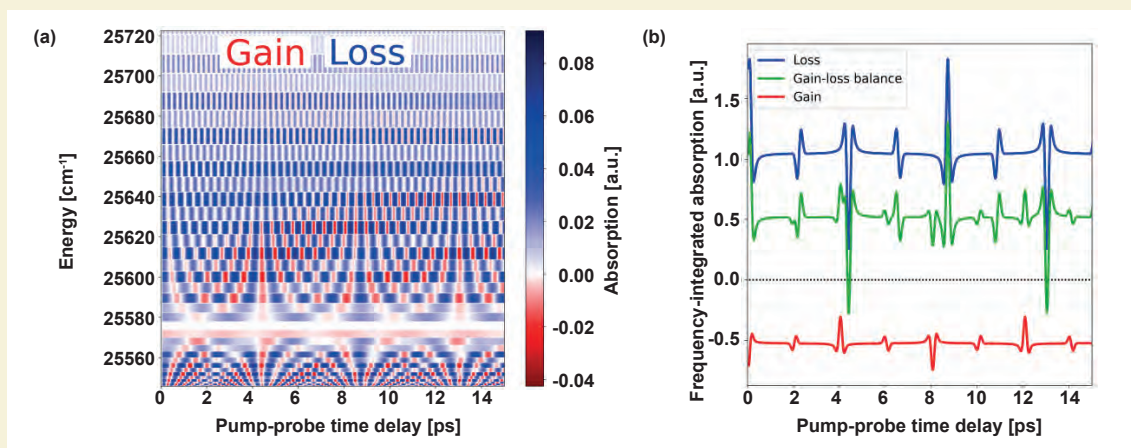


**Fig. 3:**

*Rotational quantum beat lasing without inversion. Calculations are performed for  $N_2$  molecules interacting with a 23 fs, 800 nm,  $10^{14}$  W/cm<sup>2</sup> pump pulse, a 20 fs, 391 nm,  $10^{11}$  W/cm<sup>2</sup> probe pulse. The molecules are at a room temperature (298 K). (a) Full simulation of the frequency-resolved gain (red) and loss (blue) of the weak probe interacting with the pumped system as a function of pump-probe delay. (b) Absorption (blue) and emission (negative absorption) (red) integrated over all frequencies follow the alignment dynamics of states X and B. The overall gain-loss balance integrated over all frequencies (green) shows gain windows (at  $\sim 4.3$  ps and  $\sim 13.0$  ps) for the inversionless medium.*

Opportunities for inversionless amplification of a short, time-delayed probe pulse, polarized parallel to the pump, arise when the X state molecules are anti-aligned, and the parallel  $X \rightarrow B$  absorption is suppressed. This opportunity is further enhanced if the B state molecules are aligned at this time, so that the parallel  $B \rightarrow X$  emission is enhanced. Due to the different rotational constants in X and B, their rotations go out of sync, arriving at points where the more populated X state is aligned or anti-aligned, while the B state shows no distinct alignment. These points in time correspond to temporal windows of loss and gain, respectively, that occur across the whole rotational band, leading to rotational quantum beats in the time-resolved gain-loss of the short probe pulse [RLM20], see Fig. 3. In general, gain windows open when  $P_X \langle \cos^2 \theta \rangle_{X_0}(t) - P_B \langle \cos^2 \theta \rangle_{B_0}(t) < 0$ , i.e., the product of the population and the molecular alignment measure for the ground state  $|X, v'=0\rangle$  is smaller than the corresponding product for the excited state  $|B, v'=0\rangle$ . In the frequency domain, see Fig. 3a, this leads to frequency-resolved loss and gain windows.

Fig. 3 incorporates comprehensive modeling of the pump-probe process, starting with the thermal ensemble of neutral molecules and accounting for (i) the laser-induced alignment of the neutral molecule, (ii) its alignment-dependent strong-field ionization into the laser-dressed ionic states, (iii) the coupled electronic, vibrational, and rotational dynamics in the ion, and (iv) calculations of the frequency-resolved transient absorption and emission of the probe pulse.

Together with our theoretical colleagues from the University of Ottawa, we have extended our microscopic response model, including the propagation of the probe pulse in the ionized and rotationally excited gas of  $N_2$  molecules using a coupled Maxwell-von Neumann model [LRM20]. The results confirm the role of rotational quantum beat LWI in the air lasing phenomenon. It also shows that as the total gain increases, the rotationally driven modulations of the gain start to diverge from the  $P_X \langle \cos^2 \theta \rangle_{X_0}(t) - P_B \langle \cos^2 \theta \rangle_{B_0}(t) < 0$  gain estimate. This divergent behavior occurs due to the non-flat structure of the seed spectrum that results from the growth of the gain lines at the  $B \leftrightarrow X$  transition frequencies.

## T2: Enantio-sensitive unidirectional light bending: structuring light's chirality to "bend" the enantio-sensitive response of chiral matter on ultrafast time scales

Structured light, which exhibits nontrivial intensity, phase, and polarization patterns in space, has key applications ranging from imaging and 3D micromanipulation to classical and quantum communication. However, to date, its application to molecular chirality, has been limited by the weakness of magnetic interactions. Our work [AOS20] shows how to structure light's local handedness in space to introduce and realize an enantio-sensitive interferometer for efficient chiral recognition without magnetic interactions, which can be seen as an enantio-sensitive version of Young's double slit experiment.

The chiral Young's double slit experiment involves two chiral emitters of opposite handedness, see Fig. 4(a). The combination of the achiral (left-panel) and enantio-sensitive (central panel) components of the emission leads to enantio-sensitive bending of the emitted light (right panel). The interference pattern is shifted to the right or to the left, depending on the relative positions of the left- and right-handed slits.

One way of creating chiral emitters with controlled handedness and positions is to structure the local handedness of synthetic chiral light [ANO19] (see also [NAD19]) in a way that it creates dipoles of chirality. In analogy with a dipole of charge, a dipole of synthetic chiral light changes handedness in space, from left- to right-handed, or vice versa. Such structured light can be created using two beams propagating non-collinearly, at small angles of  $\pm 5^\circ$ . Both beams contain a fundamental  $\omega$  field, linearly polarized in the plane of propagation, and a weak second harmonic, polarized orthogonal to this plane. In the overlap region, the tip of the total electric field vector draws a chiral, 3D Lissajous figure in time, at each point in space. By controlling the  $\omega$ - $2\omega$  phase delays, we can structure the field's handedness at will, in a way that it creates dipoles of chirality, either with the left-handed field on the left and the right-handed field on the right, i.e. the realizing a "LR" dimer of chiral light, or vice versa, "RL".

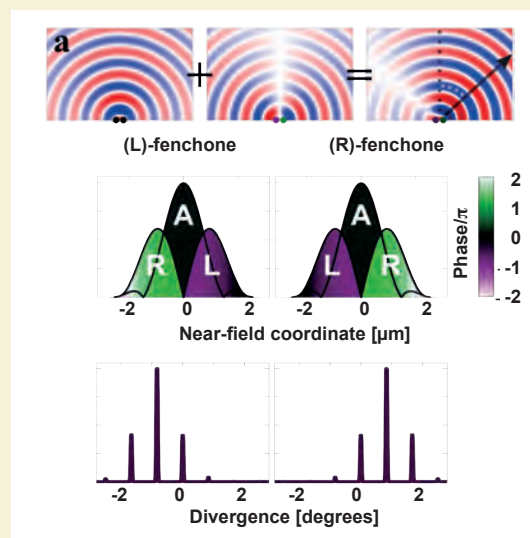


**Fig. 4:** Enantio-sensitive light bending. a, Chiral Young's double slit Gedankenexperiment: the superposition of the achiral component of the emission (even with respect to the center, left panel) and the enantio-sensitive component of emission (odd, central panel) leads to enantio-sensitive bending of the emitted light (right panel). b, Achiral (black) and chiral (green and purple) components of the nonlinear response driven by a chirality polarized field in randomly oriented left- (left panel) and right-handed (right panel) fenchone at frequency  $12\omega$  (see laser parameters in AOS20); the phase is encoded in the colours. c, Far-field emission at frequency  $12\omega$  from left- (left) and right-handed (right) randomly oriented fenchone molecules as a function of the emission angle.

Chirality-polarized light imparts amplitude and phase grating onto the nonlinear response of isotropic chiral matter, creating chiral emitters of opposite handedness at different positions in space. The relative positions of these “slits” depends on the medium’s handedness. Fig. 4(b) shows the nonlinear response of randomly oriented fenchone to a structured field with polarization of chirality, see [AOS20]. In the left-handed enantiomer (left panel), we create a sequence of slits where the left-handed slit is on the left, and the right-handed slit on the right. In the right-handed enantiomer, the positions of the emitters are exchanged.

The interference of these chiral emitters leads to unidirectional bending of the emitted light, in opposite directions in media of opposite handedness, see Fig. 4(c). Note that since the two chiral emitters have opposite handedness, the overall double-slit structure is achiral. However, the spatial arrangement of the chiral slits breaks the parity of the interference pattern. Importantly, the way parity is broken, i.e. whether the first slit is left-handed and the second slit is right-handed, or vice versa, is dictated by the medium handedness, and defines the direction of light deflection.

Our work introduces the concepts of *polarization of chirality* and *chirality-polarized light*, exposes the immense potential of sculpting light’s local handedness, and offers novel opportunities for efficient chiral discrimination, enantio-sensitive optical molecular fingerprinting and imaging on ultrafast time scales.

## T2: Evidence of Freeman resonances in intense two-color counter-rotating laser fields

The electronic structure of an atom or a molecule is modified when the system is exposed to a strong light field. This transient modification is ubiquitous and affects all aspects of light-matter interaction, with examples relevant to this project including atomic stabilization against ionization, leading to new amplification lines during laser filamentation [MMP18] and new structures in photoelectron spectra [MRP11]. The ponderomotive

Stark shift of the ionization potential and of the excited states is of particular interest, as it leads to resonant multiphoton absorption into laser-dressed states – the so-called Freeman resonances.

In this project we used the so-called bi-circular fields, which consist of two counter-rotating, circularly polarized laser fields, usually set with a frequency ratio,  $s$ , between both fields ( $s\omega_1 = \omega_2$ ). These fields enable processes that are typical of linearly polarized light only, such as high harmonic generation or re-scattering of the ionized electron, combined with processes known for circularly polarized light, such as electron spin polarization upon strong field ionization. The total electric field vector of the counter-rotating fields has a 3-fold symmetry that is imposed onto the system.

By performing Time Dependent Schrödinger Equation (TDSE) simulations of the Hydrogen atom, exposed to an 800 nm – 400 nm counter rotating bi-circular laser field, we found that the 3 fold symmetry is broken in the photoelectron angular distributions (see Fig 5(b)) [SPM20].

In particular, some features appear at low electron energy, which exhibit a completely different symmetry as that of the field (see Fig. 5(a)). The same laser applied to a Yukawa Hydrogen-like atom (which has the same ionization energy as Hydrogen, but no bound states) does not exhibit such features (see Fig. 5(b)), which serves as the first indication of the role of the excited states in the strong-field photoionization processes. Furthermore, the overall shape of the angular distribution of the hydrogen atom is also rotated with respect to the Yukawa, due to the long-range Coulomb interaction of the outgoing electrons, in the same way direct electrons drift in the case of circularly polarized light.

By doing a partial wave analysis, and by studying the dependence of this low energy asymmetric structure with respect to the intensity of the laser field, and by studying the population of Rydberg states as a function of laser intensity and pulse duration, we were able to show that the appearance of such low energy features

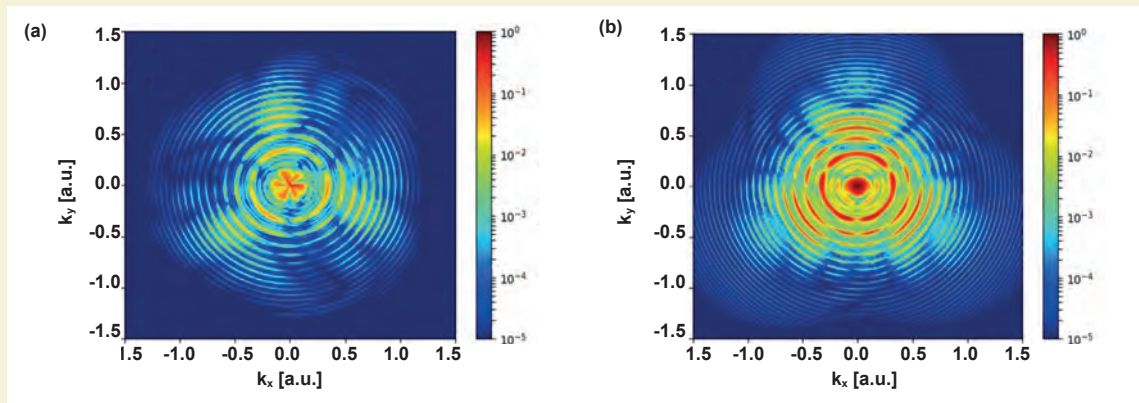


**Fig. 5:** Photoelectron momentum distribution after strong field ionization in a bicircular laser field normalized with respect to the highest intensity on logarithmic scale: from the (a) hydrogen and (b) short-range Yukawa potential. A 1-4-1 cycle pulse ( $t_{\text{on}} = t_{\text{off}} = 1$  cycle,  $t_{\text{flat}} = 4$  cycles, i.e.,  $\tau \approx 16$  fs) with the field strength of  $F_0 = 0.03065$  atomic units was used.

is due to the interference between a direct and resonant ionization pathway. This resonant pathway is controlled by the wavelength and the field strength of the incident light, which, via ac-Stark shifts, moves the states in and out of resonance [SPM20]. Bi-circular fields allowed us to show that the low-energy features manifest themselves for very short few-cycles pulses, revealing the sub-cycle nature of the excitation dynamics, and how is possible to control it by controlling the relative parameters of the field.

### T3: High-order synthetic dimensions in waveguide photonic lattices

The research in T3 has been concerned with non-linear and quantum plasmonics as well as with quantum photonics and few-photon nonlinearities in photonic structures waveguide arrays inscribed in glass.

Specifically, with regards to quantum photonics, we have investigated the properties of multi-photon states that propagate through arrays of coupled waveguides. These systems lend themselves to analyses where the relevant degrees of freedom are arranged in an abstract manner. This is precisely the idea of synthetic dimensions: coexisting frameworks in which a description via spatial coordinates, e.g. a wave function, takes another form that “lives” in a domain with dimensionalities that are quite distinct from what the structures’ (apparent) geometry would suggest. This approach is rather appealing as it can be used to access and probe dimensions beyond our 3-dimensional world and/or to simulate quantum processes.

In our recent work we have shown that a multitude of high-dimensional synthetic lattices naturally emerge in (abstract) photon-number space when a multiphoton photonic lattice is excited by  $N$  indistinguishable photons (for a simple illustration, see Fig. 6).

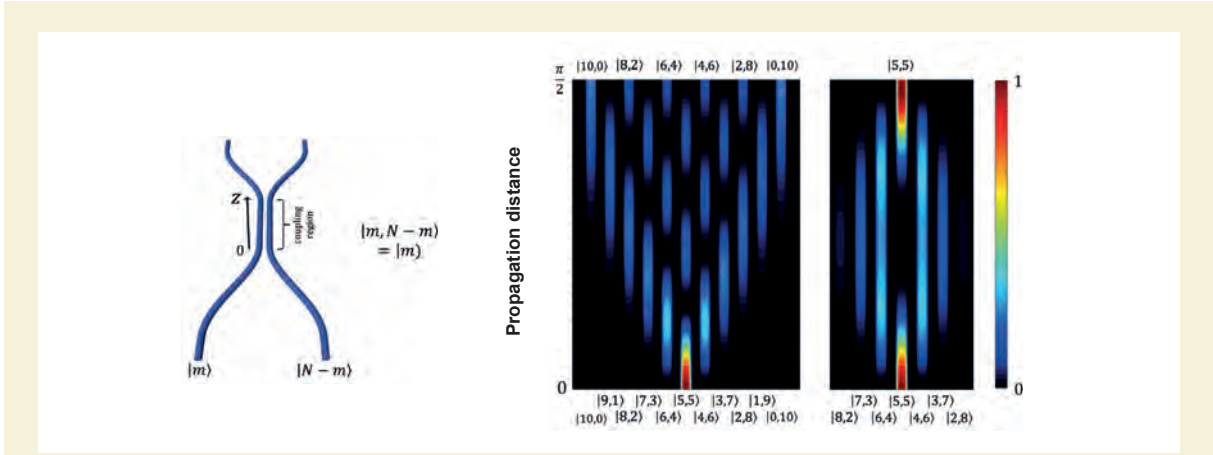


**Fig. 6:** Left panel: Scheme of a simple beam splitter that, when excited by identical photons, corresponds to an array of coupled sites in the synthetic Fock space. Right panel: Probability distribution in synthetic Fock space for the initial state with 5 identical photons propagating in the left and 5 identical photons propagating in right waveguide through a waveguide beam splitter with identical propagation constants in the waveguides (left plot) and different propagation constants (right plot). While the left plot represents the simulation of discrete diffraction, the right plot represents a simulation of Bloch oscillations. Adapted from [TLP20].

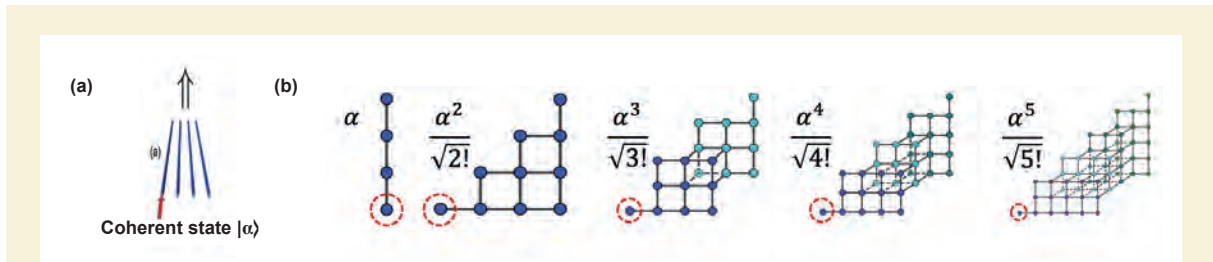


**Fig. 7:** Panel (a): Scheme of a four-waveguide array excited by a coherent state  $|\alpha\rangle$  (the red arrow indicates the excited waveguide). Panel (b): Synthetic graphs emerging from the coherent state excitation of the system in panel (a). The power of  $|\alpha\rangle$  indicates the process with corresponding photon number. Note that for more than 2 photons, we obtain non-planar graphs. Since we are exciting with a coherent state excitation, the probability amplitudes for each event (graph) are given by  $:\alpha^n/n!$ . For each graph, the node that is encircled with red-dashed lines indicates the initial condition. For instance, for the left-most, i.e. the one-photon, graph, the probability distribution is initially 1 on the encircled node and zero on all other nodes. During the propagation, the probability distribution spreads to the other node according to a quantum random walk on this graph. In other words: When exciting the system displayed in (a) with a coherent state, simultaneous quantum random walks on all graphs are executed. Adapted from [TLP20].

More precisely, the Fock-representation of N-photon states in systems composed of M evanescently coupled single-mode waveguides yields to a new layer of abstraction, where the associated states can be visualized as the energy levels of a synthetic atom. In full analogy with ordinary atoms, such synthetic atoms feature allowed and disallowed transitions between its energy levels.

These concepts have far-reaching implications as they open a route to the simultaneous realization of, in principle, an infinite number of lattices and graphs with different numbers of nodes and many dimensions. This possibility is rather appealing for realizing parallel quantum random walks where the corresponding walkers can perform different numbers of steps on different, planar and nonplanar, multidimensional graphs that depend on the number of photons involved in each process. These quantum walks can be implemented, for instance, by exciting a simple four-waveguide system with a standard quantum light source comprising infinite coherent superposition of states, e.g. a coherent state (Fig. 7).

#### T4: Dissipative Quantum Dynamics

The dynamics of a quantum system always occurs in interaction with the environment. In particular molecular dynamics in biological environments is of key importance in life but systems of biological relevance are often characterized by high complexity that imposes challenges in the theoretical description. A way out is provided by a description in the system-bath formalism. However, situations in which the “slow” protein environment leads to system-bath memory of considerable length (non-Markovian memory) still pose a challenge to the description of such dissipative quantum dynamics

In 2020 we have investigated electron transfer dynamics in *Drosophila* cryptochrome (dCRY) [RFi20], a highly conserved flavoprotein consisting of an N-terminal photolyase homology region (PHR) that binds a flavin adenine dinucleotide (FAD) cofactor, and a C-terminal  $\alpha$ -helical domain with a variable C-terminal tail (CTT, Fig. 8). The performed dissipative quantum dynamical simulations subject to the non-Markovian system-bath memory imposed by the protein environment rely on microscopically derived model Hamiltonians and solve the time evolution using the recently developed MACGIC-QUAPI method. The method allows us to rigorously account for the enzyme thermal fluctuations and provides systematic convergence to numerically exact results for arbitrary coupling strengths to the environment. In silico modeling of point mutations provides a microscopic explanation for the observed charge transfer pathways (Fig. 8). Distinguished amino acids allow to control the local electrostatic enzyme environment and crucially influence the energetics of individual charge transfer states.

The results are important for an understanding of the primary processes in dCRY following photoexcitation. Bidirectional charge separation towards the C-terminal tail in addition to the conventional Trp triad was predicted which links the direction of the primary electron transfer reaction to anticipated conformational changes. The results provide a new perspective on the microscopic understanding of light-induced primary electron transfer reactions in dCRY. Our work suggests dedicated mutation sites to control the different electron transfer pathways. Our methodological advances make it possible to model the dynamics of macromolecular, biologically and technically relevant systems using accurate ab initio parameterizations of system and bath degrees of freedom. Our recent work has additionally investigated the influence of the environment on the transfer process through

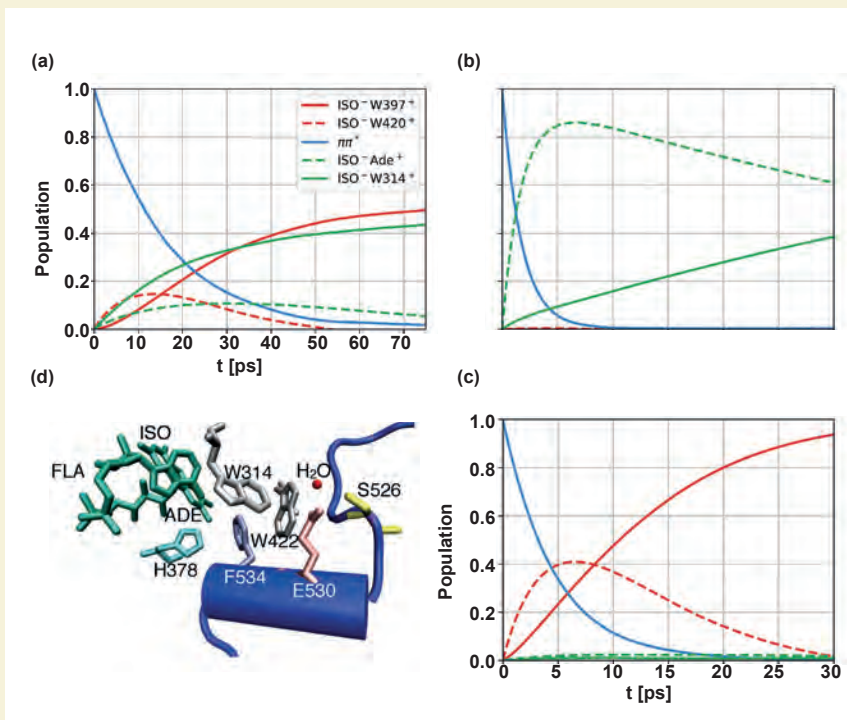


**Fig. 8:** Nonequilibrium dissipative quantum dynamics of wild-type dCRY (a), in silico mutated R298 and E398 (b), and a CTT-deficient dCRY $\Delta$  mimic (c) constructed upon neutralization of electrostatic interaction of photolyase homology region (PHR) and CTT domains; dynamics simulations were performed with the path-integral based MACGIC-QUAPI method. (d) Arrangement of FAD cofactor and tryptophan residues W314 and W422 together with residues of the CTT (F534, E530 and S526) and H378.

non-diagonal coupling to the quantum system [AOF20]. Bridge-mediated electron transfer (ET) between a donor and an acceptor is prototypical for the description of numerous most important ET scenarios. We numerically investigated with quasi-adiabatic propagator path integral simulations the impact of off-diagonal system–environment interactions on the transfer dynamics for a wide range of scenarios in the D–B–A model. We found that off-diagonal system–environment interactions can have profound impact on the bridge-mediated ET dynamics. As such we demonstrated how off-diagonal system–environment interaction mediates anomalous localization and how coherent transfer dynamics between donor D and acceptor A can be facilitated. The arising non-exponential short-time dynamics and coherent oscillations were interpreted within an equivalent Hamiltonian representation of a primary reaction coordinate model that reveals a complex vibronic interplay of vibrational and electronic degrees of freedom underlying the non-Condon effects.

### T5: Landau-Zener-Stückelberg interference in graphene

Monolayer graphene provides an ideal material to explore one of the fundamental light-field driven interference effects: Landau-Zener-Stückelberg (LZS) interference. However, direct observation of the resulting interference patterns in momentum space has not proven possible, with Landau-Zener-Stückelberg interference observed only indirectly through optically induced residual currents. In [LED21] we show that the transient electron momentum density (EMD), an object that can be obtained via Compton scattering tomography, provides an excellent description of momentum resolved charge excitation. We employ state-of-the-art time-de-

pendent density function theory calculations to demonstrate this, by direct comparison of EMD with conduction band occupancy, obtained from projecting the time propagated wavefunction onto the ground state, that the two quantities are in excellent agreement.

LZS occurs when an oscillating electromagnetic field drives intraband oscillation through the Bloch acceleration theorem  $k \rightarrow k + A(t)/c$ , where  $k$  is the quasi-momentum quantum number and  $A(t)$  is the vector potential of the driving electric field in the dipole approximation. In the region of an avoided crossing interband transitions occur even when the band gap exceeds the dominant pulse frequency, so-called Landau-Zener transitions. Upon repeated passing of the avoided crossing multiple pathways exist to the conduction band with consequent constructive and destructive interference of electron states.

This offers rich possibilities for controlling electron dynamics by intense laser light, demonstrated by the recent observation of control over optical currents underpinned by LZS interference.

In contrast to previous works that have employed simple single particle tight-binding Hamiltonians to study the LZS effect, we deploy the time dependent version of density functional theory (TD-DFT), as implemented in the ELK electronic structure code. This is a completely *ab-initio* method and requires no external parameters. TDDFT will include not only the  $\pi$  and  $\pi^*$  bands, but also the  $\sigma$  and  $\sigma^*$  bands together with all the other energy levels. Remarkably, despite electron excitation through the whole energy range of the  $\pi^*$  band (up to 10 eV above the Fermi energy, an energy range encompassing the  $\sigma^*$  bands as well as several high  $l$  character bands), it turns out that there occur almost no transitions

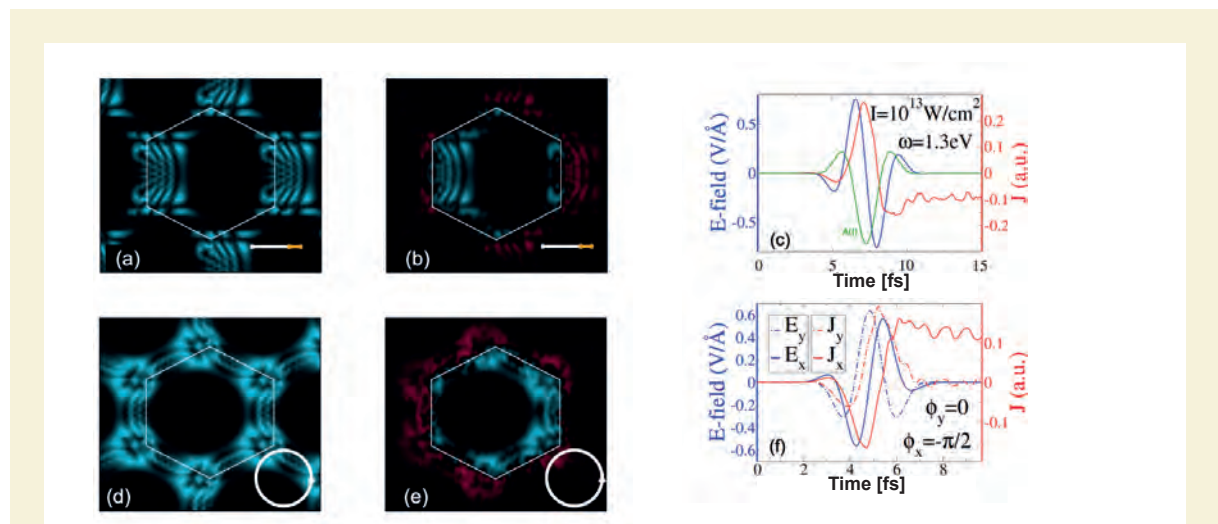


**Fig. 9:**

First column (a),(d): conduction band occupation  $N_{ex}$  as a function of  $k$ -vector. Second column (b),(e): the transient electron momentum density (tr-EMD) difference. Third column (c),(f): the electric field of the pump laser pulse (blue lines), the vector potential  $A$ -field scaled such that it can be plotted on the same axis (green lines), and the induced current density (red lines). The first row is a linear polarized pulse, while the second is circularly polarized, both have a full width half maximum of 1.935 fs, a central frequency of 1.4 eV, and peak intensity of  $5.43 \times 10^{12} \text{ W/cm}^2$ , and carrier envelope phase as indicated in the panels.

to states outside the  $\pi$ -band manifold. We attribute this to the near vanishing of the corresponding dipole matrix elements. Our calculations thus suggest that even for very significant laser excitation tight-binding based models will provide a good description of the electron dynamics.

To establish the accuracy of the EMD as a record of LZS interference we compare it with the excited electron distribution  $N_{ex}(k)$ , formed by summing over the projection of the time-dependent Kohn-Sham (TDKS) orbital with the ground state unoccupied orbitals, for each point  $k$  in reciprocal space. The transient EMD is found by subtracting the ground-state EMD from the EMD calculated just following the applied laser pulse. The EMD itself is calculated from the Fourier transform of the TDKS orbitals.

In Fig. 9, the  $N_{ex}$  and transient EMD can be compared for two different pulses with linear and circular polarization. Note, the  $N_{ex}$  is periodic in reciprocal space while the EMD is not. The first Brillouin zone (1BZ) hexagon is outlined for convenience. The interference pattern may be seen most clearly in Fig. 9 (a)&(b) where constructive and destructive fringes may be seen. For these two pulses, and many others [LED21] with different carrier-envelope phase (CEP), frequency, and intensity, we find that the pattern of excitation in momentum space generated by transient EMD and  $N_{ex}$  is nearly identical in the first BZ. Thus demonstrating the usefulness of the EMD for observing the LZS interference.

The residual current is also shown for these two pulses. In both cases, the strong, asymmetric, excitation of the 1BZ leads to a persistence current. This current includes both the so-called inter- and intra-band contributions, making it observable immediately following the laser pulse. The direction of this current is controlled by the polarization and the CEP.

In summary, we have shown that direct visualization of the interference fringes in momentum space is possible via the transient electron momentum density, establishing transient EMD as an excellent experimental tool for exploring LZS interference. The ubiquity of the avoided crossing band structure in 2d materials, found not only in the Dirac cone of graphene but also in the the semi-conducting monolayer dichalcogenides, phosphorene, silicene, and stanene, points towards the importance of LZS interferometry in controlling electron dynamics in 2d materials.

## Own Publications 2020 ff

(for full titles and list of authors see appendix 1)

- AOF20: N. Acharyya *et al.*; J. Chem. Phys. **153** (2020) 185101.
- APA20a: R. M. Arhipov *et al.*; Phys. Rev. A **101** (2020) 043838/1-6
- APA20b: R. Arhipov *et al.*; Opt. Express **28** (2020) 17020-17034
- ARF20: N. Acharyya *et al.*; *The 22nd International Conference on Ultrafast Phenomena 2020* (Optical Society of America, 2020), paper Tu4A.3
- ASR20: M. V. Arhipov *et al.*; Phys. Rev. A **101** (2020) 013803/1-7
- BHB20: A. Benoît *et al.*; Phys. Rev. Res. **2** (2020) 023025/1-9
- BMD20: I. Babushkin *et al.*; J. Phys. A **53** (2020) 445307/1-12
- DBC20: C. M. Dietrich *et al.*; Opt. Lett. **45** (2020) 5644-5647
- DCA20: T. Driver *et al.*; Phys. Rev. X **10** (2020) 041004/1-13
- DSP20: A. Davydov *et al.*; Phys. Rev. B **102** (2020) 214508/1-10
- DWE20: J.K. Dewhurst *et al.*; Phys. Rev. Lett. **124** (2020) 077203/1-6
- ESK20: P. Elliott *et al.*; Magn. Magn. Mater. **502** (2020) 166473
- ESS20: P. Elliott *et al.*; *Handbook of Materials Modeling* (Springer, Cham, 2020) 841-868
- FBM20: B. Fetić *et al.*; Phys. Rev. A **102** (2020) 023101/1-9
- FCS20: I. A. Fischer *et al.*; Phys. Rev. Mat. **4** (2020) 024601/1-10
- FGW20: M. Fleischmann *et al.*; Nano Lett. **20** (2020) 971-978
- Fin20: B. P. Fingerhut; Quantendynamik offener Systeme; Nachr. Chem. **68** (2020) 57-60.
- FRA20: S. Fiedler *et al.*; Opt. Express **28** (2020) 13938-13948
- GID20: S. Giri *et al.*; Phys. Rev. A **101** (2020) 033412/1-5
- GSS20: R. Gupta *et al.*; Phys. Rev. B **102** (2020) 235203/1-11

- HHD20: M. Hofherr *et al.*; *Sci. Adv.* **6** (2020) eaay8717/1-7
- HVG20a: W. Hartmann *et al.*; *Adv. Opt. Mat.* **8** (2020) 1901602/1-8
- HVG20b: W. Hartmann *et al.*; *Nano Lett.* **20** (2020) 2625-2631
- JHK20: A. Jašarević *et al.*; *J. Phys. A* **53** (2020) 125201/1-21
- JSS20: Á Jiménez-Galán *et al.*; *Nat. Photonics* **14**, (2020) 728-732
- KBM20: A. E. Kuvckalić *et al.*; *Symmetry* **12** (2020) 1606/1-15
- KHI20: P. T. Kristensen *et al.*; *Adv. Opt. Photonics* **12** (2020) 612-708
- KSt20: M. A. Khokhlova *et al.*; *New J. Phys.* **22** (2020) 093030/1-13
- LRH20: A. E. Lidiya *et al.*; *Opt. Comm.* **474** (2020) 126083/1-23
- LRM20: M. Lytova *et al.*; *Phys. Rev. A* **102**, 013111 (2020).
- MBe20a: D. B. Milošević *et al.*; *J. Phys. Conf. Ser.* **1508** (2020) 012001/1-10
- MBe20b: D. B. Milošević *et al.*; *Phys. Rev. A* **102** (2020) 023107/1-14
- MBG20: Z. Mašín *et al.*; *Comput. Phys. Commun.* **249** (2020) 107092/1-76
- MPV20: N. Mayer *et al.*; *J. Phys. B* **53** (2020) 164003/1-15
- MSG20: T. Müller *et al.*; *Phys. Rev. Lett.* **125** (2020) 256402/1-5
- PMD20: C. Pellegrini *et al.*; *Phys. Rev. B* **101** (2020) 144401/1-10
- PVV20: S. Patchkovskii *et al.*; *J. Phys. B* **53** (2020) 134002/1-14
- RBI20a: D. Reiche *et al.*; *Phys. Rev. A* **101** (2020) 012506/1-22
- RBI20b: D. Reiche *et al.*; *Phys. Rev. Lett.* **124** (2020) 193603/1-7
- RFi20: M. Richter and B. P. Fingerhut, *Molecules* **25** (2020) 4810.
- RIH20: D. Reiche *et al.*; *Phys. Rev. A* **102** (2020) 050203(R)/1-7
- RLM20: M. Richter *et al.*; *Optica* **7**, 586-592 (2020).
- RTP20: P. Reséndiz-Vázquez *et al.*; *Phys. Rev. Res.* **2** (2020) 013387/1-7
- SED20: N. Singh *et al.*; *Phys. Status Solidi B* **257** (2020) 1900654/1-9
- SPM20: P. Stammer *et al.*; *Phys. Rev. A* **101** (2020) 033405
- Sta20: P. Stammer; *Phys. Rev. A* **102** (2020) 062206/1-11
- SWG20: D. Steil *et al.*; *Phys. Rev. Res.* **2** (2020) 023199/1-6
- TFG20: C. Tserkezis *et al.*; *Rep. Prog. Phys.* **83** (2020) 082401/1-10
- TJB20: V. Tamulienė *et al.*; *Sci. Rep.* **10** (2020) 17437/1-12
- TKS20: E. Travkin *et al.*; *Opt. Lett.* **45** (2020) 3665-3668
- TLP20: K. Tschernig *et al.*; *Photonics Res.* **8** (2020) 1161-1170
- TSS20: C. Tailliez *et al.*; *New J. Phys.* **22** (2020) 103038/1-18
- UOJ20: A. J. Uzan *et al.*; *Nat. Photonics* **14** (2020) 183-187
- USP20: A. J. Uzan *et al.*; *Nat. Photonics* **14** (2020) 188-194
- VBu20: P. Varytis *et al.*; *Opt. Express* **28** (2020) 1714-1721
- WKS20: F. Willems *et al.*; *Nat. Comm.* **11** (2020) 871
- WPW20: K. Wang *et al.*; *J. Opt.* **22** (2020) 035801/1-7
- YQL20: C. You *et al.*; *Appl. Phys. Rev.* **7** (2020) 021404/1-10
- YWK20a: K. Yao *et al.*; *Phys. Rev. B Rapid. Comm.* **102** (2020)100405 (R)/1-6
- in press**
- AJM: D. R. Austin *et al.*; *Sci. Rep.*
- AOS20: D Ayuso *et al.*; *Nat. Comm.*
- GDC21: M. de Goede *et al.*; *Optics*
- JSS21: Á Jiménez-Galán *et al.*; *Optica*
- KKK: M. Kliem *et al.*; *Adv. Photon. Res.*
- LED: Q. Z. Li *et al.*; *Phys. Rev. B*
- NLM: Z. Nie *et al.*; *Phys. Rev. Lett.*
- SSM: P. Scheid *et al.*; *Nano Lett.*

## Other Publications

ANO19: D Ayuso *et al.*; Nat. Photonics **13** (2019) 866-871

MMP18: M Matthews *et al.*; Nat. Phys. **14** (2018) 695-700

MRP11: F Morales *et al.*; PNAS **108**, 16906-16911 (2012)

NAD19: O Neufeld *et al.*; Phys Rev X **9** (2019), 031002/1-15

SJA19: R. E. F. Silva *et al.*; Nat. Photonics **13** (2019) 849–854

SBR18: R. E. F. Silva *et al.*; Nat. Photonics **12** (2018) 266–270]

## Invited Talks at International Conferences

(for full titles see appendix 2)

W. Becker; Quantum Battles in Attoscience 2020 (University College London, United Kingdom, 2020-07)

K. Busch together with A. Perez-Leija, and K. Tschernig; SPIE Nanoscience + Engineering, 2020 (San Diego, USA, 2020-08)

K. Busch; METANANO 2020 ONLINE, V International Conference on Metamaterials and Nanophotonics (Tbilisi, Georgia, 2020-09)

B. P. Fingerhut; Ultrafast Phenomena XXII (Shanghai, China, 2020-11)

Á. Jiménez-Galán; OSA High-brightness Sources and Light-driven Interactions Congress (Prague, Czech Republic, 2020-11)

M. Khokhlova; Quantum Battles in Attoscience 2020 (University College London, United Kingdom, 2020-07)

M. Richter; 20th International Conference Foundations & Advances in Nonlinear Science and 5th International Symposium Advances in Nonlinear Photonics, FANS & ANPh (Minsk, Belarus, 2020-09)

S. Shallcross; International Psi-K Workshop, Correlated synthetic quantum matter: theory meets experiment (Bremen, Germany, 2020-02)

S. Sharma; 710. WE-Heraeus-Seminar, Spin Transport in Complex Magnetic Structures (Bad Honnef, Germany, 2020-01)

S. Sharma; Ultrafast Webinar Summer Series 2020 (Harvard, MPI-Hamburg and Arizona University, 2020-08)

S. Sharma; Vaishwik Bharatiya Vaigyanik (VAIBHAV) Summit (India, 2020-10)

S. Sharma; JEMS The Joint European Magnetic Symposia 2020 (2020-12)

O. Smirnova; 2020 ACS Fall National Virtual Meeting and Exposition (San Francisco, CA, USA, 2020-08)

O. Smirnova; 1st Annual Workshop & Joint WG meeting of CA18222 COST Action (Babeş-Bolyai University, Romania, 2020-09)

## Invited External Talks at Seminars and Colloquia

(for full titles see appendix 2)

S. Sharma, Lüscher Seminar (Klosters, Switzerland, 2020-)

S. Sharma, TRR 227 Retreat (Halle, Germany, 2020-11)

S. Sharma, Seminar series of Nijmegen and Uppsala (Sweden, 2020-12)

B. P. Fingerhut, Symposium (Thomas Young Centre, London, UK, 2020-02).

B. P. Fingerhut, Kolloquium (Physikalische Chemie und Theoretische Chemie, TU München, Germany, 2020-02)

## 1.2: Ultrafast Laser Physics and Nonlinear Optics

*Project coordinators: T. Nagy, M. Schnürer, and G. Steinmeyer  
and J. R. C. Andrade, E. Escoto, F. Furch, M. Fürtjes, O. Ghafur, L. v. Grafenstein, U. Griebner, R. Grunwald,  
A. Heilmann, A. Housakou, M. Jasiulek, M. Kretschmar, C. Mei, M. Merö, F. Morales, M. Mörbeck-Bock, V. Petrov,  
I. Radu, M. Richter, B. Schütte, A. Treffer, J. Tümmeler, L. Wang, I Will, T. Witting, Y. Zhao*

### 1. Overview

This project is the home of MBI's research activities in nonlinear optics and laser physics focusing on the development of novel light sources and time-resolved techniques.

Our primary goal is to strengthen MBI's research on ultrafast and nonlinear phenomena in light-matter interaction with state-of-the-art technology from our original research activities. Depending on the planned application of the technology, the focus of the development lies on superior pulse energy, short pulse duration, carrier-envelope phase stability, or high average power and repetition rate. A further goal is to cover a large range of the electromagnetic spectrum from THz to the soft X-rays with few-cycle pulses. Consequently, the project encompasses research on primary laser and parametric sources as well as on compression and wavelength conversion of the primary sources.

### 2. Topics and collaborations

At present the project is organized in two topics:

#### T1: Primary Sources

Partly supported by DFG (GR2116\_5-1) and EU (JRA PRISES)

Our activity concerning primary light sources is currently mostly devoted to the development of optical parametric chirped pulse amplifiers (OPCPA). In recent years, four major OPCPA systems with unique parameters have been developed and already found their way towards application in other projects. Among these laser systems, two OPCPAs are currently still under investigation for improving their performance:

- A 100 kHz two-color OPCPA producing sub-100 fs pulses at 1.5 and 3.2  $\mu\text{m}$  is currently used with two stages for reaction microscope experiments after an extensive upgrade of the system. It is planned to re-commission the third stage during 2021
- A 5  $\mu\text{m}$ , 3 mJ OPCPA system operating at 1 kHz is currently used as driver laser for MBI's time-resolved X-ray diffraction research in project. In 2020 the booster section of the parametric amplifier was redesigned for stability reasons and a fourth OPA stage was added

Moreover, extensive research is devoted to power scaling of new types of solid-state laser and amplification systems in the near-IR wavelength range around 2  $\mu\text{m}$

and beyond, with extension to longer wavelengths up to 20  $\mu\text{m}$  by parametric frequency conversion. Here the performances of novel gain media, such as rare-earth and transition metal doped crystals and ceramics, is investigated together with a large variety of new mode-locking solutions. In parallel, the properties of novel non-oxide nonlinear crystals are assessed for efficient frequency conversion into the mid-infrared. These efforts pave the way towards new high-power long-wavelength femtosecond systems based on OPCPA since they cover all the three essential aspects: pump and seed sources as well as the nonlinear medium.

#### T2: Secondary Sources

Partly supported by DFG (STE 762/11-1, GR 1782/14-2, GR 1782/16-1 and NA 1102/3-1), IBB ProFIT 10164801 OptoScope, and CSC/DAAD

In order to extend the parameter range of primary laser sources we undertake development on secondary sources concentrating on the following main directions:

##### Pulse compression

The institute has considerable expertise in high power pulse compression using hollow-core fibers: besides conventional rigid capillaries, we also develop stretched flexible hollow fiber technology, which is particularly suited for multi-mJ operation thanks to the free geometrical scalability of this kind of waveguides. Furthermore, we apply Kagome hollow-core photonic crystal fibers and multi-plate continuum generation in our high repetition-rate systems. The performance of a novel technique based on multi-pass cells is currently investigated. The various techniques are utilized for post-compression of our OPCPA systems. Further high power pulse compression activities include the compression of multi-mJ pulses from TW-level Ti:sapphire amplifiers in stretched flexible hollow fibers as well as efforts to compress high-energy few-picosecond pulses from laser systems based on Yb-, Ho- and Cr-doped materials.

##### Non-linear frequency conversion

Nonlinear frequency conversion techniques are used for the generation of intense light fields beyond the wavelengths that can be addressed by primary sources, i.e., spanning the entire wavelength regime from the THz to the XUV and X-ray domain. On the long wavelength side, we target the generation of single-cycle THz fields with field strengths of up to 10 MV/cm and beyond for use in a wide range of experiments addressing field-driven processes on attosecond to femtosecond time scales. At the other end of the wavelength spectrum, we

undertake efforts to optimize the generation of soft X-rays in the water window and beyond using HHG. The past few years have revealed a number of surprising results in HHG research, in particular at high laser intensities, high target pressures and/or multi-jet geometries, suggesting that the process is not yet fully understood and that the potential for efficient XUV/soft X-ray generation is not yet fully realized. Moreover, the dynamics underlying the generation process in multi-color fields with tailored polarization states is not yet fully explored, which places them in the focus of our research.

### Pulse characterization

Within topical focus 1, pulse characterization methods have proven an indispensable tool for recompressing the generated pulses close to the bandwidth-limit or to further increase peak powers by actively broadening the spectra in a supercontinuum process. Within the project, a number of pulse characterization techniques have either been further developed or tailored to the needs within MBI. One further important aspect is carrier-envelope phase measurement and stabilization, which play a key role in high-field or attosecond experiments.

Collaboration partners: M. Guina (ORC, Tampere, Finland), A. Demircan, U. Morgner (Leibniz Universität Hannover, Germany), R. Trebino (Georgiatech, Atlanta, GA, USA), S. Carbajo, (SLAC, USA), M. Dantus (Michigan State University, East Lansing, MI, USA), B. Hofmann (TU Chemnitz, Germany), Y. Song (Tianjin University, China), T. Feng, (Shandong University, Qingdao, China), U. Wallrabe (IMTEK, University Freiburg, Germany), metrolux GmbH (Göttingen, Germany), J. Jahns (FernUniversity, Hagen, Germany), W. Seeber (Otto Schott Institute, FSU Jena, Germany), E. McGlynn (School of Physics, Dublin City University, Dublin, Ireland), F. Güell (University Barcelona, Spain), HoloEye

Photonics AG (Berlin, Germany), F. Diaz (University Tarragona, Spain), P. Fuhrberg (LISA laser OHG, Germany), H. Zhang (Shandong University, P. R. China), F. Rotermund (Ajou University, Korea), A. Agnesi (Pavia University, Italy), J. Liu (Qindao University, China), B. Kanngießner (TU Berlin, Germany), L. Isaenko (DTIM Novosibirsk, Russia), V. Pasiskevicius, (KTH, Stockholm, Sweden), P. Schunemann (BAE Systems, Nashua, USA), V. Badikov (HTL, Krasnodar, Russia), K. Kato (Chitose, Japan), I. Buchvarov (Sofia University, Bulgaria), M. Ebrahim-Zadeh (ICFO, Barcelona, Spain), M. Eichhorn (ISL, France), V. Panyutin (Kuban State University, Russia), G. Arisholm (FFI, Norway), Z. Heiner (SALSA, HU Berlin, Germany), P. Simon (Institut für Nanophotonik Göttingen e.V.), Rodrigo Lopez-Martens (LOA, France), S. Hädrich (Active Fiber Systems GmbH), J. Limpert (Friedrich-Schiller-Universität Jena), L. Veisz (Umeå University, Sweden), B. Major (ELI-ALPS, Szeged), V. Tosa (National Institute for Research and Development of Isotopic and Molecular Technologies).

## 3. Results in 2020

### T1: Primary Sources

#### Midwave-IR OPCPA at 1 kHz

A four-stage OPCPA system is operating at a central wavelength of 5  $\mu\text{m}$  and emits pulses with 80 fs duration and 3 mJ energy at a 1 kHz repetition rate [GBU20b], i.e., targeted output parameters were achieved. Stable and reliable operation of the OPCPA system was ensured in 2020 leading to the successful implementation of the system for its intended application, that is, as driver for hard x-ray generation (see project 3.3).

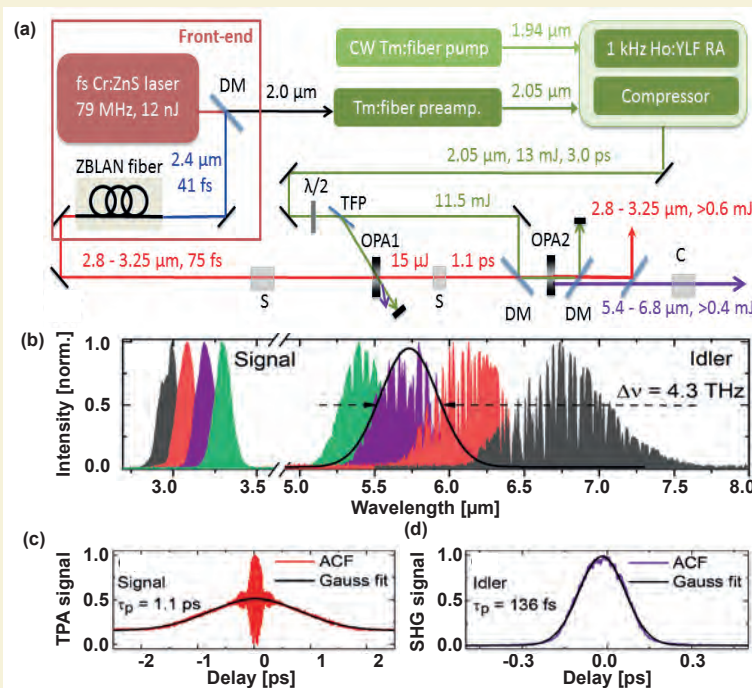


**Fig. 1:**  
Mid-IR OPCPA with Cr:ZnS based front-end.  
(a) Setup;  
(b) Spectral intensity of the signal (left) and idler pulses (right);  
(c), (d) ACFs of an uncompressed signal ( $\lambda_s = 2.9 \mu\text{m}$ ) and a compressed idler pulse ( $\lambda_i = 5.4 \mu\text{m}$ ).

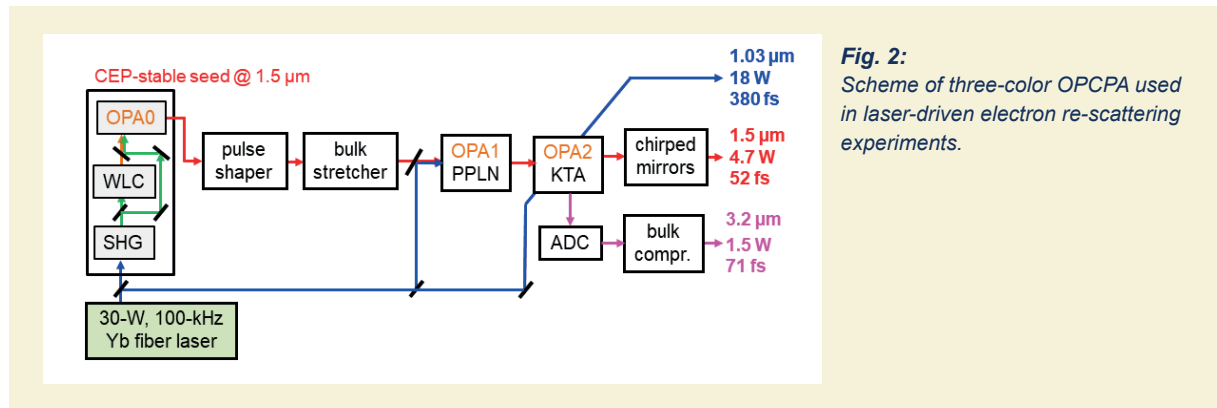


**Fig. 2:** Scheme of three-color OPCPA used in laser-driven electron re-scattering experiments.

The main activities in 2020 were devoted to reducing the complexity of the MWIR OPCPA front-end with the aim to increase stability and efficiency of OPCPAs operating at wavelengths beyond 4  $\mu\text{m}$ . For the first time, a front-end based on a fs Cr:ZnS master oscillator was implemented in a mid-IR OPCPA. Its emission spectra encompass both the pump at 2.0  $\mu\text{m}$  and the signal at 2.4  $\mu\text{m}$  [1], which significantly simplifies mid-IR OPCPA architectures and makes combinations of nonlinear effects (such as supercontinuum and difference frequency generation or OPG/OPA) obsolete.

The setup of the mid-IR OPCPA is shown schematically in Fig. 1(a). The Cr:ZnS oscillator (IPG Photonics), operating at 79 MHz repetition rate, emits 30 fs pulses with an energy of 12 nJ. The spectrum is centered at 2.4  $\mu\text{m}$  and extends from 1.9 to 2.6  $\mu\text{m}$ , providing the seed for the signal as well as the pump. Here the shortwing of the spectrum seeds the OPCPA pump without additional nonlinear frequency transformation. The pump at 2.05  $\mu\text{m}$  relies on a high-performance Ho:YLF regenerative amplifier (RA) [GBU20a], delivering 2.4 ps (FWHM) pulses with 13.8 mJ energy at a 1 kHz repetition rate.

The resulting peak power of 5.4 GW surpasses that from other 2- $\mu\text{m}$  RAs for picosecond pulses [2].

After division of the Cr:ZnS oscillator pulse spectrum, the seed pulse provided for the signal centered at 2.4  $\mu\text{m}$  still exhibits a sub-50 fs duration and 10 nJ pulse energy. Given the aim of a spectrally tunable mid-IR OPCPA, the seed pulses for the signal are shifted to longer wavelengths. This shift is performed in a ZBLAN fiber via Raman-induced soliton self-frequency shifting and results in signal pulses in the range 2.8–3.25  $\mu\text{m}$  with sub-100 fs duration and few-nJ energy.

The performance of the Cr:ZnS-based front-end demonstrated in a mid-IR OPA, with an OPA design adapted to our previous setup [GBU20a, GBU20b]. The mid-IR pulses are amplified in a two-stage OPA containing ZGP crystals (OPA1 and OPA2 – see Fig. 1(a)). Both stages are seeded with the signal. The latter is stretched using bulk materials to adapt the signal pulse duration to the one of the pump. The generated combined signal and idler energy after the collinear OPA2 amount to 1.2 mJ with an uncompressed signal pulse duration of 1.1 ps (collinear autocorrelation function (ACF), Fig. 1(c)). The idler pulse energy of >400  $\mu\text{J}$  in the 1 kHz pulse

train surpasses the highest energy reported for tunable OPAs beyond 4  $\mu\text{m}$  so far by one order of magnitude [2]. The emitted signal and idler spectra are shown in Fig. 1(b). The spectral tunability of the signal allows for the generation of idler pulses between 5.4 and 6.8  $\mu\text{m}$ . The bandwidth of the idler spectra of >4 THz (FWHM) supports a Fourier-limited duration of 80 fs. CaF<sub>2</sub> prisms are used for compression of the positively chirped idler pulses. The measured non-collinear ACF of the pulses at  $\lambda_i = 5.4 \mu\text{m}$  is presented in Fig. 1(d), indicating a pulse duration of 135 fs. Given that the OPA was not purged, water vapor absorption appears to be the main origin of structured idler spectra (Fig. 1(b)) and deviations from the transform limit. To overcome this problem, purging of the system and implementing a spectral shaper for dispersion compensation will be the next steps.

In 2021, the focus will be on the extension of the Cr:ZnS based OPCPA system to the longwave-IR, i.e., emission at wavelengths longer than 7  $\mu\text{m}$ , with few-cycle pulse duration and multi-100  $\mu\text{J}$  pulse energy.

#### 100 kHz OPCPA at 1.5 $\mu\text{m}$ / 3.2 $\mu\text{m}$

The home-built 1.5  $\mu\text{m}$  OPCPA, driven by a commercial 30 W Yb-fiber laser, was upgraded to provide a second infrared output beam at 3.2  $\mu\text{m}$ . The upgrade was based on an in-house design of a dispersion compensation unit

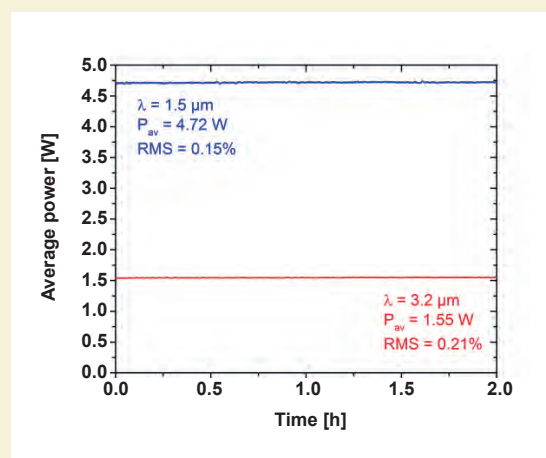


**Fig. 3:** Average power stability of the 1.5- $\mu\text{m}$ , 50-fs and of the 3.2- $\mu\text{m}$ , 70-fs arms.

that corrects angular dispersion of the idler laser beam from the noncollinear booster amplifier stage. Together with the 1.03  $\mu\text{m}$  residual output beam, a three-color OPCPA system was obtained this way (Fig. 2). The OPCPA system was equipped with several servos to allow unattended operation over  $> 100$  hours with  $< 1\%$  drift in the average power of the three output beams. Over a time period of 2 hours, the root-mean-square (RMS) fluctuations of the 1.5  $\mu\text{m}$  and 3.2  $\mu\text{m}$  pulse trains were at the 0.15% and 0.21% level, respectively (Fig. 3). The 1.03  $\mu\text{m}$  output served as the molecular alignment beam, while the 1.5 and 3.2  $\mu\text{m}$  infrared output beams provided the strong-field ionization pulses in laser-driven electron re-scattering experiments on gas-phase atoms and molecules utilizing cold target recoil ion momentum spectrometer (COLTRIMS) detector technology (see Project 2.2).

### Cage solitons

Mode-locking is traditionally explained in the framework of the Haus Master Equation, which predicts hyperbolic secant pulse shapes for various passive mode-locking techniques, e.g., polarization-rotation, Kerr-lens and additive-pulse mode-locking. While these theoretical predictions agree well with experimental results at long pulse durations, few-cycle lasers showed rather strong deviations from a sech pulse shape, more resembling a sinc functional dependence.

Rewriting the Haus partial differential equations as a set of nonlinearly coupled ordinary differential equation, we have explored a different approach for finding soliton solutions of the latter [EDS]. Using a sparse representation of only 9 frequency components, the complete solution space of the equation can be surveyed by solving an algebraic determinant, see Fig. 4. At relatively large negative dispersion values, our approach reproduces the well-known traditional soliton solutions, which roll off exponentially at either side of the spectrum. Reducing the modulus of the dispersion, limitations of the spectral gain bandwidth start to affect the pulse shape and spectrum, resulting in box-shaped spectra with corresponding sinc pulse shapes. Finally, going to even smaller absolute values of the dispersion, concave spectra result with corresponding Bessel-like temporal profiles.

The decreasing spectral convexity with vanishing dispersion is accompanied by more efficient usage of the available gain bandwidth (Fig. 4(a)) and an increase of the soliton phase (Fig. 4(b)). The latter finding explains why the carrier-envelope phase of few-cycle lasers can readily be controlled by pump power modulation. Apart from these stable solutions, we also observe partial mode-locking in the absence of a stabilizing saturable absorber mechanism. Without the saturable absorber, a laser may still be mode-locked yet shows strong degradation of the pulse-to-pulse coherence. These findings may explain a number of mysterious experimental mode-locking reports in the literature and will be tackled in the near future.

### Sub-100 fs bulk solid-state lasers in the 2- $\mu\text{m}$ spectral range

For generation of extremely short pulses near 2  $\mu\text{m}$ , we study Tm,Ho-codoped crystals and ceramics (to utilize their composite gain profile) and materials exhibiting both intrinsic structural disorder and additional compositional disorder through doping with optically passive ions for extensive inhomogeneous broadening of the active dopant spectral lines. SESAM and carbon nanostructure saturable absorbers (SAs) are employed as mode-lockers for self-starting operation but also the Kerr-effect is studied as a pulse shortening and mode-locking mechanism for support of ultimately broad bandwidths.

Among the rare-earth laser hosts, the cubic (bixbyite structure) sesquioxides  $\text{RE}_2\text{O}_3$ , where RE = Lu, Y and Sc, are of particular interest for sub-100-fs  $\sim 2\text{-}\mu\text{m}$  solid-state lasers because of their extremely broad and flat gain spectra extending up to  $\sim 2.1$   $\mu\text{m}$  due to the strong Stark splitting of the ground state of  $\text{Tm}^{3+}$  in combination with strong electron-phonon interaction and their high thermal conductivity. In contrast to such crystals, ceramic fabrication circumvents the growth problem thanks to the relatively low sintering temperature. Moreover, it is easier to mix isostructural sesquioxide ceramics for compositional disorder. The pulse duration of 54 fs achieved in 2020 by using a mixed sesquioxide Tm:LuYO<sub>3</sub> ceramic, a GaSb-based SESAM as a SA, and a group delay dispersion (GDD) compensation

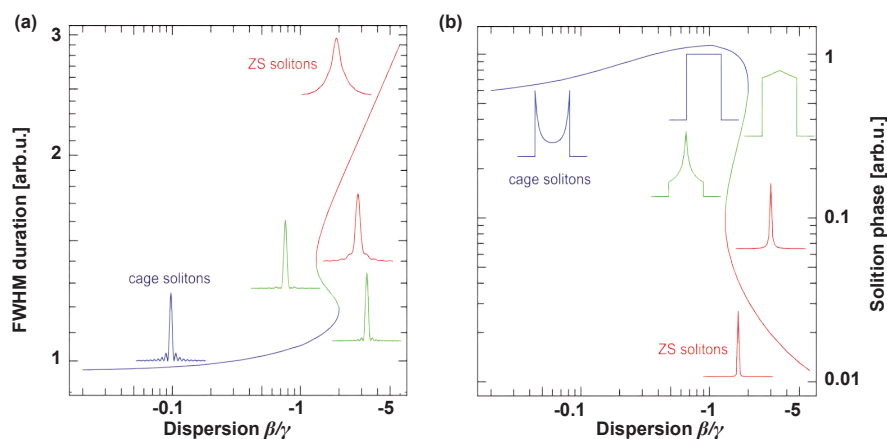


**Fig. 4:** Solitons of the Haus Master Equation of mode-locking vs. dispersion [EDS]. (a) Full width at half maximum vs. effective dispersion  $\beta/\gamma$ . Insets show temporal profiles (b) Behavior of the soliton phase  $\psi$ . Insets show corresponding spectra.

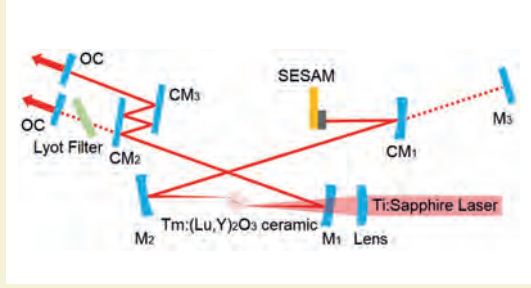


**Fig. 5:**  
Setup of a mode-locked Tm:LuYO<sub>3</sub> laser: M<sub>1</sub>-M<sub>2</sub>: concave folding mirrors, M<sub>3</sub>: rear mirror in CW operation; CM<sub>1</sub>-CM<sub>3</sub>, chirped mirrors; OC: output coupler.

scheme, represents the shortest pulse ever reported for any Tm-based bulk solid-state laser [ZWC20b]. Fig. 5 shows the schematic of the mode-locked laser. The ceramic sample was mounted on a water-cooled copper block (coolant temperature: 14 °C) and placed at Brewster's angle between two dichroic folding mirrors M<sub>1</sub> and M<sub>2</sub>. The pump source was a CW narrow-line-width Ti:sapphire laser tuned to 795.3 nm. This laser was focused into the ceramic sample with an  $f = 70$  mm lens to a beam radius of 30  $\mu\text{m}$ . The laser cavity mode inside the ceramic sample was estimated using the ABCD formalism giving a waist radius of 30 and 76  $\mu\text{m}$  in the sagittal and tangential planes, respectively. For mode-locked operation, M<sub>3</sub> was replaced by a curved chirped mirror CM<sub>1</sub> in order to create a second intra cavity beam waist on the SESAM to increase the fluence for efficient bleaching of the SA. The calculated beam radius on the SESAM was 120  $\mu\text{m}$ . The intracavity GDD was optimized by two extra plane CMs (CM<sub>2</sub> and CM<sub>3</sub>) in the other cavity arm, changing the number of bounces. All CMs had a GDD of  $-125 \text{ fs}^2$  per bounce. Applying 3, 5 and 7 bounces (single pass) on the plane CMs, the total round-trip GDD amounted to  $-887$ ,  $-1387$  and  $-1887 \text{ fs}^2$ , respectively (including the contribution of the ceramic sample:  $-137 \text{ fs}^2$ , estimated by averaging the refractive index for Y<sub>2</sub>O<sub>3</sub> and Lu<sub>2</sub>O<sub>3</sub>). For three different OCs ( $T_{\text{OC}} = 1.5\%$ ,  $0.5\%$  and  $0.2\%$ ), stable and self-starting

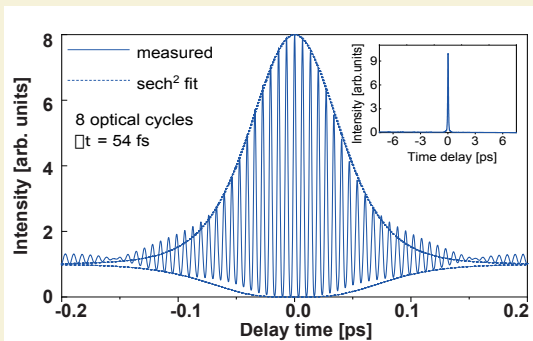


**Fig. 6:**  
Interferometric autocorrelation trace of the shortest pulses from the mode-locked Tm:LuYO<sub>3</sub> ceramic laser obtained with  $T_{\text{OC}} = 0.5\%$ . The fit assumes a  $\text{sech}^2$ -pulse shape. Inset: noncollinear autocorrelation trace on a time span of 15 ps.

sub-100-fs pulse generation was obtained with 5 bounces on the CMs. Pulses as short as 54 fs, i.e., 8 optical cycles were generated at a repetition rate of  $\sim 78$  MHz using the  $0.5\%$  OC for an average output power of 51 mW, see Fig. 6. The corresponding spectrum was centered at 2048 nm with a  $\text{sech}^2$ -fitted FWHM of 82 nm.

We also achieved, for the first time, pure Kerr-lens mode-locking in the sub-100-fs regime in 2020, using a similar mixed Tm:(Lu,Sc)<sub>2</sub>O<sub>3</sub> ceramic laser emitting at 2083 nm [ZWW20]. Nearly Fourier-transform-limited (bandwidth: 80 nm, time-bandwidth product of 0.321) 58-fs pulses, i.e., 8 optical cycles, were generated. With a  $T_{\text{OC}} = 0.2\%$  OC, an average output power of 220 mW (i.e. much higher compared to SESAM mode-locking) was achieved at a repetition rate of 84.8 MHz, yielding a single pulse energy of 2.6 nJ. In both cases a very clean fundamental beat note with a high extinction ratio of  $>75$  dBc above the noise level was observed in the radio-frequency spectra, indicating a high stability of the CW mode-locking without any unwanted multi-pulsing or Q-switching.

#### Adaptive tailoring of nondiffracting and vortex pulses

The state of the art of generating nondiffracting needle beams was comprehensively reviewed including most recent experiments at MBI [GBo20]. It was demonstrated that the spatio-spectral redistribution of few-cycle Bessel beams requires a restriction to the central lobe of the Bessel distribution to maintain the minimum pulse duration. On the other hand, the simulated influence of space-time coupling effects on the fringe contrast (Fig. 7) shows in good agreement with experiments that (i) a natural narrowing towards a single lobe is obtained (shaping a "light bullet" by linear spectral interference at free space propagation), and (ii) that this finding comes with a caveat, namely an enhanced background, i.e., vanishing zeros for very short pulses. This can be interpreted similar to the uncertainty principle or the time-bandwidth product, limiting the maximum achievable contrast of self-apodized spatial filtering.

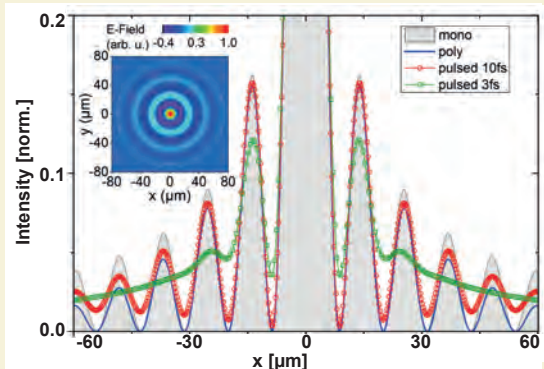


**Fig. 7:**  
Simulated intensity profiles for Bessel beams at different pulse durations (central wavelength 800 nm); grey: cw, blue line: FWHM 100 nm; red circles: 10-fs pulse; green squares: 3-fs pulse. The contrast depends on both spectral bandwidth and on space-time coupling caused by travel time differences (inset: E-field).

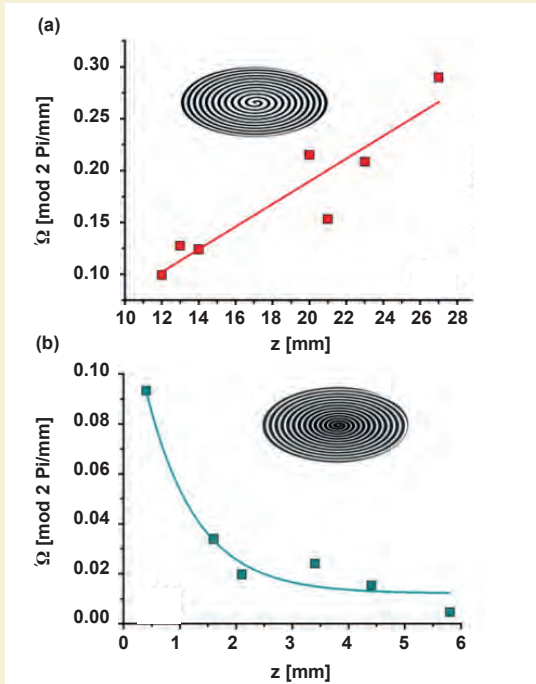


**Fig. 8:** Adaptive control of ultrashort orbital momentum pulses [LTB]. To control the propagation-dependent angular velocity of spectral Gouy rotation, spiral phase gratings with (a) radially increasing and (b) decreasing spatial frequency (“positive chirp”, “negative chirp”) were programmed into the phase map of a high-resolution (10 Megapixel) phase-only spatial light modulator. The reflective mode of operation requires to compensate the incident angle by optimizing ellipticity. Periods in vertical direction vary (a) from 58  $\mu\text{m}$  to 34  $\mu\text{m}$ , and (b) from 29  $\mu\text{m}$  to 55  $\mu\text{m}$ , respectively (center to rim). The angular velocity of rotation indicates an accelerating or decelerating spectral rotation with increasing distance, depending on the sign of chirp.

Previous experiments on the controlled propagation of spectral anomalies (“spectral eyes”) [LTB20a, LTB20b, Lie20] were essentially extended in a joint project with University Freiburg. The advantages of adaptive techniques were demonstrated by flexibly programming non-uniform spiral phase gratings, e.g., with positive and negative spatial chirp, into the phase map of an UHD (10 Megapixel) liquid-crystal-on-silicon spatial light modulator (LCoS-SLM) (Fig. 8) [LTB]. The small pitch of the pixels (3.74  $\mu\text{m}$ ) enables the realization of comparatively small phase structures without strongly violating the sampling theorem. Simultaneous 2D detection and spectral selection with tunable filters was used to obtain a much faster spectral mapping compared to fiber scan methods. Recently, we demonstrated that the high resolution of the SLM (few- $\mu\text{m}$ -range) and the fast (kHz-range) switching speed of steerable mirrors (MEMS) [BSG20] can be exploited in combined adaptive systems (to be published).

## T2: Secondary Sources

### High-energy HCF beamline

Hollow-core fibers (HCF) have been the matter of choice for compressing pulses from Ti:sapphire lasers to few-cycle duration since their invention in 1996. Thanks to the gas medium and large mode diameters, these devices have brought the energy of the compressed pulses up to the mJ level. However, further energy scaling to the multi-mJ level remains a major challenge. As laser technology evolved, the pulse compression stage became the bottleneck in energy scaling of few-cycle pulses.

With a combination of different measures, we now finally succeeded to pass a number of new milestones in high-energy few-cycle pulse compression. First, in cooperation with a French group we achieved 3.4 fs pulses with near TW peak power, which were focused to relativistic intensities for driving wake-field electron accel-

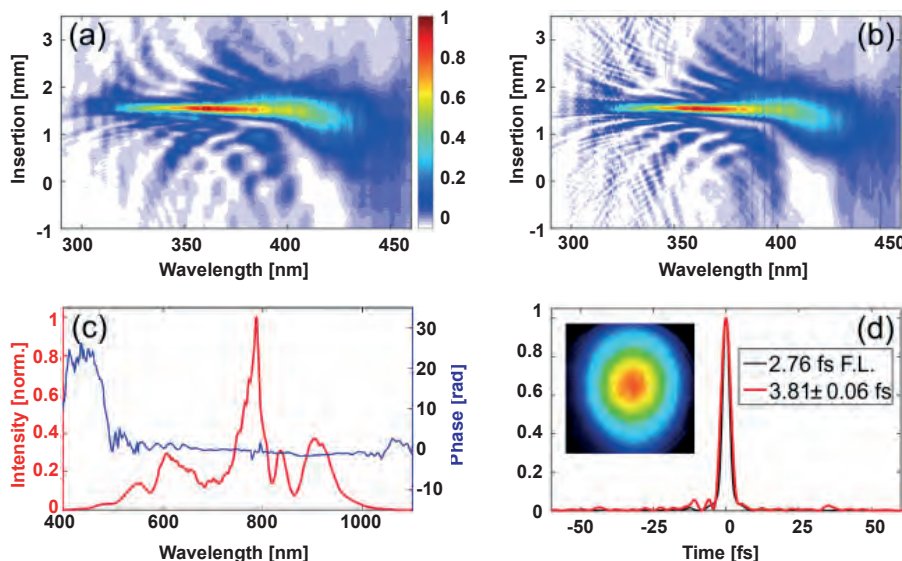


**Fig. 9:** Dispersion scan measurement. (a) and (b) are the measured and retrieved traces, respectively. (c) shows the spectrum with the retrieved spectral phase while (d) displays the pulse shape (red) together with the transform limited shape (black). The output beam profile is shown in the inset. From [NKV20].

eration [OV20]. Later, in an 8 m long beamline built at MBL, incorporating a 3.75 m long stretched flexible HCF of 530  $\mu\text{m}$  inner diameter, we compressed 15 mJ, 50 fs pulses of a kHz Ti:sapphire amplifier to 3.8 fs duration (encompassing only 1.5 optical cycles). The pulse energy reached 6.1 mJ, yielding a peak power of 1.2 TW, which breaks a 10-years old record [NKV20]. Here a major key finding was a limitation of the nonlinearity to rather moderate light-matter interaction. To this end, we kept the peak intensity at a tolerable level by scaling up the dimensions of the waveguide. At the same time we used helium, being the least nonlinear material, and circularly polarized light for further reducing the nonlinearity. The design concept of energy scaling is detailed in a subsequent overview article on high-energy few-cycle pulses later this year [NSV]. The chirped mirror compressor and an online dispersion-scan device are situated in vacuum at the beginning of a  $\sim 15$  m long HHG beamline directly connected to the HCF arrangement. The full characterization of the above-TW pulses is shown in Fig. 9.

The remarkably good phase compensation is shown in Fig. 9(c). These results were achieved by using a 2 mm KDP crystal for third-order dispersion compensation.

The intense 1.5-cycle pulses were utilized for high-harmonics generation in a 10 cm long gas cell filled with argon or neon. In the former case the energy of the filtered harmonics radiation was measured by a calibrated XUV photodiode to be 260 nJ. In case of neon, a harmonic spectrum with a continuous cut-off region reaching 100 eV was obtained, which is shown in Fig. 10.

The intense harmonics radiation will find applications in nonlinear XUV pump-probe experiments.

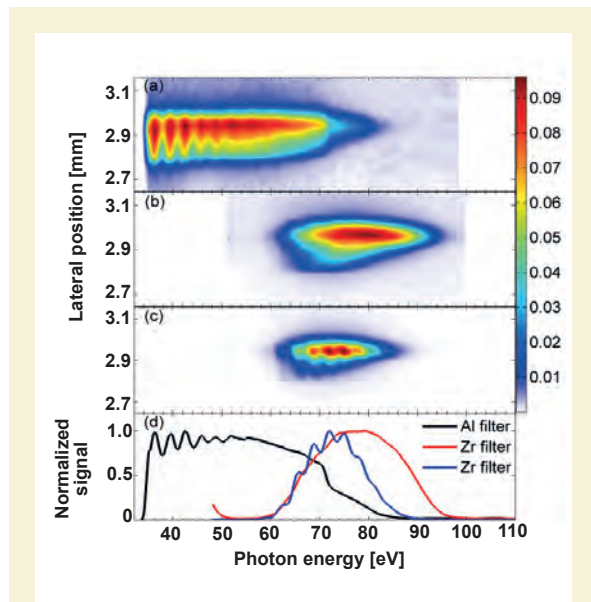


**Fig. 10:** Harmonics spectrum generated in neon, recorded behind an Al filter (a), or behind a Zr filter (b) and (c). In (b) the compressor was optimized while in (c) the driver pulses were slightly positively chirped. (d) shows the spatially integrated spectra. Taken from [NKV20].

### Spectral broadening in a multi-pass cell

An alternative approach for nonlinear pulse compression relies on multi-pass cells (MPC). In 2019 first results on the compression of 45 fs pulses from a Ti:Sapphire amplifier down to less than 12 fs were demonstrated, by utilizing a gas-filled MPC. In 2020 those results were improved to increase the energy per pulse and bring the compressed pulse duration below 8 fs.

The laser delivers 3 mJ pulses at a 1 kHz repetition rate at a central wavelength of 800 nm. The multi-pass cell was built inside a compact chamber (65 cm x 30 cm x 30 cm) filled with Ar at pressure below 2 bars. The multi-pass cell was formed by two identical concave silver-coated mirrors with a radius of curvature of 300 mm, diameter of 50 mm and a separation slightly below 600 mm. Figure 11 shows results for a mirror separation of 585 mm. After spectral broadening by 5.5 round-trips in the cell, the beam was coupled out of the cell (and the chamber) by a 12 mm diameter silver-coated mirror. After collimation with a spherical mirror the pulses were compressed utilizing a set of chirp mirrors (Ultrafast Innovations PC70) and a pair of thin fused-silica wedges.

Figure 11(a) shows a comparison between the input and output pulse spectrum, while Fig. 11(b) shows the corresponding pulses in the time domain. In this case the input pulse energy was 290  $\mu\text{J}$ , limited by ionization and the pulse energy after compression was 130  $\mu\text{J}$ , resulting in 45 % efficiency. The efficiency can be further improved by utilizing dielectrically enhanced silver mirrors and replacing the output window of the chamber (uncoated during these experiments) with an AR-coated window.

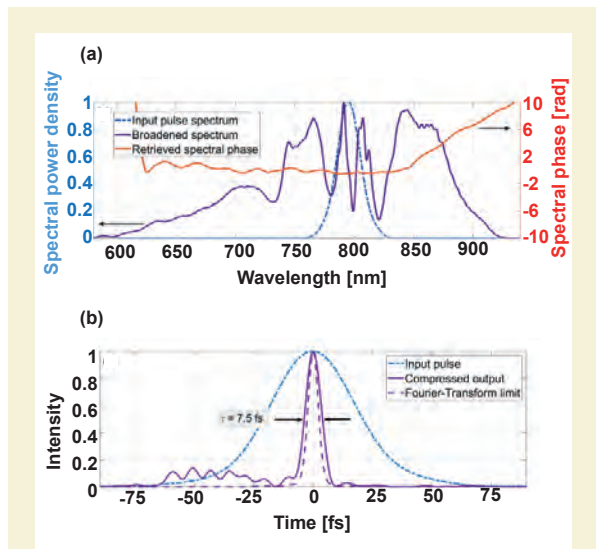


**Fig. 11:** (a) Input (dotted-dashed blue line) and output (solid violet line) spectra after spectral broadening in the multi-pass cell. The red line shows the retrieved spectral phase. (b) Retrieved pulse duration of input pulse (dotted-dashed blue line), output pulse (violet solid line), and the Fourier-transform limited pulse corresponding to the broadened spectrum (dashed violet line).

The results of this experiment are now being used as a starting point for designing a compression setup for sub-10 fs pulses with 190  $\mu\text{J}$  from a high power OPCPA, based on 3-dimensional nonlinear propagation simulations.

### Spectral Broadening in $\text{As}_2\text{S}_3$

Gain narrowing limits the achievable spectral bandwidth in high power OPCPA systems. Therefore, it appears highly favorable to implement an efficient post-compression scheme. Typically, gas cells, hollow core or photonic crystal fibers for spectral broadening show efficiencies below 50%, which stimulated us to search for alternative methods. Due to the relatively high nonlinear refractive index of chalcogenide materials like  $\text{As}_2\text{S}_3$ , spectral broadening (free of strong modulations) is achieved even at rather low peak intensities. In turn, this makes the experimental setup comparatively compact, robust and easy to adjust. Simply inserting an  $\text{As}_2\text{S}_3$ -plate into an unfocused beam of few-cycle mid-infrared pulses, spectral broadening is readily achieved with high efficiency. In a first proof-of-principle experiment, we successfully demonstrated that 2- $\mu\text{m}$ -pulses can be substantially broadened and post-compressed as can be seen in Fig. 12. Finally, one can expect multi-mJ two-cycle pulses with a peak power of 180 GW resulting in significant enhancement of the soft-x-ray flux generated within a HHG setup.

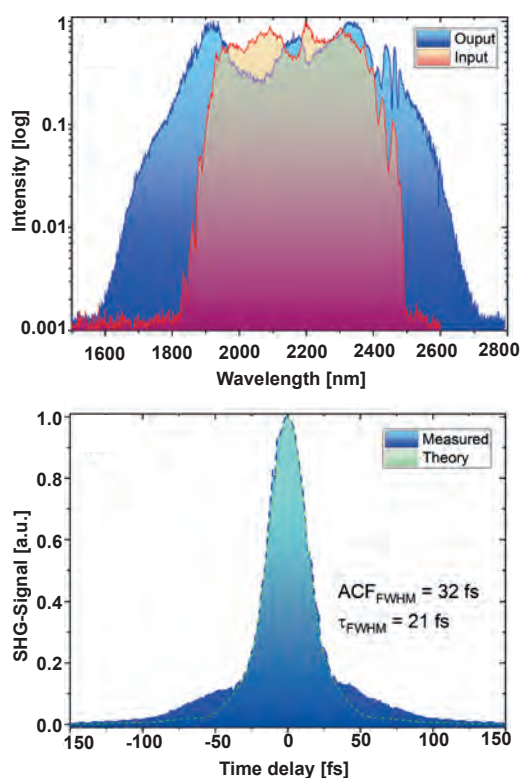


**Fig. 12:** Measured spectral broadening in  $\text{As}_2\text{S}_3$  (left) and auto-correlation trace of the compressed pulse (right). The pulse duration was reduced from 27 fs to 21 fs reaching the measuring limits of the autocorrelator.

### Elliptically polarized soft X-rays

Elliptically polarized soft X-rays (SXR) find various applications, for instance in the investigation of chiral molecules or the magnetic structure of materials. Therefore, the aim of this project is the elliptical polarization of the high harmonics (HH) generated with the 2  $\mu\text{m}$  Nano-movie OPCPA system. The setup is shown in Fig. 13 and has been implemented in the XPL lab. A BBO crystal is put in the beam path in order to produce 1  $\mu\text{m}$  radiation polarized perpendicularly to the 2  $\mu\text{m}$  light. Theory [MBe20b] then predicts the generation of even and odd order harmonics of opposite and varying helicity. The detection is performed with both a polarimeter and an XMCD measurement (not shown in Fig. 13). First results are expected in spring 2021.

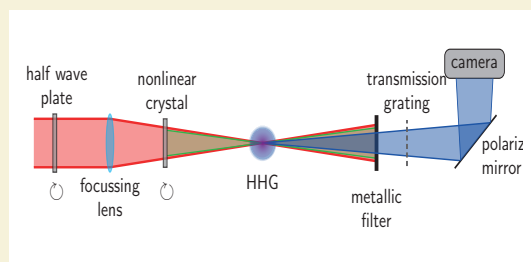


**Fig. 13:** Setup for the generation and characterization of elliptically polarized high harmonics in the water window.

### Compact intense XUV source

Intense XUV pulses are required for a broad range of applications including attosecond-pump atto-second-probe spectroscopy, nonlinear and strong-field XUV physics as well as coherent diffractive imaging of nanoscale structures and nanoparticles. Currently, however, intense XUV pulses are only available at a small number of places worldwide including free-electron laser facilities and long high-harmonic generation beamlines. This limitation clearly hinders faster progress in the afore-mentioned fields.

The standard scheme used for generating intense XUV pulses based on HHG is loose focusing of the driving laser pulses into the generating medium in order to maximize the XUV flux that can be obtained. This does not only require large setups and puts very high demands on the laser stability. The scheme also has limitations regarding the highest XUV intensities that can be achieved, since the XUV source size grows proportionally to the focal length that is used, and source demagnification factors that can be achieved using focusing optics are limited.

Recently, we have suggested and demonstrated a much more compact setup for the generation of intense XUV pulses based on HHG. In contrast to classical HHG, where the generating medium is placed at or close to the driving laser focus, we have generated harmonics in a dense gas jet that is placed several Rayleigh lengths away from the driving laser focus, see Fig. 14(a). In this way, (i) the generation volume can be optimized and (ii)

the transfer of the curved wavefronts from the NIR pulse to the generated XUV pulse means that the virtual XUV source size is much smaller than the NIR focus size, see Fig. 14(b). This resulted in a focused XUV beam waist radius of 600 nm [MGK20] using a setup with a length of only 2 meters. In this way, a high XUV peak intensity of  $2 \cdot 10^{14}$  W/cm<sup>2</sup> was achieved [MGK20], which was previously only possible using setups that are one to two orders of magnitude larger. These findings were well reproduced by numerical simulations that were carried out by our collaborators from Szeged (ELI-ALPS) and Cluj [MGK20]. To demonstrate this high XUV intensity, we have studied the multiphoton ionization of argon atoms, resulting in the generation of Ar<sup>2+</sup> and Ar<sup>3+</sup> ions (see Fig. 15), which are the result of a two-photon and a four-photon absorption process, respectively.

Our concept represents a straightforward approach for the generation of intense XUV pulses in many laboratories. In the future, even higher XUV intensities up to

$10^{17}$  W/cm<sup>2</sup> may be achieved by using higher driving pulse energies in combination with appropriate scaling of the driving beam parameters and the sizes of the optical elements.

### HHG Theory and Simulation

Optimization of High Harmonic flux depends on various parameters of the laser driver, beam propagation geometry and the generating medium. Often the search of a global maximum is hampered by experimental constraints and the interplay of different processes provides a complex physical picture. Therefore analytical calculation and numerical simulation of the process are indispensable tasks. Complete simulation of the process is very time consuming and costly. Therefore we pursue search strategies complemented by following in-depth calculation. The idea is to get confidence in optimum HHG for the existing and upcoming MIR-laser driver systems at MBI.

As a first step, code calculations were performed using a Maxwell – solver for beam propagation accounting for geometrical, dipole and dispersive caused phase shifts. Ionization is derived from an adapted ADK-model. Microscopic HHG of a given selected order is simply assumed if the necessary intensity is reached in the respective beam position. (Real HHG signal calculation will be done in a next step when narrow parameter regions have been identified.) Thus a so-called “figure-of-merit” (FOM)

$$d(\text{FOM})/dz = \text{pressure} * \cos(\text{phase}) * H(\text{intensity})$$

in dependence on beam propagation, phase shift and intensity (H is 1 or 0 concerning intensity) is calculated. The FOM indicates regions of phase-matching for a se-

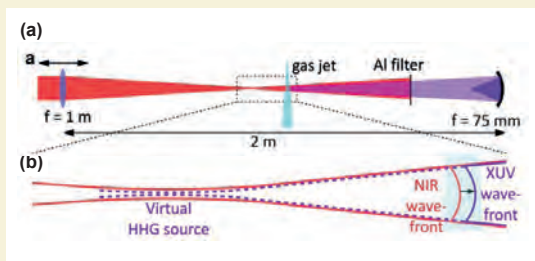


**Fig. 14:**

*Compact intense XUV source.*

a) *Experimental setup:* NIR driving pulses with a duration of 40 fs and a pulse energy of 8 mJ (for HHG in Xe) or 16 mJ (for HHG in Kr) are focused using a spherical lens with  $f = 1$  m. HHG takes place in a high-pressure gas jet that is placed in the converging or diverging NIR beam. An Al filter attenuates the NIR pulses after HHG, and the XUV pulses are focused to high intensities by a spherical mirror with  $f = 75$  mm.

b) *Zoom into the generation region, visualizing the transfer of curved wavefronts from the fundamental to the harmonic beam. This leads to a virtual HHG source size which is significantly smaller than the NIR focus size.*

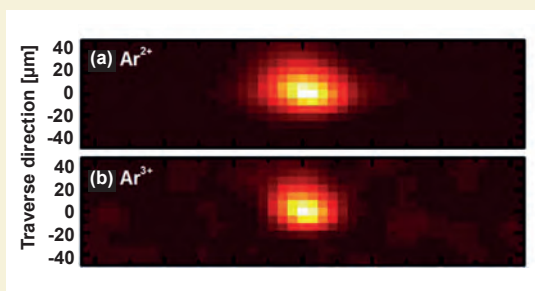


**Fig. 15:**

*XUV multiphoton ionization of Ar. (a) Ar<sup>2+</sup> and (b) Ar<sup>3+</sup> ion yields as a function of the distance from the XUV focal plane. The horizontal distribution is slightly narrower for Ar<sup>3+</sup>, reflecting the higher nonlinearity in this case.*

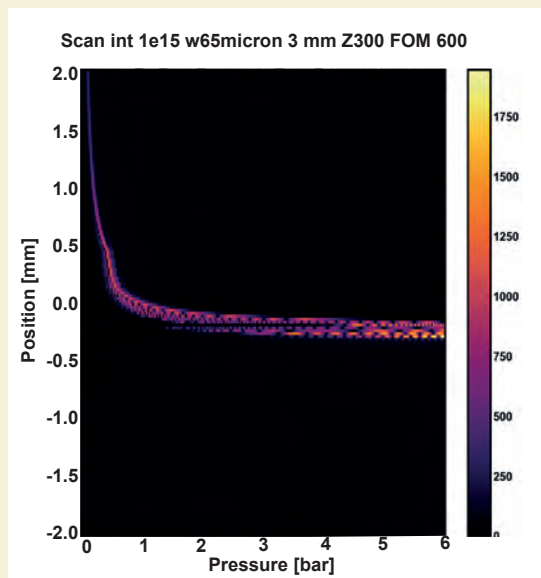


**Fig. 16:**

*Change of FOM (cf. text) – color coded – with He-pressure (x-axis) in a 3 mm gas cell and entrance position (y-axis) for harmonic order 600 (corresponds to 354 eV) of a 2.1 μm (25 fs,  $10^{15}$  W/cm<sup>2</sup>) driver.*

lected harmonic order and following signal maximum. Figure 16 displays the color-coded FOM as a function of He-gas pressure in a 3 mm extended gas cell and the entrance position of the cell in respect to the position of the focus of the drive beam.

The calculations indicate HH signal enhancement with pressure. This will be investigated at the Nanomovie 2.1  $\mu\text{m}$  OPCPA system (cf. project report 4.2) with a new powerful gas pumping system. So far, measured photon numbers (cf. 4.2) are based on He-pressure of 1 bar. Furthermore we aim to understand observed limitations in phase-matching for strategies improving the HH-yield further.

### Own Publications 2020

(for full titles and list of authors see appendix 1)

- BLM20: L. Basyrova *et al.*, SPIE Proc. **11259** (2020) 1125910/1-7
- BSG20: B. P. Bruno *et al.*, Smart Mater. Struct. **29** (2020) 075003/1-8
- CDW20: Y. Chen *et al.*, Opt. Lett. **45** (2020) 722-725
- CLS20: M. Chen *et al.*, Journal of Alloys and Compounds **813** (2020) 152176/1-8
- CLY20: M. Chen *et al.*, SPIE Proc. **11259** (2020) 1125927/1-7
- CWC20: H. M. Crespo *et al.*, Optica **7** (2020) 995-1002
- EJS20: E. Escoto *et al.*, J. Opt. Soc. Am. B **37** (2020) 74-81
- EMV20: U. Elu *et al.*, Opt. Lett. **45** (2020) 3813-3815
- ES20a: E. Escoto and G. Steinmeyer, SPIE Proc. **11265** (2020) 1126509/1-3
- ES20b: E. Escoto and G. Steinmeyer, SPIE Proc. **11263** (2020) 1126306/1-3
- FEW20: F. J. Furch *et al.*, SPIE Proc. **11268** (2020) 11268ON/1-6
- GBo20: R. Grunwald and M. Bock, Adv. Phys.-X **5** (2020) 1736950/1-25
- GBU20a: L. v. Grafenstein, *et al.*, Opt. Lett. **45** (2020) 3836-3839
- GBU20b: L. v. Grafenstein *et al.*, Opt. Lett. **45** (2020) 5998-6001
- HLC20: J. Hirschmann *et al.*, Opt. Express **28** (2020) 34093-34103
- HPM20: Z. Heiner *et al.*, Opt. Lett. **45** (2020) 5692-5695
- KBW20: K. Kato *et al.*, Opt. Lett. **45** (2020) 2136-2139
- KLV20: E. Kifle *et al.*, Opt. Lett. **45** (2020) 4060-4063
- KPM20: K. Kato *et al.*, SPIE Proc. **11264** (2020) 112641W/1-5
- KTS20: M. Kretschmar *et al.*, Opt. Express **28** (2020) 34574-34585
- KZG20: S. Krekic *et al.*, Frontiers in Plant Science **11** (2020) 547818/1-14
- KZP20: M. Kowalczyk *et al.*, J. Opt. Soc. Am. B **37** (2020) 2822-2829
- LCS20: P. Loiko *et al.*, Opt. Lett. **45** (2020) 1770-1773
- LLK20: V. Llamas *et al.*, Opt. Express **28** (2020) 3528-3540
- LMS20: R. Liao *et al.*, Phys. Rev. A **102** (2020) 013506/1-12
- LTB20a: M. Liebmann *et al.*, SPIE Proc. **11297** (2020) 12970W/1-7
- LTB20b: M. Liebmann *et al.*, Appl. Sci. **10** (2020) 4288/1-14
- MBT20: O. Melchert *et al.*, Comm. Phys. **3** (2020),
- MCT20: A. Muti *et al.*, Opt. Lett. **45** (2020) 656-659
- MPH20: M. Mero *et al.*, SPIE Proc. **11264** (2020) 112640F/1-7
- MSt20: C. Mei and G. Steinmeyer, J. Opt. Soc. Am. B **37** (2020) 2485-2497.
- MTP20: Y. Morova *et al.*, Opt. Lett. **45** (2020) 931-934
- NKV20: T. Nagy *et al.*, Opt. Lett. **45** (2020) 3313-3317
- OVB20: M. Ouillé *et al.*, Light Sci. Appl. **9** (2020) 47/1-9
- PLS20: Z. Pan *et al.*, SPIE Proceedings Series **11259** (2020) 1125911/1-6
- SER20: L. Shi *et al.*, ACS Photonics **7** (2020) 1655–1661
- SLS20: K. Subbotin *et al.*, J. Luminesc. **228** (2020) 117601/1-12
- SPG20b: P. Satapathy *et al.*, J. Semicond. **41** (2020) 032303/1-6
- TJA20: R. Trebino *et al.*, J. Appl. Phys. **128** (2020). 171103/1-43
- VLP20a: A. Volokitina *et al.*, Opt. Express **28** (2020) 9039-9048
- VLP20b: A. Volokitina *et al.*, Opt. Mater. Express **10** (2020) 2356-2369

VLP20c: A. Volokitina *et al.*, SPIE Proc. **11357** (2020) 113571T/1-7

WCZ20: L. Wang *et al.*, Opt. Lett. **45** (2020) 6142-6145

WZP20: Y. Wang *et al.*, SPIE Proc. **11259** (2020) 1125929/1-6

YLC20: F. Yue *et al.*, Opt. Express **28** (2020) 28399-28413

ZWC20a: Y. Zhao *et al.*, High Power Laser Science and Engineering **8** (2020) e25/1-5

ZWC20b: Y. Zhao *et al.*, Appl. Opt. **59** (2020) 10493-10497

ZWW20: Y. Zhao *et al.*, Opt. Lett. **45** (2020) 459-462

### in press

BLM: L. Basyrova *et al.*, Ceram. Int.

EDS: E. Escoto *et al.*, IEEE J. Quantum Electron.

EMV: U. Elu *et al.*, Nat. Photon.

NSV: T. Nagy *et al.*, Adv. Phys. X

KLR: E. Kifle *et al.*, Opt. Lett.

KMP: K. Kato *et al.*, Opt. Lett.

LKG: P. Loiko *et al.*, J. Opt. Soc. Am. B

LPS: P. Loiko *et al.*, J. Lumin.

NSV: T. Nagy *et al.*, Adv. Phys. X

PLW: Z. Pan *et al.*, J. Alloys Compd.

VDL: A. Volokitina *et al.*, J. Lumin.

WCS: L. Wang *et al.*, Opt. Lett.

ZWX: Y. Zhao *et al.*, Photonics Res.

### submitted

MGK20: B. Major, O. Ghafur, K. Kovács, K. Varjú, V. Tosa, M. J. J. Vrakking, and B. Schütte; Compact intense extreme-ultraviolet source; arXiv:2012.04566 (2020).

### Other Publications

[1] S. Vasilyev, I. Moskalev, M. Mirov, V. Smolski, S. Mirov, and V. Gapontsev, "Ultrafast middle-IR lasers and amplifiers based on polycrystalline Cr:ZnS and Cr:ZnSe," Opt. Mater. Express **7**, 2636–2650 (2017).

[2] S. Cheng, G. Chatterjee, F. Tellkamp, T. Lang, A. Ruehl, I. Hartl, and R. J. D. Miller, "Compact Ho:YLF-pumped ZnGeP<sub>2</sub>-based optical parametric amplifiers tunable in the molecular fingerprint regime," Opt. Lett. **45**, 2255-2258 (2020).

[MBe20b] D. B. Milošević and W. Becker; High-order harmonic generation by bi-elliptical orthogonally polarized two-color fields; Phys. Rev. A **102** (2020) 023107/1-14

Lie20: M. Liebmann; Highly resolved analysis regarding the spatial statistical behaviour of spectral anomalies in fs-pulsed vortex beams (Supervisor: S. Schrader, R. Grunwald), Technische Hochschule Wildau

### Invited Talks at International Conferences

(for full titles see appendix 2)

U. Griebner *together with* W. Chen, Y. Zhao, F. Rotermund, X. Mateos, P. Loiko, and V. Petrov; International Conference Laser Optics 2020, (2020-11)

U. Griebner, *together with* L. von Grafenstein, M. Bock, A. Koc, C. Hauf, M. Woerner, K. Zawilski, P. Schunemann, and T. Elsaesser; OSA High-brightness Sources and Light-driven Interactions Congress (Prague, Czech Republic, 2020-11)

M. Mero *together with* Z. Heiner, and V. Petrov; SPIE Photonics West 2020 (San Francisco, USA, 2020-02)

M. Mero *together with* V. Petrov and Z. Heiner; 22nd Photonics North conference (2020-05)

M. Mero; 19th International Conference Laser Optics, ICLO 2020 (2020-11)

T. Nagy *together with* S. Hädrich, P. Simon, A. Blumenstein, N. Walther, R. Klas, J. Buldt, H. Stark, S. Breilkopf, P. Jójárt, I. Seres, Z. Várallyay, T. Eidam, and J. Limpert; CLEO 2020 (Washington D.C., USA, 2020-05)

G. Steinmeyer, EPS Europhoton 2020 (Prague, Czech Republic, 2020-08)

G. Steinmeyer; 5th Int. Symposium - Advances in Non-linear Photonics (Minsk, Belarus, 2020-09)

## 2.1: Time-resolved XUV-science

A. Rouzée, S. Patchkovskii (project coordinators)

and M. Anus, D. Ayuso, L. Drescher, T. Fennel, F. Furch, O. Ghafur, C. Granados Buitrago, A. Harvey, L. Hecht, E. Ikonnikov, M. Ivanov, A. Jiménez Galán, A. Heilrath, A. Hoffmann, A. Husakov, K. Kolatzki, L.-M. Koll, O. Kornilov, M. Kretschmar, B. Langbehn, L. Maikowski, N. Mayer, J. Mikosch, F. Morales Moreno, T. Nagy, M. Osolodkov, M. Richter, A. Röder, D. Rupp, M. Sauppe, F. Schell, C. P. Schulz, B. Schütte, B. Senffleben, O. Smirnova, M. T. Talluri, M. J. J. Vrakking, S. Walz, T. Witting, Z.-Y. Zhang

### 1. Overview

The main goal of the project 2.1 is to visualize, understand, and steer electronic and atomic motion during transformation of finite quantum systems, starting from few-body systems to isolated nanoparticles. The project has both experimental and theoretical components. Experimentally, we are developing a framework of closely interconnected time-resolved methods, unified by the application of novel XUV/X-ray light sources. We employ both table-top sources, such as those based on high-order harmonic generation (HHG), as well as free electron laser facilities. Using photoionization as a probe step in a pump-probe configuration, we investigate attosecond electron motion in atoms, molecules and nanoparticles and its coupling to the nuclear motion. In many cases these new light sources allow combining the extreme temporal resolution (attoseconds) with atomic-scale spatial resolution. Our experimental framework is complemented by an advanced theory program aiming at (i) tracking down and resolving correlated multi-electron dynamics on the attosecond time scale, and (ii) understanding the impact of coherently excited attosecond multi-electron dynamics on the longer, femtosecond-scale nuclear motion. Together the experimental and theoretical parts of the project push atomic and molecular science beyond the present state-of-the-art towards the new, attosecond timescales in chemical and physical processes.

### 2. Topics and collaborations

Presently, the project is organized in four topics:

**T1: Attosecond electronic dynamics in strongly driven systems**

**T2: Strongly-coupled electronic and nuclear dynamics in photoexcited neutral molecules**

**T3: Ultrafast electronic decay and fragmentation dynamics at XUV and X-ray wavelengths**

**T4: Collective and correlated electron dynamics at the nanoscale**

Collaborations with: A. Rudenko, D. Rolles (Kansas State University, USA); J. Küpper (Center For Free-Electron Laser, Hamburg); H. Stapelfeldt (Aarhus University, Denmark); A. Vilesov (UCLA, USA), K. Ueda (Tohoku University, Japan); F. Calegari (CFEL, Hamburg); F. Lépine (Institut Lumière et Matière, France); D. Holland (Science and technology facility council, UK);

Th. Pfeifer (Max Planck Institute for nuclear physics, Germany); K. Varju (University of Szeged, Hungary); L. Banares (Universidad Complutense de Madrid, Spain); H. Köppel, A. Kuleff (University of Heidelberg); T. Möller (TU Berlin), K. H. Meiwes-Broer, I. Barke (Universität Rostock); B. v. Issendorff (Universität Freiburg); P. Piseri (Università di Milano, Italy); M. Kling (LMU Munich); P. Hommelhoff (FAU Erlangen); T. Brabec (University of Ottawa, Canada); G.G. Paulus (University Jena); C. Menoni (Colorado State University, USA), A. Orr-Ewing, M. Ashfold (University of Bristol, UK), F. Stienkemier (University of Freiburg).

In-house collaborations with projects 1.1, 1.2, 2.2, 3.1, and 4.1.

### 3. Results in 2020

**T1: Attosecond electronic dynamics in strongly driven systems**

In XUV-IR pump-probe experiments, the RABBITT technique (reconstruction of attosecond beating by interference of two-photon transitions) can be used both, to measure the driving laser fields with attosecond time resolution and to get insights into the light-induced processes in atomic or molecular targets, such as to measure photoionization time delays. While classical RABBITT experiments use long, multicycle IR pulses and therefore also long attosecond pulse trains, our 100 kHz OPCPA laser system produces short few-cycle IR pulses of 7 fs duration, with the consequence that fluctuations of the carrier envelope phase (CEP) have a large impact on the RABBITT measurements and should be taken into account for the retrieval of the laser fields. We have recently developed a mixed state time-domain ptychography algorithm for the retrieval of pulse ensembles under such conditions [WFK20] and applied this method to retrieve the XUV and IR pulses from experimental data of two-colour ionization of Ar atoms [OFS20]. It was shown that application of conventional reconstruction algorithms neglecting the CEP fluctuations underestimated substantially not only the temporal width of the individual XUV pulse but also the intensity envelope of the pulse train. Meanwhile, our modified algorithm retrieved a pulse train characterised by the presence of at least 7 pulses with sub-400 as duration each.

Improvements of the 100 kHz OPCPA system allowed us to demonstrate stable operation of the pump-probe setup for RABBITT experiments employing the reaction microscope (REMI) for coincident detection of ions

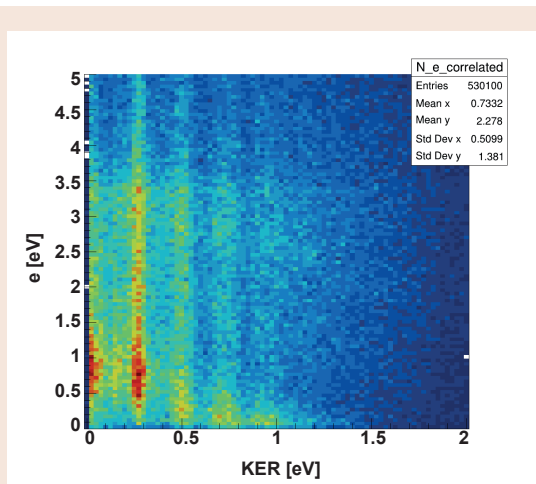


**Fig. 1:** Photoelectron energy vs.  $N^+$  kinetic energy release after ionization of  $N_2$  molecules by combined XUV and IR pulses. Red dotted line shows the correlated electron ion signal.

and electrons. As a result RABBITT measurements can now be performed routinely with up to 4 days of uninterrupted data acquisition. First RABBITT scans with gas mixtures of Ar and  $N_2$  have been recorded. The coincidence detection of ions and electrons allows separating the argon and the nitrogen RABBITT sideband signals. The Ar signal serves as a reference to characterise the XUV pulse trains in situ, which is necessary to access the time-delays in photoionized  $N_2$ . Fig. 1 shows KER vs. the photoelectron energy after excitation with XUV and IR pulses (integration over all pump-probe delays). One can clearly identify the  $N_2^+$  vibrations of the C state and the corresponding spectra.

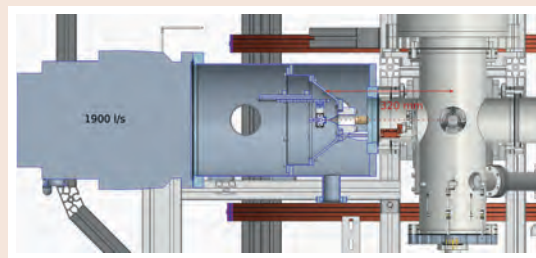


**Fig. 2:** New molecular beam source attached to the REMI. The target density has been increased by at least a factor of four compared to the previously used source. The electron count rate of Ar/ $N_2$  mixtures in RABBITT experiments using the 100 kHz OPCPA system now exceeds 20 kHz.

Due to the relatively low count rate it was difficult to record electron-ion coincidence maps as shown in Fig. 1 as a function of pump-probe delays. To solve this issue, a new molecular beam source has been installed into the reaction microscope (Fig. 2). It reduces the distance between the nozzle and the interaction point by a factor of 2. In addition, increased pumping speed allowed larger nozzle diameters. First tests showed that the count

rate for Ar target gas increased at least by a factor of four even with moderate backing pressures. The overall count rate reached values larger than 20 kHz, which is a (soft) limit for coincident electron ion detection. A remaining problem is the relatively strong portion of background counts (~40 %). This problem will be resolved in the near future by adding a differential pumping stage.

### Extreme ultraviolet spectral compression

Nonlinear optical techniques are widely used to spectrally compress or spectrally broaden ultrashort light pulses. It is difficult, however, to transfer these techniques to the XUV wavelength range, where nonlinear optical techniques are not readily available. We have recently developed a new scheme that makes it possible to spectrally compress an XUV pulse by a factor of more than 100. These results were published in Nature Photonics [DKW]. Our spectral compression is based on a process known as four-wave-mixing. In this scheme a krypton atom non-resonantly absorbs one vacuum-ultraviolet (VUV) photon from a broadband VUV pulse and two visible photons from a broadband visible pulse that copropagates with the VUV pulse, leading to the emission of a XUV photon. Due to energy conservation, the emitted XUV photon must have a frequency equal to the sum of the frequencies of all three absorbed photons. At the same time, due to momentum conservation, the velocity of the incoming light wave has to match the velocity of the outgoing wave inside the mixing medium.

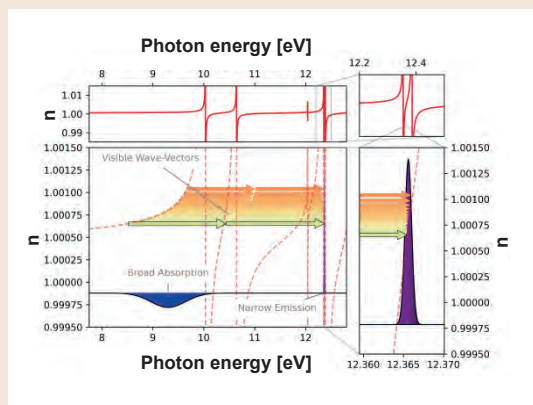


**Fig. 3:** XUV spectral compression scheme: The refractive index as a function of the photon energy is shown by the red dashed curve. In the region around 9.2 eV it changes comparably slowly (left side), whereas it changes very quickly in the region around 12.365 eV. Therefore, a broadband absorption (blue area) can lead to a narrowband emission (violet area) with the help of two visible photons (shown by the green/orange arrows).

To achieve energy and momentum conservation required to generate the narrowband XUV laser in our experiment, a VUV spectral range quite far away from any resonance, and a target XUV range between two resonances are used. In this way, the velocities of a broad range of incoming wavelengths are phase-matched to a narrow region of outgoing wavelengths leading to a

narrowband emission, as shown in Fig. 3. This scheme was experimentally demonstrated by generating an XUV pulse at 12.365 eV with a bandwidth of only about 2 meV [DKW].

The generation of narrowband XUV pulses is interesting for applications such as photoelectron spectroscopy, the investigation of resonant transitions, and the coherent diffractive imaging of nanoscale structures. In the future, this new method could also be used in the opposite direction, i.e., to spectrally broaden XUV pulses, which may result in the generation of very short XUV pulses from sources with narrower emission such as free-electron lasers.

## T2: Strongly coupled electronic and nuclear dynamics in photoexcited neutral molecules

X-ray absorption spectroscopy (XAS) is a widely used technique that allows probing the electronic structure of matter by monitoring transitions between tightly bound core-shell electrons and unoccupied atomic and molecular orbitals. With the advent of ultrashort X-ray sources based on high harmonic generation and free electron lasers with pulse durations reaching femtosecond and attosecond timescales, time-resolved X-ray absorption spectroscopy has become feasible, hence providing a mean to explore ultrafast electronic dynamics, including coupled electron-nuclear dynamics, in photoexcited molecules and materials with exquisite time resolution.

As a collaboration between project 2.1 and project 3.1, a femtosecond soft X-ray high harmonic source for time-resolved XAS experiments has been recently commissioned. The source currently provides soft X-ray pulses in a photon energy range from 200 eV to 450 eV, i.e. covering the carbon K-edge (~284 eV) and the nitrogen K-edge (~410 eV) [KEG19] with a photon flux of

~6.10<sup>6</sup> ph/s. The repetition rate of the source is 1 kHz. The relatively limited photon flux achieved in our studies, which is inherent to the low conversion efficiency of the HHG process at this high photon energy, makes the implementation of time-resolved XAS experiments very challenging. One of the limitations comes from the efficiency of the soft X-ray spectrometer. In order to improve the efficiency, we have recently designed and tested the performance of a new soft X-ray spectrometer for XAS based on refractive zone plates (RZPs) [KEW]. With respect to most soft X-ray spectrometers that are based on low reflectivity variable line spacing gratings, our spectrometer is based on the Hettrick-Underwood optical scheme and incorporates a grazing incidence spherical mirror for focusing and the aforementioned high reflectivity RZP as dispersive element (see Fig. 4).

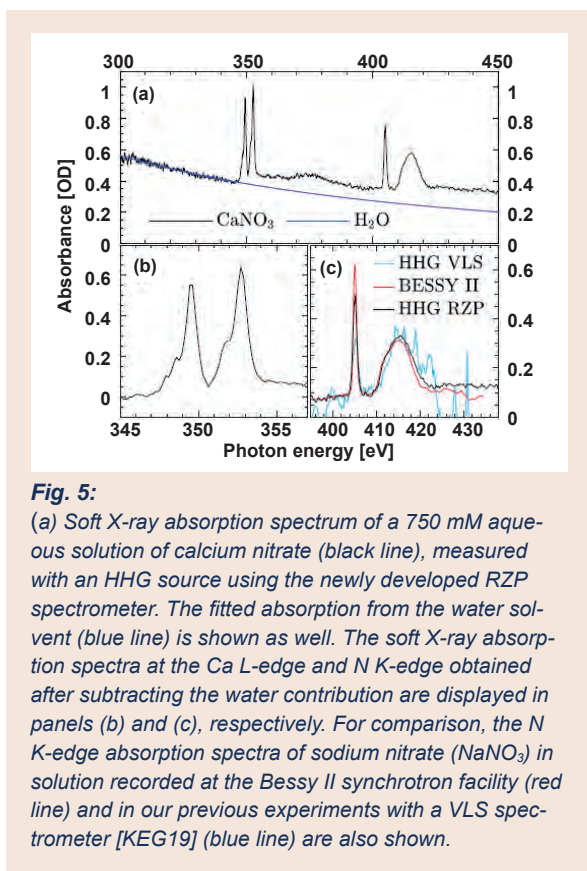


**Fig. 5:** (a) Soft X-ray absorption spectrum of a 750 mM aqueous solution of calcium nitrate (black line), measured with an HHG source using the newly developed RZP spectrometer. The fitted absorption from the water solvent (blue line) is shown as well. The soft X-ray absorption spectra at the Ca L-edge and N K-edge obtained after subtracting the water contribution are displayed in panels (b) and (c), respectively. For comparison, the N K-edge absorption spectra of sodium nitrate (NaNO<sub>3</sub>) in solution recorded at the Bessy II synchrotron facility (red line) and in our previous experiments with a VLS spectrometer [KEG19] (blue line) are also shown.

Using the spectrometer, a resolving power of 890 at a central photon energy of 410 eV and a total detected photon count rate of 400 photons/eV/s was achieved.

The soft X-ray absorption spectrum of a 750 mM aqueous solution of calcium nitrate was recorded using our newly developed spectrometer (see Fig. 5). Our measurements compare very well with previous measurements performed at the UE52\_SGM beamline at Bessy II. The large increase of the detected photon count rate provided by the RZP spectrometer enables recording of high quality soft X-ray absorption spectra in the water window spectral range and paves the way towards investigation of the transient electronic structure of both, isolated and solvated, photoexcited molecules by means of time-resolved XAS.

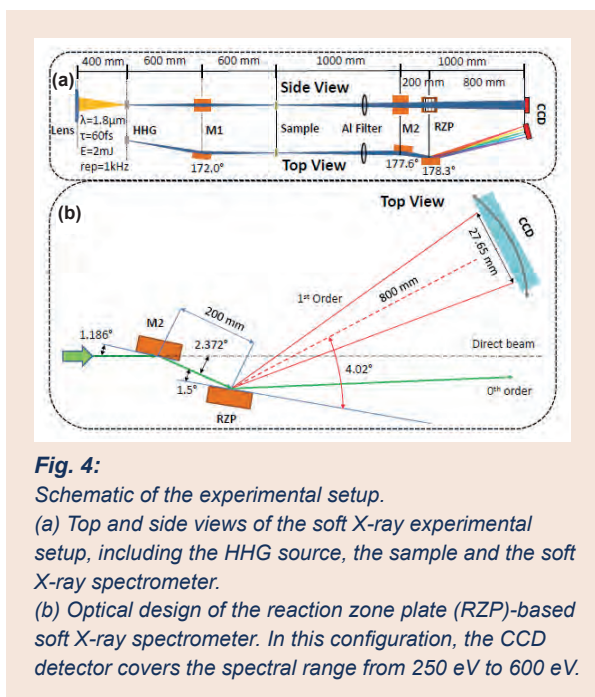


**Fig. 4:** Schematic of the experimental setup. (a) Top and side views of the soft X-ray experimental setup, including the HHG source, the sample and the soft X-ray spectrometer. (b) Optical design of the reaction zone plate (RZP)-based soft X-ray spectrometer. In this configuration, the CCD detector covers the spectral range from 250 eV to 600 eV.

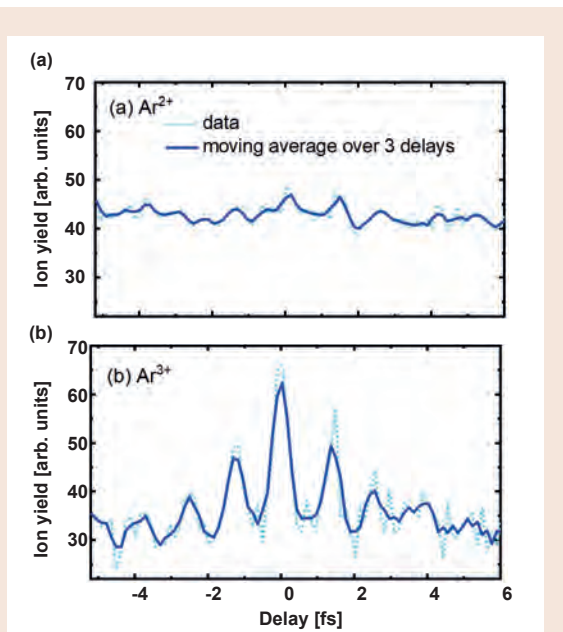


**Fig. 6:** XUV autocorrelation performed in Ar, showing a weak modulation for (a)  $Ar^{2+}$  ions and a strong modulation for (b)  $Ar^{3+}$  ions. This indicates a dominant role played by sequential (incoherent) processes in the former case, and an important role played by the direct absorption of at least two XUV photons in the latter case.

### T3: Ultrafast electronic decay and fragmentation dynamics at XUV and x-ray wavelengths

#### Attosecond XUV multiphoton ionization dynamics of argon

So far, the real-time investigation of multi-photon multi-electron dynamics occurring in atoms and molecules in interaction with intense attosecond pulses has been limited due to lack of intense attosecond light sources. In recent years, a new HHG source providing intense, attosecond pulses has been commissioned at MBI [SKH20]. The source is pumped by the output of an OPCPA system providing 40 mJ, sub-10 fs pulses at a 100 Hz repetition rate [KTS20]. Using this XUV source, the nonlinear ionization of argon atoms was studied, and charge states up to  $Ar^{6+}$  were observed following the absorption of at least 10 XUV photons [SKH20] demonstrating peak XUV intensities of up to  $10^{15}$  W/cm<sup>2</sup> [MKG20].

To understand the multi-photon multiple ionization dynamics leading to the formation of highly charged Ar ions in these studies, we have recently performed an attosecond-resolved autocorrelation measurement. Two replicas of a short attosecond pulse train with a controlled delay were generated using a split focusing mirror and the  $Ar^{n+}$  ion yields were recorded as a function of the delay between these two pulse replicas. Fig. 6(a) shows that the  $Ar^{2+}$  ion yield exhibits only weak modulations in dependence of the XUV-XUV time delay, whereas the  $Ar^{3+}$  ion yield shows strong oscillations with a period of about 1.3 fs. This corresponds to half the oscillation period of the fundamental laser, and reflects the generation

of one attosecond burst during each half cycle of the driving laser. The formation of  $Ar^{2+}$  was previously found to result from a two-photon process [SKH20]. The weak modulation observed in Fig. 6(a) indicates additionally that this two-photon absorption process is predominantly sequential. In contrast, the clear oscillations visible in  $Ar^{3+}$ , which involve a four-photon absorption process [SKH20], indicate that the simultaneous absorption of at least two XUV photons is required.

Our experiment is the first step towards the investigation of multi-photon multi-electron dynamics occurring on extremely short timescales, using attosecond XUV-XUV pump-probe spectroscopy.

#### Phase cycling of a pair of XUV pulses

Experiments within the project 2.1 strongly rely on the state-of-the-art sources of pulsed XUV radiation. The advancement towards the project's scientific goals goes hand-in-hand with the development of novel XUV sources. In line with this approach, in 2019/2020 we established a collaboration with the University of Freiburg (the group of Prof. Stienkemeier) to develop a new HHG-based source, which allows for investigation of coherent dynamics at XUV wavelengths. The method implemented at the time-delay-compensating monochromator beamline is based on phase cycling of a pair of XUV pulses and lock-in-based pathway-selective detection. The technique was demonstrated at 89 nm by generating the third-order harmonic of 266 nm radiation in Ar and Kr gases. Preservation of the phase of the driving field in the generated harmonic pulses was demonstrated. This method opens new possibilities for coherent non-linear spectroscopies at XUV wavelengths. The work was published in [WKW20].

### T4: Collective and correlated electron dynamics at the nanoscale

#### Quantum coherent diffractive imaging

Coherent diffractive imaging (CDI) using intense short-wavelength laser pulses from X-ray free-electron lasers (XFEL) has enabled structural analysis of individual nanoparticles in a single shot experiments. This method allows to track light-induced dynamics with high spatial and temporal resolution. While CDI with hard X-rays for maximal spatial resolution is likely to remain the domain of XFELs, lab-based sources have become sufficiently brilliant to enable CDI in the XUV domain, which is of particular interest for time-resolved studies due to exceptional temporal resolution and control. Moreover, despite reduced nominal spatial resolution, XUV-CDI enables wide-angle scattering measurements, and thus provides three-dimensional structural information in a single laser shot, allowing characterization of non-reproducible targets. Only recently, lab-based single-shot CDI of single Helium nanodroplets could be demonstrated with a laser-driven table-top HHG source at MBI [RML17]. Besides marking a breakthrough regarding accessibility, laser-based sources open unprecedented conceptual opportunities for CDI applications. The most obvious one results from the

temporal stability of optical laser systems and promises extremely high time resolution that is likely to reach the sub-fs range for CDI with attosecond XUV pulses.

Currently, the retrieval of structural information from scattering images in CDI experiments is based on the assumption of classical scattering in linear response. However, for strong laser fields and, in particular, for resonant excitations, both the linear and effectively incoherent classical description of the local polarization response may no longer be valid, as population depletion and stimulated emission become important. Our current activities aim at systematically exploring quantum effects in diffraction experiments. In a first theoretical study, we developed a density matrix-based scattering model that allows one to include quantum effects in the local medium response, and to explore the transition from linear to non-linear CDI for the resonant scattering from Helium nanodroplets [KLP20]. We showed substantial departures from the linear response and predicted that nonlinear spatio-temporal excitation dynamics results in rich features in the scattering, leading to the proposal of quantum coherent diffractive imaging as a promising novel branch in strong-field XUV and X-ray physics that we will explore in detail in the future.

#### Imaging ultrafast plasma formation

In a study published in Structural Dynamics [RFA20], we recorded diffraction patterns from individual xenon clusters irradiated with intense extreme ultraviolet pulses to investigate the influence of light-induced electronic changes on the scattering response. The experiments were conducted at the FLASH FEL in Hamburg. The wavelength was chosen to match different 4d inner-shell resonances of neutral and ionic xenon. This results in

distinctly different optical properties of the areas in the clusters with lower or higher charge states. Indeed, with this resonant diffraction imaging approach, the ultrafast formation of a nanoplasma, including areas of higher and lower charge states could be made directly visible.

In our measurement, we observe large-scale modulations in the radial profiles of the diffraction images (see Fig. 7(a), changing with the incoming power density of the FEL and indicating the emergence of a transient structure with a spatial extension of tens of nm within the otherwise homogeneous sample. Simulations suggest that ionization and nanoplasma formation result in an outer shell in the cluster, consisting of only highly charged xenon ions which is traced by a strongly altered refractive index. This evolution and the results of Mie-core-shell fitting are shown in Fig. 7 (b). Such a resonant scattering approach enables imaging of ultrafast electron dynamics on their natural timescale. The experimental realization of this dream is coming into reach with the current development of intense attosecond pulses at HHG beamlines and FELs.

#### A high intensity XUV beamline for nonlinear processes and HHG based CDI

In a collaboration with the projects 1.2 and 2.1, the teams of Tamas Nagy, Bernd Schütte and Daniela Rupp set up and characterized the 100 Hz beamline in the Extreme Photonics Lab at MBI (XPL), converting sub-10-fs NIR pulses with up to 40 mJ pulse energy [KTS20] into the extreme ultraviolet. In order to achieve highest XUV intensities in the experiment, a concept was employed, that requires a scaling of the experimental parameters which differs substantially from optimizing the HHG pulse energy [SKH20].

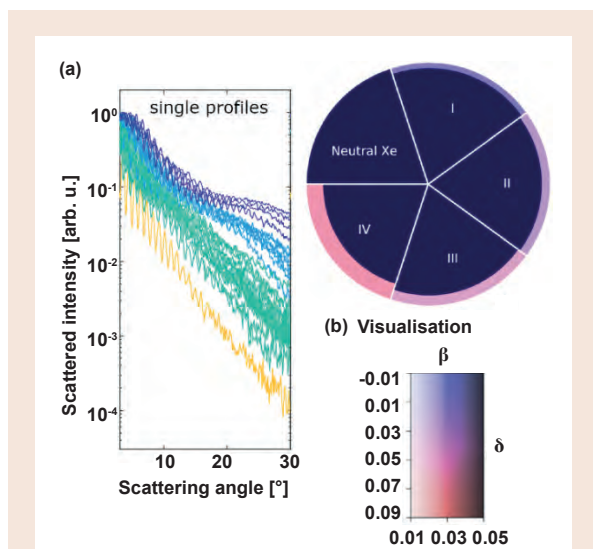


**Fig. 7:**  
 (a) Radial profiles of diffraction images from similarly sized xenon clusters, irradiated with different FEL intensities. The large-scale modulation is a fingerprint of the plasma formation.  
 (b) Visualization of the simulation and fitting results revealing a highly charged outer shell with strongly changed refractive indices. Adapted from [RFA20].

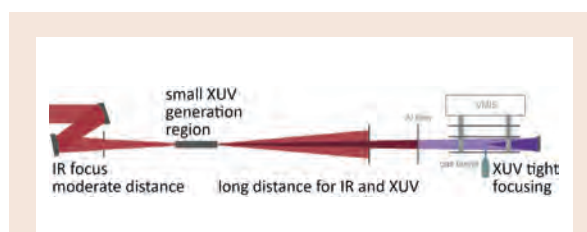


**Fig. 8:**  
 Sketch of the 100Hz beamline [SKH20].

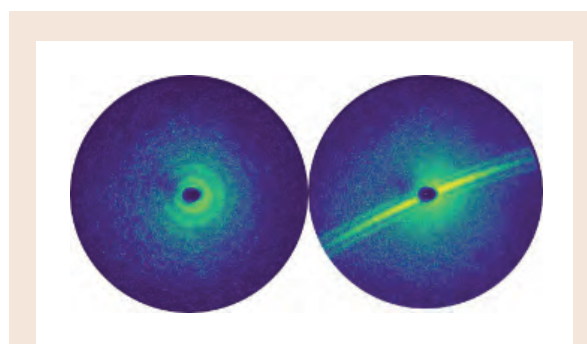


**Fig. 9:**  
 Diffraction images from helium nano-droplets at the 100 Hz HHG beamline at the MBI.

For a given laboratory size – in case of the XPL 18 meters, see Fig. 8 – the XUV intensity on target can be optimized by using an NIR focusing element with a relatively short focal length. This enables the generation of a smaller XUV beam waist radius in the experiment and a higher beamline transmission. As a result, we achieve an XUV intensity of more than  $10^{14}$  W/cm<sup>2</sup>, allowing the study of highly nonlinear processes (see Topic 3).

At the new 100 Hz beamline, first single-shot single-particle diffraction patterns could be measured from individual helium nanodroplets (see Fig. 9) and neon clusters. Time-resolved measurements are under way. The sub-10-femtosecond pulse duration and high temporal stability (or low jitter) of the beamline open a clear pathway towards imaging of ultrafast electron dynamics in nanoparticles.

### Own Publications in 2020 ff

(for full titles and list of authors see appendix 1)

CGS20: S. W. Crane, *et al.*; Chem. Phys. Lett. **738** (2020) 136870/1-7

DVM20: L. Drescher, *et al.*; J. Phys. B **53** (2020) 164005/1-9

FAB20: R. Forbes, *et al.*; J. Phys. B **53** (2020) 224001/1-13

HKL20: J. Hummert, *et al.*; J. Phys. B **53** (2020) 154003/1-8

KLP20: B. Kruse, *et al.*, J. Phys. Photonics **2** (2020) 024007/1-10

KTS20: M. Kretschmar, *et al.*; Opt. Express **28** (2020) 34574-34585

LSS20: Q. Liu, *et al.*; ACS Photonics **7** (2020) 3207-3215

MKG20: B. Major, *et al.*; J. Phys. Photonics **2** (2020) 034002/1-10

MPV20: N. Mayer, *et al.*; J. Phys. B **53** (2020) 164003/1-15

OFS20: M. Osolodkov, *et al.*; J. Phys. B **53** (2020) 194003/1-8

OKS20: T. Oelze, *et al.*; Opt. Express **28** (2020) 20686-20703

PIB20: S. Pathak, *et al.*; Nat. Chemistry **12** (2020) 795-800

RFA20: D. Rupp, *et al.*; Struct. Dyn. **7** (2020) 034303/1-10

SKH20: B. Senfftleben, *et al.*; J. Phys. Photonics **2** (2020) 034001/1-12

WFK20: T. Witting, *et al.*; J. Phys. B **53** (2020) 194001/1-8

WKW20: A. Wituschek, *et al.*; New J. Phys. **22** (2020) 092001/1-10

### in press

DKW: L. Drescher, *et al.*; Extreme-ultraviolet spectral compression by four-wave mixing; Nat. Photon.

### Submitted

KEW : C Kleine, M. Ekimova, M.-O. Winghart, S. Eckert, O. Reichel, H. Löchel, J. Probst, C. Braig, C. Seifert, A. Erko, A. Sokolov, M. J. J. Vrakking, E. T. J. Nibbering, and A. Rouzée, Highly efficient soft x-ray spectrometer for transient absorption spectroscopy with broadband table-top high harmonic sources

### Other Publications

KEG19: C. Kleine, M. Ekimova, G. Goldsztejn, S. Raabe, C. Strüber, J. Ludwig, S. Yarlagadda, S. Eisebitt, M. J. J. Vrakking, T. Elsaesser, E. T. J. Nibbering, and A. Rouzée; Soft X-ray Absorption Spectroscopy of Aqueous Solutions Using a Table-Top Femtosecond Soft X-ray Source, J. Chem. Phys. Lett. **10** (2019) 52

RML17: D. Rupp, N. Monserud, B. Langbehn, M. Sauppe, J. Zimmermann, Y. Ovcharenko, T. Möller, F. Frassetto, L. Poletto, A. Trabattini, F. Calegari, M. Nisoli, K. Sander, C. Peltz, M. J. J. Vrakking, T. Fennel and A. Rouzée, Coherent diffractive imaging of single helium nanodroplets with a high harmonic generation source, Nat. Comm. **8** (2017) 483

### Invited Talks at International Conferences

(for full titles see appendix 2)

T. Fennel; CMD 2020 GEFES, Joint conference of the condensed matter divisions of EPS CMD and RSEF GEFES, (Madrid, Spain, 2020-01): *Origin of strong-field-induced low-order harmonic generation in amorphous quartz*

M. J. J. Vrakking; CLEO 2020 (Washington D.C., USA, 2020-05): *Attosecond science using high average power and high peak power optical parametric chirped pulse amplifiers*

M. J. J. Vrakking; Quantum Battles in Attoscience 2020 (University College London, United Kingdom, 2020-07): *Attosecond entanglement and coherence*

M. J. J. Vrakking; SMART-X EU Marie Curie international training network, kick-off meeting (2020-07): *ITNs – tips, pitfalls and other experiences*

## 2.2: Strong-field Few-body Physics

*F. Morales Moreno, J. Mikosch (project coordinators)  
and D. Ayuso, W. Becker, U. Bengs, F. Branchi, T. Bredtmann, K. Dickson, U. Eichmann, M. Ivanov, Á. Jiménez,  
T. Kalousdian, J. Kaushal, J. Kirks, S. Meise, L. Merkel, M. Merö, J. Mikosch, D. B. Milošević, A. Ordoñez, S. Patchkovskii,  
H. R. Reiss, M. Richter, A. Rouzée, F. Schell, B. Schütte, O. Smirnova, P. Stammer, M. T. Talluri, S. Yarlagadda,  
N. Zhavoronkov*

### 1. Overview

On a sub-femtosecond temporal and Ångström spatial scale the project aims at

- understanding strong field induced dynamics in atoms and molecules,
- employing strong field processes as a tool for imaging and comprehending atomic and molecular electron dynamics and molecular structural changes,
- using tailored light pulses to manipulate electronic motion, generate high-order harmonics with specific polarization characteristics and investigate chiral phenomena.

We put specific focus on the fundamental aspects of strong field induced multi-electron dynamics, on the excitation of neutrals, on the forces exerted on these neutrals, on the role played by molecular structure and dynamics and on manipulating electronic dynamics. The strong field regime of interaction of light with matter is typically entered at light intensities beyond  $10^{13}$  Watt/cm<sup>2</sup> in the infrared spectral range. There, the electric field of the light wave starts to become comparable with the intra-atomic/intra-molecular field experienced by the valence electrons.

### 2. Topics and collaborations

We address our objectives via experiment and closely linked theory focusing on these topics:

**T1: Recollision physics and dynamic imaging in intense laser fields**

**T2: Strong-field processes in few-body systems**

**T3: Strong field excitation and HHG in tailored fields**

**T4: Coulomb Explosion Imaging of Photochemical Dynamics**

Collaboration partners: S. P. Goreslavski, S. V. Popruzhenko (National Research Nuclear University (MEPhi), Moscow, Russia), A. Saenz (HU Berlin), Y. Mairesse (CELIA, Université Bordeaux, Bordeaux, France), N. Dudovich (Weizmann Institute, Rehovot, Israel), J. Marangos (Imperial College, London, UK), X. J. Liu (Chinese Academy of Sciences, Wuhan, China), J. Chen (Beijing Univ., Beijing, China), T. Marchenko (Université Pierre et Marie Curie, Paris, France), J. M. Bakker, G. Berden, B. Redlich (FOM-Institute for Plasma Physics, Rijnhuizen, The Netherlands), A. Stolow, A. E. Boguslavskiy (National Research Council

of Canada, Ottawa, Canada and University of Ottawa), F. Martín (Universidad Autónoma de Madrid, Madrid, Spain), H. Stapelfeldt (Aarhus Univ., Aarhus, Denmark), J. Küpper, A. Rubio (Center for Free Electron Laser, Univ. Hamburg), T. Fennel (Univ. Rostock), A. I. Kuleff (Univ. Heidelberg), M. Krikunova (TU Berlin), V. R. Bhardwaj (Univ. of Ottawa, Canada), R. Cireasa (Institut des Sciences Moléculaires d'Orsay, France), F. Legare (ALLS Montreal, Canada), H. Köppel (Univ. Heidelberg), V. S. Makhija, (University of Mary Washington, USA), J. P. Wolf (Univ. Geneva, Switzerland), M. Kleber (TU München), R. Forbes (Stanford, USA), M. Spanner (National Research Council, Ottawa, Canada) In-house collaborations with projects 1.1, 2.1, and 4.1.

### 3. Results in 2020

**T1: Recollision physics and dynamic imaging in intense laser fields**

Reaction Microscope studies of laser-driven electron recollision at mid-infrared wavelengths

In strong-field spectroscopies the kinetic energy of the returning electron scales with the ponderomotive potential  $U_p$ . The latter is proportional to the intensity and the square of the wavelength. Since the maximum intensity is limited by saturation, the viable way to increase the recollision energy is to increase the wavelength of the driving field. Femtosecond lasers in the mid-infrared (mid-IR) wavelength range are hence a very interesting source for driving High Harmonic Generation (HHG) and laser-driven electron recollision. However, for longer laser cycles the tunnel-ionized continuum wave packet has more time to disperse during propagation. Therefore the efficiency of HHG and the probability of electron rescattering decrease sharply for increasing wavelength. Hence mid-IR lasers with a high repetition rate are needed which nonetheless deliver a sufficient pulse energy. A particularly interesting source for such experiments at MBI is the recently developed 100 kHz mid-IR OPCPA laser system [MHP18].

In 2020, we have implemented a tight-focusing option in our Reaction Microscope. It allows to reach intensities  $\geq 6 \times 10^{13}$  Watt/cm<sup>2</sup> for the Idler pulses from a two-stage version of the OPCPA. The two-stage version is entirely pumped by a fiber laser and very stable. It delivers 14  $\mu$ J of pulse energy for the Idler at a central wavelength of 3.2  $\mu$ m and a pulse duration of 70 fs. Water-cooled Helmholtz coils allow the creation of a homogeneous magnetic field that is sufficient to guide photoelectrons with up to 500 eV transverse kinetic energy onto the time- and position-sensitive detector. In this

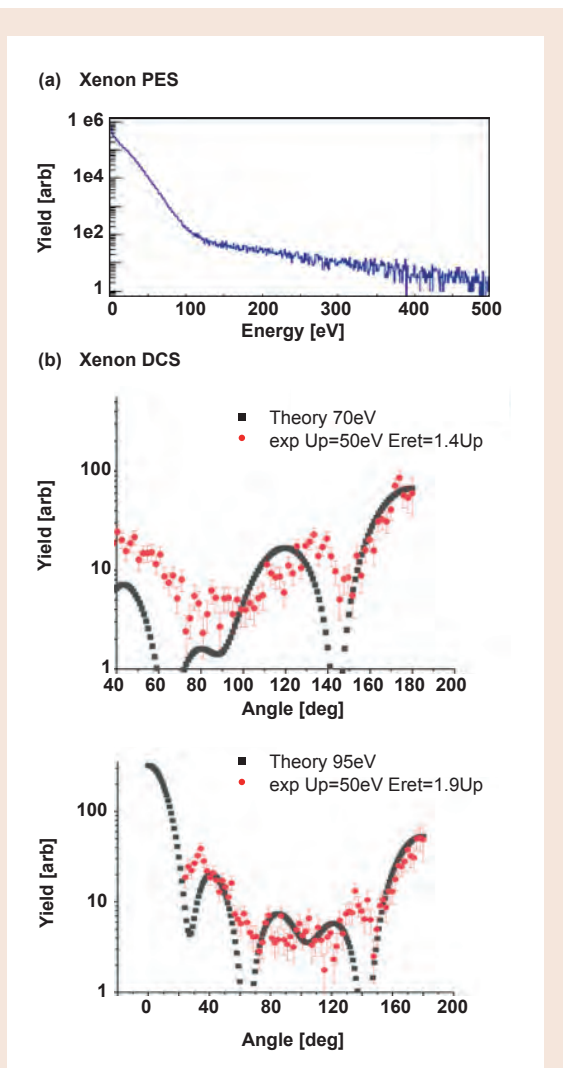


**Fig. 1:**  
 (a) Photoelectron spectrum from strong-field ionization of Xenon atoms at a wavelength of  $3.2 \mu\text{m}$  and an intensity of  $6 \times 10^{13} \text{ W/cm}^2$ , as measured in a Reaction Microscope. The recollision tail extends to 500 eV kinetic energy. (b) Differential Cross Section (DCS) for electron diffraction, extracted for two different return energies, and the result of a theoretical calculation of the elastic electron scattering cross section using the ELSEPA package [SJP05].

way we can perform experiments with linear polarization parallel to the plane of the detector, thus largely avoiding the detrimental effect of nodal planes in the electron trajectories.

A prototypical photoelectron spectrum (PES) obtained with the Idrler pulses is shown in Fig. 1(a), for Xenon atoms. The transition point between the direct electrons, strongly exponentially decreasing in yield with increasing kinetic energy, and the recollision tail at higher energies is located at around 110 eV. The assumption that this point is located at  $2 U_p$  leads to an intensity of  $6 \times 10^{13} \text{ W/cm}^2$ . The value is consistent with other, independent methods of intensity calibration. Note the low yield in the recollision tail in the figure, which originates from the dispersion of the continuum wave packet.

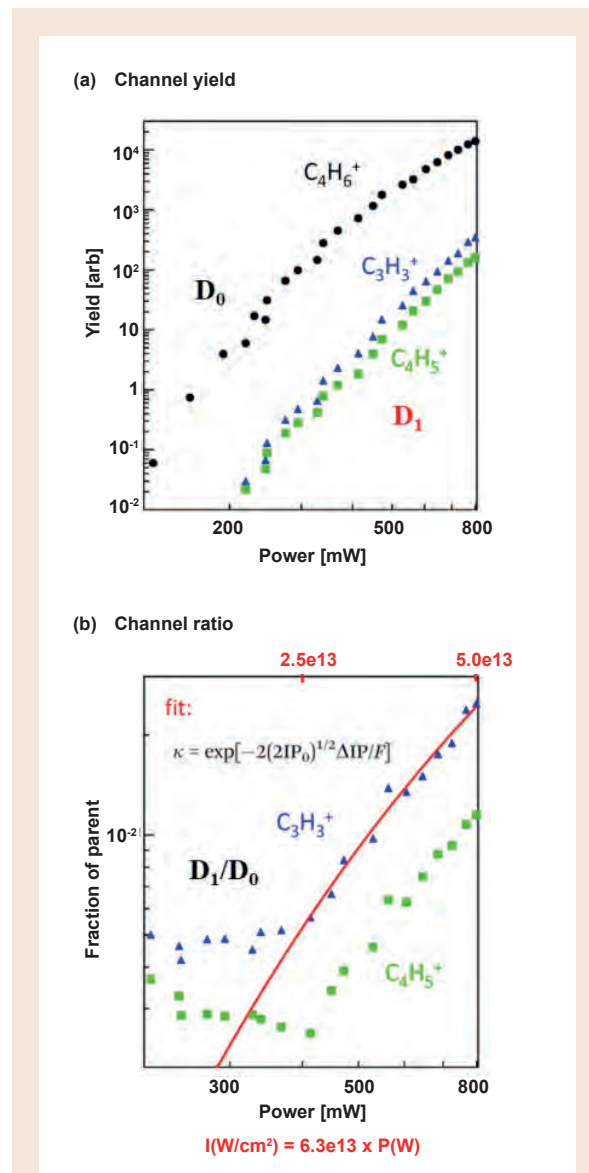


**Fig. 2:**  
 (a) Intensity-dependent yield of parent and fragment ions from strong-field ionization of 1,3-butadiene molecules, tagging the  $D_0$  and  $D_1$  ionization channel, respectively. (b) Ratio of  $D_0$  and  $D_1$  ionization, which is well described by a fit based on a Keldysh ionization model.

The Differential Cross Section (DCS) for electron diffraction in Xenon was extracted from the measured momentum map for two different return energies (see Fig. 1(b)). It is compared to theoretical elastic cross sections obtained using the ELSEPA package [SJP05]. This software performs a relativistic (Dirac) partial wave analysis for an effective local central-interaction potential. A good degree of qualitative agreement is evident, with the origin of the remaining deviations between measurement and model being under investigation.

The tests performed for Xenon pave the way to extend our recent studies of complex molecules to mid-IR wavelengths. In Fig. 2(a) we show the yield of parent ( $\text{C}_4\text{H}_6^+$ ) and fragment ( $\text{C}_3\text{H}_3^+/\text{C}_4\text{H}_5^+$ ) ions from strong-field ionization of 1,3-butadiene, as a function of the

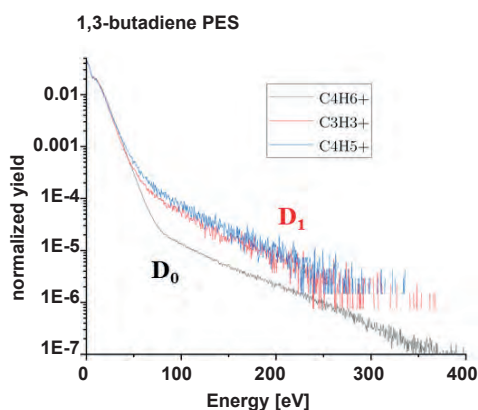


**Fig. 3:** Photoelectron spectra for strong-field ionization at  $3.2 \mu\text{m}$  via the  $D_0$  and  $D_1$  channel for unaligned 1,3-butadiene molecules. The recollision probability is significantly higher for the excited-state channel, which can be explained with the shape of the continuum wave packet.

laser power in front of the Reaction Microscope. The series of measurements was performed with different gas mixtures of 1,3-butadiene and helium and normalized accordingly. Parent and fragment ions tag  $D_0$  and  $D_1$  strong-field ionization, respectively. The ratio is shown in Fig. 2(b) and fitted with a Keldysh model which assumes a constant difference in the ionization potentials for the two channels (i.e. neglects potential Stark shifts). The fit serves on the one hand side as a consistency check of the tagging of the two different ionization channels, and delivers on the other hand an independent intensity calibration that is consistent with the  $2 U_p$  point in the PES (see Fig. 1 and 3).

In Fig. 3, the channel-resolved PES is shown for 1,3-butadiene molecules, at an intensity of  $4 \times 10^{13} \text{ W/cm}^2$ . In line with our earlier findings at  $1.3 \mu\text{m}$  and  $1.55 \mu\text{m}$  we find a much larger high-angle scattering probability for the  $D_1$  channel as compared to  $D_0$ . This effect originates from the different shape of the  $D_0$  and  $D_1$  continuum wave packets, which can be qualitatively explained by the structure of the Dyson orbitals [SBS18].

Laser-driven electron recollision in the mid-IR will allow us to extract the channel-resolved DCS in a regime where the deBroglie wavelength of the rescattered electron is shorter than the inter-atomic distances in the molecule.

#### Probing the dissociation dynamics of OCS by strong field ionization

The photoexcitation dynamics of carbonyl sulfide (OCS) in its first absorption band has been intensively investigated. For linear ground-state OCS, dipole transitions to the excited  $1^1\Sigma^+$  and  $1^1\Delta$  states are forbidden by symmetry. However, upon bending due to Renner-Teller interactions, degeneracies are lifted and the transitions become weakly allowed, with the transition strengths increasing with increasing bending angle. OCS dissociates predominantly to form rotationally excited CO ( $X^1\Sigma^+$ ) fragment in its electronic and vibrational ground state and an electronically excited sulfur atom ( $S(^1D_2)$ ). A second, weaker, dissociation channel is responsible for the formation of ground state CO ( $X^1\Sigma^+$ ) and  $S(^3P_J)$  products. The major dissociation channel is well understood and mainly attributed to prompt dissociation following the excitation of the  $2^1A'$  and  $1^1A''$  states. However, the mechanism responsible for the formation of  $S(^3P_J)$  remains to be elucidated.

So far, the experimental investigations of the photoexcitation of OCS were limited to frequency-resolved spec-

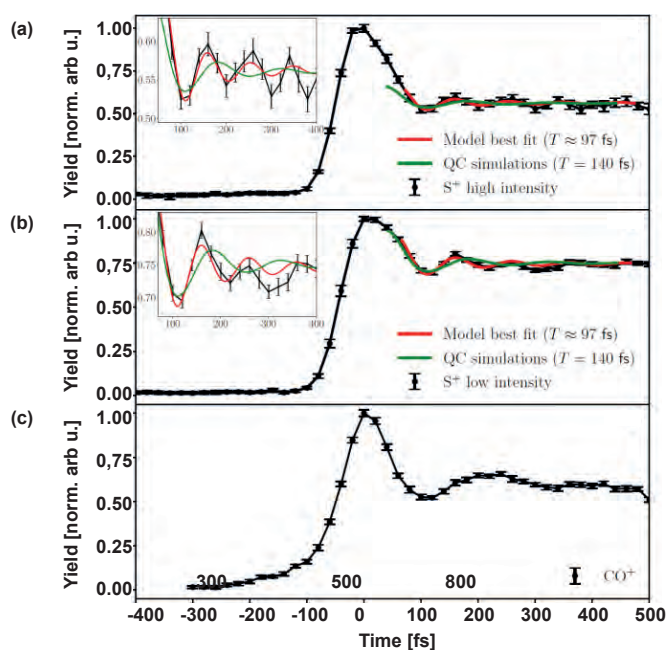


**Fig. 4:** Time-dependent  $S^+$  and  $CO^+$  yields. (a, b)  $S^+$  ions with a kinetic energy of  $0.22 \text{ eV}$  for UV and NIR pulse energies of (a)  $10 \mu\text{J}$  and  $1.3 \text{ mJ}$  and (b)  $4.5 \mu\text{J}$  and  $300 \mu\text{J}$ , respectively. The (black) experimental  $S^+$  yields are compared to (red and green) simulations considering a modified ADK ionization rate for the sulfur atom due to the rotational motion of the CO fragment calculated following prompt dissociation from excitation of the  $2^1A'$  and  $1^1A''$  states. The insets show a magnified view on the oscillations for better visibility. (c)  $CO^+$ -ions with a kinetic energy of  $0.38 \text{ eV}$  for UV and NIR pulse energies of  $10 \mu\text{J}$  and  $1.3 \text{ mJ}$ , respectively.

troscopy techniques, using nanosecond laser pulses such as by resonant enhanced multiphoton ionization spectroscopy (REMPI). While such experimental studies have provided a wealth of information of the photodissociation products and their final state distributions, no time-resolved studies have been reported to probe the transient electronic and nuclear structure of the molecule along the various dissociation pathways. In collaboration with the group of Jochen Küpper (CFEL), we recently investigated the dissociation dynamics of the OCS molecule following UV excitation with a 237 nm femtosecond laser pulse [KYP20]. A second, time-delayed, 800 nm femtosecond laser pulse was used to ionize the UV-excited molecules and the velocity distribution of the  $S^+$  and  $CO^+$  fragment ions were recorded (see Fig. 4) as a function of the delay between the UV and 800 nm laser pulses. For both fragments, a strong enhancement of the fragment ions yield was observed during and after the overlap of the UV and 800 nm laser pulses, which we attributed to the UV-induced dissociation of the molecule prior to the ionizing 800 nm laser pulse. In addition, our experimental study has revealed weak but pronounced oscillations of the  $S^+$  ionization yield at positive time delays (see inset in Fig. 4a,b). In order to understand the physical mechanism responsible for the observed oscillations, quantum chemistry simulations taking into account the prompt dissociation following excitation of the  $2^1A'$  and  $1^1A''$  states to form  $S(^1D_2)$  products, which correspond to the main dissociation channel, were coupled to a simple model for calculating strong-field-ionization rates (for details, see [KYP20]). This model was unable to reproduce the fast oscillations of the  $S^+$  ions yield observed experimentally. Our study provides strong indications that vibrational wavepackets in the  $2^1A''$  and  $2^3A''$  states are also formed by UV excitation, which then predissociate to form  $S(^3P_J)$ . This first time-resolved investigation of the dissociation dynamics of OCS clearly demonstrates the need for further advanced experimental and theoretical studies to elucidate the underlying physical processes responsible for the fast oscillations observed experimentally.

## T2: Strong-field processes in few-body systems

### Recollision physics and dynamic imaging in intense laser fields

While the ionization of atoms and molecules by an intense laser field has been intensively investigated both experimentally and theoretically, the physical mechanisms responsible for strong field dissociation of molecules remain to be elucidated. Strong field dissociation represents a dynamically much more complex process, often involving the interplay between electronic and nuclear degrees of freedom. Recent studies performed in  $H_2^+$  have shown that the initial vibrational and rotational state distribution of the molecular ion can influence the strong field dissociation process. The interpretation of these experiments was however complicated by the number of states initially populated, as the molecular  $H_2^+$  ions were prepared by a discharge source. In order to have a better understanding of the strong field dissociation dynamics of  $H_2^+$ , we propose to perform experiments in a state-selected  $H_2^+$  molecular ensemble

prepared by the well-known pulsed field ionization (PFI) technique.

As a first step towards these studies, we have recently developed a new experimental setup combining a tunable XUV source, a time-delayed 800 nm laser pulse and a velocity map imaging spectrometer to perform time-resolved photoion and photoelectron spectroscopy in  $H_2$  molecules. The tunable XUV pulse allows to prepare the molecule into highly excited Rydberg states, which is the first step towards the preparation of state-selected molecular ions using the pulsed field ionization technique. In our experiment, the XUV wavelength was set just above the first ionization threshold of the molecule. Following single XUV photon absorption, a wavepacket composed of highly excited Rydberg states ( $np^1\Sigma_u$  &  $1^1\Pi_u$ ,  $n>3$ ) of the hydrogen molecule was prepared. The resulting wavepacket dynamics were mapped into the time-dependent photoelectron spectrum, which was recorded following single photon ionization of the excited molecules by the time-delayed 800 nm laser pulse. Fig. 5 displays the time-dependent photoelectron spectrum recorded for a selected XUV wavelength of 15.5 eV. The photoelectron spectrum is composed of peaks that can be assigned to the ionization by the 800 nm laser pulse of the excited molecules into different vibrational states ( $v^*=0\dots6$ ) of the ground electronic state of the molecular ion. For a final vibrational state, the oscillations of the photoelectron yield with the time delay can be assigned to the beating between the different highly excited Rydberg states that are populated by the XUV pulse. In order to understand the observed oscillations of the photoelectron spectrum, simulations of the vibronic wavepacket dynamics induced by the XUV pulse based on solving the time-dependent Schrödinger equation are underway. This experiment represents the first step towards the investigation of strong field induced dissociation of state-selected molecular ions  $H_2^+(v,J)$ .

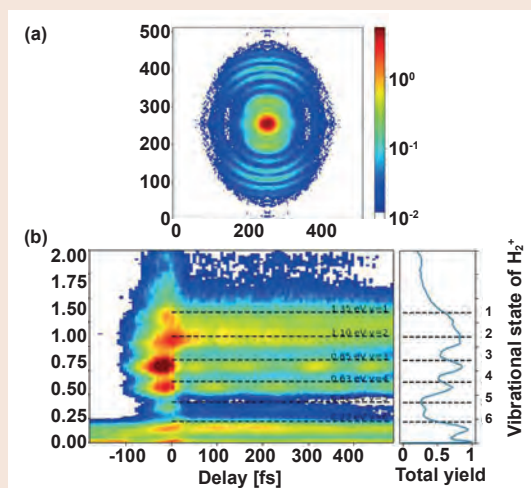


**Fig. 5:** Electron momentum distribution following single-photon ionization of highly excited  $H_2$  molecules by an 800 nm laser pulse. (b) Time-dependent photoelectron kinetic energy spectrum recorded in  $H_2$  as a function of the XUV and 800 nm time delay. For this experiment, the XUV wavelength was set to 15.5 eV.

### T3: Strong field excitation and HHG in tailored fields

Circular or highly elliptical pulses in the extreme ultraviolet spectral range offer numerous applications in chiral-sensitive light-matter interactions in both gas and condensed phase, ranging from chiral recognition to time-resolved magnetization dynamics and spin currents. Until recently, such radiation has only been available at large-scale facilities (e.g. synchrotrons, XFELs), with ultrafast time resolution requiring free electron lasers. On the other hand, laboratory-based sources of pulses of attosecond duration (1 as =  $10^{-18}$  s) are becoming broadly available. However, the available attosecond pulses are typically linearly polarized and thus unable to probe and control spin and chiral dynamics. The latter requires the generation of attosecond pulses with controllable degree of polarization. One practical solution to this problem is to use two-color driving fields in the so-called bicircular configuration (TCBC schema), originally proposed in [EEN15]. The bi-circular configuration consists of combining a circularly polarized fundamental field “w” with its counterrotating harmonic “rw”. The combined laser field has a folded 3D rosette shape with some maxima per fundamental period depending on “r”. The examples of Lissajous Figures of the resulting field for  $r=2$  and  $r=3$  are shown in Fig. 6.

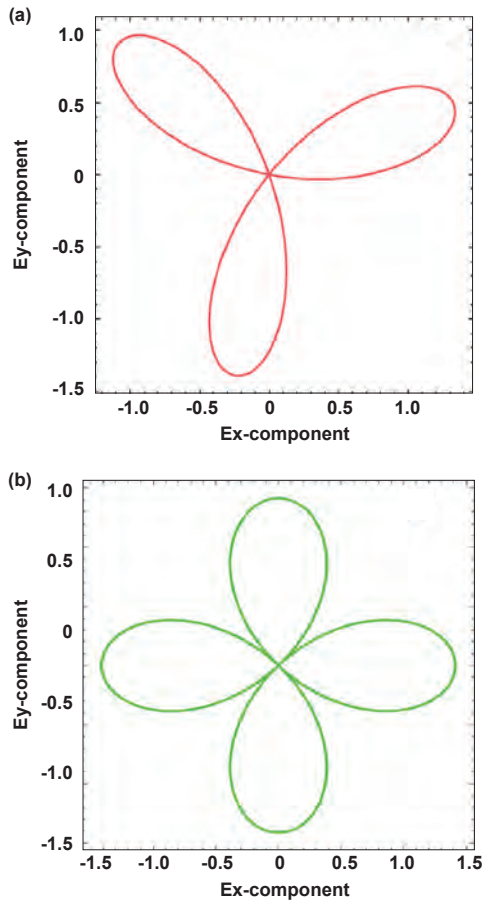


**Fig. 6:** Lissajous figures of  $\omega+2\omega$  (a) and  $\omega+3\omega$  (b) bi-circular field with equal intensity for both field components.

The two-colour bi-circular (TCBC) approach offers full polarization control of generated harmonics without decreasing the up-conversion efficiency. The exact spectral position and separation of the harmonic orders depend on spectral content of the driving radiation [Mil18], where the frequency ratio of driving fields is decisive for specific selection rules. Using the dynamical symmetry of the bi-circular field, one can derive the following selection rule for the  $n$ th harmonic and its ellipticity  $\varepsilon_n$  [Mil18]

$$\varepsilon_n = +/-1 \text{ for } n = q(r + 1) +/- 1 \text{ (q-integer)} \quad (1)$$

In the  $w+2w$  ( $w+3w$ ) variant the field symmetric with respect to a rotation of 120 (90) (see Fig.6.). Each of the leaves in the rosette generates an attosecond burst, totalling three/four burst per laser cycle. In the frequency domain, the  $w+2w$  field produces circularly-polarized harmonic peaks at  $(3N+1)$  and  $(3N+2)$  values, with the helicity of the fundamental field and the second harmonic, respectively, while  $3N$  harmonic lines are symmetry forbidden. In the  $w+3w$  variant only odd harmonics are allowed with the helicity having opposite signs for any neighbour harmonics. So far most of the efforts was directed to explore the  $w+2w$  variant of TCBC approach with, promising a generation of highly elliptical XUV radiation if the form of train of pulses [Zhl17] as well as isolated attosecond pulses [ZhB20] (to be published). In this project we investigate  $w+3w$  variant of the TCBC approach aiming to explore its potential for generation and characterisation of circularly polarized attosecond pulses.

Experiments have been performed with a Ti:sapphire-based laser system with a single stage regenerative amplifier producing 35 fs pulses with up to 6 mJ energy and central wavelength of 795 nm at 1 kHz repetition rate. The CEP of the pulses was not locked. The 80 % of the system output was directed towards an OPA (TOPAS-Prime). Generated radiation from the signal path was centred at 1200 nm forming a fundamental  $w$ -beam with 35 fs pulse duration and average power as much as 0,8 W. The 20% radiation left of the system output was compressed in a separate grating compressor and doubled in a 0.1 mm thick BBO crystal. Both beams passed through corresponding achromatic broadband  $\lambda/2$  and  $\lambda/4$  wave plates where they become circularly polarized, with an ellipticity as high as  $\varepsilon=0,9$  for 400 nm and  $\varepsilon=0,87$  for IR beams. The driving beams are combined together in collinear geometry and focused with a Ag-mirror at  $f/100$  into a 1-mm-long gas cell containing argon. The maximal intensities in the so-called “top-hat” shape were estimated to be  $I(1200)=3,5 \times 10^{14}$  W/cm<sup>2</sup> and  $I(400)= 2 \times 10^{14}$  W/cm<sup>2</sup>. The focal point was placed on approximately 2 mm before the target. The cell was initially sealed with a metal foil which is burned through by the laser beam at the start of the experiment while keeping the gas pressure insight the cell constant at 40 mbar. After passing the gas cell the XUV radiation was directed towards an XUV spectrometer, placed insight the vacuum chamber differentially separated from the interaction chamber. The XUV-spectrometer is based on a 1 m toroidal mirror and a 600 grooves/mm plane grating. The generated radiation was detected by a double-microchannel plate (MCP) with a phosphor screen and

recorded by fast CMOS camera. The harmonic of orders up to 130 were observed if only IR linear driver was applied. Fig. 7 demonstrates the shape of XUV-spectra for bi-circular  $w+3w$  driving fields. With these spectra alone, the difference to the usual HHG generated in a one colour linear driving field is not really observable. The even harmonics are suppressed, but the difference is that the harmonics must be elliptically polarized with different helicity. The  $4n+1$  and  $4n-1$  order should have helicity corresponding to "blue" and "IR" beams respectively.

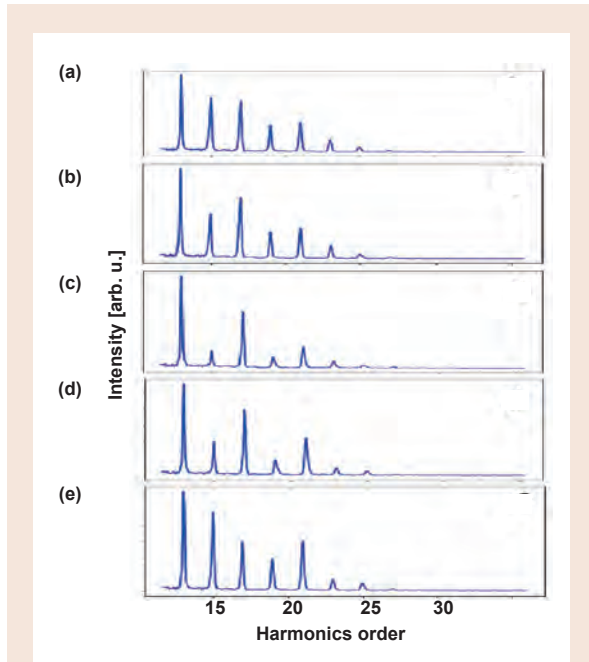


**Fig. 7:** XUV spectra for  $w+3w$  combined driving field as a function of ellipticity of the driving  $3w$  field with ellipticity  $\epsilon$  equal to 0.67 (a), 0.83 (b), 0.90 (c), 0.63 (d), 0.5 (e) and orientation angle  $\phi$  30 (a), 60 (b), 90 (c), 120 (d) and 150 (e) degree.

The XUV spectra were measured as a function on ellipticity of the driving "blue" field. The observed spectra are strongly ellipticity dependent, with the steadily decreasing difference in the intensities between the right- and the left-rotating harmonics by decreasing ellipticity. Importantly, the spectrum observed with best possible ellipticity demonstrate the highest contrast between left and right polarised harmonics. The larger the difference in the emission of  $4n+1$  right- versus  $4n-1$  left-circularly polarized high harmonics, the larger is final the ellipticity of the generated APT.

In conclusion, we have demonstrated that tuning the ellipticity of the driving field in the  $w+3w$  approach is a simple and practical possibility to control the ellipticity of attosecond pulses in a smooth and predictable way. The contribution of  $4n+1$  and  $4n-1$  can be changed in a broad range, leading to tunable chirality of APTs. The polarimetry of the original ellipticity of harmonics is in progress.

## Own Publications 2020

(for full titles and list of authors see appendix 1)

BBK20: F. Brausse, et al.; Phys. Rev. Lett. 125 (2020) 123001/1-6

BEP20: A.W. Bray, et al.; Phys. Rev. Lett. 124 (2020) 233202/1-6

ERM20: U. Eichmann, et al.; Science 369 (2020) 1630-1633

SBS20: F. Schell, et al.; Springer proceedings in Physics Series 220 (2020) Springer, Singapore

TJB20: V. Tamulienė, et al.; Sci. Rep. 10 (2020) 17437/1-12

TSS20: C. Tailliez, et al.; New J. Phys. 22 (2020) 103038/1-18

KSD20: M. Kübel, et al.; Nat. Comm. 11 (2020) 2596/1-8

## in press

KYP20: E. T. Karamatskos, et al.; Faraday Disc.

## Other Publications

EEN15: H. Eichmann, et al. Phys. Rev. A 51 (1995) R3414

Mil18: D. B. Milosevic; Phys. Rev. A 98 (2018) 033405/1-7

MHP18: M. Mero, et al.; Opt. Lett. 43 (2018) 5246-5249

SBS18: F. Schell, et al.; Sci. Adv. 4 (2018) eaap8148/1-7

SJP05: F. Salvat, et al.; Comput. Phys. Commun. 165 (2005) 157

ZhB20: private communication N. Zhavoronkov and U. Bengs

ZhI17: N. Zhavoronkov and M. Ivanov, Opt. Lett. 42 (2017) 4720

## Invited Talks at International Conferences

(for full titles see appendix 2)

U. Eichmann; 11th Ringberg Workshop on Science with FELs (Schloss Ringberg, 2020-02)

## 3.1: Dynamics of Condensed Phase Molecular Systems

E. T. J. Nibbering, O. Kornilov (project coordinators)

and N. Acharyya, M.-A. Codescu, S. Eckert, B. P. Fingerhut, C. Granados, P. Han, E. Ikonnikov, C. Kleine, A. Kundu, J. Lebendig-Kuhla, J. Ludwig, A. Lübcke, M. Oßwald, R. Ovcharenko, E. Palacino-González, H.-H. Ritze, J. Schauss, M.-O. Winghart, J. Zhang

### 1. Overview

This project aims at a real-time observation of ultrafast molecular processes in the condensed phase, addressing the dynamics of elementary excitations, photoinduced chemical reactions and ultrafast changes of the electronic and/or chemical structure of molecular systems. The project makes use of a broad range of experimental techniques including all-optical pump-probe spectroscopy in a range from the ultraviolet to mid-infrared, infrared photon-echo and multidimensional vibrational spectroscopies, and photoelectron spectroscopy using ultrashort VUV, XUV, and soft-X-ray pulses.

### 2. Topics and collaborations

Research in this project has been structured into four major topical directions:

#### T1: Dynamics and interactions in hydrated biomimetic and biomolecular systems

Collaboration partners: J. T. Hynes (University of Colorado, Boulder, USA), D. Laage (École Normale Supérieure, Paris, France), E. Pines (Ben Gurion University of the Negev, Beer-Sheva, Israel)..

#### T2: Water-mediated proton transport dynamics between acids and bases

Collaboration partners: M. Odelius (Stockholm University, Sweden), Ph. Wernet (Uppsala University, Sweden), N. Huse (University of Hamburg), D. Sebastiani (Martin-Luther-University Halle-Wittenberg, Germany).

#### T3: Electron transport dynamics in donor-acceptor molecular systems

Collaboration partner: V. S. Batista (Yale University, New Haven, CT, USA).

#### T4: Electronic excited state dynamics in molecular model systems

Collaboration partners: O. Rader (Helmholz Zentrum Berlin), D. Arbi (University of Buenos Ayres), L. Banares (Complensa University, Madrid). R. Mitric (Universität Würzburg), S. Haacke (University of Strasbourg), M. Olivucci (University of Sienna), S. Gozem (State University of Georgia).

Internal collaborations with Projects 1.1, 2.1 and 3.3 have been established.

### 3. Results in 2020

#### T1: Dynamics and interactions in hydrated biomimetic and biomolecular systems

(DFG FI 2034/1-1; ERC-2018-ADG-BIOVIB, ERC-2018-STG-NONABVD)

Biomimetic and biomolecular systems and their interactions with water and ions are studied to unravel the couplings between the different molecular entities and the fluctuating water shells in the electronic ground state. Hydration dynamics of RNA and DNA oligomers [KSF20, FKS20a] in water solution, native salmon DNA in thin films and solution, and dimethylphosphate ions in water as DNA model systems [FSK20, KSF20b] are the main topics in recent years. Most recently, we successfully extended the investigations to the complex folded RNA structures of transfer RNA (tRNA) [SKF].

The water shell around RNA has a strong impact on its structural and functional properties. In aqueous environment the negatively charged phosphate groups are distinct docking points for water molecules of the hydration shell. Their presence reduces the repulsive

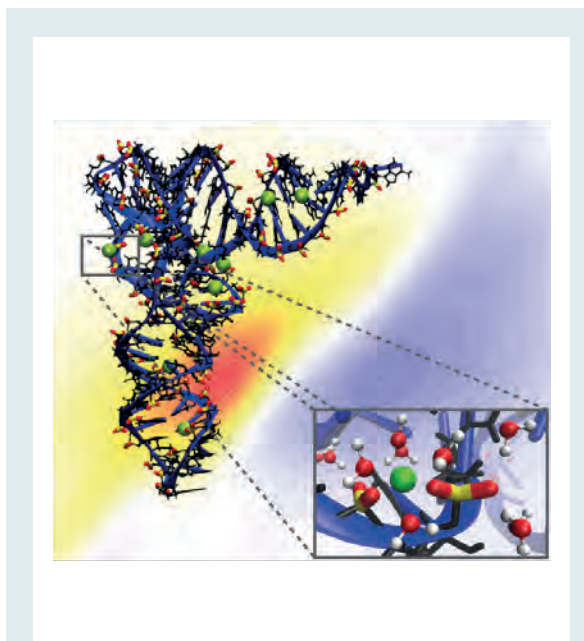


**Fig. 1:**

*Tertiary molecular structure of transfer RNA (tRNA). The so-called folded cloverleaf structure is shown together with magnesium ions ( $Mg^{2+}$ , green spheres). The inset displays a particular site at which a  $Mg^{2+}$  ion forms a contact pair with a phosphate group, separated from the neighboring phosphate group by a single water layer.*

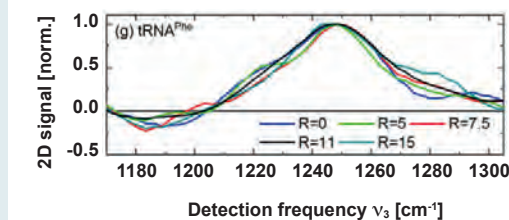
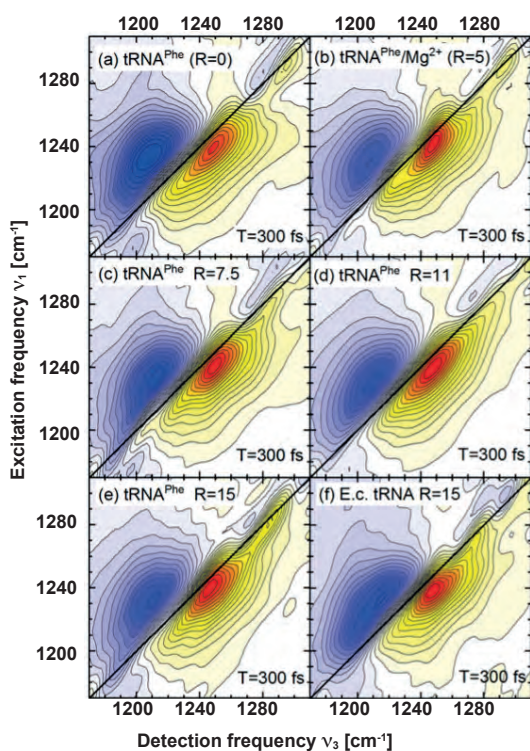


**Fig. 2:** 2D-IR spectra of tRNA in water in the range of the asymmetric phosphate stretching ( $\nu_{AS}(\text{PO}_2^-)$ ) band. (a–e) 2D-IR spectra of dialyzed tRNA<sup>Phe</sup> for increasing  $\text{Mg}^{2+}$  concentration  $c(\text{Mg}^{2+})$ . The quantity  $R = c(\text{Mg}^{2+})/c(\text{tRNA})$  defines the ratio of  $\text{Mg}^{2+}$  to tRNA concentration. Absorptive 2D signals are plotted as a function of the excitation frequency  $\nu_1$  and the detection frequency  $\nu_3$ , yellow-red contours represent signals due to the fundamental ( $\nu = 0$  to 1) transition, and blue contours, the excited state  $\nu = 1$  to 2 absorption. (f) 2D-IR spectrum of E.c. tRNA for  $R = 15$ . (g) Cuts of the 2D-IR spectra of tRNA<sup>Phe</sup> along a diagonal line through  $(\nu_1, \nu_3) = (1240, 1250) \text{ cm}^{-1}$ .

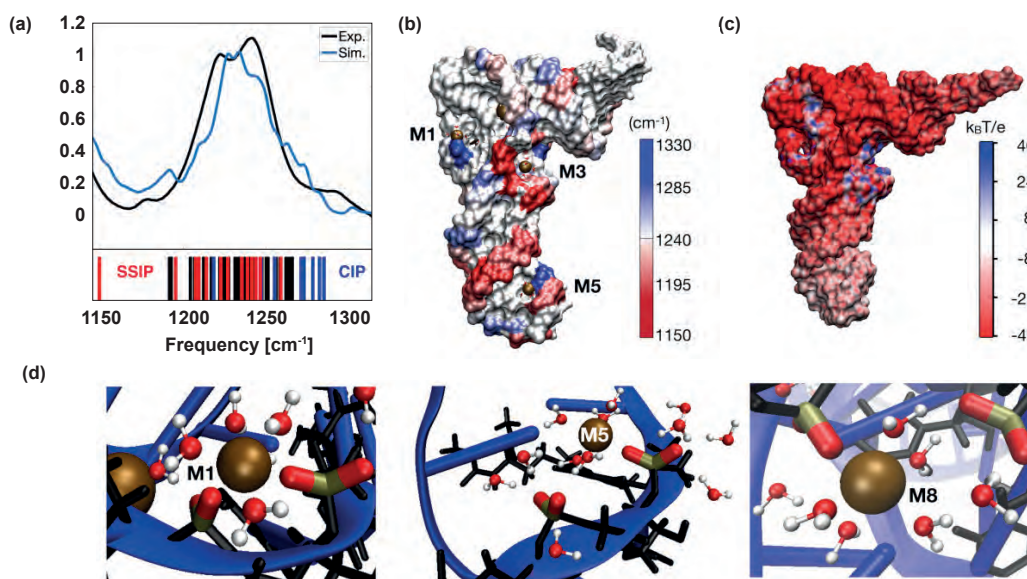


**Fig. 3:** Results of *ab-initio* QM/MM and MD simulations for tRNA<sup>Phe</sup> from yeast. (a) Simulated and experimental linear infrared absorption spectra in the frequency range of the asymmetric phosphate stretching vibration  $\nu_{AS}(\text{PO}_2^-)$ . Simulations are compared to the experimental infrared spectrum of undialyzed tRNA<sup>Phe</sup> in water. The simulated vibrational DOS of the  $\nu_{AS}(\text{PO}_2^-)$  band color-codes the frequency positions of contact ion pairs of the  $(\text{PO}_2^-)$  group with  $\text{Mg}^{2+}$  ions (CIP, blue) and of SSIPs (red), frequency positions of the remaining  $(\text{PO}_2^-)$  groups are indicated in black. (b) Simulated spatial distribution of  $\nu_{AS}(\text{PO}_2^-)$  vibrational frequencies. The surface color of the sugar-phosphate backbone encodes the local  $\nu_{AS}(\text{PO}_2^-)$  frequency. (c) Electrostatic surface potential of tRNA<sup>Phe</sup> obtained from MD simulations. (d) Prototype solvation geometries around  $(\text{PO}_2^-)$  groups. Solvation structure M1 (left) shows bidentate inner-sphere coordination of  $\text{Mg}^{2+}$  by two adjacent  $(\text{PO}_2^-)$  groups, M5 (middle) shows contact ion pair formation of the  $(\text{PO}_2^-)$  group and  $\text{Mg}^{2+}$  in the anticodon loop with first-solvation shell waters shared by  $\text{Mg}^{2+}$  and the adjacent  $(\text{PO}_2^-)$  and M8 shows a CIP within the D-loop and SSIP mediated interstrand contact to the TΨC loop.

electrostatic interaction between phosphate groups and stabilizes the secondary RNA structure. In general, changes in secondary structure occur during RNA folding, RNA replication or RNA melting at elevated temperature. They are inevitably connected with changes of the hydration pattern around the sugar-phosphate backbone. We have discerned the different hydration geometries of backbone phosphate groups of an RNA double helix at the molecular level [KSF20, FKS20]. Employing two-dimensional infrared (2D-IR) spectroscopy we have demonstrated that RNA melting at elevated temperature is connected with a transition from predominantly ordered water structures, with a chain-like arrangement of water molecules linking neighboring phosphate groups, to local hydration shells around phosphate units. Comparative experiments with a DNA double helix demonstrate that the local phosphate group hydration motifs preferentially populated at high temperature are very similar to the hydration shells around the  $(\text{PO}_2)^-$  groups in DNA.

Theoretical simulations show that the thermal transition from ordered water structures to DNA-like local phosphate hydration shells is accompanied by an increase in the average number of phosphate water hydrogen bonds and, thus, an increase in the hydration free energy. Such energy changes are shown to be on the same order of magnitude as those due to self-association of nucleobases. They are a non-negligible part of the free energy balance upon RNA self-association and melting.

An extension to biomolecular structures of higher complexity revealed the crucial role of contact ion pairs with phosphate groups in stabilizing the macromolecular structure of tRNA (Fig. 1) [SKF]. In the folded cloverleaf structure of tRNA, the repulsive electric force between the negatively charged phosphate groups needs to be compensated by positively charged ions and by water molecules of the environment. The relevant molecular level arrangements have, so far, evaded direct experimental quantification. Combining 2D-IR spectroscopic experiments (Fig. 2) and detailed theoretical calculations of molecular interactions and dynamics (Fig. 3) we have identified contact pairs of positively charged magnesium ions and negatively charged phosphate groups as a decisive structural element for minimizing the electrostatic energy of tRNA and, thus, stabilizing its tertiary structure. Experiments at different concentrations of magnesium ions show that a single tRNA molecule forms up to six contact ion pairs, preferentially at locations where the distance between neighboring phosphate groups is small and the corresponding negative charge density high. The contact ion pairs make the main contribution to lowering the electrostatic energy and, consequently, stabilizing the tertiary tRNA structure. In contrast, mobile ions in the first five to six water layers around tRNA are less relevant for stabilizing the tRNA structure. The results give detailed quantitative insight in the electric properties of a key biomolecule. They underscore the high relevance of molecular probes for elucidating the relevant molecular interactions and the need for theoretical descriptions at the molecular level.

## **T2: Water-mediated proton transport dynamics between acids and bases**

(DFG NI 492/13-1; ERC-2017-ADG-XRayProton)

Aqueous acid-base neutralization predominantly proceeds in a sequential way via water bridging acid and base molecules. This line of research builds on previous ultrafast studies of aqueous proton transfer using photoacids. Experimental techniques include transient UV/IR and UV/soft-X-ray absorption spectroscopies. Mid-IR absorption spectroscopy probes vibrational marker modes of particular species generated during proton transport between acid and base, as well as locally monitors hydrogen bond interactions of these species. X-ray absorption spectroscopy (XAS) probes transitions from inner-shell levels to unoccupied molecular orbitals, making it a tool to monitor electronic structure with chemical element specificity. Ultrafast UV/IR spectroscopy enables the elucidation of proton transfer pathways and the associated time scales for individual proton transfer steps [CKN20, CWB]. Much effort has been devoted in recent years to develop steady-state and time-resolved soft-x-ray spectroscopy of acids and bases in water-poor and water-rich solutions [EKL, EWK20]. Here novel liquid flatjet technology is utilized with soft-X-ray sources at synchrotrons [EKL, EWK20], free-electron lasers [EEM] as well as table-top laser-based high-order harmonic systems, to elucidate the electronic structural evolution of proton transfer pathways.

We have further explored the proton transport mechanism between the proton donating OH-group and the proton accepting quinoline unit of the bifunctional photoacid 7-hydroxyquinoline (7HQ). In previous years proton transfer dynamics of 7HQ in water/methanol mixtures. Current activities have focused on the role of bases added to the solution, with which a possible change in reaction pathways can be imposed onto 7HQ [CKN20, CWB]. First results on the 7HQ-formate reaction pair in methanol have shown that the outcome of the proton transfer dynamics can be quantitatively changed for high base concentrations (2.0 – 4.0 M). Whereas proton exchange from the proton accepting quinoline unit towards the proton donating OH-group of 7HQ occurs through a proton vacancy methoxide transfer hopping mechanism along a methanol solvent bridge, the added formate anion accelerates the first proton transfer to take place from the 7HQ OH-group. The experimental results suggest a proton transport mediating function by the formate anion when the formate is located inbetween the proton donating OH-group and the N site of the quinoline aromatic ring system of 7HQ.

We have developed an acetonitrile flatjet system fully operational under vacuum conditions, and have measured O K-edge spectra of hydrated proton complexes [EKL].

We have further developed our approach to explore acid-base interactions with soft-X-ray spectroscopy and have performed transient soft-X-ray spectroscopic measurements of photoacid molecules during a beamtime at HZB-BESSYII, demonstrating that this approach using flatjet technology is feasible [EWK20].

Unfortunately further exploration of photoacid photochemistry with transient soft-X-ray spectroscopy had been halted in 2020 with beamtimes being cancelled due to the COVID-19 pandemic.

### T3: Charge transport in biomimetic and biological systems

(SAW-2016-MBI-1)

In this topical area, elementary charge transport dynamics in solution are investigated from the viewpoint of their functional role in biochemical processes. The objective is to elucidate the underlying mechanisms for electron transfer, proton transfer as well as proton-

coupled electron transfer in donor-acceptor molecular systems. This line of research builds on previous ultrafast studies of photoinduced electron transfer processes in donor-acceptor complexes. Experimental techniques include, besides ultrafast UV/IR spectroscopy, ultrafast UV/soft-X-ray measurement methods using laboratory-based table-top laser systems and large-scale facilities (storage rings, free electron lasers).

For the table-top approach it is possible to record steady-state soft-x-ray absorption spectra in transmission mode at the C and N K-edges of molecular systems in aqueous solution. This set-up has been implemented with a new X-ray spectrometer, equipped with a reflective zone plate as diffractive element for the extreme high-order harmonic (HHG) pulses covering 200-450 eV and an X-ray CCD detector to detect the extreme HHG pulses with a frequency resolution sufficient to distinguish pre-edge and main-edge spectral features typical for mid-sized organic molecules in solution. Current activities involve further developments towards ultrafast soft-X-ray spectroscopic measurements of molecular systems in the gas-phase (in collaboration with Project 2.1) and ultimately in liquid solution.

In a collaboration with the Batista group (Yale University, New Haven, CT) we have explored the photodissociation of ICN in the  $1\Pi_1$  excited state (Fig. 4), with emphasis on the transient response in the soft-X-ray spectral region as described by the ab initio spectral lineshape averaged over the nuclear wavepacket probability density (Fig. 5). In particular the carbon K-edge spectral region reveals a rich transient response that provides direct insights into the dynamics of frontier orbitals during the I—CN bond cleavage process. The simulated UV-pump/soft-X-ray-probe spectra exhibit detailed dynamical information, including a time-domain signature for coherent vibration associated with the photogenerated CN fragment.

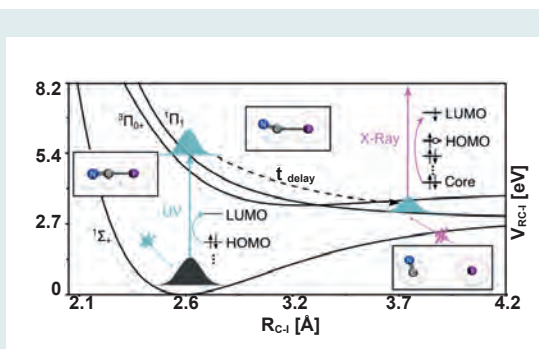


**Fig. 4:** Photoinduced dissociation of ICN: a UV pump pulse photoexcites the initial wavepacket upon the  $1\Pi_1 \leftarrow 1\Sigma^+$  transition, while an X-ray probe pulse monitors the transient vibronic dynamics through absorbance changes at the carbon K-edge. The figure illustrates the potential energy surface along the C—I bond, where the photodissociation dynamics involves the breaking of the C—I bond coupled to the rotational motion of the photogenerated CN fragment.

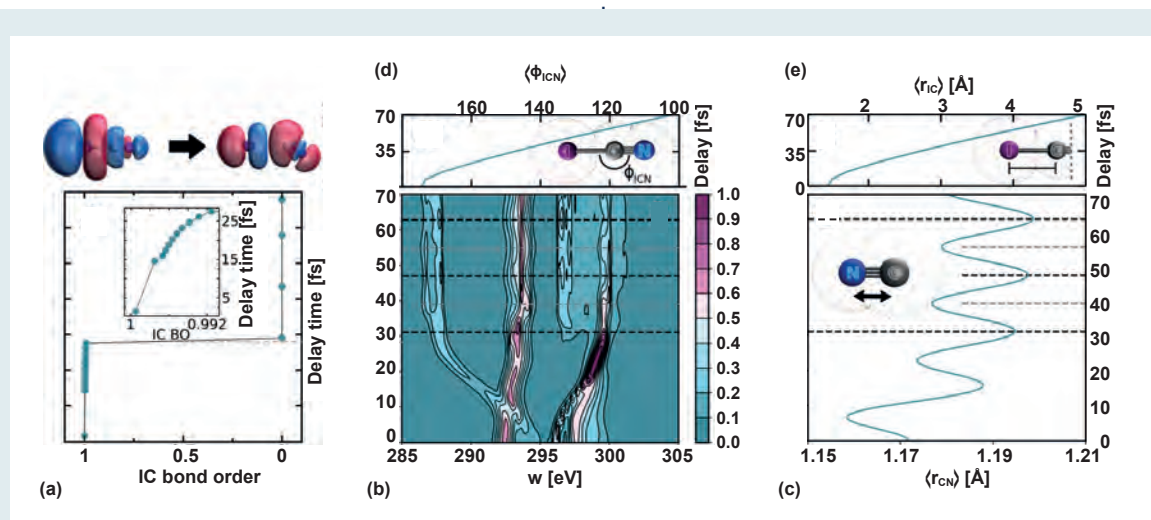


**Fig. 5:** (a) Time-dependent bond order of the dissociating I-C bond, computed as a function of time during the photodissociation dynamics in the  $1\Pi_1$  excited state as probed by the simulated UV/X-ray spectra. (b) Carbon K-edge transient X-ray spectrum of ICN following  $1\Pi_1 \leftarrow 1\Sigma^+$  photoexcitation by the UV pulse. (c) Time-dependent C-N bond-length during the ICN photodissociation dynamics in the  $1\Pi_1$  excited state. Dashed lines indicate the time of amplitude maxima (black) and minima (grey). (d,e) Time-dependent ICN angle and I-C bond-length during the ICN photodissociation dynamics.

**T4: Electronic excited state dynamics in molecular model systems**  
(DFG KO 4920/1-1)

Determination of the ultrafast electronic excited state dynamics of organic molecules in solution is the main objective of this topical area. Photophysical events such as internal conversion, and photochemical transformations, trans/cis isomerization, ring opening or closure are examples of elementary processes to be studied in detail. The experiments address dynamics in electronically excited states with time-resolved photoionization methods. For this, an XUV time delay compensating monochromator coupled to a high-order harmonic generation set-up provides pulsed, wavelength-selected XUV radiation. A NIR/vis pump pulse is used to excite organic solute molecules dissolved in microliquid jets, which are then ionized by the probe XUV pulses. The photoelectrons are detected using a magnetic bottle time-of-flight spectrometer.

One of the particular challenges for the photoelectron spectroscopy experiments is the ab initio quantum chemistry theory support, that is required for a full interpretation of photoelectron spectra. This task is particularly challenging for the experimental data generated within this topical area, since only a limited number of research groups in the world have the expertise and infrastructure required to calculate time-resolved photoelectron spectra for molecules of substantial size surrounded by a solvent. The collaboration with the Mitrić group (Würzburg University), established in 2019, has led to a first joint publication on ultrafast relaxation of aminoazobenzenes [THI].

Using ultrafast XUV photoelectron spectroscopy as a method of choice, further activities on trans/cis isomerization dynamics of chromophores in solution, including collaboration with the Haacke, Olivucci and Gozem-groups, on open-quantum systems in the gas-phase and in solution, and on optically active molecular systems have been started in 2020.

In addition to that a collaboration with the Institute for Zoo- and Wildlife (IZW) research and the Immunology institute of Free University of Berlin has continued in 2020 on the investigation of non-linear interaction of laser radiation with living organisms, such as cells or common worm parasites. Progress was strongly hampered by the COVID-19 pandemic due to reduced personal interactions between the different institutes.

**Own Publications 2020 ff**

(for full titles and list of authors see appendix 1)

AOF20: N. Acharyya, *et al.*; J. Chem. Phys. **153** (2020) 185101/1-12

ARF20: A. Acharyya, *et al.*; in *The 22nd International Conference on Ultrafast Phenomena 2020*, F. Kärtner, M. Khalil, R. Li, F. Légaré, and T. Tahara eds. (Washington, D.C., USA, 2020)

CKN20: M.-A. Codescu, *et al.*; in *The 22nd International Conference on Ultrafast Phenomena 2020*, F. Kärtner, M. Khalil, R. Li, F. Légaré, and T. Tahara eds. (Washington, D.C., USA, 2020)

EWK20: S. Eckert, *et al.*; in *The 22nd International Conference on Ultrafast Phenomena 2020*, F. Kärtner, M. Khalil, R. Li, F. Légaré, and T. Tahara eds. (Washington, D.C., USA, 2020)

FKS20: B. P. Fingerhut, *et al.*; in *The 22nd International Conference on Ultrafast Phenomena 2020*, F. Kärtner, M. Khalil, R. Li, F. Légaré, and T. Tahara eds. (Washington, D.C., USA, 2020)

FSK20: B. P. Fingerhut, *et al.*; Z. Phys. Chem. **234** (2020) 1453-1474

HKL20: J. Hummert, *et al.*; J. Phys. B **53** (2020) 154003/1-8

KSF20a: A. Kundu, *et al.*; J. Phys. Chem. B **124** (2020) 2132-2138

KSF20b: A. Kundu, *et al.*; in *The 22nd International Conference on Ultrafast Phenomena 2020*, F. Kärtner, M. Khalil, R. Li, F. Légaré, and T. Tahara eds. (Washington, D.C., USA, 2020)

MVS20: U. N. Morzan, *et al.*; Angew. Chem. Int. Edit. **59** (2020) 20044–20048

**in press**

CWB: M.-A. Codescu, *et al.*; J. Phys. Chem. A

EEM: R. Y. Engel, *et al.*; Struct. Dyn.

SKF: J. Schauss, *et al.*; J. Phys. Chem. B

THI: E. Titov, *et al.*; Faraday Disc.

**submitted**

EKL: M. Ekimova, *et al.*; Science

KSP: E. Kozari, *et al.*; ChemPhysChem

### **Invited Talks at International Conferences**

(for full titles see appendix 2)

T. Elsaesser; 55th Winter Seminar: Biophysical Chemistry, Molecular Biology and Cybernetics of Cell Functions (Klosters, Switzerland, 2020-01)

B. P. Fingerhut; Modelling Photoinduced Processes in Molecular Systems (MPPM) (Imperial College London, UK, 2020-02)

B. P. Fingerhut together with A. Kundu, J. Schauss, and T. Elsaesser; Ultrafast Phenomena XXII (Shanghai, China, 2020-11)

O. Kornilov; ATTOCHEM COST meeting (2020-08)

## 3.2: Solids and Nanostructures: Electrons, Spins, and Phonons

*C. von Korff Schmising, S. Sharma and M. Woerner (project coordinators) and V. Bender, M. Borchert, K. Busch, J. R. Cardoso de Andrade, P. Elliott, G. Folpini, A. Ghalgaoui, R. Grunwald, M. Hennecke, P. Jürgens, T. Kang, L. Koll, Q. Li, F. Loth, A. Mermil-Iod-Blondin, T. Noll, A. Perez-Leija, B. Pfau, L. Rammelt, D. Reiche, K. Reimann, M. Runge, P. Scheid, D. Schick, P. Singh, S. Shallcross, T. Sidiropoulos, R. Smith, C. Somma, F. Stein-bach, K. Taehee, J. W. Tomm, A. Treffer, K. Tschernig, F. Willems, K. Yao.*

### 1. Overview

This project addresses ultrafast and nonlinear phenomena in solids and nanostructures. In correlated condensed-matter systems, interaction of electrons, phonons and spins lead to a broad range of novel and unusual phenomena, which are interesting from the point of view of both fundamental research and practical applications. To gain new insight into fundamental phenomena in this thriving field of research, experiments are performed with ultrafast time resolution and in a very wide spectral range extending from terahertz to X-ray frequencies. The work includes studies in the regime of nonperturbative light-matter interactions.

Our basic research is complemented by studies of light-matter interactions in materials processing with ultrashort optical pulses and by work on optoelectronic devices. The project includes five topics.

### 2. Topics and collaborations

Research in this project has been structured into five major topical directions:

#### T1: Nonlinear THz and mid-infrared spectroscopy

Cooperation partners: K. Biermann, Paul-Drude-Institut, Berlin, C. Flytzanis, Ecole Normale Supérieure, Paris, A. Tkatchenko, University of Luxembourg, G. Cassabois and B. Gil, Université de Montpellier, France, M. Lazzeri, Sorbonne, Paris, France, G. Fugallo, Université de Nantes, France, B. Bhattacharya, A. A. L. Michalchuk, D. Silbernagl, M. Rautenberg, T. Schmid, T. Feiler, H. Sturm, F. Emmerling, Bundesanstalt für Materialforschung und -prüfung, Berlin

#### T2: Material modification with femtosecond laser pulses

Projects: DFG ME 4427/1-2, SAW LAPTON, DFG-ANR NA 1102/3-1.

Collaborations: Thomas Fennel (University of Rostock), Gunnar Bottger (Fraunhofer IZM, Berlin) Gustavo Torchia (Optical Research Center, La Plata, Argentina), Razvan Stoian (LabHC, Saint-Etienne).

#### T3: Optoelectronic devices

Spectroscopic analyses of GaAs and GaN-based devices are carried out together with scientists from the Ferdinand-Braun-Institut gGmbH Leibniz-Institut für Höchstfrequenztechnik such as S. Einfeld, C. Netzel

and P. Crump. This involves both charge carrier kinetics in optoelectronic devices and materials and thermal properties of high power diode lasers. Work on devices is also being done with F. Yue of East China Normal University in Shanghai, China, and J. Jimenez of the University of Valladolid, Spain.

#### T4: Magnetism and transient electronic structure

Cooperation partners are various principal investigators within the Collaborative Research Center TRR 227 "Ultrafast Spin Dynamics" (MBI projects: A02, A04), J. Lüning, HZB, Berlin, Germany, S. Bonetti, Stockholm University, Uppsala University, Sweden, Christian Gutt, University Siegen, M. Albrecht, Augsburg University, E. K. U. Gross, MPI Halle, M. Schultze MPQ Garching, M. Münzenberg, Greifswald University.

#### T5: Joint HU-MBI Group on Theoretical Optics

Projects: within the DFG-SPP-1839 "Tailored Disorder", project Bu 1107/10-1, Bu 1107/10-2 "Light-path engineering in disordered waveguiding systems" and Bu 1107/12-2 "Non-Markovian continuous-time quantum random walks of multiple interacting particles".

Cooperation partners: W. Pernice, University of Münster, A. Szameit, University of Rostock, N. A. Mortensen, University of Southern Denmark, R. de Jesus Leon-Mortiel, Universidad Nacional Autonoma de Mexico, and S. Linden, University of Bonn.

## 3. Results in 2020

#### T1: Nonlinear THz and mid-infrared spectroscopy

Two-dimensional terahertz (2D-THz) spectroscopy is our key experimental concept for studying the nonlinear response of condensed matter in the spectral range between 300 GHz and 30 THz. In one of the highlights of this annual report, new results on field-induced tunneling ionization and terahertz-driven electron dynamics in liquid water were presented [GKS20].

In another experiment, we investigated in detail the terahertz field enhancement with a bow-tie antenna [RES20]. This work is motivated by the need for strong THz electric fields in nonlinear THz experiments addressing, e.g., the field-driven optical response of solids and/or liquids. Moreover, charge transport in the nonlinear regime, i.e., beyond Ohm's law, becomes accessible this way.

Electric fields in the multi-MV/cm range cannot be easily generated in a frequency range around 1 THz. Such frequencies are very high for generation by electronic means and very low for generation by nonlinear optical frequency conversion, which results in both cases in a very low generation efficiency. By concentrating the limited energy of a THz pulse to a small volume, it is possible to achieve high electric fields. Whereas with lenses and mirrors the smallest possible volume is of the order of  $\lambda^3$  ( $\lambda$ : THz wavelength), with metallic antenna structures it is possible to achieve volumes considerably smaller than this limit.

The field enhancement by bow-tie antennas was studied in a wide range of antenna parameters (Fig. 1(a)). The antennas were fabricated by electron-beam lithography on 10  $\mu\text{m}$  thick ZnTe crystals, which allow for a direct measurement of the electric field by electrooptic sampling (Fig. 1(b)). The spatial resolution of this method is determined by the spot size (3  $\mu\text{m}$ ) of the near-infrared readout pulse used. This readout pulse measures the birefringence of the ZnTe crystal induced by the THz field. With an applied electric field  $<110>$  ZnTe becomes birefringent, which results in a polarization rotation of the probe pulse and a difference signal from two photodiodes, each measuring one polarization component. This signal is proportional to the applied electric field. In this way, one obtains the instantaneous electric field at the instant in time when the read-out pulse hits the ZnTe crystal. By varying the delay between the short read-out pulse and the much longer THz pulse one measures the electric field as a function of time.

Two representative THz electric field transients are shown in Fig. 1(c). The black line gives the transient far away from the antenna and the red line the transient in the center of the antenna. The corresponding spectra are shown in Fig. 1(d) together with their ratio (blue line). Above a frequency of 1 THz there is essentially no difference between the amplitudes with and without the antenna. At lower frequencies, however, the antenna enhances the electric field by up to a factor of four. Spatially resolved measurements (Fig. 1(f)) show that the enhancement is particularly strong at the antenna surface. The observed values from the experiment agree very well with the values from a simulation (Fig. 1(e)). The calculations suggest a depth range of some 10  $\mu\text{m}$  over which the THz field is enhanced. By varying the dimensions of the antenna, it is possible to shift the frequency of the maximum field enhancement to any desired value.

In future experiments, the antenna structures will be placed on a THz-transparent substrate, to be used as the front window of a liquid-sample cell. In this, nonlinear field-induced changes of the dielectric and/or vibrational properties of liquids and solutions will be studied.

## T2: Material modification with femtosecond laser pulses

Under suitable irradiation conditions (tight focusing, intensity on the order of 10  $\text{TW}/\text{cm}^2$ ), the interaction of ultrashort (sub-ps duration) laser pulses with transparent solid materials results in a permanent re-

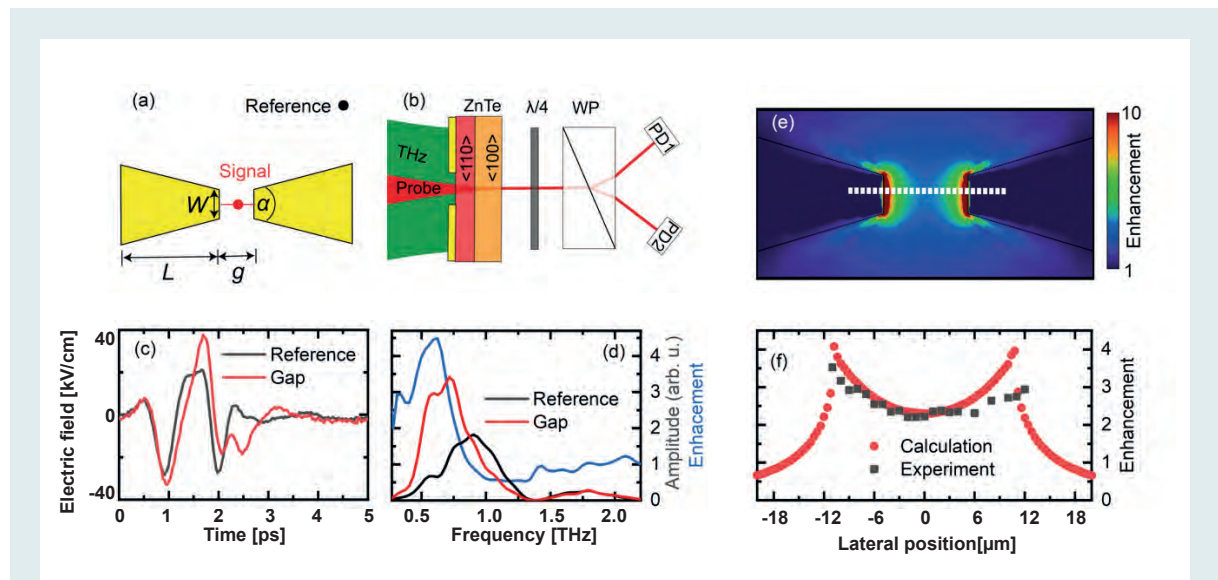


**Fig. 1:**

(a) Structure and dimensions of the bow-tie antenna. The antenna consists of two arms of length  $L$  separated by the gap  $g$ . (b) Detection scheme for the local THz electric field using electrooptic sampling. The THz beam (green) and the near-infrared probe beam (red) are focused by a parabolic mirror onto the antenna deposited on the ZnTe crystal. The THz electric field is read out by a detection system consisting of a quarter-wave plate, a Wollaston polarizer (WP) and a pair of balanced photodiodes (PD1 and PD2). (c) The THz field as a function of time measured in the antenna gap [red dot in (a), red line] and far away from the antenna [black dot in (a), black line]. (d) Corresponding spectra. Blue line: frequency-dependent electric field enhancement. (e) Spatial dependence of the electric-field enhancement in a bow-tie antenna with  $L = 53 \mu\text{m}$  and  $g = 22 \mu\text{m}$  from a simulation. (f) Electric-field enhancement at different positions [white line in (e)] along the antenna gap at a frequency of 0.7 THz from experiment (black squares) and simulation (red dots).

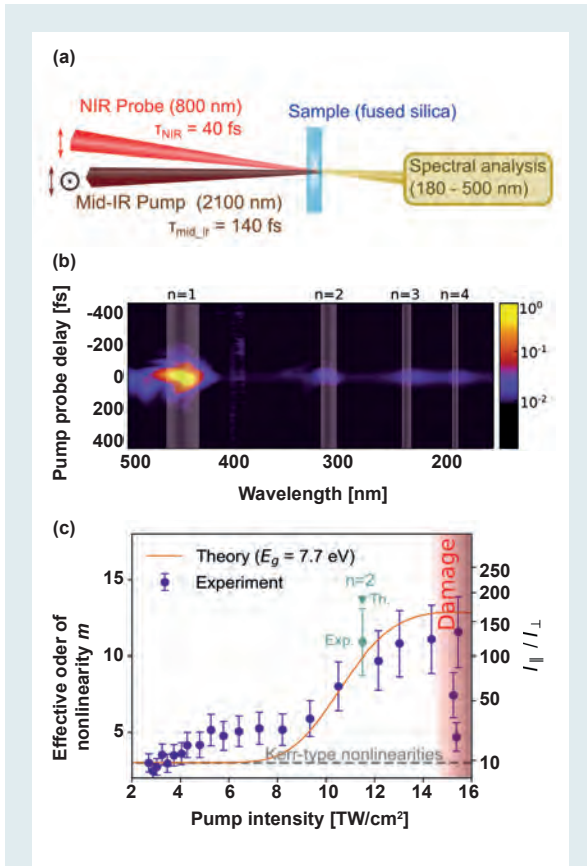


**Fig. 2:** Low-order harmonic emission during laser-induced plasma formation. (a) Experimental setup (b) Time-resolved emission spectrum for a pump intensity of ca. 11 TW/cm<sup>2</sup>. Pump and probe beams were collinearly polarized. (c) Effective order of nonlinearity as a function of the pump intensity for the harmonic order n=1.

fractive index change in the irradiated region. These localized refractive index changes can be exploited to manufacture micro-optical circuits. The laser-induced structural modifications imprinted in the substrate are initiated by the formation of an electron-hole plasma building up during laser irradiation. Such an intrapulse evolution makes the study of plasma formation highly complex.

By focusing an intense ultrashort pulse (at frequency  $\omega_0$ , see Fig. 2(a)) together with a weak, time-delayed probe pulse (at frequency  $\omega_1$ ) in a fused silica sample, we observe the emission of the harmonic spectrum shown in Fig. 2(b). Such a spectrum consists of harmonics at frequencies  $2n\omega_0 + \omega_1$ , where n is the harmonic order.

The main physical process responsible for the harmonic emission at these low orders is usually assigned to the response of the bound electrons (the Kerr response), characterized by an effective nonlinearity of order  $m = 2n + 1$ , i.e.,  $m=3$  for  $n=1$ . In the frame of a collaboration with the group of Prof. Fennel (University of Rostock), we have developed an experimental method in order to characterize the effective order of nonlinearity m. In brief, m can be estimated by taking the square root of the ratio  $I_{\text{par}}/I_{\text{perp}}$ , where  $I_{\text{par}}$  and  $I_{\text{perp}}$  correspond to the harmonics

intensity obtained with pump and probe beams co- and cross-polarized, respectively (see y-scales in Fig. 2(c)).

In Fig. 2(c), we represent the evolution of m as the pump intensity increases. At low pump intensities (typically 2-4 TW/cm<sup>2</sup>), the harmonic emission is due to the nonlinear response of the bound electrons (Kerr response). Correspondingly, we find  $m \sim 3$ . As the pump intensity increases and approaches the material's damage threshold, the effective order of nonlinearity goes up to  $m > 10$ . Such a high value can not be explained in terms of conventional four wave mixing. With the help of complementary plasma diagnostics (not shown here), we could attribute the highly nonlinear harmonic emission to strong field ionization resulting in the persistent transfer from carriers from the valence to the conduction band.

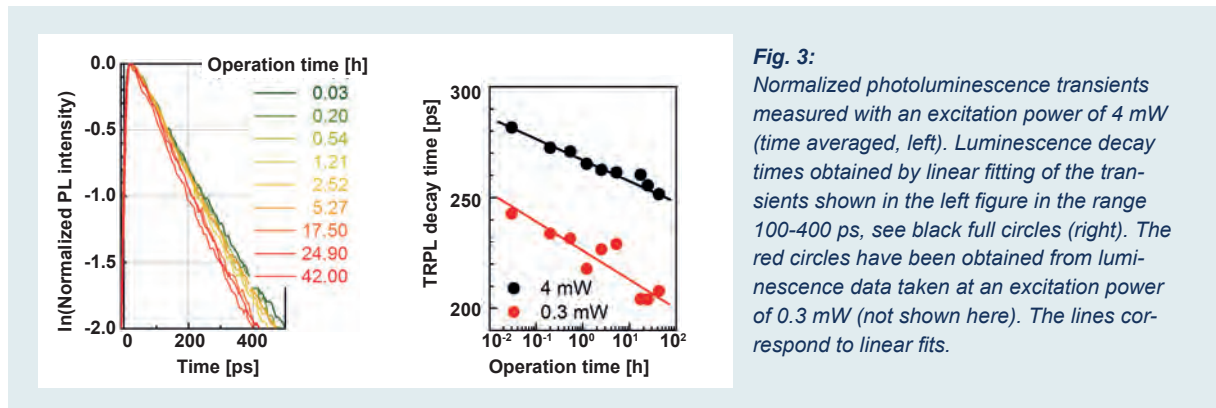
As a conclusion, we have established that the low-order harmonics emitted during irradiation are directly related to ionization dynamics when the laser intensity approaches the material's damage threshold. These findings are crucial to characterize, control and optimize the electron-hole plasma formation and further improve fs laser micromachining capabilities.

### T3: Optoelectronic devices

In this application-oriented topic, we deal with the properties of optoelectronic devices and materials that can be used as active laser materials. With investigations on light emitting diodes for the UVB range (280-315 nm) and materials for mid-infrared lasers we cover not only a broad spectral range but also a wide range of applications.

The goal of the work on UVB LEDs was to quantify a specific degradation effect, namely the increase in non-radiative recombination during device operation [RGM20]. For this purpose, an experimental approach was established for *in-situ* time resolved measurements of the quantum well (QW) luminescence of a LED, generated by two different pump mechanisms, namely operation by direct current ("regular operation") and short-pulse optical excitation. Non-radiative recombination is shown to increase with operation time. A saturable process on a time scale below 10 ps and slower mechanisms on a time scale of several 100 ps were found. For instance, a reduction of the time-resolved photoluminescence decay time from 250 to 200 ps within the first 42 hours of current stress was observed ( Fig. 3). Saturation effects, as evident from the different slopes in Fig. 3, indicate a limited number of defects acting as non-radiative recombination centers, which are continuously emerging in the QW during device operation.

This work on GaN-based LEDs is complemented by research on the GaN material itself [NHT20, TTK20] and on GaN-based diode lasers [MHW20]. Temperature-dependent transport of photoexcited charge carriers through a nominally undoped, c-plane GaN layer toward buried InGaN quantum wells is investigated by time-resolved photoluminescence spectroscopy [NHT20].



The temperature dependence of the diffusion constant indicates that the diffusivity at room temperature is limited by optical phonon scattering. Consequently, higher diffusion constants in GaN-based devices require a reduced operation temperature. In another study, we report a novel GaN-growth mechanism that allows the incorporation of Si into GaN nanowires up to and beyond the solubility limit [TTK20]. Such high Si concentrations were verified by secondary-ion mass spectrometry, transient photoluminescence and Raman spectroscopy together with quantum chemical modelling. There is even the possibility of the formation of a Ga(Si)N solid solution. The microscopic mechanism responsible for heavy doping (and even alloying) is diffusion driven by the mechano-chemical effect, which allows for the extremely efficient injection of Si atoms into the nanowires from the step bunches at the vicinal SiC/Si substrates.

#### T4: Magnetism and transient electronic structure

In recent years, research in femto-magnetism has started to focus on more complex, multi-component magnetic systems, where functionality emerges through the interaction of elements with distinct properties. Prominent examples include all-optical switching in rare-earth/transition metal alloys or multilayers, i.e., the deterministic reversal of the magnetization direction upon short-pulse excitation, or terahertz emission at a ferromagnetic/heavy metal interface via the Inverse Spin Hall Effect. For the exploration and further development of such new material properties that arise via a non-equilibrium, transient state of matter, a thorough understanding of the microscopic processes is essential. To this end, we have continued to apply [DWE20, KWS20, and WKS20] and to develop [YWK20b] magnetic circular dichroism (MCD) in the extreme ultraviolet (XUV) spectral range to disentangle the *element-specific* response on an ultrafast time scale. These experiments are guided by state-of-the-art time-dependent density functional theory.

##### Optical Intersite Spin Transfer in CoPt alloys

Optically driven spin transport is the fastest and most efficient process to manipulate macroscopic magnetization as it does not rely on secondary mechanisms to dissipate angular momentum. In a joint theoretical and experimental study, we were able to show

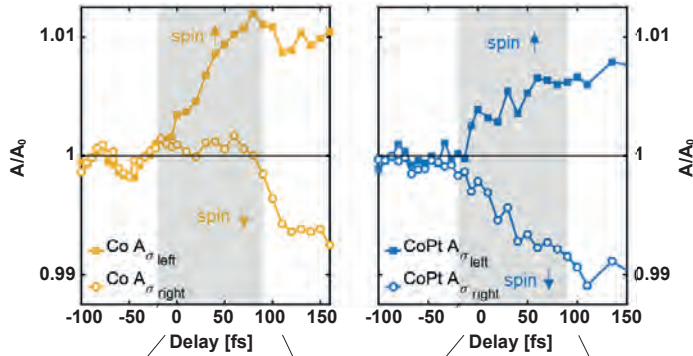
that such an optical inter-site spin transfer (OISTR) from Pt to Co emerges as a dominant mechanism governing the ultrafast magnetization dynamics of a CoPt alloy [WKS20]. To demonstrate this, we investigated the transient changes of helicity dependent absorption in the extreme ultraviolet spectral range. In Fig. 4 we show the measured and calculated resonant absorption at the Co  $M_{2,3}$  edge for left,  $\sigma_{\text{left}}$ , and right,  $\sigma_{\text{right}}$ , circularly polarized light. Comparison between the ultrafast response for a pure Co film and a CoPt alloy reveals a pronounced difference for  $\sigma_{\text{right}}$  radiation (open symbols). Because we can link helicity dependent absorption to relative changes of the spin-dependent occupations changes, the observed ultrafast loss of absorption for  $\sigma_{\text{right}}$  photons is caused by efficient filling of previously empty minority states above the Fermi energy. With additional measurements at the Pt  $N_7$  edge, we were able to identify that these additional minority electrons indeed originate from Pt atoms. This exemplifies that the efficiency and directionality of OISTR is determined by the available states above the Fermi level. This makes OISTR a general phenomenon in optical manipulation of multi-component magnetic systems and opens up the opportunity to tailor the ultrafast magnetic response by density of state engineering.

##### Distinct spectral response in M-edge magnetic circular dichroism

While the understanding that the transient shape of dichroic absorption and MCD spectra may reveal details about the microscopic origin of different types of spin excitations has been predicted theoretically already in the seventies, only in the last years scientist have started to explore this in ultrafast XUV experiments. In a simplified view, one can differentiate Heisenberg-like *transverse* spin excitations and Stoner-like *longitudinal* spin-flip processes, while only the latter can be associated with a spectrally reshaping response function during ultrafast demagnetization. However, up to date, it has remained very challenging to access the spectral response function of a magnetic material characterized by a non-equilibrium electron distribution, both experimentally and theoretically.

In helicity-, energy-, and time dependent absorption experiments around the  $M_{2,3}$  resonances, we were able to present experimental support of a distinct spectral response function, evidenced by a delayed onset of the ultrafast MCD signal [YWKa20]. In our study including

(a) measurement at  $E_{ph} = 60.3$  eV



(b) ab-initio calculation

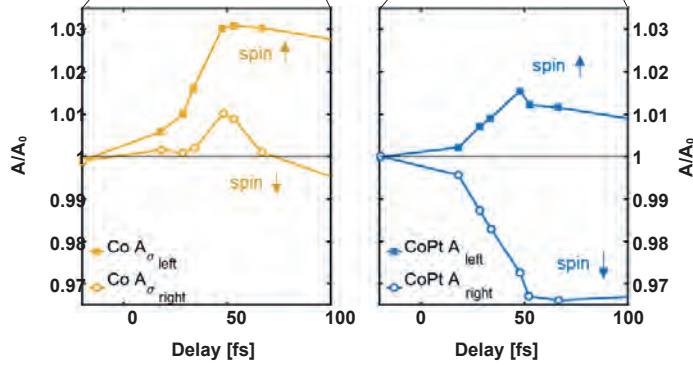


**Fig. 4:**

Measured (a) and calculated (b) ultrafast changes of the helicity dependent absorption at the Co  $M_{2,3}$  resonance at a photon energy of 60.3 eV for a Co film (yellow) and a CoPt alloy (blue). Right circularly polarized radiation,  $\sigma_{right}$ , probes predominantly the relative changes in the occupations of spin-down electrons. Reduction of absorption is consequently a direct measure of an ultrafast and efficient filling of unoccupied spin-down states of Co. This filling occurs via optically transferred spin-down electrons originating from Pt.

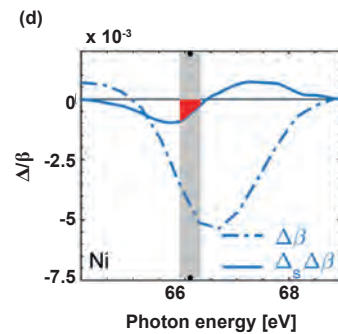
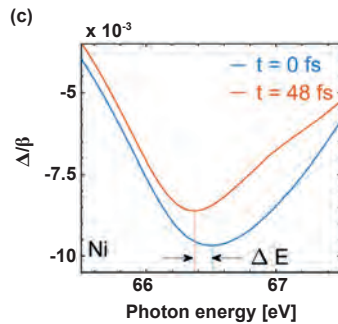
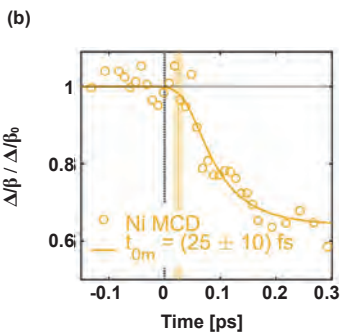
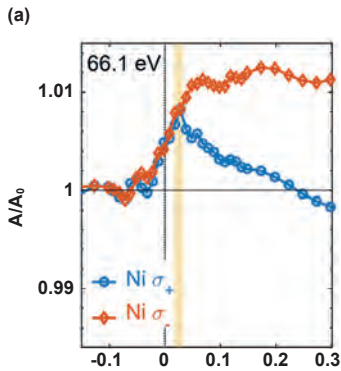


**Fig. 5:**

(a) Helicity dependent absorption changes of a Ni film measured at 66.1 eV, approximately 0.6 eV below the maximum of the  $M_{2,3}$  resonance (cf.  $\Delta\beta$  in (d)). We observe a rapid and identical increase of the absorption of left and right circularly polarized light. Distinct, helicity dependent absorption dynamics only start after 25 fs and indicates the onset of  $\Delta\beta/\Delta\beta_0 \propto \ln(A(\sigma_-)/A(\sigma_+))$  (cf. panel (b)). (c) Calculation of the absorptive part of the magneto-optical functions  $\Delta\beta(E)$  for Ni before and after optical excitation. We observe a reduction of the amplitude of  $\Delta\beta$  and a spectral shift,  $\Delta\beta$ , to lower photon energies. Panels (d) shows measured values of  $\Delta\beta(E)$  (dashed lines) and difference spectra,  $\Delta_s\Delta\beta(E) = \Delta\beta(E - 0.15 \text{ eV}) - \Delta\beta(E)$  while keeping the amplitude of  $\Delta\beta$  constant (solid lines). The red areas indicate an increase of the MCD signal due to the spectral reshaping at the specific probing photon energy Adapted from [YWKa20].

the transition metals Fe, Co, and Ni (cf. Fig. 5), as well as the two magnetic alloys FeNi and GdFe, we find delays of tens of femtoseconds for single-element systems and up to  $(111 \pm 50)$  fs in a FeNi alloy, too large to reflect the onset of changes in the macroscopic magnetization itself. Instead, we provide an explanation based on a transiently shifted and reshaped spectrum of the absorptive part of the optical as well as magneto-optical functions due to laser-generated nonequilibrium electron distributions and corresponding, energy-dependent *longitudinal* spin flip excitations. This hypothesis was qualitatively supported by state-of-the-art ab initio calculations. Hence, we understand the apparent delay between the electronic and magnetic response as the result of two competing processes. Namely, the increase of the MCD signal due to an effective shift of the spectrum into the narrow XUV probing window and, on the other hand, by the decrease of the MCD signal due to ultrafast demagnetization. These findings are summarized in Fig. 5.

Furthermore, we stress that these results are of importance for experiments at FEL and HHG radiation sources operating with a finite bandwidth in the XUV spectral range which are becoming increasingly common tools for investigations of ultrafast magnetization dynamics.

#### Extending solid-state calculations to ultra long-range length scales

Density functional theory (DFT) has had a tremendous impact on solid-state physics and is, due to its computational efficiency, at the heart of modern computer based material research. While DFT offers in-depth understanding of microscopic properties, so far it cannot tell anything about physics on larger, mesoscopic length scales. Such effects include long-ranged quasiparticles, magnons, skyrmions, magnetic domains, or spatially dependent electric fields. As DFT is a formally exact theory, the underlying physics for such phenomena is readily at hand, yet actual calculations remain very difficult. While it is, in principle, possible to use ever larger super-cells, in practice one quickly reaches the limit of computational viability.

Recently, we have developed a fundamentally different approach to drastically extend the length scale of DFT calculations without significantly increasing the computational cost [MSG20]. This approach relies on altered Bloch states by introducing an additional sum in the Bloch states over a finer grid in reciprocal space around each k-point. The resulting densities then become a Fourier series with a controllable periodicity, which may extend to nanometers.

To demonstrate the power of the new method, we have performed a calculation, which is too large for a conventional super-cell. Calculations were performed for 3456 LiF units under a random potential – for demonstration purposes in the shape of an Elk (See Fig. 6). The calculation was performed on 480 CPU cores and each iteration took about 40 minutes. The convergence was achieved in 24 iterations. This level of performance for an all-electron calculation indicates

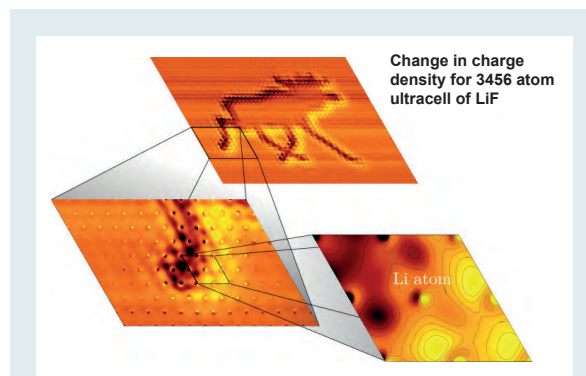


**Fig. 6:** *Self-consistent density for a 3456 atom cell of LiF with an artificial external potential. The physics at the length scale of single atom and physics at ultra long-range length scales is treated at the same footing, bringing mesoscopic length scales within the realm of DFT calculations. [MSG20]*

that physical phenomena involving modulations of the electronic state over hundreds or thousands of unit cells are within reach of this approach, paving the way to calculations of mesoscopic systems, such as magnetic domain walls or skyrmions, which have so far been too “computationally expensive” and hence out of reach for ab-initio methods.

#### **T5: Joint HU-MBI Group on Theoretical Optics**

##### Defect-state lasing in photonic lattices of metal-organic microcavities

In 2020, the research in T5 has been concerned with the design and modeling of random spectrometers, the implementation and testing of the Landau-Lifshitz-Gilbert equations for modeling micro-magnetic systems, and the modeling of lasing action in a novel class of complex micro-cavities.

Specifically, with regards to the lasing action in complex micro-cavities, we have embarked upon a collaboration project with the group of Prof. Karl Leo (Technical University Dresden). Prof. Leo’s group has fabricated and measured a novel type of micro-cavity laser. This system consists of a one-dimensional DBR cavity, where the DBR structure is comprised of alternating SiO<sub>2</sub> and TiO<sub>2</sub> layers with quarter-wavelength thicknesses and the cavity (of half-wavelength thickness) contains Alq<sub>3</sub>-DCM as the (organic) gain material. This basic cavity is augmented by depositing a metal grating (periodically spaced silver stripes) in the cavity region, thus providing distributed feedback in lateral direction (cf Fig. 7). Furthermore, removing individual stripes facilitates the controlled introduction of defect states in the grating. In total, three distinct types of micro-cavities emerge: the basic one-dimensional cavity, and two plasmonically enhanced cavities, the DFB-cavity and the defect-cavity.

In order to model such systems, we have – to the best of our knowledge for the first time – implemented focused beams and rate equations into the DGTD finite-element

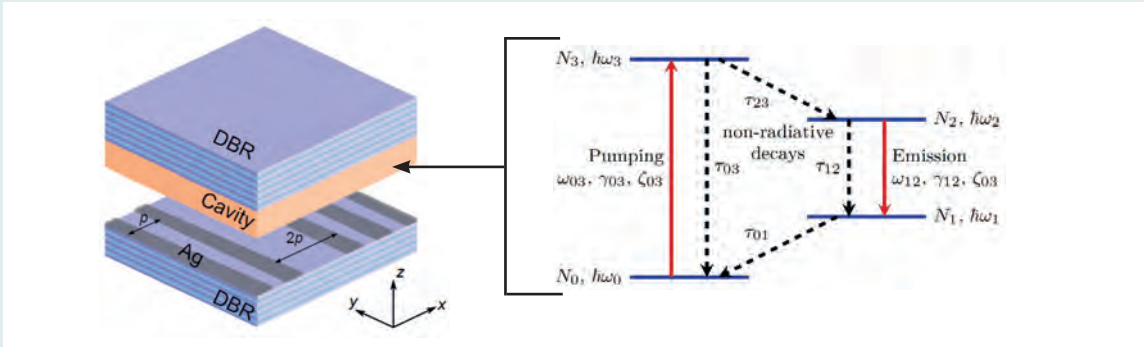


**Fig. 7:**

Left panel: Scheme of a plasmonically enhanced micro-cavity (DBR and Ag-grating with defect) that is equipped with a gain material (orange). Right panel: The gain material is modeled via a four-level rate equation with the relevant parameters indicated. Adapted from [KKK21].

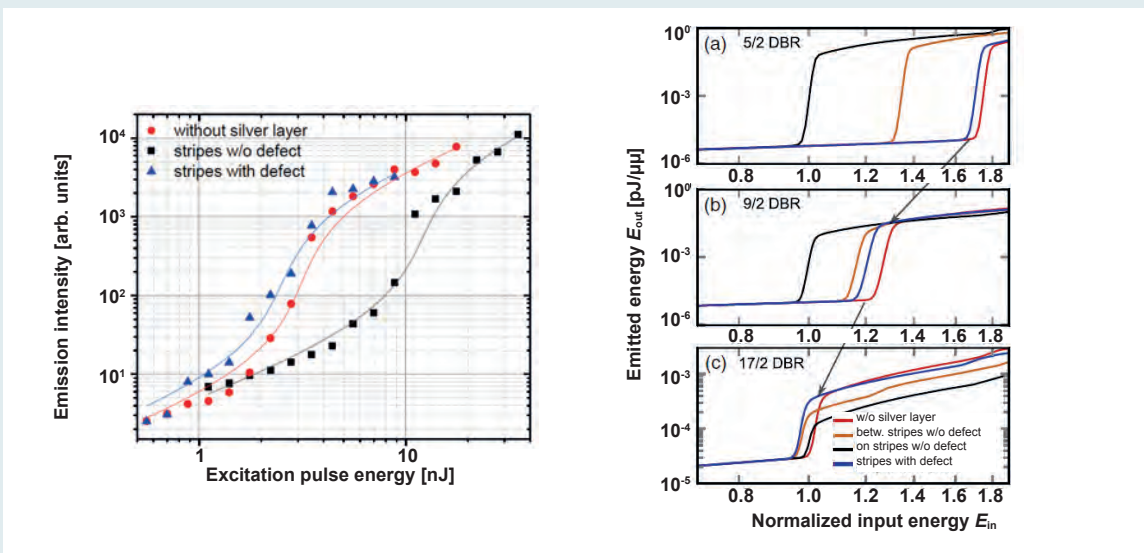


**Fig. 8:**

Left panel: Input-output-curves of lasing action in different micro-cavities: Basic one-dimensional cavity without metal (red dots), DFB-cavity with silver stripe grating (black squares), and defect-cavity with a grating that includes a defect (blue triangles). The period length of the gratings is  $p = 7.0 \mu\text{m}$ . Maxwell-Bloch equations were used to fit the data. Right panel: Computational results for different numbers of alternating  $\text{SiO}_2$  and  $\text{TiO}_2$  layers that make up the basic DBR structure. Adapted from [KKK].

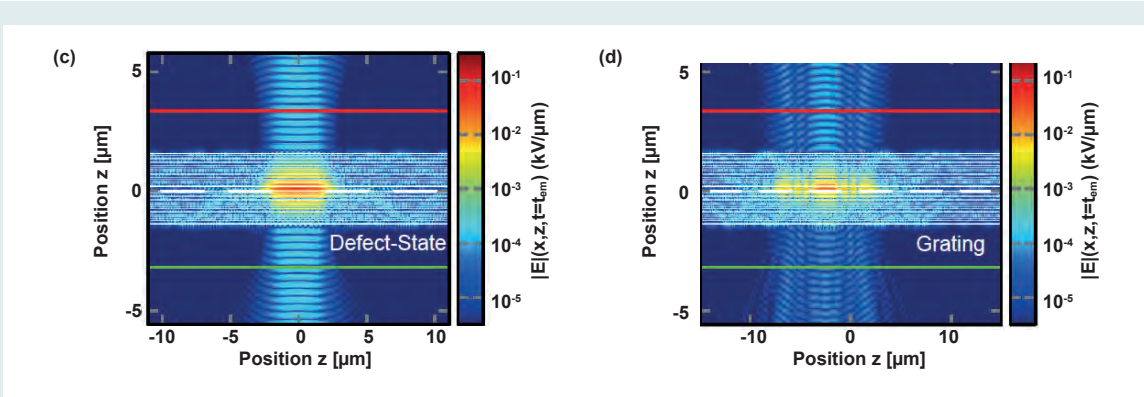


**Fig. 9:**

Field patterns of the radiating defect (c) and "band edge" (d) mode at  $t = 6 \text{ ps}$  (the pump pulse ended at  $t = 4 \text{ ps}$ ) as well as the scattered field within the DBR micro-cavities. Adapted from [KKK].

framework and have investigated the lasing thresholds of the different types of micro-cavities and different parameter ranges. In a nutshell, for the plasmonically enhanced cavities, we have been able to demonstrate the existence of two competing modes, one associated with the extended “band edge” mode of the grating and one associated with a localized defect mode. We further confirmed the experimental finding that the DFB-cavity leads to a larger lasing threshold relative to the basic cavity because the losses incurred by introducing the grating material are not fully compensated by the DFB effect of the grating. The corresponding far-field patterns are tightly localized. The situation is reversed for the defect cavity because the corresponding defect mode features considerably enhanced field strengths that is predominantly located inside the gain material and thus overcompensates the losses originating from the metal. As a result, the defect-cavity exhibits a lower laser threshold compared with that of the basic cavity and the corresponding far-field patterns are rather delocalized. Furthermore, an increase in pump intensity above lasing threshold for the DFB-cavity leads to the formation of several equidistant lasing modes at  $\pi$  or  $2\pi$  states of the Brillouin zone, depending on parity. These findings demonstrate how the incorporation of metallic films into active micro-cavities enables a fine-tuning of their lasing properties. By varying the grating or introducing defects, the lasing mode can be changed from an extended (super-)mode with strong directionality to a strongly confined, low-threshold lasing mode with a broad angular emission (see Figs. 8 and 9).

### Own Publications 2020

(for full titles and list of authors see appendix 1)

BMS20: B. Bhattacharya *et al.*; *Angew. Chem. Int. Edit.* **59** (2020) 5557-5561

DWE20: J. K. Dewhurst *et al.*; *Phys. Rev. Lett.* **124** (2020) 077203/1-6

ESK20: P. Elliott, *et al.*; *J. Magn. Magn. Mater.* **502** (2020), 166473

FGW20: M. Fleischmann *et al.*; *Nano Letters* **20** (2020)

FEW20: F. Furch *et al.*; *SPIE Proc.* **11268** (2020) 109050O/1-6

GFR20: A. Ghalgaoui *et al.*; in *The 22nd International Conference on Ultrafast Phenomena 2020*, F. Kärtner, M. Khalil, R. Li, F. Légaré, and T. Tahara eds. (Washington, D.C., USA, 2020)

GKS20: A. Ghalgaoui *et al.*; *J. Phys. Chem. Lett.* **11** (2020) 7717–7722

GRW20: A. Ghalgaoui *et al.*; *Phys. Rev. Lett.* **125** (2020) 027401/1-5

GSt20: A. Ghalgaoui and M. Sterrer; *J. Phys. Chem. C* **124** (2020) 4190-4195

HHD20: M. Hofherr *et al.*; *Sci. Adv.* **6** (2020) 8717/1-8

HML20: M. Hennes *et al.*; *Phys. Rev. B* **202** (2020) 174437/1-12

HVG20a: W. Hartmann *et al.*; *Advanced Optical Materials* **8**, (2020) 1901602/1-8

HVG20b: W. Hartmann *et al.*; *Nano Letters* **20**, (2020) 2625-2631

JLK20: P. Jürgens *et al.*; *Nature Phys.* **16** (2020) 1035-1039

KWS20: C. von Korff Schmising *et al.*; *Appl. Sci.* **10** (21) (2020) 7580/1-15

MHW20: F. Mao *et al.*; *AIP Adv.* **10** (2020) 055311/1-10

MSG20: T. Müller *et al.*; *Phys. Rev. Lett.* **125**, 256402 (2020)

NHT20: C. Netzel *et al.*; *phys. status solidi b* **257** (2020) 2000016/1-7

PMD20: C. Pellegrini *et al.*; *Phys. Rev. B* **101** (2020) 144401/1-10

RES20: M. Runge *et al.*; *Opt. Express* **28** (2020) 24389-24398

RGM20: J. Ruschel *et al.*; *Appl. Phys. Lett.* **117** (2020) 121104/1-5

RGW20: K. Reimann *et al.*; in *The 22nd International Conference on Ultrafast Phenomena 2020*, F. Kärtner, M. Khalil, R. Li, F. Légaré, and T. Tahara eds. (Washington, D.C., USA, 2020) Online

SED20: N. Singh *et al.*; *Phys. Status Solidi B* **257** (2020) 1900654/1-9

SWG20: D. Steil *et al.*; *Phys. Rev. Research* **2** (2020) 023199/1-6

TKS20: E. Travkin *et al.*; *Optics Letters* **45**, (2020) 3665-3668

TTK20: V. G. Talalaev *et al.*; *Nanotechnology* **31** (2020) 294003/1-8

VBu20: P. Varytisand and K. Busch, *Optics Express* **28** (2020), 1714-1721

WKS20: F. Willems *et al.*; *Nat. Commun.* **11** (2020) 871/1-7

YWK20a: K. Yao *et al.*; *Phys. Rev. B* **102** (2020) 100405(R)/1-6

YWK20b: K. Yao *et al.*; *Rev. Sci. Instrum.* **91** (2020) 093001/1-10

### **in press**

GFR: A. Ghalgaoui *et al.*; Phys. Rev. Lett.

KKK: M. Kliem *et al.*; Advanced Photonics Research

LED: Q. Z. Li *et al.*; Phys. Rev. B

SSM: P. Scheid *et al.*; Nano Letters

SSN: D. Schick *et al.*; Meas. Sci. Technol.

### **submitted**

AHR: R. M. Abrudan *et al.*; Phys. Stat. Solidi

BKS: M. Borchert *et al.*; Phys. Rev. B

PSY: S. Pal *et al.*; Phys. Rev. X

TJC: K. Tschernig, *et al.*; Nat. Comm.

WGR: M. Woerner *et al.*; J. Chem. Phys.

### **Invited Talks at International Conferences**

(for full titles see appendix 2)

P. Elliott; Ultrafast Webinar Summer Series 2020 (USA, 2020-08)

S. Sharma; Ultrafast Webinar Summer Series 2020 (USA, 2020-08)

S. Sharma; JEMS The Joint European Magnetic Symposia 2020 (Lisbon, Portugal, 2020-12)

S. Sharma; 710. WE-Heraeus-Seminar, Spin Transport in Complex Magnetic Structures (Bad Honnef, Germany, 2020-01)

C. von Korff Schmising, TRR 227 Retreat (Halle, Germany, 2020-04)

F. Willems; Photonics Europe 2020 - Digital Forum (Strasbourg, France, 2020-04)

A. Mermillod-Blondin, Photonics West 2020, Laser-based Micro- and Nano-processing XIV (San Francisco, USA, 2020-02)

## 3.3: Transient Structures and Imaging with X-rays

*M. Woerner, B. Pfau (project coordinators)*

*and K. Gerlinger, C. Hauf, A. Hernandez Salvador, A. Jonas, P. Hessian, L.-M. Kern, A. Koç C. von Korff Schmising, A. Lübcke, T. Noll, S. Priyadarshi, M. Schneider, H. Stiel, J. Tümmler*

### 1. Overview

The aim of project is the development and application of XUV and X-ray sources for structure analysis and imaging with high spatial and temporal resolution down to atomic length scales. The current applications focus on ultrafast optically induced structural dynamics as, e.g., strain waves, phase transitions, and transient charge densities investigated with time-resolved X-ray diffraction and absorption spectroscopy. A second focus is on imaging the spin structure in nanometer-scale magnetic materials in equilibrium and after excitation. The evaluation of new imaging techniques utilizing the light from coherent, highly brilliant soft-X-ray sources as well as the user operation of a laboratory-based X-ray microscope for the water window region are subjects of collaboration with partners from academia and industry.

### 2. Topics and collaborations

Research in this project has been structured into two major topical directions:

#### **T1: Nanoscale imaging and spectroscopy with soft X-rays**

The topic is centered around imaging and spectroscopy of nanometer-scale objects with XUV and soft-X-ray radiation produced at synchrotron-radiation sources and free-electron lasers as well as by laser-driven laboratory sources. Part of the research in this topic is performed in the framework of the Berlin Laboratory for Innovative X-ray Technologies (BLiX) which is jointly operated by the TU Berlin and MBI (cf. Project 4.2).

Collaborations: F. Büttner (HZB, Berlin), G. S. D. Beach (MIT, USA), E. Jal, B. Vodungbo (Sorbonne Universités, UPMC University Paris, France), A. Madsen, L. Wei (XFEL, Germany), J. Gräfe, G. Schütz (MPI-IS, Stuttgart, Germany), Y. Mokrousov, S. Blügel (FZ Jülich, Germany), C. M. Günther (ZELMI, TU Berlin), HZB (Berlin, Germany), Fraunhofer ILT (Aachen, Germany), optiX fab GmbH (Jena, Germany), GIST (Gwangju, Korea), KTH (Stockholm, Sweden), FSU Jena (Jena, Germany), greateyes GmbH (Berlin, Germany).

#### **T2: Femtosecond X-ray diffraction and absorption**

Investigation of phase transitions and structural dynamics in solids, in close collaboration with projects 1.2 and 3.2.

### 3. Results in 2020

#### **T1: Nanoscale imaging and spectroscopy with soft X-rays**

##### Imaging with soft X-rays

Imaging with coherent radiation of nanometer-scale wavelength is one of the core activities in this topic. On the one hand, we further develop these techniques in order to improve, e.g., the spatial resolution or sensitivity [GPG20, MWP20, BSW20]. On the other hand, we apply coherent imaging methods, in particular X-ray Fourier-transform holography, to investigate nanometer-scale functional materials with a strong focus on magnetic materials [BPG20, BPB].

The spatial resolution of microscopic images acquired via X-ray Fourier-transform holography is limited by the source size of the reference wave and by the numerical aperture of the detector. In a methodical study [GPG20], we analyzed the interplay between both influences and how they are matched in practice. Based on numerical post-processing methods such as numerical deconvolution, we further demonstrated that image details smaller than the source size of the reference beam can be recovered up to the diffraction limit of the hologram. Our findings motivate the intentional application of a large reference-wave source enhancing the image contrast in applications with low photon numbers such as single-shot experiments at free-electron lasers or imaging at laboratory sources.

In addition to the application of coherent imaging methods, we also jointly operate a laboratory-based soft-X-ray full-field microscope [KDS20] together with TU Berlin within the BLiX cooperation (see also project 4.2). The microscope is based on laser-driven nitrogen plasma source emitting radiation with 2.9 nm wavelength. This X-ray microscope was now equipped with an optical microscope precisely aligned to the X-ray source in order to pre-investigate and locate samples as well as align the tomographic rotation axis [DSS20].

##### Ultrafast small-angle scattering at X-ray free-electron lasers

The research on ultrafast magnetization dynamics in combination with nanometer-scale spatial resolution is predominately carried out at X-ray free-electron laser (XFEL) facilities. In particular, small-angle scattering using ultrashort X-ray pulses delivered by XFELs has developed into a valuable and widely applied tool to investigate optically induced magnetization dynamics in magnetic systems with nanometer-scale lateral spin structure. In 2020, we reported on results from three

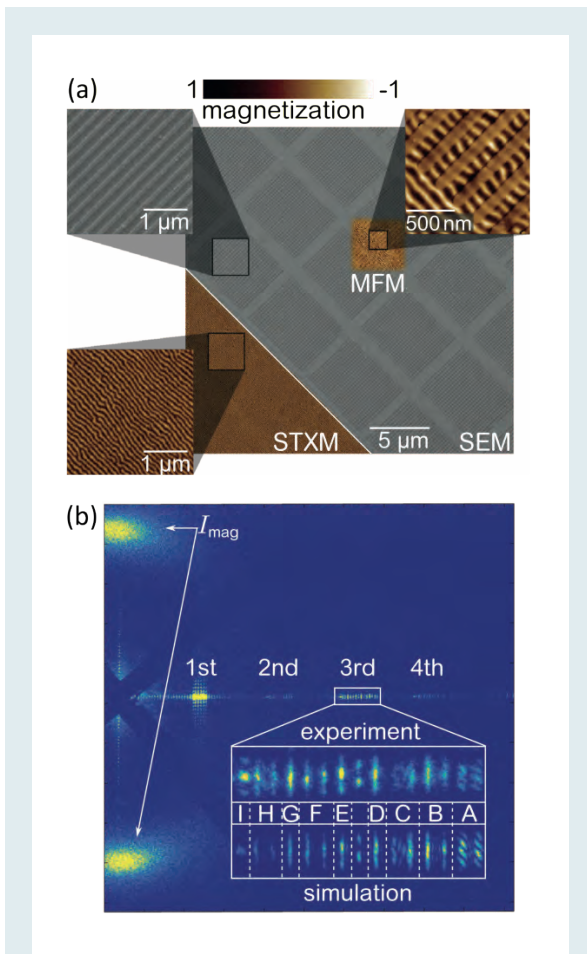


**Fig. 1:** Use of transient magnetic gratings on a nanometer scale. (a) Scanning electron microscope (SEM) image of a part of the nanostructured sample displaying the substrate (light gray) and the Al grating mask (dark gray), arranged in several grating units. The magnified section in the upper left corner shows individual Al grating bars with a width of about 100 nm. The other insets show the nanometer-scale domain pattern of the magnetic film measured via scanning transmission X-ray microscopy (STXM) and via magnetic force microscopy (MFM). (b) Typical diffraction pattern from the nanostructured sample, acquired with XUV pulses of 20.8 nm wavelength. The detector captures scattering intensity up to the fourth diffraction order (horizontal direction), originating from the vertically aligned Al gratings. The first-order magnetic domain diffraction appears in the vertical direction, originating from the horizontally aligned magnetic domains.

dependent) lifetime of hot electrons which is on the order of 10 fs. Together with the Fermi velocity, this defines the relevant spatial scale which is on the order of 10 nm. We developed a scattering experiment relying on a spatially periodic optical excitation in a Co/Pd ferromagnetic multilayer as a new technique to access non-local magnetization dynamics. The spatially modulated excitation pattern is imprinted on the sample using Al near-field masks with varying grating periods and line-to-space ratios (Fig. 1(a)). The resulting periodic optical excitation imprints a corresponding demagnetization pattern, the temporal evolution of which is probed via diffraction exploiting magnetic circular dichroism contrast. In particular, looking at initially forbidden diffraction peaks defined by appropriate line-to-space ratios provides sub-wavelength in-plane sensitivity for the transient changes in the magnetic structure (Fig. 1(b)). Assisted by simulations, we found that any lateral expansion of the initially demagnetized regions of the magnetic film mediated by hot-electron and spin transport remains confined to below three nanometers [WKG20]

In a second study, we investigated the interaction of the ferromagnetic material with the probing X-ray pulse itself. It was previously reported that high X-ray fluences lead to a reduced, non-linear response of the resonant magnetic scattering intensity. We therefore systematically studied the fluence dependence of the resonant scattering cross-section from magnetic domains in Co/Pd-based multilayers. The samples were probed with single XFEL pulses of 70 fs and 120 fs duration tuned to the Co  $M_{3,2}$  absorption resonance at 20.8 nm wavelength. Based on X-ray optics integrated into samples for shot-to-shot fluence normalization, we were able quantitatively determine the fluence-dependent scattering cross-section over three orders of magnitude in fluence up to  $10^4$  mJ/cm<sup>2</sup>/pulse. We observe a progressive quenching of the diffraction cross-section with fluence. Compression of the same pulse energy into a shorter pulse – implying an increased peak electric field of the probe – results in a reduced quenching of the resonant diffraction. We concluded that the quenching effect observed for resonant scattering involving the short-lived Co 3p core vacancies is non-coherent in nature, in contrast to effects reported for scattering in resonance with the longer-lived 2p core level. A phenomenological model based on X-ray-induced ultrafast demagnetization reproduced our entire set of experimental data. Beyond clarifying the mechanism, our results are of practical consequence for the design and interpretation of resonant scattering experiments at XFELs [SPG20a].

very different studies in this field. Two studies will be presented below, the third one on the ultrafast creation of magnetic skyrmions [BPB] is detailed as highlight in this annual report.

In the first study, we investigated laser-driven non-local electron dynamics in ultrathin metallic magnetic samples [WKG20]. Hot-electron and associated spin transport is considered one of the key processes in ultrafast magnetism. However, the experimental access in metals has been challenging due to the short (spin-

## T2: Femtosecond X-ray diffraction and absorption

The analysis of the transient electron density  $\rho(\mathbf{r},t)$  allows resolving atomic motion or relocation of electronic charge on atomic time and length scales.  $\rho(\mathbf{r},t)$  is typically extracted from femtosecond X-ray diffraction measurements employing an optical-pump/X-ray-probe method, where changes of diffracted intensity  $\Delta I/I$  on the order of 1% have to be reliably measured. In order to measure even smaller  $\Delta I/I$ , or to conduct experiments

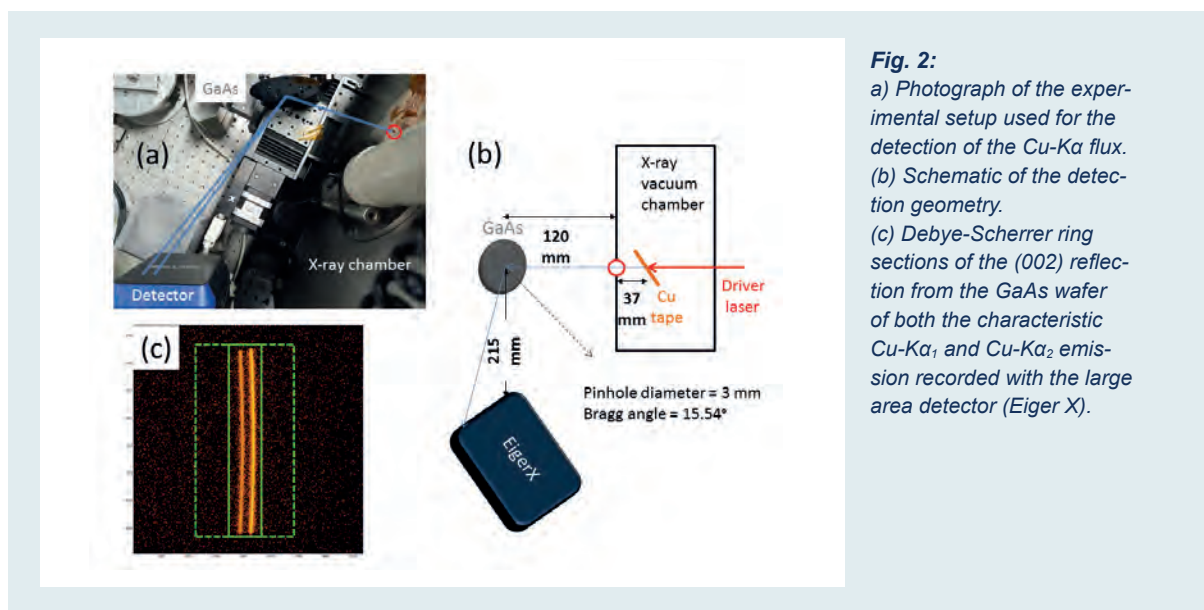


**Fig. 2:**  
 a) Photograph of the experimental setup used for the detection of the Cu-K $\alpha$  flux.  
 (b) Schematic of the detection geometry.  
 (c) Debye-Scherrer ring sections of the (002) reflection from the GaAs wafer of both the characteristic Cu-K $\alpha_1$  and Cu-K $\alpha_2$  emission recorded with the large area detector (Eiger X).

in a much faster fashion than up to now, femtosecond hard X-ray sources with a significantly higher photon flux and a detector technology with high frame rates are required.

In 2020 we demonstrated a novel compact high-flux hard X-ray source which is driven by femtosecond mid-infrared pulses at a 1-kHz repetition rate. Details are discussed in one of the highlights of this annual report [KHW].

In parallel to the completion of the novel femtosecond X-ray source we implemented new X-ray detector technology. In typical femtosecond X-ray diffraction measurements an optical-pump/X-ray-probe method is applied, in which the diffracted intensity of a pumped sample is compared with that of an unpumped sample. One achieves the optimal signal-to-noise ratio in an experimental scheme, in which alternately one femtosecond X-ray pulse measures a diffraction image of the pumped sample and next X-ray pulse the unpumped sample. Such a scheme requires an extremely high frame rate of the X-ray detector. The novel source working at a 1-kHz repetition rate [KHW] requires an identical frame rate of the X-ray detector.

In typical femtosecond powder diffraction experiments an area detector with 1000  $\times$  1000 pixels is required, each having almost 100% quantum efficiency for the detection of Cu-K $\alpha$  photons. In 2020 we implemented an Eiger X detector, DECTRIS, Switzerland, which fulfils all requirements simultaneously.

A setup for determining the Cu-K $\alpha$  flux emitted by the new source is shown in Fig. 2. A lead pinhole with a diameter of 3 mm is placed directly after the exit of the vacuum chamber at a distance of 37 mm behind the Cu tape target, reducing the number of unwanted high-energy Bremsstrahlung photons from the X-ray chamber that impinge on the detector. Such photons cannot be distinguished from Cu-K $\alpha$  photons, since the detector is not energy resolving. The X-ray photons transmitted through the pinhole pass a single crystalline GaAs wafer

(orientation (001)), placed at a distance of 120 mm from the pinhole. The wafer orientation is in accordance with the Bragg angle of the (002) reflection of 15.8°. The large X-ray area detector with a readout rate of up to 3 kHz and a pixel size of 72  $\mu\text{m} \times 72 \mu\text{m}$  for a total of 1028  $\times$  1062 pixels detects the (002) reflection from the GaAs wafer. The detector surface is oriented parallel to the GaAs wafer surface. As a result, the (002) reflection of the divergent polychromatic X-ray flux is diffracted as circular Debye-Scherrer rings sections on the detector (Fig. 2(c)). The distance of 215 mm between the GaAs wafer and the detector was selected such that both reflections of the individual Cu-K $\alpha_1$  and Cu-K $\alpha_2$  components are well separated.

The lead pinhole also limits the polar angle  $\Delta\varphi$ , resulting in the Debye-Scherrer ring sections shown in Fig. 2(c). From the pixel size of the detector and the Cu-K $\alpha_1$  and Cu K $\alpha_2$  photon energies (8047.78 eV and 8027.83 eV), the radius of the (circular) Debye-Scherrer rings can be calculated which allows for an absolute characterization of detected Cu-K $\alpha_1$  and Cu-K $\alpha_2$  photons per femtosecond X-ray pulse [KHW].

When looking at individual frames one observes that a single pixel receives a Cu-K $\alpha$  photon diffracted off the GaAs wafer with a probability  $P < 0.01$ . As a result, we are in the regime of shot-noise-limited X-ray photon detection. In this regime the shot noise dominates all other sources for noise in the experiment, e.g., additional intensity fluctuations of the femtosecond X-ray source occurring on various time scales.

The shot-noise-limited character of X-ray photon detection can be simply checked by calculating the ratio  $R = \sum_n N_{2n+1} / \sum_n N_{2n}$  with the sum of detected Cu-K $\alpha_1$  and Cu-K $\alpha_2$  photons in odd frames  $2n+1$  and even frames  $2n$  counted in a consecutive series of frames. In shot-noise-limited detection schemes the deviation of  $R$  from 1 should be that of Poisson distributions as fully confirmed in our experiments. This behavior was verified in the experiments.

In summary, the implementation of the new X-ray detector technology with high frame rates effectively suppresses the influence of intensity fluctuations of the femtosecond X-ray source occurring on various time scales.

### Own Publications 2020 ff

(for full titles and list of authors see appendix 1)

BPG20: R. Blukis *et al.*; *Geochemistry, Geophysics, Geosystems* **21** (2020) e2020GC009044/1-13

BSW20: K. Bagschik *et al.*; *Opt. Lett.* **45** (2020) 5591-5594

DSS20: A. Dehlinger *et al.*; *Microsc. Microanal.* **26** (2020) 1124-1132

GPG20: J. Geilhufe *et al.*; *Ultramicroscopy* **214** (2020) 113005/1-9

JDS20: A. Jonas *et al.*; *Anal. Chem.* **92** (2020) 15611-15615

KDS20: M. Kördel *et al.*; *Optica* **7** (2020) 658-674

LFN20: W. Lu *et al.*; *X-Ray Lasers 2018*, in *X-Ray Lasers 2018, Proceedings of the 16th International Conference on X-Ray Lasers*, M. Kozlová and J. Nejd (eds.) (Springer, Heidelberg, 2020) 131-137

MWP20: E. Malm *et al.*; *Opt. Express* **28** (2020) 394-404

SEG20: H. Stiel *et al.*, *X-Ray Lasers 2018*, in *X-Ray Lasers 2018, Proceedings of the 16th International Conference on X-Ray Lasers*, M. Kozlová and J. Nejd (eds.) (Springer, Heidelberg, 2020) 147-154

SPG20a: M. Schneider *et al.*; *Phys. Rev. Lett.* **125** (2020) 127201/1-5

TZH20: F. Tuitje *et al.*; *X-Ray Lasers 2018*, *Proceedings of the 16th International Conference on X-Ray Lasers ICXRL 2018* (2020) 155-162

WKG20: D. Weder *et al.*; *Struct. Dyn.* **7** (2020) 054501/1-13

### In press (as of Jan. 2020)

BPB: F. Büttner *et al.*; *Nat. Materials*

HWE: C. Hauf *et al.*; in *Structures on different time scales*; D. Schaniel, T. Woike (Eds., DeGruyter)

KHW: A. Koç *et al.*; *Opt. Lett.*

### Invited Talks at International Conferences (for full titles see appendix 2)

S. Eisebitt; Euroscience Open Forum 2020 (Triest, Italy, 2020-09)

S. Eisebitt; European XFEL Science Seminar (DESY, Hamburg, Germany, 2020-12)

U. Griebner; OSA High-brightness Sources and Light-driven Interactions Congress (Prague, Czech Republic, 2020-11)

B. Pfau; 2020 European XFEL Users' Meeting (Hamburg, Germany, 2020-01)

B. Pfau; PETRA IV workshop "Earth, Environment, and Materials for Nanoscience and Information Technology" (Hamburg, Germany, 2020-11)

H. Stiel; 17. International Conference on X-Ray Lasers 2020 (ICXRL) (EMPA, Dübendorf, Switzerland, 2020-12)

# 4.1: Implementation of Lasers and Measuring Techniques

*I. Will, F. Furch, U. Griebner (project coordinators)*

*and U. Bengs, F. Furch, L. von Grafenstein, C. Kleine, G. Klemz, M. Kretschmar, L. Lochner, T. Noll, M. Osolodkov, J. Tümmeler, T. Nagy, T. Witting*

## 1. Overview

The general goal of this project is the development of laser-based sources and optical measurement systems tailored to applications specific to the MBI or laboratories of collaboration partners.

Some of the unique OPCPA systems developed in the last few years within the institute are now ready to be implemented in particular applications. The goal within this project is to further engineer these systems and optimize their characteristics to the needs of the particular applications in topical areas 2 and 3.

## 2. Topics and collaborations

The project is organized in the following topics:

### T1: Lasers for particle accelerators

This topic contributes to the development of Free Electron Lasers (FELs) and other advanced accelerator based x-ray sources by providing highly specialized photo injector drive lasers and laser systems for application experiments. This work is carried out in cooperation with DESY, the Helmholtz-Zentrum Dresden-Rossendorf (HZDR), and the Helmholtz-Zentrum Berlin für Materialien und Energie (HZB).

### T2: OPCPA engineering

Several OPCPA systems in the near- and mid-infrared have been developed in the last few years. The implementation of these OPCPA sources into particular experiments in Program Areas 2 and 3 require robust and reliable and reproducible day-to-day operation of these systems. Therefore, the constant improvement and engineering of these OPCPAs is the focus of this topic. The topic is divided in three subtopics:

#### Terawatt OPCPA

A high-power OPCPA system that is pumped by a high-power thin-disk laser was developed and installed in the previous years. During 2020 this OPCPA system was applied for the generation of high energy XUV beams through high-order harmonic generation. It is capable of delivering pulses with a peak power >4 TW, having a pulse energy of 40 mJ with <9 fs duration. The system runs at a repetition rate of 100 Hz.

#### Near-IR high repetition rate OPCPAs

The development of high repetition-rate non-collinear OPCPA systems (repetition rate  $\geq 100$  kHz) is the goal

of this topic. Two OPCPAs have been established. A 100 kHz OPCPA that delivers sub-7 fs pulses with 190  $\mu$ J of energy and a 400 kHz OPCPA that delivers sub-7 fs pulses with 10  $\mu$ J of energy. The systems are intended for experiments in attosecond pump-probe spectroscopy with coincidence detection (project 2.1) and novel material processing applications (project 3.2).

#### Midwave-IR OPCPA driver for x-ray generation

This midwave-IR OPCPA system operates at 1 kHz repetition rate and delivers 80 fs pulses with up to 3.2 mJ of energy at a central idler wavelength of 5.0  $\mu$ m. The system is pumped at 2.0  $\mu$ m by a Ho:YLF CPA developed in-house. The application for this OPCPA is to serve as the driver laser for a Cu-K $\alpha$  source utilized for time-resolved x-ray diffraction experiments (project 3.3)

### T3: Implementation of experimental and measuring techniques

The topic is concerned with the improvement of particular technologies, experimental methods and measuring techniques and their implementation within the institute for the benefit of Program Areas 2 and 3.

## 3. Results in 2020

### T1: Lasers for particle accelerators

This topic deals with the development and systematic improvement of photocathode lasers for linear accelerators (Linacs) of FELs, as well as with other lasers used at particle accelerators and storage rings. Photocathode lasers are needed to drive the photo injectors, where electron bunches are generated which are then subsequently accelerated in the accelerator modules. Thus, the parameters of the photocathode laser, in particular its wavelength, synchronization accuracy, pulse shape, and stability, have a substantial influence on proper operations of the Linacs and FELs. At present, several photocathode lasers developed at the MBI are in operation at DESY, both for the European XFEL as well as for FLASH and PITZ, at HZB and at the superconducting RF gun at HZDR. As in previous years, we have ensured operation of the lasers at PITZ and at HZDR (Rossendorf). In addition, MBI has produced several critical components, in particular Pockels cell drivers optimized mainly for burst-mode operation of the lasers at DESY Hamburg, PITZ and HZDR.

We have further proceeded in the development of the photocathode laser for bERLinPro. This complete system will contain two dedicated lasers that differ in their basic operation frequencies. One of them operates

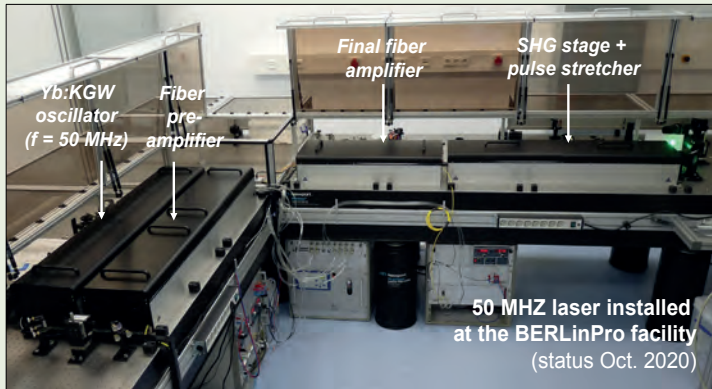


**Fig. 1:**  
50 MHz photocathode laser installed at the laser room of the bERLinPro facility at Berlin-Adlershof

at the repetition rates of 50 MHz and below, while the second laser will operate with 1300 MHz basic frequency. In 2020, the final version of the 50 MHz photocathode laser was installed at bERLinPro facility. This laser generates green picosecond pulses with 50 MHz repetition rate with more than 5 W average power. It focusses on a tunable pulse duration (2...30 ps), variable temporal pulse patterns and a repetition rate adjustable between 1 Hz and 50 MHz. The laser starts with a Yb:KGW oscillator that produces pulse of 0.8 ps duration at 50 MHz repetition rate that are electronically synchronized to the RF frequency of the bERLinPro linear accelerator. After stretching these pulses to 100 ps duration, they are amplified to  $\geq 20$  W power in a three-stage fiber amplifier. This fiber amplifier chain also contains two acousto-optic pulse selectors for separating pulses with a programmable temporal pattern and for reducing the repetition rate. The recompressed pulses are then converted to green light and finally stretched to 2–30 ps duration in a variable grating stretcher.

Fig. 1 shows the laser system installed at the laser room of the bERLinPro facility at Berlin-Adlershof. The laser is currently being used by our cooperation partners at this facility to set up the optical beamline to the RF gun.

Another part of our work in 2020 was focused on the following improvements of a laser system developed within this project for use at the MAXYMUS x-ray microscope, which is operated at BESSY II by the Max Planck Institute for Intelligent Systems.

The following improvements were realized:

- Polarization control of the laser pulses on the sample, allowing to switch between circular and linear polarisation.
- Online measurement of the average power of the laser pulses directly in the fiber cable that delivers the pulses to the vacuum chamber.

This laser is used for joint experiments on the manipulation of magnetization with light pulses on a picosecond timescale in Project 3.3. In 2020, this laser was successfully used during two beamtimes in time-resolved pump-probe imaging experiments with optical excitation on a timescale of several picoseconds. It was shown that the complete system is well suited for producing the desired laser pulses and focusing them

onto the sample with the required precision and stability, within the tight spatial constraints of the scanning x-ray microscope.

## T2: OPCPA engineering

### Terawatt OPCPA

The major goal of this topic is the reliable supply of few-fs TW-level pump pulses for high-order harmonic generation (HHG). The description of the OPCPA amplifier setup and the application of the resulting high energy near-infrared (NIR) driving pulses for HHG have recently been published in [KTB20]. A schematic setup of the high power OPCPA is shown in Fig. 2. The HHG source is capable of delivering XUV pulses centered at 25 eV with an energy  $>500$  nJ (at the source) for the application in (Proj. 2.1):

- XUV-pump XUV-probe experiments investigating XUV-driven intensity autocorrelations to further understand the underlying multiphoton multi-electron dynamics
- time-resolved coherent diffractive imaging studies

Most of the beam time was used for optimizing and adapting of the HHG XUV source to the above mentioned applications. In total the OPCPA system was applied for these tasks for more than 170 days. The work on the OPCPA system focused on the following topics:

- Installation of an adaptive mirror setup to enable the control and optimization of the focus of the NIR laser beam.
- Optimization of the beam pointing stabilization to ensure a controlled XUV-beam at the final position of the experiments.
- Optimization / tunability of beam characteristics (CEP, polarization)

The major upgrade in the past year was the installation of an adaptive mirror system. Previous measurements of the NIR focus showed a clear presence of high-order spatial phase distortions such as coma and spherical aberration which originate from our telescope with high magnification. This telescope magnifies the beam to a large diameter, which is required for the pulse

compression in the glass-compressor. To compensate for these aberrations, an adaptive mirror system has been installed. The new components are marked in Fig. 2 by light yellow boxes. A Shack-Hartman wavefront sensor allows for a precise measurement of spatial phase distortions giving a feedback signal on the large scale deformable mirror placed in the high-energy NIR beam in front of the pulse compressor. A final optimization of the focus is achieved through its direct measurement with another wavefront detection camera. Fig. 3 shows a direct comparison of a phase-distorted focus measured prior to the feedback (Fig. 3(a)) to a focus achieved after the described feedback mechanism (Fig. 3(b)). The characteristics of the focus were significantly improved. An estimated Strehl ratio exceeding 0.9 can be regularly achieved.

In addition to the optimized focus, a significant improvement of the pointing stability of the XUV beam was achieved. In previous attempts, the NIR driving beam pointing characteristics were detected prior to the HHG generation chamber. This made the subsequent XUV beam propagation of 13 m into another separated laboratory susceptible to distortions. An upgrade has been installed in which the near field of the beam stabilization is measured at the position of the focusing chamber and the far field is measured in the

application laboratory directly at the experimental side. This significantly improved the beam stability for time-resolved XUV-pump XUV-probe experiments.

Further upgrades improved the online CEP detection and feedback by installing a better environmentally shielded detection scheme. Additionally, a quickly accessible switch to change the high-energy NIR output beam polarization between s- and p-polarization has been realized to allow for an adjustment of the NIR and HHG polarization properties to the applied optics in the experimental site.

In order to enable the generation of high energy isolated attosecond pulses, the driving pulse duration needs to be shortened to the few-cycle regime which corresponds to <5 fs pulses. For the latter, the installation of a spectral broadening and post-compression setup based on self-phase modulation in several meters long stretched hollow-core fibers is planned.

#### Near-IR high repetition rate OPCPAs

Two high repetition rate OPCPAs have been developed within this topic and in the last few years utilized for different applications related to projects 1.2, 2.2, 2.3 and 3.2. Both OPCPAs operate at a central wavelength of

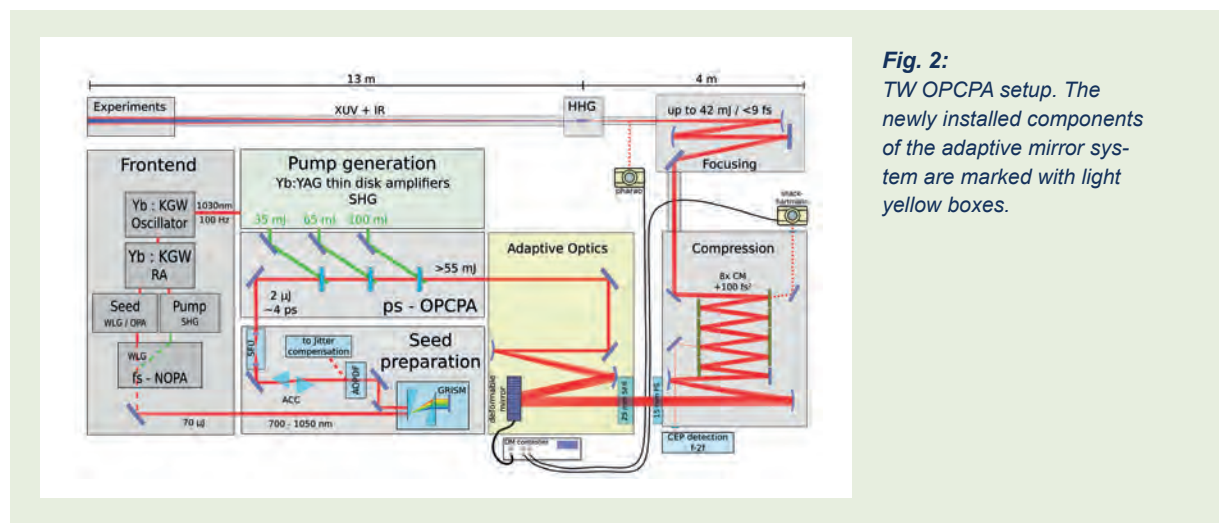


**Fig. 2:**  
TW OPCPA setup. The newly installed components of the adaptive mirror system are marked with light yellow boxes.

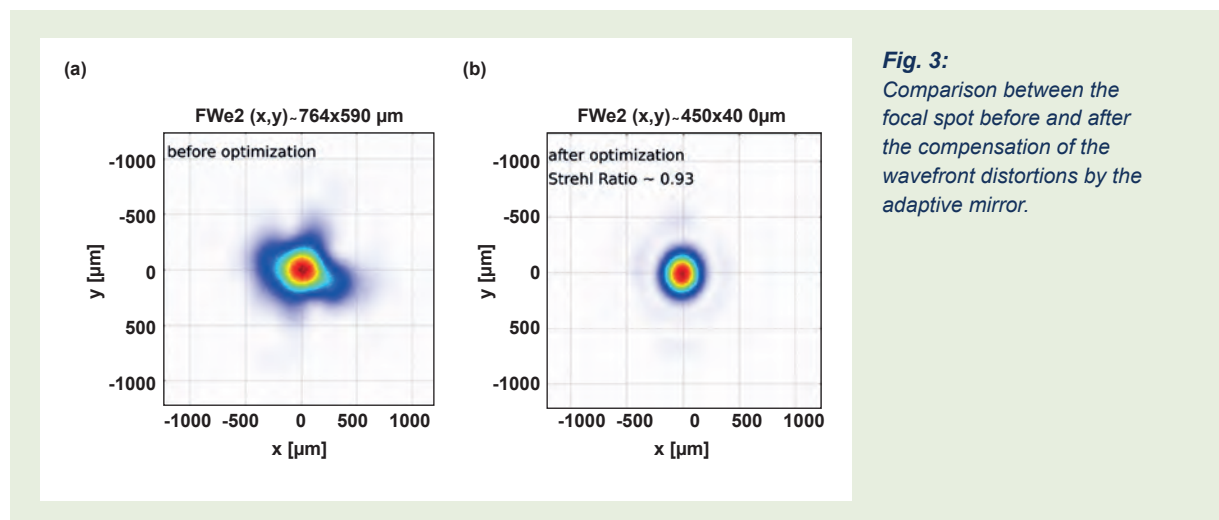


**Fig. 3:**  
Comparison between the focal spot before and after the compensation of the wavefront distortions by the adaptive mirror.

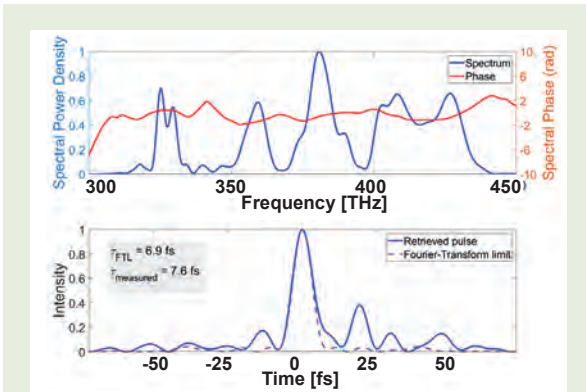


**Fig. 4:** Reconstruction of the compressed pulse (400 kHz NIR OPCPA). Top: reconstructed spectrum and spectral phase. Bottom: reconstructed pulse envelope compared to the Fourier-transform limited pulse.

800 nm, and are seeded by an ultra-broadband carrier-envelope phase-stable Ti:Sapphire oscillator. A small fraction of the oscillator spectrum around 1030 nm is also used to seed a chirped pulse amplification (CPA) system that provides the pump pulses for the OPCPA stages. In one OPCPA the pump pulses are provided by the second harmonic of a CPA based on a Yb:YAG thin-disk regenerative amplifier operating at 100 kHz. The second OPCPA is pumped by a fiber-CPA operating at 400 kHz.

For several years these two systems operated in the same laboratory sharing the front end (the Ti:Sapphire oscillator). During 2020, in the context of the SAW project “On-chip Laser-written Photonic Circuits for Classical and Quantum Applications”, a new Ti:Sapphire oscillator was acquired and the 400 kHz OPCPA was moved to a different laboratory. In the new laboratory the OPCPA was rebuilt with a slightly different design, reducing the footprint and complexity, and incorporating a pump-seed delay stabilization system developed for the 100 kHz OPCPA in order to improve the short- and long-term stability of the output. Compared to the previous design, the new setup does not incorporate a pulse-shaper to pre-compensate high order dispersion terms in the spectral phase, and therefore pulse compression after amplification is achieved solely utilizing chirped mirrors and a pair of thin-fused silica wedges. Since November 2020 the system is fully operational and has been commissioned for experiments in the corresponding SAW project linked to project 3.2. The system operates, as before, at a repetition rate of 400 kHz and delivers sub-8 fs pulses with energy per pulse exceeding 8  $\mu$ J. Figure 4 shows a SPIDER reconstruction of the compressed pulses at the output of the OPCPA.

In the 100 kHz OPCPA further improvements to the pump-seed delay stabilization system and control of the output beam pointing allowed improved long-term performance that enabled running attosecond pump-probe experiments with coincidence detection during several days uninterrupted (see project 2.1).

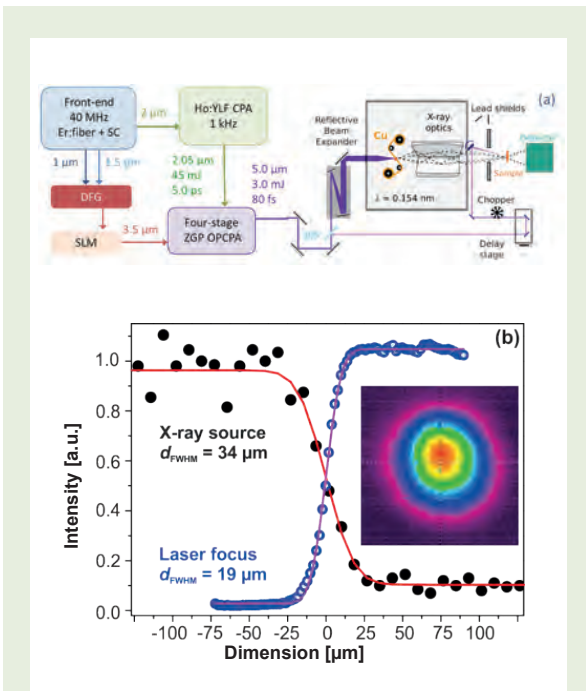


**Fig. 5:** (a) Conceptual scheme of the the 5- $\mu$ m driver laser system and the setup for the generation and characterization of the hard X-ray pulses. (b) Knife-edge measurements of the focal spot of the 5- $\mu$ m beam (open blue circles, magenta line) and the X-ray source (black circles, red line). The inset shows a 2D profile of the 5- $\mu$ m beam before expansion.

#### Midwave-IR OPCPA driver for x-ray generation

Another large scale OPCPA system operating at 5- $\mu$ m wavelength was developed during the previous years (see project 1.2). The MWIR OPCPA system operating at a 1 kHz repetition rate was successfully implemented as driver for hard x-ray generation, its intended application in MBI’s time-resolved X-ray diffraction research (see project 3.3). The main activities were devoted to sustain a stable and reliable operation of the OPCPA system. The latter was mainly achieved through the modification of the last OPA booster stage. As a consequence the system was virtually uninterrupted available as driver laser for the Cu-K $\alpha$  source in 2020.

The conceptual layout of the laser-driven hard X-ray source is shown in Fig. 5a. Details of our four-stage mid-IR OPCPA have been reported in [GBU20b]. Compared to the setup applied there, the last two stages of the parametric amplifier were modified by changing the pump arrangement of the fourth OPA stage to a direct pumping geometry, i.e., no more using the residual pump after the third OPA stage.

The main components of the OPCPA are a three-color front-end based on fs Er: fiber sources, the ps Ho:YLF CPA at 2.05  $\mu$ m as pump, and the OPA stages, all equipped with ZGP crystals. The 2.05- $\mu$ m pump delivers compressed pulses with 5 ps duration, adapted for the OPA stages, and 45 mJ energy at 1 kHz. Sub-30 fs signal pulses at 3.5  $\mu$ m are generated via DFG and subsequently shaped spectrally by a SLM. For stretching of the signal and compression of the idler pulses different

bulk materials are used. The output pulse energy of the idler after the four OPA stages amounts to 3.0 mJ. Its spectrum covers a wavelength range from 4.2 to 5.5  $\mu\text{m}$  supporting a FTL pulse duration of  $\sim 50$  fs. Successful recompression is achieved resulting in linearly polarized pulses with a duration of 80 fs. The long-term power fluctuations are only 1.2% and the beam quality is nearly diffraction limited with an  $M^2 \leq 1.3$  (Fig. 5(b)).

These unique output parameters qualify the 5- $\mu\text{m}$  OPCPA as driver for ultrafast hard X-ray generation. The 5- $\mu\text{m}$  beam is focused to a spot size of 19  $\mu\text{m}$  onto a 20- $\mu\text{m}$  thick Cu target (Fig. 1(b)). The characteristic  $K\alpha$  emission was recorded with an area detector. First at all an excellent agreement of the measured X-ray flux values with the theoretical prediction has to be emphasized. A maximum flux of  $1.5 \times 10^9$  photons per pulse, corresponding to  $1.5 \times 10^{12}$  photons per second in the full solid angle, is retrieved. These numbers surpass the X-ray flux when using a Ti:Sapphire laser driver at 0.8  $\mu\text{m}$  by 30-times. For detailed results with respect to the hard x-ray see the report of project 3.3.

### **T3: Implementation of experimental and measuring techniques**

The temporal as well as the spatio-temporal structure of our laser pulses is important for successful pump-probe experiments and the employment of our laser pulses for secondary sources, e.g., attosecond pulse generation via high harmonic generation (HHG). Spatio-temporal distortions can occur frequently in non-collinear parametric amplifiers (OPCPA). This type of laser source is now becoming prevalent at MBI at various wavelengths. Therefore a diagnostic that can accurately measure few-cycle pulses including spatio-temporal distortions at wavelengths from 800 nm to a few micrometers is important.

The spatially-encoded arrangement filter-based spectral phase interferometry for direct electric field reconstruction (SEA-F-SPIDER) method is a descendant of the SPIDER technique. The complex electric field of an unknown laser pulse is reconstructed from an interference pattern. No iterative algorithms are needed, which is a major advantage of SPIDER over other methods (e.g. FROG, d-scan). The retrieval algorithm is purely algebraically. SEA-F-SPIDER enables high fidelity measurements of pulses down to single-cycle durations with live display of the retrieved pulse. It is our method of choice to optimize the 1 kHz hollow-fiber compressed Ti:Sapphire and the 100 kHz, and 400 kHz, 800 nm OPCPA few-cycle laser systems. Our SEA-F-SPIDER apparatus has also already been adapted to measure longer wavelength pulses at 2500 nm. Due to the sum-frequency generation (SFG) one can mix the unknown pulse (e.g. at SWIR to mid-IR wavelengths) with a shorter wavelength pulse if available, which is most often the case for our OPCPA systems. The resulting sum-frequency signal can therefore be shifted into a responsive region of standard silicon based CCD cameras. We have been able to measure the broadband pulses with a spectrum ranging from 1.8 to 2.4  $\mu\text{m}$  (centered at 2.1  $\mu\text{m}$ ) from the newly commissioned

'NANOMOVIE' OPCPA system (project 4.2). In 2020 funds were made available to build a replica SEA-F-SPIDER that can be moved around MBI to wherever few-cycle and/or spatio-temporal metrology is needed.

### **Publications**

Publications which have emerged from work in this infrastructure project are listed under the relevant projects (1.2, 2.1, 2.2 and 3.2).

## 4.2: Application Laboratories and Technology Transfer

### NanoMovie – Application Laboratory for nanoscopic spectroscopy and imaging

M. Schnürer (project coordinator)

and L. Ehrentraut, P. Friedrich, A. Heilmann, G. Komml, M. van Mörbeck-Bock

#### 1. Overview

The goal of the NanoMovie project is to establish an application laboratory where soft X-rays with photon energies above 100 eV are reliably generated with high stability for use in application experiments. Application interest starts at the spectral region around 150 eV, giving access to the giant absorption resonances and magnetically dichroic transitions in the lanthanides. The so-called water window (284 eV – 543 eV) is of particular interest as it allows access to the 1s core levels for the biologically relevant light elements carbon, nitrogen and oxygen. Most challenging, photon energies beyond 450 eV allow reaching the L-edges of the 3d transition metals. Thus, p-d transitions allow probing the d-electron system with element sensitivity, which is important in the study of magnetic materials as well as metal-organic compounds on an ultrafast timescale. Cofunded through the European Regional Development Fund (ERDF), the NanoMovie laboratory will enable fundamental and applied research with ultrashort soft x-rays pulses. Focus areas are

- spectroscopy and scattering with coherent soft X-rays
- study of dynamical processes at the nanometer scale
- development of laser-based soft x-ray technology
- providing a reliable experiment and testing platform for internal and external users, including SMEs.

The project includes the development of two high average power OPCPA systems in an architecture integrating reliable commercial components where possible. The infrared femtosecond pulses derived from OPCPA drive High Harmonic Generation (HHG). The HHG-beam is delivered via suitable optics to experimental end stations. The aim is to establish stable sources of femtosecond soft X-ray pulses for spectroscopy, scattering and imaging applications. While there has been continuous progress in reaching higher photon energies in HHG in the past, the limited photon flux in and beyond the water window has so far precluded a widespread application beyond HHG expert groups in academia. The decreasing photon flux when tuning the HHG towards shorter wavelengths into the soft X-ray regime is an inherent consequence of the HHG generation process. In recent years it has been demonstrated that IR driver lasers with longer wavelength can access the soft X-ray region more easily as compared to single cycle pulses with higher carrier frequency. The principal system design was devised in cooperation with projects 1.2 and 4.1. Optimization of the HHG process is aided by model calculations and numerical simulations within project 1.1. As a result, the project strategy is to develop two laser systems, operating at 2.1  $\mu\text{m}$  and 3.1  $\mu\text{m}$ , to drive the HHG process in order to access the desired soft X-ray photon energy range.

As an important milestone in 2020, 33 W, 22 fs pulses with 10 kHz repetition rate were achieved with the new 2.1  $\mu\text{m}$  OPCPA system. Photon flux measurements in HHG experiments with the 2.1  $\mu\text{m}$  wavelength laser system were carried out. Furthermore, a first pump – probe experiment probing magnetization dynamics in  $\text{Gd}_{24}\text{Fe}_{76}$  thin film (10nm) sample was realized successfully at the magnetically dichroic  $\text{Gd N}_{4,5}$  absorption resonance in the spectral region around 150 eV. In parallel, the second OPCPA system operating at 3.1  $\mu\text{m}$  was designed in further detail and a second pump laser (DIRA 500) as well as a new frontend (Fastlite) were installed.

#### 2. Results in 2020

The NanoMovie 2.1  $\mu\text{m}$  and 3.1  $\mu\text{m}$  systems feature a monolithic concept, deriving the seed and the pump beam for the OPCPA stages from the same pump laser. This approach is compact and avoids synchronization problems but has to rely on superior characteristics of pump-laser and frontend. The implementation of this novel concept takes advantage of the fact that suitable pump lasers and frontend systems for signal generation have recently become commercially available. Both the pump-laser (500 W Thin Disk Laser (TDL) DIRA500 by *Trumpf Scientific GmbH*) and frontend (*Fastlite*) are “first of its kind” products. MBI is pioneering their integration into a reliable OPCPA laser system. Although by now several of these systems have been produced, it turned out that still time-consuming stability improvement work in close collaboration with the companies is necessary.

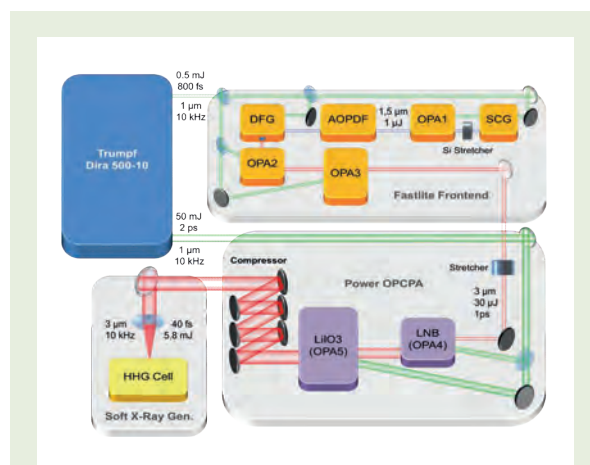


**Fig. 1:** Schematic Layout of the monolithic 3.1  $\mu\text{m}$  OPCPA system under construction. The Yb:YAG thin disk laser (500 W, 10 kHz repetition rate) acts as both pump and signal generation source.

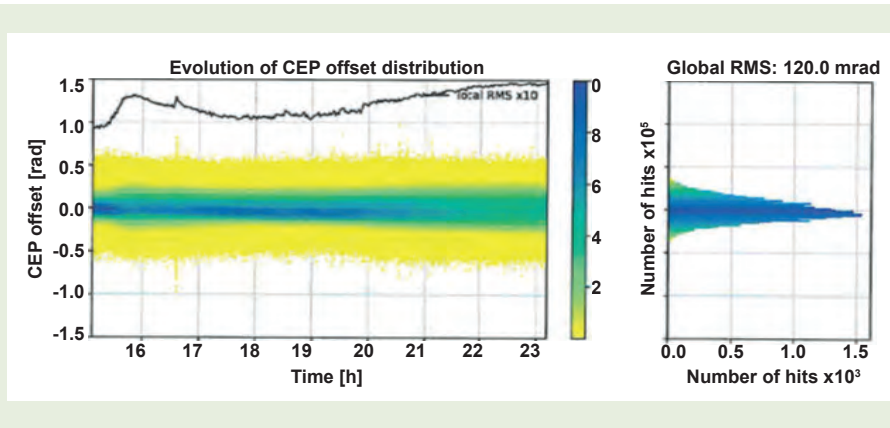


**Fig. 2:**  
EP stability measured for the 3.1  $\mu\text{m}$  frontend.

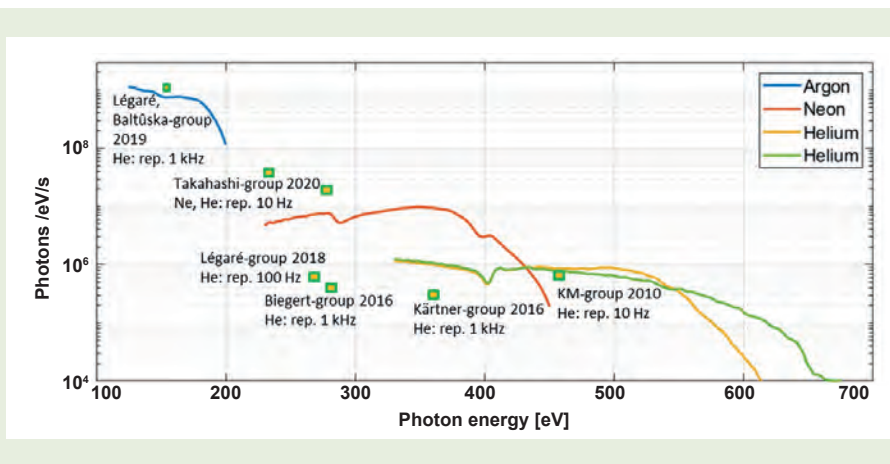


**Fig. 3:**  
Photon numbers achieved via HHG using the 2.1  $\mu\text{m}$  OPCA system and comparison to published values, shown numbers per second from systems with different repetition rates have been calculated accordingly.

### System layout

The architecture of the 3.1  $\mu\text{m}$  OPCA, very similar to the 2.1  $\mu\text{m}$  system [FHB20] is shown schematically in Fig. 1. The DIRA500 thin disk laser has a pulse duration of 2 ps (0.9 ps Fourier limit). To generate the seed for the final power OPA stages, 0.5 mJ of the DIRA output is separately compressed to  $\sim 0.9$  ps. In the frontend, the seed pulse is generated from a fraction of this 0.5 mJ pulse via supercontinuum generation (SCG), followed by an OPA stage and an acousto-optic programmable dispersive filter (AOPDF, Dazzler, Fastlite) for dispersion management. After difference frequency generation (DFG) the pulse energy is further increased by two subsequent OPA stages. The frontend output of  $\sim 0.34$   $\mu\text{J}$  (0.5 ps) is stretched further and seeded into two power OPA stages, using  $\sim 100$  W and  $\sim 350$  W to pump the first and second OPA-stage, respectively. Sysifos code simulations predict an output of 50 W (5 mJ @ 10 kHz). The bandwidth of the pulses offers a Fourier transform limit (FTL) of 40 fs. Temporal pulse compression is realized by a set of specifically designed chirped mirrors, in contrast to the pulse compression scheme using a bulk medium in the 2.1  $\mu\text{m}$  OPCA system. Due to different dispersion characteristics of media and possible reflection designs of mirrors one always tries to attempt a solution which minimizes accumulation of phase errors.

### CEP frontend characteristics:

In principle, the super continuum generation (SCG) used in the frontend offers a passively stabilized carrier

phase envelope. This has been demonstrated many times in different experimental setups. However, it is inherently coupled to the stability of the pump-laser. In response to the large phase-jitter witnessed in the 2.1  $\mu\text{m}$  frontend, a specifically designed spatial filter was integrated in the new 3.1  $\mu\text{m}$  frontend at the input of the SCG seed, reducing the beam pointing fluctuation. As a result, a CEP-stabilization as shown in Fig. 2 could be achieved. CEP-stabilization becomes more important for the shot-to-shot stability of the soft X-ray output if pulses with only few cycles are used to drive HHG or if streaking methods are to be applied.

### High Harmonic Generation:

Using a CCD-camera and a grating assembly with absolute sensitivity calibration by the German metrology institute PTB, we measure the spectrally resolved photon flux obtained via HHG with the 2.1  $\mu\text{m}$  driver system. Fig. 3 shows achieved photon flux in different spectral regions in comparison to values in the literature. The flux increase compared to the 2019 MBI annual report is mainly due to an improved design of the HHG gas cell. Not all technical bottlenecks are solved satisfactory and need further attention. Typically we drive HHG in Ar and Ne with  $5 \times 10^{14}$  W/cm<sup>2</sup> and He with  $1 \times 10^{15}$  W/cm<sup>2</sup>. While the average photon flux compares favorably to results in the literature, questions concerning the single shot IR-driver to HHG-output efficiency are still open and provide a potential route for further flux increase. Therefore, together with colleagues from the theory department (project 1.1 and cf. result in project 1.2) extensive parameter simula-

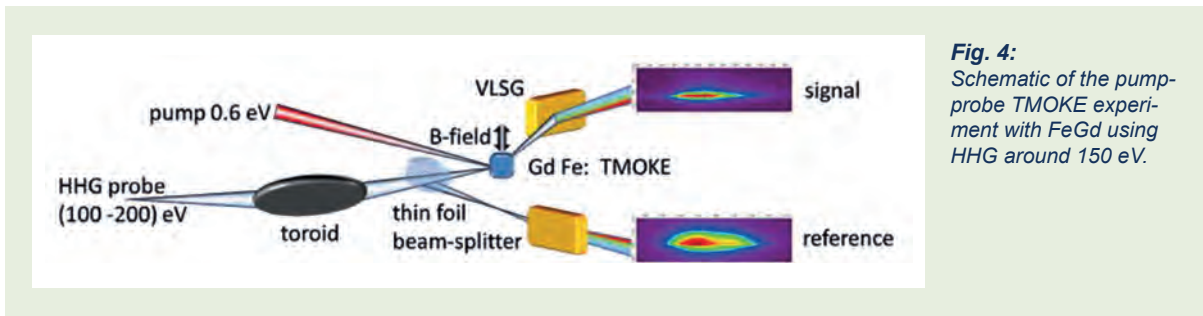


**Fig. 4:**  
Schematic of the pump-probe TMOKE experiment with FeGd using HHG around 150 eV.

tions for HHG optimization are under way.

Application experiment on ultrafast optical demagnetization:

A complete IR-pump – (150 +/- 50) eV probe setup in transverse magneto-optical Kerr effect (TMOKE) geometry with variable angle of incidence (cf. Fig. 4) was realized to study the optical switching of magnetization with FeGd-samples. The experiment makes use of magnetically dichroic optical response at the giant resonance of Gd at 150 eV. Data analysis and interpretation is under way within project 3.2. With the soft X-ray flux available and in conjunction with an intensity normalization scheme, very satisfactory signal to noise ratios in time-resolved TMOKE spectra were obtained, allowing to extrapolate with respect to pump-probe experiments with significantly higher photon energies.

OPA-simulations were carried out in collaboration with G. Arisholm, Forsvarets forskningsinstitut, using the Sysifos5 software.

**3. Users and publications**

The infrastructure is currently under construction.

Publication is referenced in project 1.2.

# Berlin Laboratory for innovative X-ray Technologies (BLiX)

H. Stiel (project coordinator)

## 1. Overview

The Berlin Laboratory for innovative X-ray Technologies (BLiX, [www.blix.tu-berlin.de](http://www.blix.tu-berlin.de)) is jointly operated by the Institut für Optik und Atomare Physik (IOAP) of the Technische Universität Berlin and the Max-Born-Institut (MBI). BLiX is the „Leibniz-Applikationslabor“ of MBI. It operates at the interface of scientific research and industrial application with the goal to transfer research results into instrument prototypes, with a focus on instruments and techniques that can be used in a laboratory environment without the need for large scale facilities. BLiX is supposed to be a place of collaborative technology development in the knowledge triangle of research - innovation - education.

The main fields of activity in BLiX are:

- Soft X-ray imaging using laboratory X-ray microscopy
- Confocal micro X-ray fluorescence analysis
- Detection of chemical species
- X-ray absorption spectroscopy in the laboratory
- Customer inspired development of hard X-ray zspectrometers based on highly annealed pyrolytic graphite optics.

MBI contributes to BLiX predominantly via:

- The support of development and operation of a soft X-ray absorption spectroscopy beamline based on a laser produced plasma X-ray source and novel X-ray optics
- The upgrade of a full field laboratory transmission X-ray microscope (LTXM) capable of tomographic nanoscale imaging and support of LTXM user operation
- The transfer of know-how concerning the development and application of laser based sources, optics and detectors for the soft and hard X-ray region.

### Near-edge X-ray absorption fine structure spectroscopy in the laboratory

A laser produced plasma (LPP) source based on long time experience of MBI in laser plasma dynamics has been implemented at BLiX in collaboration between IOAP/TU Berlin and BESTEC GmbH. The pump laser is a high average power commercial Yb:YAG – thin disk laser system (TRUMPF Laser Technology) which is modified with a variable pulse length seed-diode (AMPHOS, 0.5 ns – 30 ns) in order to adapt the pulse duration to the experimental needs. In standard operation mode the system delivers 1 ns laser pulses with 100 Hz repetition rate, up to 250 mJ single pulse energy and

an  $M^2 < 1.2$ . The laser pulses are focused onto a rotating and translating metal cylinder, forming a small hot dense plasma, which emits the desired soft X-rays. The target material can be exchanged with Cu and W the standard materials for line emission or quasi-continuous spectra, respectively. A real-time feedback system ensures source position stability, while the laser and the emission intensity are monitored during measurements. Two beamlines offer the possibility of two simultaneous experiments. The LPP source delivers soft X-ray pulses in the photon energy range between 200 and 1200 eV at a maximum average brightness in selected emission lines of up to  $10^{11}$  ph/s\*mm<sup>2</sup>\*mrad<sup>2</sup>.

For investigations of samples relevant for users from life and environmental sciences an X-ray absorption beamline has been implemented. It is equipped with a novel two-channel reflection zone-plate (RZP) spectrometer combining a probe and a reference channel (collaboration with HZB and nob GmbH, Berlin) for near edge X-ray absorption fine structure (NEXAFS) spectroscopy investigations with a spectral resolution up to  $E/\Delta E = 1000$  at the carbon K-edge. A beam splitter inserted in the laser beamline in conjunction with a delay line allows for pump-probe experiments with a sub-ns resolution.

### Laboratory X-ray microscopy

The full field laboratory transmission X-ray microscope (LTXM) operated at BLiX enables the detection of high quality nanoscopic images at 500 eV with a magnification up to 1000 in a field of view of about 30  $\mu\text{m}$ , a spatial resolution of 30 nm and a typical data accumulation time of less than one minute.

The soft X-ray radiation of the LTXM is provided by a laser-generated plasma. A high average power laser beam is focused onto a nitrogen cryo-jet. Line emission from the resulting hot dense plasma is collected by a multilayer condenser mirror (Optixfab GmbH, Jena), monochromatized and focused on the sample. Behind the sample, a zone plate objective, projects the image onto a cooled back illuminated X-ray CCD-camera Roper Scientific, 2048x2048 pixels).

The LTXM is equipped with a high-precision cryo-stage for the sample which allows tomographic measurements.

## 2. Results in 2020

### Results with direct participation of MBI personnel

#### Pump-probe NEXAFS spectroscopy in the photon energy range 200 – 1000 eV

In order to make pump-probe NEXAFS spectroscopy with sub-ns resolution available to a community mainly interested in investigations on organic molecules, the work in 2020 has been focused on pump-probe experiments on thin layers of organic molecules prepared on Si<sub>3</sub>N<sub>4</sub> substrates and on improvement of data acquisition processes using sCMOS detectors.

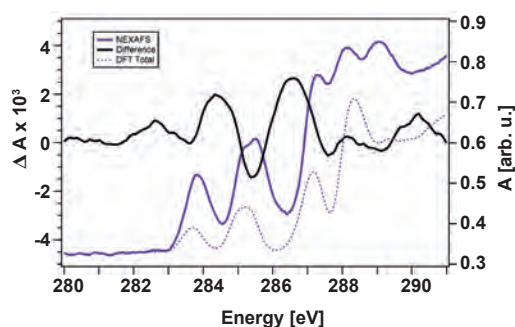


**Fig. 1:** Optical pump soft X-ray probe setup for time-resolved NEXAFS investigations on TAP. For details see [JDS20].

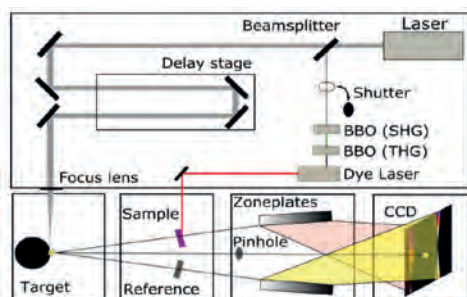


**Fig. 2:** NEXAFS spectrum of a 200 nm thick film of TAP (blue). For comparison the results of DFT calculations are also shown (dashed blue line). The difference spectrum for the pumped and unpumped sample ( $\Delta A$ , black line) averaged for delay times  $> 1$  ns show a feature assigned to a transition to partially depleted HOMO (282.5 eV). Features at higher photon energies originate mainly from the reduction of the density of unoccupied states in the excited molecule. For details see [JDS20].

Fig. 1 shows the setup used for optical pump soft X-ray probe investigations on a thin film (200 nm) of a metal free tetra-(tert)butyl-porphyrazine (TAP), allowing

for pump-probe delays from 100 ps to 40 ns. We have found changes in the carbon K-edge near edge absorption fine structure between the pumped and unpumped molecule (cp. Fig. 2). DFT calculations helped to understand these features in relation to the electronic structure of the molecule (DFG project #313838950, I. Mantouvalou, TU Berlin and JDS20).

#### Nanoscale imaging in the water window

The redesign of the LTXM setup started in 2019 has been finished. In order to increase the stability of the laser-produced plasma source of the LTXM a thin disk laser system developed at MBI is currently under commissioning.

The Collaborative Research Center 1340 (Sonderforschungsbereich SFB 1340) "Matrix in Vision" is dedicated to systematically exploring the interaction of magnetic nanoparticles with glycosaminoglycans (GAGs) as a basis for non-invasive imaging of inflammatory diseases such as atherosclerosis. X-ray microscopy in the water window could help to understand these processes on a cellular or even sub-cellular level. In 2020 our work has been concentrated on introduction of a correlative workflow between light microscopy and soft X-ray microscopy. Because the field of view in LTXM is usually limited to a few tens of micrometers, it is complicated to localize areas and objects of interest in the sample. To overcome this limitation we have integrated a visible light microscope (VLM) in our setup. The principle workflow is shown in Fig. 3. At 90° rotation (VLM-mode), an overview over the sample can be gained and the selected object of interest is moved to the center of the VLM's field of view using the translation motors of the sample stage. The position of the object of interest now coincides with both the rotation axis of the goniometer and the field of view of the LTXM. The approach has been successfully applied to imaging of THP1-cells in the context of CRC 1340 research [cp. DSS20].

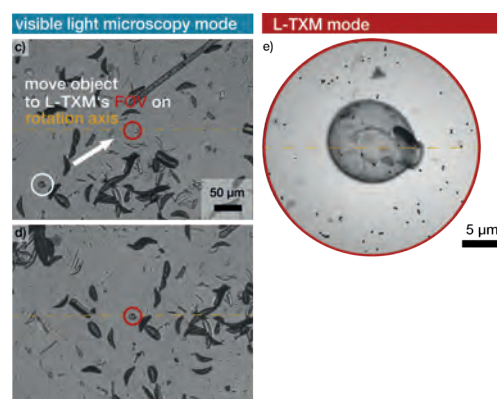


**Fig. 3:** Illustration of the workflow to rapidly detect a region of interest (ROI) for the LTXM using the VLM. For further details [DSS20].

## Results by TU Berlin personnel, without participation of MBI scientists

In the following, results by non-MBI staff within BLiX are briefly summarized to allow for a complete picture of the BLiX activities.

The instrumentation for X-ray spectroscopy and microscopy developed in BLiX has reached a state, where it can be used in applications. Currently, BLiX researchers develop one NEXAFS and one XANES spectrometer for research at the Max-Planck-Institute for Chemical Energy Conversion. Within BLiX, the current emphasis is on performing demonstration applications in order to facilitate further commercialization of the instruments with companies. Therefore, interdisciplinary research collaborations were a focus of BLiX activities in 2020, in addition to the ongoing development activities.

### X-ray absorption spectroscopy (XANES, EXAFS)

The BLiX spectrometer is capable of producing XANES spectra with moderate energy resolution and excellent EXAFS spectra within reasonable acquisition times. Application projects are carried out with various partners::

- Catalysis within the Cluster of Excellence 'Unifying Systems in Catalysis', UniSysCat
- Environmental Chemistry Phosphor cycle in water sediments, Removal of toxic chromium from water
- Materials research: Cement
- Quantitative analysis of species mixtures

### Confocal micro-X-ray fluorescence spectroscopy (XRF)

A dedicated laboratory for micro-XRF and confocal micro-XRF is operated within BLiX. In 2020, the main focus was on biological samples, including the investigation of cryo-fixated samples. Ongoing application projects focus on:

- Mineral exchange between host plant and cuscuta parasite
- Shape and distribution of Pt patches in self-activated catalysis particles
- Interface dynamics in teeth close to restoration
- Metal distribution in cacao beans

The experiments for assessing the performance of high brilliance metal jet sources with polycapillary optics were continued (co-operation with Excillum Ltd. and Helmut Fischer GmbH).

Funding for the joint research project IXdent was approved by the DFG. IXdent targets to investigate dental inter-zones by multi-modal quantitative imaging. Charite, Helmholtz Center Berlin and Bundesanstalt für Materialforschung und -prüfung (BAM) are partners.

### Angle-resolved X-ray fluorescence spectroscopy (XRF)

Three different setups for angle-resolved XRF are operational, in part with custom hardware solutions developed at BLiX. While the main focus is still on the

improvement of the setups, a first application project is in progress:

- inter- and intra-layer diffusion processes in water window multilayer optics
- Compositional gradients in CIGSe solar cells.

The long term cooperation with the X-ray Spectrometry group at PTB was continued. In joint experiments with PTB, Bruker Nano and BLiX, laboratory methods were evaluated and validated using calibrated instrumentation at the PTB laboratory at BESSY II.

### Design of X-ray optics

A BMBF funded joint research project with the University of Hamburg has been started. It aims at the design and application of highly annealed pyrolytic graphite (HAPG) based X-ray optics for X-ray fluorescence imaging at high photon energies for medical applications.

## 3. Users and publications

The infrastructure is currently under construction

Publication is referenced in project 1.2.

## 4.3: Nanoscale Samples and Optics

W. D. Engel (project coordinator)

and D. Sommer, S. Petz, M. Schneider, C. M. Günther (TU Berlin/guest)

### 1. Overview

The Laboratory for Nanoscale Samples and Optics supports several experiments in different scientific projects of the MBI. We develop and produce thin-film sample systems on various substrates with the focus on magnetic multilayers and alloys using magnetron sputtering and thermal evaporation. The close integration of deposition, structuring and characterization of these systems with experiments promotes fast feedback on sample performance and rapid development cycles. We collaborate closely with several MBI projects as well as with external cooperation partners to provide custom sample-related services.

To enable new experimental techniques as for example Spin Hall Effect measurements, skyrmion nucleation via high current density and nanoscale electric field enhancement of THz generation, a UV-lithography system is used to create masks, which enables necessary structuring and lift-off processes. Topographic, structural and magnetic characterization is carried out via atomic and magnetic force microscopy (AFM/MFM), electron microscopy (SEM, EDX), X-ray reflectivity and diffraction, Kerr magnetometry and Kerr microscopy.

In close cooperation with the central facility for electron microscopy (ZELMI) at the TU Berlin the 3D patterning on a few-micrometer and nanometer scale via electron beam lithography (EBL) and focused ion beam milling (FIB) is carried out.

Main external collaborations: ZELMI (TU Berlin), M. Albrecht (Augsburg University), F. Kronast (Helmholtz-Zentrum Berlin, HZB), R. Ernstorfer (Fritz-Haber-Institut, FHI), G.S.D. Beach (Massachusetts Institute of Technology, MIT), S. Bonetti (Stockholm University), C. Gutt (Siegen University), S. Wall (ICFO), K. Höflich (Helmholtz-Zentrum Berlin, HZB)

### 2. Results in 2020

Last year, the laboratory was expanded and upgraded to enable the lateral structuring of our samples and the production of contacts for wire bonding. Furthermore, an X-ray diffractometer was acquired in the area of sample characterization, which will significantly improve the quality assurance and reproducibility of the manufacturing processes.

The new UV-lithography system was successfully installed and put into operation, which enabled us to lithograph, very fast and flexible in design, masks in e.g. PMMA, which are then used for patterning of our samples. The minimum feature size in this setup is 2 $\mu$ m. As an example, we show in Fig.1 (left) a mask in PMMA for Hall bars, and (right) a silicon chip on which the magnetic functional layer was created with magnetron sputtering in the shape of Hall-bars using UV lithography and a lift-off process. Subsequently, in a second lithography and lift-off step, the gold contacts were produced by e-beam evaporation.

A new benchtop X-Ray diffractometer (XRR/XRD) was installed to extend the capabilities of sample characterization. With this diffractometer we can determine the crystalline structure by grazing incidence X-ray diffraction and additionally measure the thickness and interface roughness of the thin layers via X-ray reflectometry (see Fig.2). This gives us a complementary measurement method in the laboratory to the existing EDX/SEM system for characterizing all the thin film systems we produce.

We extended the existing electron beam evaporator system with a second evaporation source, giving us access to 16 materials for layer deposition without vacuum break. We had the priority to produce Al- and Ag-filters with different thicknesses (200nm up to 1 $\mu$ m) and with

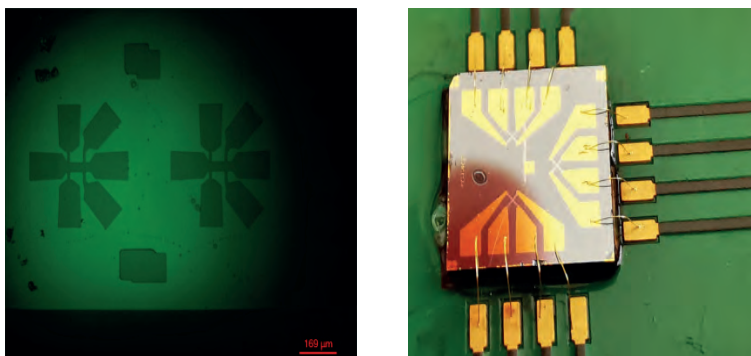


**Fig. 1:**  
(left) Mask for Hall bars written in PMMA by UV-lithography. (right) Si-chip with Hall-bars and Au contacts produced by UV-lithography, magnetron sputtering and e-beam evaporation.

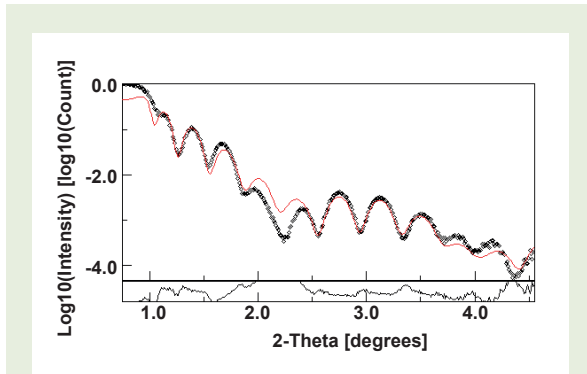


**Fig. 2:**  
X-ray reflectivity measurement (black dots) and fit (red line) of a Ta/Tb<sub>28</sub>Fe<sub>72</sub>(21)/Ta thin film system.

free apertures up to 1cm, as e.g. XUV/IR beamsplitters in high harmonic generation. Al-based heat sinks to avoid static heating in pump-probe experiments and Cr/Al as well as TiN films for plasmonic experiments are further applications of this deposition method.

In addition, at the end of the year it could be demonstrated, that ferrimagnetic (GdFe) alloys, ferromagnetic multilayers (Co/Pt) and anti-ferromagnetic films (NiO) can be grown with this evaporator system.

At the magnetron sputtering system we focused on the development and growth of magnetic thin-film samples as alloys of different ferromagnetic and metallic materials, including ferrimagnetic rare earth-transition metal (RE-TM) alloys.

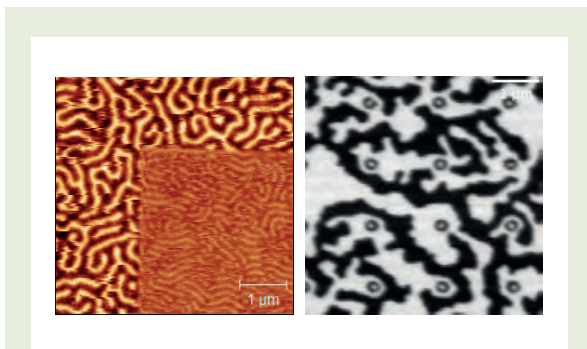


**Fig. 3:**  
Examples of artificial magnetic pattern produced by He-ion FIB. (left) MFM measurement of a CoFeB multilayer after irradiation with He-ions (250 ions/nm<sup>2</sup>). The domain size is clearly decreased. (right) Artificial dot pattern made by He-ion irradiation influencing the as grown domain pattern (STXM, MAXYMUS HZB).

For instance ferrimagnetic alloys made of rare earth (Gd, Tb, Dy) and transition metals (Fe, Co, Ni) interfaced with ferromagnetic (Co, CoFe, CoFeB) films are frequently used in MBI projects 3.2 and 3.3 to study ultrafast magnetization dynamics. It is therefore important to have sample systems available which reliably show the desired response to optical excitation e.g. hosting magnetic skyrmions. For example, high-quality ferromagnetic single- and multi-layers of type Pt/CoFeB/

MgO have been produced and optimized concerning domain size, coercive field, perpendicular magnetic anisotropy and Dzyaloshinskii-Moriya interaction.

In collaboration with HZB, He-ion irradiation using a He-ion microscope was employed to locally change the morphology of magnetic domains. Such samples are of interest in research the domain nucleation and annihilation mechanisms in response to picosecond laser pulses (examples shown in Fig.3).

## Own Publication 2020

Publications which have emerged from work in this project are listed under the respective projects 3.2 and 3.3.

# Appendices



# Appendix 1

## Publications

- AOF20: N. Acharyya, R. Ovcharenko, and B. P. Fingerhut; On the role of non-diagonal system-environment interactions in bridge-mediated electron transfer; *J. Chem. Phys.* **153** (2020) 185101/1-12
- APA20a: R. M. Arkipov, A. V. Pakhomov, M. V. Arkipov, A. Demircan, U. Morgner, N. N. Rosanov, and I. Babushkin; Coherently controlled generation of single-cycle terahertz pulses from a thin layer of nonlinear medium with low-frequency resonances; *Phys. Rev. A* **101** (2020) 043838/1-6
- APA20b: R. Arkipov, A. Pakhomov, M. Arkipov, A. Demircan, U. Morgner, N. Rosanov, and I. Babushkin; Selective ultrafast control of multi-level quantum systems by subcycle and unipolar pulses; *Opt. Express* **28** (2020) 17020-17034
- ARF20: A. Acharyya, M. Richter, and B. P. Fingerhut; Oscillatory dynamics of the spin-Boson model with ultra-strong in-teractions with the environment; in *The 22nd International Conference on Ultrafast Phenomena 2020*, F. Kärtner, M. Khalil, R. Li, F. Légaré, and T. Tahara (eds.) (OSA Publishing, Washington, D.C., USA, 2020); doi.org/10.1364/UP.2020.Tu4A.35
- ASR20: M. V. Arkipov, A. A. Shimko, N. N. Rosanov, I. Babushkin, and R. M. Arkipov; Self-induced-transparency mode locking in a Ti:sapphire laser with an intracavity rubidium cell; *Phys. Rev. A* **101** (2020) 013803/1-7
- BBK20: F. Brausse, F. Bach, F. Krečinić, M. J. J. Vrakking, and A. Rouzée; Evolution of a molecular shape resonance along a stretching chemical bond; *Phys. Rev. Lett.* **125** (2020) 123001/1-6
- BEP20: A. W. Bray, U. Eichmann, and S. Patchkovskii; Dissecting strong-field excitation dynamics with atomic-momentum spectroscopy; *Phys. Rev. Lett.* **124** (2020) 233202/1-6
- BHB20: A. Benoît, A. Husakou, B. Beaudou, B. Debord, F. Gérôme, and F. Benabid; Raman-Kerr comb generation based on parametric wave mixing in strongly driven Raman molecular gas medium; *Phys. Rev. Res.* **2** (2020) 023025/1-9
- BLM20: L. Basyrova, P. Loiko, R. Maksimov, V. Shitov, J. M. Serres, M. Aguiló, F. Díaz, U. Griebner, V. Petrov, and X. Mateos; Efficient laser operation of Yb:Lu3Al5O12 transparent ceramics fabricated from laser ablated nanopowders; *SPIE Proc.* **11259** (2020) 1125910/1-7
- BMD20: I. Babushkin, U. Morgner, and A. Demircan; Stability of quantum linear logic circuits against perturbations; *J. Phys. A* **53** (2020) 445307/1-12
- BMS20: B. Bhattacharya, A. A. L. Michalchuk, D. Silbernagl, M. Rautenberg, T. Schmid, T. Feiler, K. Reimann, A. Ghalgaoui, H. Sturm, B. Paulus, and F. L. Emmerling; A mechanistic perspective on plastically flexible coordination polymers; *Ang. Chemie-Int. Ed.* **59** (2020) 5557-5561
- BPG20: R. Blukis, B. Pfau, C. M. Günther, P. Hessian, S. Eisebitt, J. Einsle, and R. J. Harrison; Nanoscale imaging of high field magnetic hysteresis in meteoritic metal using xray holography; *Geochem., Geophys., Geosys.* **21** (2020) e2020GC009044/1-29
- BRS20: V. Bragaglia, M. Ramsteiner, D. Schick, J. E. Boschker, R. Mitzner, R. Calarco, and K. Holldack; Phonon anharmonicities and ultrafast dynamics in epitaxial Sb<sub>2</sub>Te<sub>3</sub>; *Sci. Rep.* **10** (2020) 12962/1-9
- BSG20: B. P. Bruno, R. Schütze, R. Grunwald, and U. Wallrabe; Micro Fresnel mirror array with individual mirror control; *Smart Mater. Struct.* **29** (2020) 075003/1-8
- BSW20: K. Bagschik, M. Schneider, J. Wagner, R. Buss, M. Riepp, A. Philippi-Kobs, L. Müller, W. Roseker, F. Trinter, M. Hoesch, J. Viefhaus, S. Eisebitt, G. Grübel, H. P. Oepen, and R. Frömter; Enabling time-resolved 2D spatial-coherence measurements using the Fourier-analysis method with an integrated curved-grating beam monitor; *Opt. Lett.* **45** (2020) 5591-5594
- CDW20: Y. Chen, M. Ding, J. Wang, L. Wang, Q. Liu, Y. Zhao, Y. Liu, D. Shen, Z. Wang, X. Xu, and V. Petrov; High-energy 2 μm pulsed vortex beam excitation from a Q-switched Tm:LuYAG laser; *Opt. Lett.* **45** (2020) 722-725
- CGS20: S. W. Crane, O. Ghafur, L. Saalbach, M. J. Patterson, and D. Townsend; The influence of substituent position on the excited state dynamics operating in 4-, 5-and 6-hydroxyindole; *Chem. Phys. Lett.* **738** (2020) 136870/1-7
- CKN20: M.-A. Codescu, O. Kornilov, and E. T. J. Nibbering; Switching between ultrafast proton vacancy and excess proton transfer along a methanol solvent bridge; in *The 22nd International Conference on Ultrafast Phenomena 2020*, F. Kärtner, M. Khalil, R. Li, F. Légaré, and T. Tahara (eds.) (OSA Publishing, Washington, D.C., USA, 2020); doi.org/10.1364/UP.2020.M4B.13
- CLS20: M. Chen, P. Loiko, J. M. Serres, S. Veronesi, M. Tonelli, M. Aguiló, F. Díaz, S. Y. Choi, J. E. Bae, F. Rotermund, S. Dai, Z. Chen, U. Griebner, V. Petrov, and X. Mateos; Fluorite-type Tm<sup>3+</sup>:KY<sub>3</sub>F<sub>10</sub>: A promising crystal for watt-level lasers at ~ 1.9 μm; *J. Alloy. Compd.* **813** (2020) 152176/1-15

- CLY20: M. Chen, P. Loiko, F. Yue, V. Jambunathan, A. Lucianetti, T. Mocek, J. M. Serres, M. Aguiló, F. Díaz, T. G. Park, J. E. Bae, F. Rotermund, X. Xu, J. Xu, S. Dai, Z. Chen, U. Griebner, V. Petrov, X. Mateos, and A. Major; Multi-watt continuous-wave and passively Q-switched Tm:CaYAlO<sub>4</sub> micro-lasers; *SPIE Proc.* **11259** (2020) 1125927/1-7
- CWC20: H. M. Crespo, T. Witting, M. Canhota, M. Miranda, and J. W. G. Tisch; In situ temporal measurement of ultrashort laser pulses at full power during high-intensity laser–matter interactions; *Optica* **7** (2020) 995-1002
- DAA20: W. Decking, I. Will et al.; A MHz-repetition-rate hard X-ray free-electron laser driven by a superconducting linear accelerator; *Nat. Photonics* **14** (2020) 391–397
- DBC20: C. M. Dietrich, I. Babushkin, J. R. Cardoso de Andrade, H. Rao, A. Demircan, and U. Morgner; Higher-order dispersion and the spectral behavior in a doubly resonant optical parametric oscillator; *Opt. Lett.* **45** (2020) 5644-5647
- DCA20: T. Driver, B. Cooper, R. Ayers, R. Pipkorn, S. Patchkovskii, V. Averbukh, D. R. Klug, J. P. Marangos, L. J. Frasinski, and M. Edelson-Averbukh; Two-dimensional partial-covariance mass spectrometry of large molecules based on fragment correlations; *Phys. Rev. X* **10** (2020) 041004/1-13
- DSP20: A. Davydov, A. Sanna, C. Pellegrini, J. K. Dewhurst, S. Sharma, and E. K. U. Gross; Ab initio theory of plasmonic superconductivity within the Eliashberg and density-functional formalisms; *Phys. Rev. B* **102** (2020) 214508/1-10
- DSS20: A. Dehlinger, C. Seim, H. Stiel, S. Twamley, A. Ludwig, M. Kördel, D. Grötzsch, S. Rehbein, and B. Kanngießler; Laboratory soft x-ray microscopy with an integrated visible-light microscope–correlative workflow for faster 3D cell imaging; *Microsc. Microanal.* **26** (2020) 1124-1132
- DVM20: L. Drescher, M. J. J. Vrakking, and J. Mikošch; Attosecond transient absorption spectroscopy without inversion symmetry; *J. Phys. B* **53** (2020) 164005/1-9
- DWE20: J. K. Dewhurst, F. Willems, P. Elliott, Q. Z. Li, C. von Korff Schmising, C. Strüber, D. W. Engel, S. Eisebitt, and S. Sharma; Element specificity of transient extreme ultraviolet magnetic dichroism; *Phys. Rev. Lett.* **124** (2020) 077203/1-6
- EJS20: E. Escoto, R. Jafari, G. Steinmeyer, and R. Trebino; Linear chirp instability analysis for ultrafast pulse metrology; *J. Opt. Soc. Am. B* **37** (2020) 74-81
- EMV20: U. Elu, L. Maidment, L. Vamos, T. Steinle, F. Haberstroh, V. Petrov, V. Badikov, D. Badikov, and J. Biegert; Few-cycle mid-infrared pulses from BaGa<sub>2</sub>GeSe<sub>6</sub>; *Opt. Lett.* **45** (2020) 3813-3815
- ERM20: U. Eichmann, H. Rottke, S. Meise, J.-E. Rubenson, J. Söderström, M. Agåker, C. Sâthe, M. Meyer, T. M. Baumann, R. Boll, A. D. Fanis, P. Grychtol, M. Ilchen, T. Mazza, J. Montano, V. Music, Y. Ovcharenko, D. E. Rivas, S. Serkez, R. Wagner, and S. Eisebitt; Photon-recoil imaging: expanding the view of nonlinear X-ray physics; *Science* **369** (2020) 1630-1633
- ESK20: P. Elliott, N. Singh, K. Krieger, E. K. U. Gross, S. Sharma, and J. K. Dewhurst; The microscopic origin of spin-orbit mediated spin-flips; *J. Magn. Magn. Mater.* **502** (2020) 166473
- ESS20: P. Elliott, M. Stamenova, J. Simoni, S. Sharma, S. Sanvito, and E. K. U. Gross; Time-dependent density functional theory for spin dynamics; in *Handbook of Materials Modeling*, W. Andreoni, S. Yip (eds.) (Springer, Cham, 2020) 841-868
- EST20a: E. Escoto and G. Steinmeyer; Pseudo mode-locking; *SPIE Proc.* **11263** (2020) 1126306/1-3
- EST20b: E. Escoto and G. Steinmeyer; How equidistant are microresonator frequency combs?; *SPIE Proc.* **11265** (2020) 1126509/1-3
- EWK20: S. Eckert, M.-O. Winghart, C. Kleine, A. Bannerjee, M. Ekimova, J. Ludwig, J. Harich, R. Mitzner, D. Aminov, D. Pines, E. Pines, N. Huse, P. Wernet, M. Odellius, and E. T. J. Nibbering; Deciphering photoacidity by following electronic charge distribution changes along the photoacid Förster cycle with time-resolved nitrogen K-edge x-ray absorption spectroscopy; in *The 22nd International Conference on Ultrafast Phenomena 2020*, F. Kärtner, M. Khalil, R. Li, F. Légaré, and T. Tahara (eds.) (OSA Publishing, Washington, D.C., USA, 2020); doi.org/10.1364/UP.2020.Tu2A.6
- FAB20: R. Forbes, F. Allum, S. Bari, R. Boll, M. Brouard, P. Bucksbaum, N. Ekanayake, B. Erk, A. Howard, P. Johnsson, J. Lee, B. Manschwetus, R. Mason, C. Passow, J. Peschel, D. Rivas, A. Roerig, A. Rouzee, C. Vallance, F. Ziaee, D. Rolles, and M. Burt; Time-resolved site-selective imaging of predissociation and charge transfer dynamics: the CH<sub>3</sub>I B-band; *J. Phys. B* **53** (2020) 224001/1-13
- FBM20: B. Fetić, W. Becker, and D. B. Milošević; Extracting photoelectron spectra from the time-dependent wave function: Comparison of the projection onto continuum states and window-operator methods; *Phys. Rev. A* **102** (2020) 023101/1-9
- FCS20: I. A. Fischer, C. J. Clausen, D. Schwarz, P. Zaumseil, G. Capellini, M. Virgilio, M. C. da Silva Figueira, S. Birner, S. Koelling, P. M. Koenraad, M. R. S. Huang, C. T. Koch, T. Wendav, K. Busch, and J. Schulze; Composition analysis and transition energies of ultrathin Sn-rich GeSn quantum wells; *Phys. Rev. Mat.* **4** (2020) 024601/1-10
- FEW20: F. Furch, W. D. Engel, T. Witting, A. Perez-Leija, D. Biasetti, G. Torchia, M. J. J. Vrakking, and A. Mermilod-Blondin; Photoinscription of optical microstructures in fused silica with few-cycle pulses; *SPIE Proc.* **11268** (2020) 112680N/1-6

- FGW20: M. Fleischmann, R. Gupta, F. Wullschläger, S. Theil, D. Weckbecker, V. Meded, S. Sharma, B. Meyer, and S. Shallcross; Perfect and controllable nesting in minimally twisted bilayer graphene; *Nano Lett.* **20** (2020) 971-978
- FHB20: T. Feng, A. Heilmann, M. Bock, L. Ehrentraut, T. Witting, H. Yu, H. Stiel, S. Eisebitt, and M. Schnürer; 27W 2.1  $\mu\text{m}$  OPCPA system for coherent soft X-ray generation operating at 10 kHz; *Opt. Express* **28** (2020) 8724-8733
- Fin20: B. Fingerhut; Quantendynamik offener Systeme; *Nachrichten aus der Chemie* **68** (2020) 11/57-60
- FKS20: B. P. Fingerhut, A. Kundu, J. Schauss, and T. Elsaesser; Impact of RNA melting on hydrating water structure mapped by femtosecond 2D-IR spectroscopy; in *The 22nd International Conference on Ultrafast Phenomena 2020*, F. Kärtner, M. Khalil, R. Li, F. Légaré, and T. Tahara (eds.) (OSA Publishing, Washington, D.C., USA, 2020); doi.org/10.1364/UP.2020.M2A.1
- FRA20: S. Fiedler, S. Raza, R. Ai, J. Wang, K. Busch, N. Stenger, N. A. Mortensen, and C. Wolff; Importance of substrates for the visibility of “dark” plasmonic modes; *Opt. Express* **28** (2020) 13938-13948
- FSK20: B. P. Fingerhut, J. Schauss, A. Kundu, and T. Elsaesser; Aqueous contact ion pairs of phosphate groups with  $\text{Na}^+$ ,  $\text{Ca}^{2+}$  and  $\text{Mg}^{2+}$  - structural discrimination by femtosecond infrared spectroscopy and molecular dynamics simulations; *Zeitschrift für Physikalische Chemie* **234** (2020) 1453-1474
- GBo20: R. Grunwald and M. Bock; Needle beams: A review; *Adv. Phys. X* **5** (2020) 1736950/1-25
- GBU20a: L. v. Grafenstein, M. Bock, D. Ueberschaer, A. Koç, U. Griebner, and T. Elsaesser; 2.05  $\mu\text{m}$  chirped pulse amplification system at a 1 kHz repetition rate – 2.4 ps pulses with 17 GW peak power; *Opt. Lett.* **45** (2020) 3836-3839
- GBU20b: L. v. Grafenstein, M. Bock, D. Ueberschaer, E. Escoto, A. Koç, K. Zawilski, P. Schunemann, U. Griebner, and T. Elsaesser; Multi-millijoule, few-cycle 5  $\mu\text{m}$  OPCPA at 1 kHz repetition rate; *Opt. Lett.* **45** (2020) 5998-6001
- GFR20: A. Ghalgaoui, B. P. Fingerhut, K. Reimann, M. Woerner, and T. Elsaesser; Nonlinear terahertz response of solvated electrons in liquid water; in *The 22nd International Conference on Ultrafast Phenomena 2020*, F. Kärtner, M. Khalil, R. Li, F. Légaré, and T. Tahara (eds.) (OSA Publishing, Washington, D.C., USA, 2020); doi.org/10.1364/UP.2020.Th4A.4
- GID20: S. Giri, M. Ivanov, and G. Dixit; Signatures of the orbital angular momentum of an infrared light beam in the two-photon transition matrix element: A step toward attosecond chronoscopy of photoionization; *Phys. Rev. A* **101** (2020) 033412/1-5
- GKS20: A. Ghalgaoui, L.-M. Koll, B. Schütte, B. P. Fingerhut, K. Reimann, M. Woerner, and T. Elsaesser; Field-induced tunneling ionization and terahertz-driven electron dynamics in liquid water; *J. Phys. Chem. Lett.* **11** (2020) 7717-7722
- GPG20: J. Geilhufe, B. Pfau, C. M. Günther, M. Schneider, and S. Eisebitt; Achieving diffraction-limited resolution in soft-x-ray Fourier-transform holography; *Ultramicroscopy* **214** (2020) 113005/1-29
- GRW20: A. Ghalgaoui, K. Reimann, M. Woerner, T. Elsaesser, C. Flytzanis, and K. Biermann; Frequency upshift of the transverse optical phonon resonance in GaAs by femtosecond electron-hole excitation; *Phys. Rev. Lett.* **124** (2020) 027401/1-5
- GSS20: R. Gupta, T. Saunderson, S. Shallcross, M. Gradhand, J. Quintanilla, and J. Annett; Superconducting subphase and substantial Knight shift in  $\text{Sr}_2\text{RuO}_4$ ; *Phys. Rev. B* **102** (2020) 235203/1-11
- GSt20: A. Ghalgaoui and M. Sterrer; Direct spectroscopic observation of cyanide-induced restructuring of Pt at the solid-liquid interface; *J. Phys. Chem. C* **124** (2020) 4190-4195
- HHD20: M. Hofherr, S. Häuser, J. K. Dewhurst, P. Tengdin, S. Sakshath, H. T. Nembach, S. T. Weber, J. M. Shaw, T. J. Silva, H. C. Kapteyn, M. Cinchetti, B. Rethfeld, M. M. Murnane, D. Steil, B. Stadtmüller, S. Sharma, M. Aeschlimann, and S. Mathias; Ultrafast optically induced spin transfer in ferromagnetic alloys; *Sci. Adv.* **6** (2020) eaay8717/1-7
- HKL20: J. Hummert, M. Kubin, S. López, J. I. Fuks, F. Morales, M. J. J. Vrakking, O. Kornilov, and D. G. Arbo; Retrieving intracycle interference in angle-resolved laser-assisted photoemission from argon; *J. Phys. B* **53** (2020) 154003/1-8
- HLC20: J. Hirschmann, R. Lemons, E. Chansky, G. Steinmeyer, and S. Carbajo; Long-term hybrid stabilization of the carrier-envelope phase; *Opt. Express* **28** (2020) 34093-34103
- HML20: M. Hennes, A. Merhe, X. Liu, D. Weder, C. von Korff Schmising, M. Schneider, C. M. Günther, B. Mahieu, G. Malinowski, M. Hehn, D. Lacour, F. Capotondi, E. Pedersoli, I. P. Nikolov, V. Chardonnet, E. Jal, J. Lüning, and B. Vodungbo; Laser-induced ultrafast demagnetization and perpendicular magnetic anisotropy reduction in a  $\text{Co}_{88}\text{Tb}_{12}$  thin film with stripe domains; *Phys. Rev. B* **102** (2020) 174437/1-12
- HPM20: Z. Heiner, V. Petrov, and M. Mero; Efficient, sub-4-cycle, 1- $\mu\text{m}$ -pumped optical parametric amplifier at 10  $\mu\text{m}$  based on  $\text{BaGa}_4\text{S}_7$ ; *Opt. Lett.* **45** (2020) 5692-5695
- HVG20a: W. Hartmann, P. Varytis, H. Gehring, N. Walter, F. Beutel, K. Busch, and W. Pernice; Waveguide-integrated broadband spectrometer based on tailored disorder; *Adv. Opt. Mat.* **8** (2020) 1901602/1-8

- HVG20b: W. Hartmann, P. Varytis, H. Gehring, N. Walter, F. Beutel, K. Busch, and W. Pernice; Broadband spectrometer with single-photon sensitivity exploiting tailored disorder; *Nano Lett.* **20** (2020) 2625-2631
- JDS20: A. Jonas, K. Dammer, H. Stiel, B. Kanngiesser, R. Sánchez-de-Armas, and I. Mantouvalou; Transient sub-nanosecond soft x-ray NEXAFS spectroscopy on organic thin films; *Anal. Chem.* **92** (2020) 15611-15615
- JHK20: A. Jašarević, E. Hasović, R. Kopold, W. Becker, and D. B. Milosevic; Application of the saddle-point method to strong-laser-field ionization; *J. Phys. A* **53** (2020) 125201/1-21
- JLK20: P. Jürgens, B. Liewehr, B. Kruse, C. Peltz, D. Engel, A. Husakou, T. Witting, M. Ivanov, M. J. J. Vrakking, T. Fennel, and A. Mermillod-Blondin; Origin of strong-field-induced low-order harmonic generation in amorphous quartz; *Nat. Physics* **16** (2020) 1035-1039
- JSS20: Á. Jiménez-Galán, R. E. F. Silva, O. Smirnova, and M. Ivanov; Lightwave control of topological properties in 2D materials for sub-cycle and non-resonant valley manipulation; *Nat. Photonics* **14** (2020) 728-732
- KBM20: A. E. Kuvckalić, W. Becker, and D. B. Milošević; Application of the phase-space path integral to strong-field-assisted electron-ion radiative recombination: a gauge-covariant formulation; *Symmetry* **12** (2020) 1606/1-15
- KBW20: K. Kato, V. V. Badikov, L. Wang, V. L. Panyutin, K. V. Mitin, K. Miyata, and V. Petrov; Effective nonlinearity of the new quaternary chalcogenide crystal BaGa<sub>2</sub>G<sub>2</sub>eSe<sub>6</sub>; *Opt. Lett.* **45** (2020) 2136-2139
- KDS20: M. Kördel, A. Dehlinger, C. Seim, U. Vogt, E. Fogelqvist, J. A. Sellberg, H. Stiel, and H. M. Hertz; Laboratory water-window x-ray microscopy; *Optica* **7** (2020) 658-674
- KHI20: P. T. Kristensen, K. Herrmann, F. Intravaia, and K. Busch; Modeling electromagnetic resonators using quasinormal modes; *Adv. Opt. Photonics* **12** (2020) 612-708
- KLP20: B. Kruse, B. Liewehr, C. Peltz, and T. Fennel; Quantum coherent diffractive imaging; *J. Phys. Photonics* **2** (2020) 024007/1-10
- KLR20a: E. Kifle, P. Loiko, C. Romero, J. R. Vázquez de Aldana, V. Zakharov, A. Veniaminov, U. Griebner, V. Petrov, P. Camy, A. Braud, M. Aguiló, F. Díaz, and X. Mateos; Ultrafast laser inscription and ~2 μm laser operation of Y-branch splitters in monoclinic crystals; *J. Light. Technol.* **38** (2020) 4374-4384
- KLR20b: E. Kifle, P. Loiko, C. Romero, J. R. Vázquez de Aldana, M. Aguiló, F. Díaz, P. Camy, U. Griebner, V. Petrov, and X. Mateos; Watt-level ultrafast laser inscribed Thulium waveguide lasers; *Prog. Quantum Electron.* **72** (2020) 100266/1-20
- KLV20: E. Kifle, P. Loiko, J. R. Vázquez de Aldana, C. Romero, V. Llamas, J. M. Serres, M. Aguiló, F. Díaz, L. Zhang, Z. Lin, H. Lin, G. Zhang, V. Zakharov, A. Veniaminov, V. Petrov, U. Griebner, X. Mateos, L. Wang, and W. Chen; Low-loss fs-laser-written surface waveguide lasers at >2 μm in monoclinic Tm<sup>3+</sup>:MgWO<sub>4</sub>; *Opt. Lett.* **45** (2020) 4060-4063
- KPM20: K. Kato, V. Petrov, and K. Miyata; Phase-matching properties of LiIn(S<sub>x</sub>Se<sub>1-x</sub>)<sub>2</sub>; *SPIE Proc.* **11264** (2020) 112641W/1-6
- KSD20: M. Kübel, M. Spanner, Z. Dube, A. Yu. Naumov, S. Chelkowski, A. D. Bandrauk, M. J. J. Vrakking, P. B. Corkum, D. M. Villeneuve, and A. Staudte; Probing multiphoton light-induced molecular potentials; *Nat. Comm.* **11** (2020) 2596/1-8
- KSF20a: A. Kundu, J. Schauss, B. P. Fingerhut, and T. Elsaesser; Change of hydration patterns upon RNA melting probed by excitations of phosphate backbone vibrations; *J. Phys. Chem. B* **124** (2020) 2132-2138
- KSF20b: A. Kundu, J. Schauss, B. P. Fingerhut, and T. Elsaesser; Structural discrimination of phosphate contact ion pairs in water by femtosecond 2D-IR spectroscopy; in *The 22nd International Conference on Ultrafast Phenomena 2020*, F. Kärtner, M. Khalil, R. Li, F. Légaré, and T. Tahara (eds.) (OSA Publishing, Washington, D.C., USA, 2020); doi.org/10.1364/UP.2020.M4B.9
- KSt20: M. A. Khokhlova and V. V. Strelkov; Highly efficient XUV generation via high-order frequency mixing; *New J. Phys.* **22** (2020) 093030/1-13
- KTS20: M. Kretschmar, J. Tuemmler, B. Schütte, A. Hoffmann, B. Senftleben, M. Mero, M. Sauppe, D. Rupp, M. J. J. Vrakking, I. Will, and T. Nagy; Thin-disk laser-pumped OPCPA system delivering 4.4 TW few-cycle pulses; *Opt. Express* **28** (2020) 34574-34585
- KWS20: C. von Korff Schmising, F. Willems, S. Sharma, K. Yao, M. Borchert, M. Hennecke, D. Schick, I. Radu, C. Strüber, D. W. Engel, V. Shokeen, J. Buck, K. Bagnick, J. Viefhaus, G. Hartmann, B. Manschewitz, S. Grunewald, S. Düsterer, E. Jal, B. Vodungbo, J. Lüning, and S. Eisebitt; Element-specific magnetization dynamics of complex magnetic systems probed by ultrafast magneto-optical spectroscopy; *Appl. Sci.* **10** (2020) 7580/1-15
- KZG20: S. Krekic, T. Zakar, Z. Gombos, S. Valkai, M. Mero, L. Zimányi, Z. Heiner, and A. Dér; Nonlinear optical investigation of microbial chromoproteins; *Frontiers in Plant Science* **11** (2020) 547818/1-14
- KZP20: M. Kowalczyk, X. Zhang, V. Petrov, P. Loiko, X. Mateos, S. Guo, Z. Wang, X. Xu, and J. Sotor; Self-frequency-doubling Yb:CNGS lasers operating in the femtosecond regime; *J. Opt. Soc. Am. B* **37** (2020) 2822-2829
- LAH20d: Zs. Lécz, A. Andreev, and N. Hafz; Substantial enhancement of betatron radiation in cluster targets; *Phys. Rev. E* **102** (2020) 053205/1-6

- LAn20a: Zs. Lécz and A. Andreev; Angular dispersion boost of high order laser harmonics with Carbon nano-rods; *Opt. Express* **28** (2020) 5355-5366
- LAn20b: Zs. Lécz and A. Andreev; Magnetic dipole moment generated in nano-droplets irradiated by circularly polarized laser pulse; *Phys. Rev. Res.* **2** (2020) 023088/1-8
- LAn20c: Zs. Lécz and A. Andreev; Diagnostics of peak laser intensity by pair production from thin foil target; *Las. Phys. Lett.* **17** (2020) 056101/1-6
- LBA20: Zs. Lécz, J. Budai, A. Andreev, and S. Ter-Avetisyan; Thickness of natural contaminant layers on metal surfaces and its effects on laser-driven ion acceleration; *Phys. Plasm.* **27** (2020) 013105/1-8
- LCS20: P. Loiko, M. Chen, J. M. Serres, M. Aguiló, F. Díaz, H. Lin, G. Zhang, L. Zhang, Z. Lin, P. Camy, S.-B. Dai, Z. Chen, Y. Zhao, L. Wang, W. Chen, U. Griebner, V. Petrov, and X. Mateos; Spectroscopy and high-power laser operation of a monoclinic  $\text{Yb}^{3+}:\text{MgWO}_4$  crystal; *Opt. Lett.* **45** (2020) 1770-1773
- LFN20: W. Lu, B. Friedrich, T. Noll, K. Zhou, J. Hallmann, G. Ansaldi, T. Roth, S. Serkez, G. Geloni, A. Madssen, and S. Eisebitt; Progresses of a hard x-ray split and delay line unit for the MID station at the European XFEL; in *X-Ray Lasers 2018, Proceedings of the 16th International Conference on X-Ray Lasers*, M. Kozlová and J. Nejdil (eds.) (Springer, Heidelberg, 2020) 131-137
- LLK20: V. Llamas, P. Loiko, E. Kifle, C. Romero, J. R. Vázquez de Aldana, Z. Pan, J. M. Serres, H. Yuan, X. Dai, H. Cai, Y. Wang, Y. Zhao, V. Zakharov, A. Veniaminov, R. Thouroude, M. Laroche, H. Gilles, M. Aguiló, F. Díaz, U. Griebner, V. Petrov, P. Camy, and X. Mateos; Ultrafast laser inscribed waveguide lasers in  $\text{Tm}:\text{CALGO}$  with depressed-index cladding; *Opt. Express* **28** (2020) 3528-3540
- LMS20: R. Liao, C. Mei, Y. Song, A. Demircan, and G. Steinmeyer; Spontaneous emission noise in mode-locked lasers and frequency combs; *Phys. Rev. A* **102** (2020) 013506/1-12
- LRH20: A. E. Lidiya, R. V. J. Raja, and A. Husakou; Pulse compression and pedestal suppression by self-similar propagation in nonlinear optical loop mirror; *Opt. Comm.* **474** (2020) 126083/1-23
- LRM20: M. Lytova, M. Richter, F. Morales, O. Smirnova, M. Ivanov, and M. Spanner;  $\text{N}_2^+$  lasing: Gain and absorption in the presence of rotational coherence; *Phys. Rev. A* **102** (2020) 013111/1-12
- LSS20: Q. Liu, L. Seiffert, F. Süßmann, S. Zherebtsov, J. Passig, A. Kessel, S. A. Trushin, N. G. Kling, I. Ben-Itzhak, V. Mondes, C. Graf, E. Rühl, L. Veisz, S. Karsch, J. Rodriguez-Fernandez, M. I. Stockman, J. Tiggesbäumker, K.-H. Meiwes-Broer, T. Fennel, and M. F. Kling; Ionization-induced subcycle metallization of nanoparticles in few-cycle pulses; *ACS Photonics* **7** (2020) 3207-3215
- LTB20a: M. Liebmann, A. Treffer, M. Bock, U. Wallrabe, and R. Grunwald; Controlling the spectral rotation of ultrashort vortex pulses; *SPIE Proc.* **11297** (2020) 112970W/1-7
- LTB20b: M. Liebmann, A. Treffer, M. Bock, U. Wallrabe, and R. Grunwald; Ultrashort vortex pulses with controlled spectral Gouy rotation; *Appl. Sci.* **10** (2020) 4288/1-14
- MBe20a: D. B. Milošević and W. Becker; Generation of elliptically polarized soft x rays using high-order harmonic generation with orthogonal two-color laser fields; *J. Phys. Conf. Ser.* **1508** (2020) 012001/1-10
- MBe20b: D. B. Milošević and W. Becker; High-order harmonic generation by bi-elliptical orthogonally polarized two-color fields; *Phys. Rev. A* **102** (2020) 023107/1-14
- MBG20: Z. Mašín, J. Benda, J. D. Gorfinkiel, A. G. Harvey, and J. Tennyson; UKRmol+: A suite for modelling electronic processes in molecules interacting with electrons, positrons and photons using the R-matrix method; *Comput. Phys. Commun.* **249** (2020) 107092/1-76
- MBT20: O. Melchert, C. Brée, A. Tajalli, A. Pape, R. Arkhipov, S. Willms, I. Babushkin, D. Skryabin, G. Steinmeyer, U. Morgner, and A. Demircan; All-optical supercontinuum switching; *Comm. Phys.* **3** (2020) 146/1-8
- MCT20: A. Muti, F. Canbaz, M. Tonelli, J. Eun Bae, F. Rotermund, V. Petrov, and A. Sennaroglu; Graphene mode-locked operation of  $\text{Tm}^{3+}:\text{YLiF}_4$  and  $\text{Tm}^{3+}:\text{KY}_3\text{F}_{10}$  lasers near 2.3  $\mu\text{m}$ ; *Opt. Lett.* **45** (2020) 656-659
- MHW20: F. Mao, J. Hong, H. Wang, Y. Chen, C. Jing, P. Yang, J. W. Tamm, J. Chu, and F. Yue; Infrared emission bands and thermal effects for 440-nm-emitting GaN-based laser diodes; *AIP Adv.* **10** (2020) 055311/1-6
- MKG20: B. Major, M. Kretschmar, O. Ghafur, A. Hoffmann, K. Kovács, K. Varjú, B. Senftleben, J. Tümmler, I. Will, T. Nagy, D. Rupp, M. J. J. Vrakking, V. Tosa, and B. Schütte; Propagation-assisted generation of intense few-femtosecond high-harmonic pulses; *J. Phys. Photonics* **2** (2020) 034002/1-17
- MPH20: M. Mero, V. Petrov, and Z. Heiner; Progress in ultrafast, mid-infrared optical parametric chirped pulse amplifiers pumped at 1  $\mu\text{m}$ ; *SPIE Proc.* **11264** (2020) 112640F/1-7
- MPV20: N. Mayer, P. Peng, D. M. Villeneuve, S. Patchkovskii, M. Yu. Ivanov, O. Kornilov, M. J. J. Vrakking, and H. Niikura; Population transfer to high angular momentum states in infrared-assisted XUV photoionization of helium; *J. Phys. B* **53** (2020) 164003/1-15
- MSG20: T. Müller, S. Sharma, E. K. U. Gross, and J. K. Dewhurst; Extending solid-state calculations to ultra-long-range length scales; *Phys. Rev. Lett.* **125** (2020) 256402/1-5

- MSt20: C. Mei and G. Steinmeyer; Tailoring the waveguide dispersion of nonlinear fibers for supercontinuum generation with superior intrapulse coherence; *J. Opt. Soc. Am. B* **37** (2020) 2485-2497
- MTP20: Y. Morova, M. Tonelli, V. Petrov, and A. Sennaroglu; Upconversion pumping of a 2.3  $\mu\text{m}$   $\text{Tm}^{3+}:\text{KY}_3\text{F}_{10}$  laser with a 1064 nm ytterbium fiber laser; *Opt. Lett.* **45** (2020) 931-934
- MVS20: U. N. Morzan, P. E. Videla, M. B. Soley, E. T. J. Nibbering, and V. S. Batista; Vibronic dynamics of photodissociating ICN from simulations of ultrafast x-ray absorption spectroscopy; *Ang. Chemie-Int. Ed.* **59** (2020) 20044-20048
- MWP20: E. Malm, H. Wikmark, B. Pfau, P. Villanueva-Perez, P. Rudawski, J. Peschel, S. Maclot, M. Schneider, S. Eisebitt, A. Mikkelsen, A. L'Huillier, and P. Johnsson; Singleshot polychromatic coherent diffractive imaging with a high-order harmonic source; *Opt. Express* **28** (2020) 394-404
- NHT20: C. Netzel, V. Hoffmann, J. W. Tomm, F. Mahler, S. Einfeldt, and M. Weyers; Temperature-dependent charge carrier diffusion in [0001] direction of GaN determined by luminescence evaluation of buried In-GaN quantum wells; *Phys. Status Solidi B* **257** (2020) 2000016/1-7
- NKV20: T. Nagy, M. Kretschmar, M. J. J. Vrakking, and A. Rouzée; Generation of above-terawatt 1.5-cycle visible pulses at 1 kHz by post-compression in a hollow fiber; *Opt. Lett.* **45** (2020) 3313-3316
- NMV20: N. Novakovic, M.-A. Mawass, O. Volkov, P. Makushko, W. D. Engel, D. Makarov, and F. Kronast; From stripes to bubbles: Deterministic transformation of magnetic domain patterns in Co/Pt multilayers induced by laser helicity; *Phys. Rev. B* **102** (2020) 174412/1-8
- OFS20: M. Osolodkov, F. J. Furch, F. Schell, P. Susnjar, F. Cavalcante, C. Menoni, C. P. Schulz, T. Witting, and M. J. J. Vrakking; Generation and characterization of few-pulse attosecond pulse trains at 100 kHz repetition rate; *J. Phys. B* **53** (2020) 194003/1-8
- OKS20: T. Oelze, O. Kulyk, B. Schütte, U. Frühling, E. Klimešová, B. Jagielski, L. Dittrich, M. Drescher, R. Pan, N. Stojanovic, V. Polovinkin, K. P. Khakurel, K. Muehlig, I. J. Bermudez Macias, S. Düsterer, B. Faatz, J. Andreasson, M. Wieland, and M. Krikunova; THz streak camera performance for single-shot characterization of XUV pulses with complex temporal structures; *Opt. Express* **28** (2020) 20686-20703
- OVB20: M. Ouillé, A. Vernier, F. Böhle, M. Bocoum, A. Jullien, M. Lozano, J.-P. Rousseau, Z. Cheng, D. Gustas, A. Blumenstein, P. Simon, S. Haessler, J. Faure, T. Nagy, and R. Lopez-Martens; Relativistic-intensity near-single-cycle light waveforms at kHz repetition rate; *Light Sci. Appl.* **9** (2020) 47/1-9
- PIB20: S. Pathak, L. M. Ibele, R. Boll, C. Callegari, A. Demidovich, B. Erk, R. Feifel, R. Forbes, M. Di Fraia, L. Giannessi, C. S. Hansen, D. M. P. Holland, R. A. Ingle, R. Mason, O. Plekan, K. C. Prince, A. Rouzée, R. J. Squibb, J. Tross, M. N. R. Ashfold, B. F.E. Curchod, and D. Rolles; Tracking the ultraviolet-induced photochemistry of thiophenone during and after ultrafast ring opening; *Nat. Chemistry* **12** (2020) 795–800
- PIS20: J.-S. Pae, S.-J. Im, K.-S. Song, C.-S. Ri, K.-S. Ho, Y.-H. Han, and J. Herrmann; Deep subwavelength flow-resonant modes in a waveguide-coupled plasmonic nanocavity; *Phys. Rev. B* **101** (2020) 245420/1-5
- PLS20: Z. Pan, P. Loiko, J. M. Serres, H. Yuan, X. Dai, H. Cai, M. Aguiló, F. Díaz, P. Camy, Y. Wang, U. Griebner, V. Petrov, and X. Mateos; Growth, spectroscopy and laser operation of  $\text{Yb}^{3+}$ ,  $\text{Na}^+/\text{Li}^+$ -codoped CNGG-type garnets promising for ultrafast lasers; *SPIE Proc.* **11259** (2020) 1125911/1-6
- PMD20: C. Pellegrini, T. Müller, J. K. Dewhurst, S. Sharma, A. Sanna, and E. K. U. Gross; Density functional theory of magnetic dipolar interactions; *Phys. Rev. B* **101** (2020) 144401/1-10
- PVV20: S. Patchkovskii, M. J. J. Vrakking, D. M. Vileneuve, and H. Niikura; Selection of the magnetic quantum number in resonant ionization of neon using an XUV-IR two-color laser field; *J. Phys. B* **53** (2020) 134002/1-14
- RBI20a: D. Reiche, K. Busch, and F. Intravaia; Quantum thermodynamics of overdamped modes in local and spatially dispersive materials; *Phys. Rev. A* **101** (2020) 012506/1-22
- RBI20b: D. Reiche, K. Busch, and F. Intravaia; Nonadditive enhancement of nonequilibrium atom-surface interactions; *Phys. Rev. Lett.* **124** (2020) 193603/1-7
- RES20: M. Runge, D. Engel, M. Schneider, K. Reimann, M. Woerner, and T. Elsaesser; Spatial distribution of electric-field enhancement across the gap of terahertz bow-tie antennas; *Opt. Express* **28** (2020) 24389-24398
- RFA20: D. Rupp, L. Flückiger, M. Adolph, A. Colombo, T. Gorkhover, M. Harmand, M. Krikunova, J. P. Müller, T. Oelze, Y. Ovcharenko, M. Richter, M. Sauppe, S. Schorb, R. Treusch, D. Wolter, C. Bostedt, and T. Möller; Imaging plasma formation in isolated nanoparticles with ultrafast resonant scattering; *Struct. Dyn.* **7** (2020) 034303/1-10
- RFi20: M. Richter and B. P. Fingerhut; Regulatory impact of the C-terminal tail on charge transfer pathways in drosophila cryptochrome; *Molecules* **25** (2020) 4810/1-14
- RGM20: J. Ruschel, J. Glaab, F. Mahler, T. Kolbe, S. Einfeldt, and J. W. Tomm; In-situ spectroscopic analysis of the recombination kinetics in UVB LEDs during their operation; *Appl. Phys. Lett.* **117** (2020) 121104/1-5

- RGW20: K. Reimann, A. Ghalgaoui, M. Woerner, T. Elsaesser, C. Flytzanis, and K. Biermann; Blueshift of the TO phonon resonance in GaAs by femtosecond electron-hole excitation; in *The 22nd International Conference on Ultrafast Phenomena 2020*, F. Kärtner, M. Khalil, R. Li, F. Légaré, and T. Tahara (eds.) (OSA Publishing, Washington, D.C., USA, 2020); doi.org/10.1364/UP.2020.Tu3B.3
- RHD20: G. Reitsma, J. Hummert, J. Dura, V. Loriot, M. J. J. Vrakking, F. Lépine, and O. Kornilov; Delayed relaxation of highly excited naphthalene cations; *J. Phys. Conf. Ser.* **1412** (2020) 072044/1-2
- RIH20: D. Reiche, F. Intravaia, J.-T. Hsiang, K. Busch, and B. L. Hu; Nonequilibrium thermodynamics of quantum friction; *Phys. Rev. A* **102** (2020) 050203(R)/1-7
- RLM20: M. Richter, M. Lytova, F. Morales, S. Haessler, O. Smirnova, M. Spanner, and M. Ivanov; Rotational quantum beat lasing without inversion; *Optica* **7** (2020) 586-592
- RTP20: P. Reséndiz-Vázquez, K. Tschernig, A. Pérez-Leija, K. Busch, and R. de J. León-Montiel; Topological protection in non-Hermitian Haldane honeycomb lattices; *Phys. Rev. Res.* **2** (2020) 013387/1-7
- SBS20: F. Schell, T. Bredtmann, C.-P. Schulz, M. J. J. Vrakking, S. Patchkovskii, and J. Mikosch; Separation of strong-field ionization continua in laser-driven electron rescattering in the molecular frame; in *Proceedings of the 6th international conference on Attosecond Physics*, Wei, Z. ed., Springer proceedings in Physics Series 220 (Springer, Singapore, 2020)
- SED20: N. Singh, P. Elliott, J. K. Dewhurst, E. K. U. Gross, and S. Sharma; Ab-initio real-time magnon dynamics in ferromagnetic and ferrimagnetic systems; *Phys. Status Solidi B* **257** (2020) 1900654/1-9
- SEG20: H. Stiel, D. Engel, L. Glöggler, A. Jonas, I. Mantouvalou, and J. Tümmler; Time-resolved near-edge x-ray absorption spectroscopy in the water window and beyond using laboratory-based laser plasma sources; in *X-Ray Lasers 2018, Proceedings of the 16th International Conference on X-Ray Lasers*, M. Kozlová and J. Nejdil (eds.) (Springer, Heidelberg, 2020) 147-154
- SER20: L. Shi, A. B. Evlyukhin, C. Reinhardt, I. Babushkin, V. A. Zenin, S. Burger, R. Malureanu, B. N. Chichkov, U. Morgner, and M. Kovacev; Progressive self-boosting anapole-enhanced deep-ultraviolet third harmonic during few-cycle laser radiation; *ACS Photonics* **7** (2020) 1655-1661
- SKH20: B. Senfftleben, M. Kretschmar, A. Hoffmann, M. Sauppe, J. Tümmler, I. Will, T. Nagy, M. J. J. Vrakking, D. Rupp, and B. Schütte; Highly nonlinear ionization of atoms induced by intense high-harmonic pulses; *J. Phys. Photon.* **2** (2020) 034001/1-12
- SLS20: K. Subbotin, P. Loiko, S. Slimi, A. Volokitina, A. Titov, D. Lis, E. Chernova, S. Kuznetsov, R. M. Solé, U. Griebner, V. Petrov, M. Aguiló, F. Díaz, P. Camy, E. Zharikov, and X. Mateos; Monoclinic zinc monotonigstate Yb<sup>3+</sup>,Li<sup>+</sup>:ZnWO<sub>4</sub>: Part I. Czochralski growth, structure refinement and Raman spectra; *J. Lumin.* **228** (2020) 117601/1-12
- SPG20a: M. Schneider, B. Pfau, C. M. Günther, C. von Korff Schmising, D. Weder, J. Geilhufe, J. Perron, F. Capotondi, E. Pedersoli, M. Manfredda, M. Hennecke, B. Vodungbo, J. Lüning, and S. Eisebitt; Ultrafast demagnetization dominates fluence dependence of magnetic scattering at Co M edges; *Phys. Rev. Lett.* **124** (2020) 127201/1-5
- SPG20b: P. Satapathy, A. Pfuch, R. Grunwald, and S. K. Das; Enhancement of photocatalytic activity by femtosecond-laser induced periodic surface structures of Si; *J. Semicond.* **41** (2020) 032303/1-6
- SPM20: P. Stammer, S. Patchkovskii, and F. Morales; Evidence of ac-Stark-shifted resonances in intense two-color circularly polarized laser fields; *Phys. Rev. A* **101** (2020) 033405/1-8
- Sta20: P. Stammer; State distinguishability under weak measurement and postselection: A unified system and device perspective; *Phys. Rev. A* **102** (2020) 062206/1-11
- SWG20: D. Steil, J. Walowski, F. Gerhard, T. Kiessling, D. Ebke, A. Thomas, T. Kubota, M. Oogane, Y. Ando, J. Otto, A. Mann, M. Hofherr, P. Elliott, J. K. Dewhurst, G. Reiss, L. Molenkamp, M. Aeschlimann, M. Cinchetti, M. Münzenberg, S. Sharma, and S. Mathias; Efficiency of ultrafast optically induced spin transfer in Heusler compounds; *Phys. Rev. Res.* **2** (2020) 023199/1-8
- TFG20: C. Tserkezis, A. I. Fernandez-Dominguez, P. A. D. Gonçalves, F. Todisco, J. D. Cox, K. Busch, N. Stenger, S. I. Bozhevolnyi, N. A. Mortensen, and C. Wolff; On the applicability of quantum-optical concepts in strong-coupling nanophotonics; *Rep. Prog. Phys.* **83** (2020) 082401/1-10
- TJA20: R. Trebino, R. Jafari, S. A. Akturk, P. Bowlan, Z. Guang, P. Zhu, E. Escoto, and G. Steinmeyer; Highly reliable measurement of ultrashort laser pulses; *J. Appl. Phys.* **128** (2020) 171103/1-43
- TJB20: V. Tamulienė, G. Juškevičiūtė, D. Buožius, V. Vaičaitis, I. Babushkin, and U. Morgner; Influence of tunnel ionization to third-harmonic generation of infrared femtosecond laser pulses in air; *Sci. Rep.* **10** (2020) 17437/1-12
- TKS20: E. Travkin, T. Kiel, S. Sadofev, S. Kalusniak, K. Busch, and O. Benson; Dispersion control in a near-infrared subwavelength resonator with a tailored hyperbolic metamaterial; *Opt. Lett.* **45** (2020) 3665-3668
- TLP20: K. Tschernig, R. de J. León-Montiel, A. Pérez-Leija, and K. Busch; Multiphoton synthetic lattices in multiphoton waveguide arrays: synthetic atoms and Fock graphs; *Photonics Res.* **8** (2020) 1161-1170

- TSS20: C. Tailliez, A. Stathopoulos, S. Skupin, D. Buožius, I. Babushkin, V. Vaičiaitis, and L. Bergé; Terahertz pulse generation by two-color laser fields with circular polarization; *New J. Phys.* **22** (2020) 103038/1-18
- TTK20: V. Talalaev, J. W. Tomm, S. A. Kukushkin, A. V. Osipov, I. Shtrom, K. Kotlyar, F. Mahler, J. Schilling, R. Reznik, and G. E. Cirlin; Ascending Si diffusion into growing GaN nanowires from the SiC/Si substrate: up to the solubility limit and beyond; *Nanotechnology* **31** (2020) 294003/1-8
- TZH20: F. Tuitje, M. Zürch, T. Helk, J. Gautier, F. Tissandier, J.-P. Goddet, E. Oliva, A. Guggenmos, U. Kleineberg, H. Stiel, S. Sebban, and C. Spielmann; Ptychography and single-shot nanoscale imaging with plasma-based laser sources; in *X-Ray Lasers 2018, Proceedings of the 16th International Conference on X-Ray Lasers*, M. Kozlová and J. Nejdls eds. (Springer, Heidelberg, 2020) 155-162
- UOJ20: A. J. Uzan, G. Orenstein, Á. Jiménez-Galán, C. McDonald, R. E. F. Silva, B. D. Bruner, N. D. Klimkin, V. Blanchet, T. Arusi-Parpar, M. Krüger, A. N. Rubtsov, O. Smirnova, M. Ivanov, B. Yan, T. Brabec, and N. Dudovich; Attosecond spectral singularities in solid-state high-harmonic generation; *Nat. Photonics* **14** (2020) 183-187
- USP20: A. J. Uzan, H. Soifer, O. Pedatzur, A. Clergerie, S. Larroque, B. D. Bruner, B. Pons, M. Ivanov, O. Smirnova, and N. Dudovich; Spatial molecular interferometry via multidimensional high-harmonic spectroscopy; *Nat. Photonics* **14** (2020) 188-194
- VBu20: P. Varytis and K. Busch; Negative asymmetry parameter in plasmonic core-shell nanoparticles; *Opt. Express* **28** (2020) 1714-1721
- VLP20a: A. Volokitina, P. Loiko, A. Pavlyuk, S. Slimi, R. M. Solé, E. Ben Salem, E. Kifle, J. M. Serres, U. Griebner, V. Petrov, M. Aguiló, F. Díaz, and X. Mateos; Laser operation of cleaved single-crystal plates and films of Tm:KY(MoO<sub>4</sub>)<sub>2</sub>; *Opt. Express* **28** (2020) 9039-9048
- VLP20b: A. Volokitina, P. Loiko, A. Pavlyuk, J. M. Serres, S. Slimi, E. Ben Salem, E. Kifle, U. Griebner, V. Petrov, L. Wang, W. Chen, R. M. Solé, M. Aguiló, F. Díaz, and X. Mateos; Spectroscopy and efficient laser operation of cleaving Yb:KY(MoO<sub>4</sub>)<sub>2</sub> crystal; *Opt. Mater. Express* **10** (2020) 2356-2369
- VLP20c: A. Volokitina, P. Loiko, A. Pavlyuk, J. M. Serres, S. Slimi, E. Ben Salem, R. M. Solé, M. Baranov, E. Kifle, M. Aguiló, F. Díaz, U. Griebner, V. Petrov, and X. Mateos; Efficient laser operation in cleaved single-crystal plates of Yb:KY(MoO<sub>4</sub>)<sub>2</sub>: a novel molybdate compound; *SPIE Proc.* **11357** (2020) 113571T/1-7
- WCZ20: L. Wang, W. Chen, Y. Zhao, Y. Wang, Z. Pan, H. Lin, G. Zhang, L. Zhang, Z. Lin, J. E. Bae, T. G. Park, F. Rotermund, P. Loiko, X. Mateos, M. Mero, U. Griebner, and V. Petrov; Single-walled carbon-nanotube saturable absorber assisted Kerr-lens mode-locked Tm:MgWO<sub>4</sub> laser; *Opt. Lett.* **45** (2020) 6142-6145
- WFK20: T. Witting, F. J. Furch, O. Kornilov, M. Osolodkov, C. P. Schulz, and M. J. J. Vrakking; Retrieval of attosecond pulse ensembles from streaking experiments using mixed state time-domain ptychography; *J. Phys. B* **53** (2020) 194001/1-8
- WKG20: D. Weder, C. von Korff Schmising, C. M. Günther, M. Schneider, D. Engel, P. Hessian, C. Strüber, M. Weigand, B. Vodungbo, E. Jal, X. Liu, A. Merhe, E. Pedersoli, F. Capotondi, J. Lüning, B. Pfau, and S. Eisebitt; Transient magnetic gratings on the nanometer scale; *Struct. Dyn.* **7** (2020) 054501/1-13
- WKS20: F. Willems, C. von Korff Schmising, C. Strüber, D. Schick, D. W. Engel, J. K. Dewhurst, P. Elliott, S. Sharma, and S. Eisebitt; Optical inter-site spin transfer probed by energy and spin-resolved transient absorption spectroscopy; *Nat. Comm.* **11** (2020) 871/1-7
- WKW20: A. Wituschek, O. Kornilov, T. Witting, L. Mai-kowski, F. Stienkemeier, M. J. J. Vrakking, and L. Bruder; Phase cycling of extreme ultraviolet pulse sequences generated in rare gases; *New J. Phys.* **22** (2020) 092001/1-10
- WPW20: K. Wang, A. Perez-Leija, S. Weimann, and A. Szameit; Non-adiabatic dynamic-phase-free geometric phase in multiport photonic lattices; *J. Opt.* **22** (2020) 035801/1-7
- WZP20: Y. Wang, Y. Zhao, Z. Pan, S. Suomalainen, A. Härkönen, M. Guina, U. Griebner, L. Wang, P. Loiko, X. Mateos, W. Chen, and V. Petrov; 73-fs SESAM mode-locked Tm:Ho:CNGG laser at 2061 nm; *SPIE Proc.* **11259** (2020) 1125929/1-6
- YLC20: F. Yue, P. Loiko, M. Chen, J. M. Serres, Y. Wang, J. Li, L. Basyrova, E. Dunina, A. Kornienko, L. Fomicheva, S. Dai, Z. Chen, J. E. Bae, T. G. Park, F. Rotermund, V. Jambunathan, A. Lucianetti, T. Mocek, M. Aguiló, F. Díaz, U. Griebner, V. Petrov, and X. Mateos; Spectroscopy and diode-pumped laser operation of transparent Tm:Lu<sub>3</sub>Al<sub>5</sub>O<sub>12</sub> ceramics produced by solid-state sintering; *Opt. Express* **28** (2020) 28399-28413
- YQL20: C. You, M. A. Quiroz-Juárez, A. Lambert, N. Bhusal, C. Dong, A. Perez-Leija, A. Javaid, R. de J. León-Montiel, and O. S. Magaña-Loaiza; Identification of light sources using machine learning; *Appl. Phys. Rev.* **7** (2020) 021404/1-10
- YWK20a: K. Yao, F. Willems, C. von Korff Schmising, I. Radu, C. Strueber, D. Schick, D. Engel, A. Tsukamoto, J. K. Dewhurst, S. Sharma, and S. Eisebitt; Distinct spectral response in M-edge magnetic circular dichroism; *Phys. Rev. B* **102** (2020) 100405R/1-6
- YWK20b: K. Yao, F. Willems, C. v. Korff Schmising, C. Strüber, P. Hessian, B. Pfau, D. Schick, D. Engel, K. Gerlinger, M. Schneider, and S. Eisebitt; A tabletop set-up for ultrafast helicity-dependent and element-specific absorption spectroscopy and scattering in the extreme ultraviolet spectral range; *Rev. Sci. Instrum.* **91** (2020) 093001/1-9

ZWC20a: Y. Zhao, L. Wang, W. Chen, J. Wang, Q. Song, X. Xu, Y. Liu, D. Shen, J. Xu, X. Mateos, P. Loiko, Z. Wang, X. Xu, U. Griebner, and V. Petrov; 35 W continuous-wave Ho:YAG single-crystal fiber laser; High Power Laser Sci. **8** (2020) e25/1-5

ZWC20b: Y. Zhao, L. Wang, W. Chen, Z. Pan, Y. Wang, P. Liu, X. Xu, Y. Liu, D. Shen, J. Zhang, M. Guina, X. Mateos, P. Loiko, Z. Wang, X. Xu, J. Xu, M. Mero, U. Griebner, and V. Petrov; SESAM mode-locked Tm:LuYO<sub>3</sub> ceramic laser generating 54-fs pulses at 2048 nm; Appl. Opt. **59** (2020) 10493-10497

ZWW20: Y. Zhao, L. Wang, Y. Wang, J. Zhang, P. Liu, X. Xu, Y. Liu, D. Shen, J. E. Bae, T. G. Park, F. Rotermund, X. Mateos, P. Loiko, Z. Wang, X. Xu, J. Xu, M. Mero, U. Griebner, V. Petrov, and W. Chen; SWCNT-SA mode-locked Tm:LuYO<sub>3</sub> ceramic laser delivering 8-optical-cycle pulses at 2.05  $\mu\text{m}$ ; Opt. Lett. **45** (2020) 459-462

### in press

JM: D. R. Austin, A. S. Johnson, F. McGrath, D. Wood, L. Miseikis, T. Siegel, P. Hawkins, A. Harvey, Z. Mašín, S. Patchkovskii, M. Vacher, J. P. Malhado, M. Y. Ivanov, O. Smirnova, and J. P. Ma-rangos; Extracting sub-cycle electronic and nuclear dynamics from high harmonic spectra; Sci. Rep.

BLM: L. Basyrova, P. Loiko, R. Maksimov, V. Shitov, J. M. Serres, U. Griebner, V. Petrov, M. Aguiló, F. Díaz, and X. Mateos; Comparative study of Yb:Lu<sub>3</sub>Al<sub>5</sub>O<sub>12</sub> and Yb:Lu<sub>2</sub>O<sub>3</sub> laser ceramics produced from laser-ablated nanopowders; Ceram. Int.

BPB: F. Büttner, B. Pfau, M. Böttcher, M. Schneider, G. Mercurio, C. M. Günther, P. Hessian, C. Klose, A. Wittmann, K. Gerlinger, L.-M. Kern, C. Strüber, von Korff Schmising, C., J. Fuchs, D. Engel, A. Churikova, S. Huang, D. Suzuki, I. Lemesh, M. Huang, L. Caretta, D. Weder, S. Zayko, K. Bagschik, R. Carley, L. Mercadier, J. Schlappa, A. Yaroslavtsev, L. Le Guyarder, N. Gerasimova, A. Scherz, C. Deiter, R. Gort, D. Hickin, J. Zhu, M. Turcato, D. Lomidze, F. Erdinger, A. Castoldi, S. Maffesanti, M. Porro, A. Samartsev, M. Kuster, C. Ropers, J. Sinova, J. H. Mentink, B. Dupé, G. S. D. Beach, and S. Eisebitt; Observation of fluctuation-mediated picosecond nucleation of a topological phase; Nat. Materials

CWB: M.-A. Codescu, M. Weiß, M. Brehm, O. Kornilov, D. Sebastiani, and E. T. J. Nibbering; Switching between proton vacancy and excess proton transfer pathways in the reaction between 7-hydroxyquinoline and formate; J. Phys. Chem. A

DKW: L. Drescher, O. Kornilov, T. Witting, V. Shokeen, M. J. J. Vrakking, and B. Schütte; Extreme-ultraviolet spectral compression by four-wave mixing; Nat. Photon.

EDS: E. Escoto, A. Demircan, and G. Steinmeyer; Cage Solitons; IEEE J. Quantum Electron.

EEM: R. Y. Engel, M. Ekimova, P. S. Miedema, C. Kleine, J. Ludwig, M. Ochmann, B. Grimm-Lebsanft, R. Ma, M. Teubner, S. Dziarzhyski, G. Brenner, M.-K. Czwalińska, B. Rösner, T. Kyu Kim, C. David, S. Herres-Pawlis, M. Rübhausen, E. T. J. Nibbering, N. Huse, and M. Beye; Shot noise limited soft X-ray absorption spectroscopy in solution at a SASE-FEL using a transmission grating beam splitter; Struct. Dynam.

EMV: U. Elu, L. Maidment, L. Vamos, F. Tani, D. Novoa, M. H. Frosz, V. Badikov, D. Badikov, V. Petrov, P. St. J. Russell, and J. Biegert; Seven-octave high-brightness and carrier-envelope-phase-stable light source; Nat. Photon.

GDC: M. d. Goede, M. Dijkstra, L. Chang, N. Acharyya, G. Kozyreff, R. Obregón, E. Martínez, and S. M. García-Blanco; Mode-splitting in a microring resonator for self-referenced biosensing; Opt. Express

GFR: A. Ghalgaoui, B. P. Fingerhut, K. Reimann, T. Elsaesser, and M. Woerner; Terahertz polaron oscillations of electrons solvated in liquid water; Phys. Rev. Lett.

HWE: C. Hauf, M. Woerner, and T. Elsaesser; Femtosecond diffraction with laser-driven hard x-ray sources: Nuclear motions and transient charge densities; in *Structures on different time scales*, D. Schaniel, and T. Woike (eds.) (De Gruyter)

JSK: A. Jonas, S. Staack, B. Kanngießer, H. Stiel, and I. Mantouvalou; Laboratory quick near edge X-ray absorption fine structure spectroscopy in the soft X-ray range with 100 Hz frame rate; Rev. Sci. Instrum.

KHW: A. Koç, C. Hauf, M. Woerner, L. von Grafenstein, D. Ueberschaer, M. Bock, U. Griebner, and T. Elsaesser; Compact high-flux hard X-ray source driven by femtosecond mid-infrared pulses at a 1 kHz repetition rate; Opt. Lett.

KKK: M. Kliem, T. Kiel, M. Kück, S. Meister, A. Mischok, H. Fröb, K. Busch, and K. Leo; Defect-State lasing in photonic lattices of metal-organic microcavities; Adv. Photon. Res.

KLR: E. Kifle, P. Loiko, C. Romero, J. Rodríguez Vázquez de Aldana, V. Zakharov, Y. Gurova, A. Veniaminov, V. Petrov, U. Griebner, R. Thouroude, M. Laroche, P. Camy, M. Aguiló, F. Díaz, X. Mateos; Tm<sup>3+</sup> and Ho<sup>3+</sup> colasing in in-band pumped waveguides fabricated by femtosecond laser writing; Opt. Lett.

KMP: K. Kato, K. Miyata, and V. Petrov; Refined Sellmeier equations for AgGaSe<sub>2</sub> up to 18  $\mu\text{m}$ ; Appl. Opt.

KYP: E. T. Karamatskos, S. Yarlagadda, S. Patchkovskii, M. J. J. Vrakking, R. Welsch, J. Küpper, and A. Rouzée; Time-resolving the UV-initiated photodissociation dynamics of OCS; Faraday Disc.

LED: Q. Z. Li, P. Elliott, J. K. Dewhurst, S. Sharma, and S. Shallcross; Ab-initio study of ultrafast charge dynamics in graphene; Phys. Rev. B

- LKG: P. Loiko, E. Kifle, L. Guillemot, J.-L. Doualan, F. Starecki, A. Braud, M. Aguiló, F. Diaz, V. Petrov, X. Mateos, and P. Camy; Highly efficient 2.3  $\mu\text{m}$  thulium lasers based on a high-phonon-energy crystal: evidence of vibronic-assisted emissions; *J. Opt. Soc. Am. B*
- LPS: P. Loiko, A. Pavlyuk, S. Slimic, R. M. Solé, E. Ben Salem, E. Dunina, A. Kornienko, P. Camy, U. Griebner, V. Petrov, F. Díaz, M. Aguiló, and X. Mateos; Growth, spectroscopy and laser operation of monoclinic Nd:Cs-Gd(MoO<sub>4</sub>)<sub>2</sub> crystal with a layered structure; *J. Lumin.*
- MEV: L. Maidment, U. Elu, L. Vamos, T. Steinle, F. Haberstroh, V. Badikov, V. Petrov, and J. Biegert; Few-cycle mid-IR pulses by DFG in BaGa<sub>2</sub>GeSe<sub>6</sub>; *SPIE Proceedings Series*
- NLM: Z. Nie, F. Li, F. Morales, S. Patchkovskii, O. Smirnova, W. An, N. Nambu, D. Matteo, K. A. Marsh, F. Tsung, W. B. Mori, and C. Joshi; In-situ generation of high-energy spin-polarized electrons in a beam-driven plasma wakefield accelerator; *Phys. Rev. Lett.*
- NSV: T. Nagy, and P. Simon, L. Veisz; High-energy few-cycle pulses: post-compression techniques; *Adv. Phys. X* online
- OSm: A. F. Ordonez and O. Smirnova; Inducing enantiosensitive permanent multipoles in isotropic samples with two-color fields; in *Molecular Beams in Physics and Chemistry: From Otto Stern's Pioneering Exploits to Present-Day Feats*, B. Friedrich, and H. Schmidt-Böcking (eds.) (Springer)
- PLW: Z. Pan, P. Loiko, Y. Wang, Y. Zhao, H. Yuan, K. Tang, X. Dai, H. Cai, J. M. Serres, S. Slimi, E. B. Salem, E. Dunina, A. Kornienko, L. Fomicheva, J.-L. Doualan, P. Camy, W. Chen, U. Griebner, V. Petrov, M. Aguiló, F. Díaz, R. M. Solé, and X. Mateos; Disordered Tm<sup>3+</sup>, Ho<sup>3+</sup>-codoped CNGG garnet crystal: Towards efficient laser materials for ultrashort pulse generation at  $\sim 2 \mu\text{m}$ ; *J. Alloys Compd.*
- SKF: J. Schauss, A. Kundu, B. P. Fingerhut, and T. Elsaesser; Magnesium contact ions stabilize the tertiary structure of transfer RNA: electrostatics mapped by two-dimensional infrared spectra and theoretical simulations; *J. Phys. Chem. B* online
- SSM: P. Scheid, S. Sharma, G. Malinowski, S. Mangin, and S. Lebègue; Ab initio study of helicity dependent light induced demagnetization: from the optical regime to the XUVs; *Nano Lett.*
- SSN: D. Schick, F. Steinbach, T. Noll, C. Strueber, W. D. Engel, C. von Korff-Schmising, B. Pfau, and S. Eisebitt; High-speed spatial encoding of modulated pump-probe signals with slow area detectors; *Meas. Sci. Technol. Online*
- THI: E. Titov, H. Hummert, E. Ikonnikov, R. Mitrić, and O. Kornilov; Electronic relaxation of aqueous aminoazobenzenes studied by time-resolved photoelectron spectroscopy and surface hopping TDDFT dynamics calculations *Faraday Disc.*
- TMS: K. Tschernig, C. Müller, M. Smoor, T. Kroh, J. Wolters, O. Benson, K. Busch, and A. Perez-Leija; Direct observation of the particle exchange phase of photons; *Nat. Photon.*
- VDL: A. Volokitina, S. P. David, P. Loiko, K. Subbotin, A. Titov, D. Lis, R. M. Solé, V. Jambunathan, A. Lucianetti, T. Mocek, P. Camy, W. Chen, U. Griebner, V. Petrov, M. Aguiló, F. Díaz, and X. Mateos; Monoclinic zinc monocation state Yb<sup>3+</sup>, Li<sup>+</sup>:ZnWO<sub>4</sub>: Part II. Polarized spectroscopy and laser operation; *J. Lumin. online*
- WCS: L. Wang, W. Chen, P. Schunemann, A. Schirmacher, E. Büttner, A. A. Boyko, N. Ye, G. Zhang, Y. Zhao, V. Petrov; Nanosecond optical parametric oscillator with midinfrared intracavity difference-frequency mixing in orientation-patterned GaAs; *Opt. Lett.*
- ZWX: Y. Zhao, L. Wang, X. Xu, P. Loiko, X. Mateos, Z. Wang, X. Xu, D. Shen, W. Chen, U. Griebner, and V. Petrov; Structured laser beams: Towards 2-micron femtosecond laser vortices; *Photonics Res.*

## Submitted

AHR: R. M. Abrudan, M. Hennecke, F. Radu, T. Kachel, K. Holldack, R. Mitzner, A. Donges, S. Khmelevskiy, A. Deak, L. Szunyogh, U. Nowak, S. Eisebitt, and I. Radu; Element-specific magnetization damping in ferrimagnetic alloys revealed by ultrafast X-ray measurements; *Phys. Status Solidi-R*

AOD: D. Ayuso, A. Ordonez, P. Decleva, M. Ivanov, and O. Smirnova; Enantio-sensitive unidirectional light bending; *Nat. Comm.*

AOI: D. Ayuso, A. Ordonez, M. Ivanov, and O. Smirnova; Ultrafast optical rotation for extremely sensitive enantio-discrimination; *Phys. Rev. X*

BKS: M. Borchert, C. von Korff Schmising, D. Schick, D. Engel, S. Sharma, and S. Eisebitt; Manipulation of ultrafast demagnetization dynamics by optically induced intersite spin transfer in magnetic compounds with distinct density of states; *Phys. Rev. B*

EKL: M. Ekimova, C. Kleine, J. Ludwig, M. Ochmann, T. E. G. Agrenius, E. Kozari, E. Pines, N. Huse, P. Wernet, M. Odelius, and E. T. J. Nibbering; Covalent nature and hydration of the Zundel cation in solution; *Science*

HBM: D. Habibović, W. Becker, and D. B. Milošević; High-order harmonic generation by aligned heteronuclear diatomic molecules in an orthogonally polarized two-color field; *Eur. Phys. J. D*

HDJ: M. Hempel, S. Dadgostar, J. Jiménez, R. Kernke, A. Gollhardt, and J. W. Tomm; COD defect propagation in 450-nm emitting diode lasers at high emission powers controlled by artificially generated seed points; *IEEE J. Sel. Top. Quantum Electron.*

KEW: C Kleine, M. Ekimova, M.-O. Winghart, S. Eckert, O. Reichel, H. Löchel, J. Probst, C. Braig, C. Seifert, A. Erko, A. Sokolov, M. J. J. Vrakking, E. T. J. Nibbering, and A. Rouzée, Highly efficient soft x-ray spectrometer for transient absorption spectroscopy with broadband table-top high harmonic sources

KSP: E. Kozari, M. Sigalov, D. Pines, B. P. Fingerhut, and E. Pines; Infrared and NMR spectroscopic fingerprints of the asymmetric  $H_7^+O_3$  complex in solution; ChemPhysChem

LXH: M. Q. Liu, S. P. Xu, S. L. Hu, W. Becker, W. Quan, X. J. Liu, and J. Chen; Unified perspective of Rydberg-state excitation and low-energy above-threshold ionization in an intense laser field; Phys. Rev. Lett.

OSma: A. F. Ordonez and O. Smirnova; Disentangling enantiosensitivity from dichroism using bichromatic fields; Phys. Rev. A

OSmb: A. F. Ordonez and O. Smirnova; On the molecular information revealed by photoelectron angular distributions of isotropic samples; Phys. Rev. A

PSY: S. Pal, N. Strkalj, C.-J. Yang, M. C. Weber, M. Trassin, M. Woerner, and M. Fiebig; The origin of terahertz soft-mode nonlinearities in ferroelectric perovskites; Phys. Rev. X

RWE: K. Reimann, M. Woerner, T. Elsaesser; Two-dimensional terahertz spectroscopy of condensed-phase molecular systems; J. Chem. Phys.

SKB: S. Staeck, Y. Kayser, J. Baumann, A. Jonas, I. Mantouvalou, R. Hartmann, B. Kanngießner, and H. Stiel; Towards soft x-ray fluorescence measurements in the laboratory using a laser-produced plasma source and a complementary metal-oxide semiconductor detector; J. Instrum.

TJC: K. Tschernig, Á. Jiménez-Galán, D. N. Christodoulides, M. Y. Ivanov, K. Busch, M. A. Bandres, and A. Pérez-Leija; Two-photon edge states in photonic topological insulators: topological protection versus entanglement; Nat. Comm.

WGR: M. Woerner, A. Ghalgaoui, K. Reimann, and T. Elsaesser; Two-color two-dimensional terahertz spectroscopy: A new approach for exploring even-order nonlinearities in the nonperturbative regime; J. Chem. Phys.

ZJW: D. Zahn, F. Jakobs, Y. W. Windsor, H. Seiler, T. Vasileiadis, T. A. Butcher, Y. Qi, D. Engel, U. Atxitia, J. Vorberger, and R. Ernstorfer; Lattice dynamics and ultrafast energy flow between electrons, spins, and phonons in a 3d ferromagnet; Phys. Rev. Research

## General Publications

Smi20a: O. Smirnova; On-chip tunnel management; Nat. Phys. **16** (2020) 241-242

Smi20b: O. Smirnova; Nasca patterning in the microworld; Nat. Photonics **14** (2020) 527-528

## Master and PhD Theses

### Master Theses

Lie20: M. Liebmann; *Highly resolved analysis regarding the spatial statistical behaviour of spectral anomalies in fs-pulsed vortex beams* (Supervisor: S. Schrader and R. Grunwald), Technische Hochschule Wildau, 2020-02

Ste20: F. Steinbach; *All-optical switching with structured illumination* (Supervisor: S. Eisebitt), Technische Universität Berlin, 2020-01

Kol20: L.-M. Koll; *Two-dimensional time-resolved nonlinear THz spectroscopy* (Supervisor: T. Elsaesser), Humboldt-Universität zu Berlin, 2020-03

Run20: M. Runge; *Imaging of electric-field enhancement in resonant terahertz antennas* (Supervisor: T. Elsaesser), Humboldt-Universität zu Berlin, 2020-04

Küc20: M. Kück; *Tailoring the correlation of path-entangled two-photon states* (Supervisor: A. Pérez-Leija and K. Busch), Humboldt-Universität zu Berlin, 2020-12

Mer20: L. Mertenskötter; *Entangled-Photon absorption spectroscopy with varying pump wavelength* (Supervisor: A. Pérez-Leija and K. Busch), Humboldt-Universität zu Berlin, 2020-11

Sch20: M. Schilling; *Digital quantum simulation of bosons* (Supervisor: A. Pérez-Leija and K. Busch), Humboldt-Universität zu Berlin, 2020-06

Sta20: P. Stammer; *Weak measurement in strong field physics* (Supervisor: O. Smirnova), Technische Universität Berlin, 2020-

### PhD theses

Dre20: L. Drescher; *Transient dipole-interactions on sub-cycle timescales* (Supervisor: J. Mikosch and M. Vrakking), Freie Universität Berlin, 2020-04

Esc20: E. Escoto; *Regularization strategies for advanced laser pulse shape reconstruction* (Supervisor: G. Steinmeyer), Humboldt-Universität Berlin, 2020-02

Jue20: P. Juergens; *Strong-field induced plasma formation in solid dielectrics* (Supervisor: M. Vrakking and T. Baumert), Freie Universität Berlin, 2020-12

Hen20: M. Hennecke; *Ultrafast spin dynamics of a ferromagnet revealed by femtosecond soft X-ray and XUV radiation* (Supervisor: S. Eisebitt), Technische Universität Berlin, 2020-08

Kho20: N. Khodakovskiy; *Methods of ultra-fast laser contrast diagnostics and optimization* (Supervisor: M. Vrakking, and M. Kalashnikov), Freie Universität Berlin

Oel20: M. Oelschläger; *Theory of Fluctuation-induced Phenomena in Nanophotonic Systems* (Supervisor: K. Busch), Humboldt-Universität zu Berlin, 2020-03

Raa20: N. Raabe; *Fundamental carrier-envelope phase noise limitations during pulse formation and detection* (Supervisor: M. Vrakking and G. Steinmeyer), Freie Universität Berlin, 2020-01

Sau20: M. Sauppe; *Zeitaufgelöste Dynamik von Clustern in intensiven extrem ultravioletten Doppelpulsen* (Supervisor: D. Rupp, T. Möller, and B. von Issendorff), Technische Universität Berlin, 2020-11

Sch20: F. Schell; *Sub-femtosecond processes in molecules studied by coincidence spectroscopy* (Supervisor: C. P. Schulz and M. Vrakking), Freie Universität Berlin, 2020-09  
Kho20: N. Khodakovskiy; *Methods of ultra-fast laser contrast diagnostics and optimization* (Supervisor: M. Vrakking, and M. Kalashnikov), Freie Universität Berlin

## Appendix 2

### External Talks, Teaching

#### Invited talks at conferences

W. Becker; Quantum Battles in Attoscience 2020 (University College London, United Kingdom, 2020-07): *The strong-field approximation: strengths and shortcomings*

K. Busch together with A. Perez-Leija, and K. Tschernig; SPIE Nanoscience + Engineering, 2020 (San Diego, USA, 2020-08): *Multiphoton dynamics in tight-binding lattices: From fundamental physics to applied quantum photonics*

K. Busch; METANANO 2020, V International Conference on Metamaterials and Nanophotonics (Tbilisi, Georgia, 2020-09): *Multiphoton dynamics in tight-binding lattices*

U. Eichmann; 11th Ringberg Workshop on Science with FELs (Schloss Ringberg, 2020-02): *Neutral metastable atom de-tection: a new route to study nonlinear X-ray photon processes*

S. Eisebitt; Euroscience Open Forum 2020 (Triest, Italy, 2020-09): *Filming electrons in motion: magnetic data stor-age*

S. Eisebitt; European XFEL Science Seminar (DESY, Hamburg, Germany, 2020-12): *Topological phase transitions and nonlinear interaction of X-Rays with matter*

P. Elliott; Ultrafast Webinar Summer Series 2020 (USA, 2020-08): *Ultrafast Spin Excitation in 2d Materials*

T. Elsaesser; 55th Winter Seminar: Biophysical Chemistry, Molecular Biology and Cybernetics of Cell Functions (Klosters, Switzerland, 2020-01): *Electric interactions of hydrated DNA and RNA probed by femtosecond vibrational spectroscopy*

T. Elsaesser; Ultrafast Phenomena in Cooperative Systems (GRS) 2020 (Lucca (Barga), Italy, 2020-02): *High field interactions - discussion leader*

T. Fennel; CMD 2020 GEFES, Joint conference of the condensed matter divisions of EPS CMD and RSEF GEFES, (Madrid, Spain, 2020-01): *Origin of strong-field-induced low-order harmonic generation in amorphous quartz*

B. P. Fingerhut; Modelling Photoinduced Processes in Molecular Systems (MPPM) (Imperial College London, UK, 2020-02): *Emergent coherent dynamics in the relaxation of photo-excited molecules*

B. P. Fingerhut together with A. Kundu, J. Schauss, and T. Elsaesser; Ultrafast Phenomena XXII (Shanghai, China, 2020-11): *Impact of RNA melting on hydrating water structure mapped by femtosecond 2D-IR spectroscopy*

F. J. Furch together with T. Witting, M. Osolodkov, F. Schell, C. P. Schulz, and M. J. J. Vrakking; OSA High-brightness Sources and Light-driven Interactions Congress (Prague, Czech Republic, 2020-11): *High repetition rate OPCPA driving an attosecond pump-probe beamline*

U. Griebner together with W. Chen, Y. Zhao, F. Roter-mund, X. Mateos, P. Loiko, and V. Petrov; 19th International Conference Laser Optics - ICLO 2020 (St. Petersburg, Russia, 2020-11): *1D and 2D carbon nano-structures for solid-state laser mode-locking in the 2- $\mu$ m spectral range and beyond*

U. Griebner together with L. v. Grafenstein, M. Bock, A. Koç, C. Hauf, M. Woerner, K. Zawilski, P. Schunemann, and T. Elsaesser; OSA High-brightness Sources and Light-driven Interactions Congress (Prague, Czech Republic, 2020-11): *Midwave-infrared OPCPA driver for femtosecond hard X-ray generation at a 1 kHz repetition rate*

M. Y. Ivanov; QUTIF Annual Meeting (Berlin, Germany, 2020-02): *The matter of Kramers and Henneberger*

Á. Jiménez-Galán; CLEO 2020 (Washington D.C., USA, 2020-05): *Lightwave topology for strong-field valleytronics*

Á. Jiménez-Galán; OSA High-brightness Sources and Light-driven Interactions Congress (Prague, Czech Republic, 2020-11): *Topological physics in strong light fields: From imaging to controlling topology*

M. Khokhlova together with G. S. J. Armstrong, M. Lab-eye, A. S. Maxwell, E. Pisanty, and M. Ruberti; Quantum Battles in Attoscience 2020 (University College London, United Kingdom, 2020-07): *Quantum Battle 3 – Numerical vs Analytical*

O. Kornilov; ATTOCHEM COST meeting (2020-08): *Relaxation at complex resonances studied by wave-length-selected XUV pulses*

A. Mermillod-Blondin together with F. J. Furch, W. D. Engel, T. Witting, and M. J. J. Vrakking; Photonics West 2020, Laser-based Micro- and Nanoprocessing XIV (2020-02): *Photoinscription of optical microstructures in fused silica with few-cycle pulses*

M. Mero together with Z. Heiner, and V. Petrov; SPIE Photonics West 2020 (San Francisco, USA, 2020-02): *Progress in ultrafast mid-infrared optical parametric chirped pulse amplifiers pumped at 1 $\mu$ m*

- M. Mero together with V. Petrov, and Z. Heiner; 22nd Photonics North conference (Quebec, Canada, 2020-05): *Towards 100 W average power few-cycle optical parametric amplifiers in the mid-infrared*
- M. Mero; 19th International Conference Laser Optics, ICLO 2020, virtual (St. Petersburg, Russia, 2020-11): *A high-average-power, 1.5/3.2- $\mu$ m OPCPA driver for a high-flux soft x-ray beamline and attosecond strong-field spectroscopy*
- T. Nagy together with S. Hädrich, P. Simon, A. Blumenstein, N. Walthers, R. Klas, J. Buldt, H. Stark, S. Breikopf, P. Jójárt, I. Seres, Z. Várallyay, T. Eidam, and J. Limpert; CLEO 2020 (Washington D.C., USA, 2020-05): *Pulse compression to 3-cycle duration beyond 300 W average power*
- V. Petrov together with V. V. Badikov, D. V. Badikov, G. S. Shevyrdyaeva, K. Kato, K. Miyata, K. V. Mitin, L. Wang, V. Panyutin; MICS Mid-Infrared Coherent Sources 2020 (Washington D.C., USA, 2020-11): *Barium nonlinear optical crystals for the mid-IR: Characterization and applications*
- B. Pfau; 2020 European XFEL Users' Meeting (Hamburg, Germany, 2020-01): *Nucleation dynamics of skyrmion lattice from magnetic fluctuations phase*
- B. Pfau; PETRA IV workshop "Earth, Environment, and Materials for Nanoscience and Information Technology" (DESY Hamburg, Germany, 2020-11): *Coherent magnetic imaging*
- M. Richter together with M. Lytova, F. Morales, S. Haessler, O. Smirnova, M. Spanner, and M. Y. Ivanov; 20th International Conference Foundations & Advances in Nonlinear Science and 5th International Symposium Advances in Nonlinear Photonics, FANS & ANPh (Minsk, Belarus, 2020-09): *Rotational quantum beat lasing without inversion*
- B. Schütte; EAS - Extreme Atomic Systems Meeting (Riezlern, Österreich, 2020-01): *XUV spectral compression by four-wave mixing*
- S. Shallcross; International Psi-K Workshop, Correlated synthetic quantum matter: theory meets experiment (Bremen, Germany, 2020-02): *Twist and stacking faults in graphene like systems*
- S. Sharma; 710. WE-Heraeus-Seminar, Spin Transport in Complex Magnetic Structures (Bad Honnef, Germany, 2020-01): *Ultrafast spin dynamics: TDDFT's killer app*
- S. Sharma; Ultrafast Webinar Summer Series 2020 (Harvard, MPI-Hamburg and Arizona University, 2020-08): *Ultrafast Laser Induced Spin and Charge Dynamics*
- S. Sharma; Vaishwik Bharatiya Vaigyanik (VAIBHAV) Summit (India, 2020-10): *Ultrafast spin and charge dynamics: ab-initio description*
- S. Sharma; JEMS The Joint European Magnetic Symposia 2020 (Lisbon, Portugal, 2020-12): *Ultrafast spin and charge dynamics: ab-initio description*
- O. Smirnova; 2020 ACS Fall National Virtual Meeting and Exposition (San Francisco, CA, USA, 2020-08): *Synthetic chiral light for controlling ultrafast chiral dynamics (Award talk)*
- O. Smirnova; 1st Annual Workshop & Joint WG meeting of CA18222 COST Action (Faculty of Physics, Babeş-Bolyai University, Romania, 2020-09): *Efficient chiral light matter interaction: challenges and opportunities*
- G. Steinmeyer; 5th Int. Symposium - Advances in Nonlinear Photonics (Minsk, Belarus, 2020-09): *Cage solitons*
- H. Stiel; 17. International Conference on X-Ray Lasers 2020 (ICXRL) (EMPA, Dübendorf, Switzerland, 2020-12): *Ultrafast NEXAFS spectroscopy in the lab using laser-based sources and advanced X-ray optics*
- M. J. J. Vrakking; CLEO 2020 (Washington D.C., USA, 2020-05): *Attosecond science using high average power and high peak power optical parametric chirped pulse amplifiers*
- M. J. J. Vrakking; Quantum Battles in Attoscience 2020 (University College London, United Kingdom, 2020-07): *Attosecond entanglement and coherence*
- M. J. J. Vrakking; SMART-X EU Marie Curie international training network, kick-off meeting (2020-07): *ITNs – tips, pitfalls and other experiences*
- M. J. J. Vrakking; The European Research Council (ERC) – Webinar for Starting and Consolidator Grants (EU Office of Charité, Berlin, 2020-10): *Testimonial of an ERC panel member*
- F. Willems; Photonics Europe 2020 - Digital Forum (Strasbourg, France, 2020-04): *Optically induced spin-transfer probed by energy and spin-resolved transient absorption spectroscopy*

## Invited external talks at seminars and colloquia

- B. P. Fingerhut, Kolloquium (Physikalische Chemie und Theoretische Chemie, TU München, Germany, 2020-02): *Emergent coherent dynamics in the relaxation of photo-excited molecules*
- B. P. Fingerhut, Symposium "Modelling Photoinduced Processes in Molecular System" (Thomas Young Centre, London, UK, 2020-02)
- R. Grunwald, together with M. Liebmann, A. Treffer, and M. Bock; Seminar (Friedrich-Schiller-Universität Jena, Germany, 2020-02): *Ultrafast Optics at Max-Born-Institute*
- M. Ivanov, Moscow State University, Institute of Quantum Electronics colloquium, (Moscow, Russia, 2020-05) *Ultrafast Strong Field Physics in Topological Systems*

- M. Ivanov, QUOLS seminar, Imperial College London (London, UK, 2020-05) *Towards optically-driven topological electronics in two-dimensional materials*
- M. Ivanov, MURI-MIR annual meeting (Washington DC, USA, 2020-06) *Optically-driven topological electronics with MIR fields in two-dimensional quantum materials*
- M. Ivanov, ICFO seminar and Optologic kick-off meeting (Barcelona, Spain, 2020-11) *Towards optically-driven topological electronics*
- M. Ivanov, DESY and Hamburg University Colloquium (Hamburg, Germany, 2020-11) *Towards optically-driven topological electronics in two-dimensional materials*
- M. Ivanov, Physics Department, Ulm University, Colloquium, (Ulm, Germany, 2020-11) *Towards optically-driven topological electronics in two-dimensional materials*
- O. Kornilov; Seminar at Instiut Lumière Matière (Villeurbanne CEDEX, France, virtuell, 2020-12): *Electronic structure and relaxation of solvated molecules studied by time-resolved photoelectron spectroscopy*
- S. Sharma, Lüscher Seminar (Klosters, Switzerland, 2020-): *Attosekunden Spindynamik*
- S. Sharma, TRR 227 Retreat (Halle, Germany, 2020-11): *Ultrafast spin and charge dynamics: ab-initio description*
- S. Sharma, Seminar series of Nijmegen and Uppsala (Sweden, 2020-12): *Ultrafast spin and charge dynamics: ab-initio description*
- G. Steinmeyer, Seminar (University of Maryland, College Park, MA, USA, 2020-02): *Pseudo mode-locking and the coherent artifact - 50 years of self-deception*
- G. Steinmeyer, Seminar (Leibniz-Universität Hannover, Germany, 2020-03): *Caged solitons*
- G. Steinmeyer, Summer School Lecture (Prague, Czech Republic, 2020-08): *Pulse characterization*
- C. von Korff Schmising, TRR 227 Retreat (Halle, Germany, 2020-04): *Spin dependent carrier dynamics studied by transient absorption spectroscopy in the extreme ultraviolet spectral range*
- K. Busch, Vorlesung, 2 SWS (Humboldt-Universität zu Berlin, WS 2019/20): *Statistische Physik*
- K. Busch, together with F. Intravaia, and D.-N. Huynh; Übung, 2 SWS (Humboldt-Universität zu Berlin, WS 2019/20): *Statistische Physik*
- K. Busch, together with O. Benson, A. Peters, A. Saenz, S. Ramelow, F. Intravaia, and M. Krutzik; Seminar, 2 SWS (Humboldt-Universität zu Berlin, SS 2020): *Optik/ Photonik: Projekt und Seminar*
- K. Busch, together with F. Intravaia, D.-N. Huynh, and B. Beverungen; Vorlesungen und Übungen, 10 SWS (Humboldt-Universität zu Berlin, SS 2020): *Theoretische Physik III: Quantenmechanik*
- K. Busch, together with F. Loth; Vorlesungen und Übungen, 4 SWS (Humboldt-Universität zu Berlin, SS 2020): *Computerorientierte Photonik*
- K. Busch, together with F. Intravaia, D.-N. Huynh, and B. Beverungen; Tutorium, 2 SWS (Humboldt-Universität zu Berlin, SS 2020): *Theoretische Physik III: Quantenmechanik*
- K. Busch, together with F. Intravaia, and D.-N. Huynh; Vorlesungen und Übungen, 10 SWS (Humboldt-Universität zu Berlin, WS 2020/21): *Theoretische Physik IV: Fortgeschrittene Quantenmechanik, / Fortgeschrittene Quantentheorie*
- K. Busch, Tutorium, 2 SWS (Humboldt-Universität zu Berlin, WS 2020/21): *Theoretische Physik IV: Fortgeschrittene Quantenmechanik, / Fortgeschrittene Quantentheorie*
- S. Eichmann, together with O. Dopfer; Vorlesung und Übungen, 4 SWS (Technische Universität Berlin, WS 2019/20): *Atome, Moleküle, Cluster I*
- S. Eichmann, Vorlesung, 2 SWS (Technische Universität Berlin, WS 2020/21): *Höhere Atomphysik*
- S. Eisebitt, together with B. Kanngießer, and T. Möller; Vorlesung und Übungen, 4 SWS (Technische Universität Berlin, Institut für Optik und Atomare Physik, WS 2019/20): *Röntgenphysik I*
- S. Eisebitt, together with B. Kanngießer, and T. Möller; Vorlesung und Übungen, 4 SWS (Technische Universität Berlin, Institut für Optik und Atomare Physik, WS 2019/20): *Röntgenphysik I*
- S. Eisebitt, together with B. Kanngießer; Vorlesung und Übungen, 4 SWS (Technische Universität Berlin, Institut für Optik und Atomare Physik, SS 2020): *Röntgenphysik II*
- T. Elsaesser and A. Saenz, Vorlesung, 4 SWS (Humboldt-Universität zu Berlin, WS 2019/20): *Laserphysik*
- T. Elsaesser and A. Saenz, Vorlesung, 4 SWS (Humboldt-Universität zu Berlin, WS 2020/21): *Laserphysik*

## Academic teaching

- K. Busch, together with O. Benson, A. Peters, A. Saenz, S. Ramelow, F. Intravaia, and M. Krutzik; Seminar, 2 SWS (Humboldt-Universität zu Berlin, WS 2019/20): *Optik/ Photonik: Projekt und Seminar*
- K. Busch, together with A. Perez-Leija, and K. Tschernig; Übung, 2 SWS (Humboldt-Universität zu Berlin, WS 2019/20): *Diskrete Quantenoptik*
- K. Busch, together with A. Perez-Leija; Vorlesung, 2 SWS (Humboldt-Universität zu Berlin, WS 2019/20): *Diskrete Quantenoptik*

- I. V. Hertel, Seminar, 2 SWS (Humboldt-Universität zu Berlin, WS 2019/2020): *Forschungspraktikum mit Seminar*
- I. V. Hertel, Seminar, 2 SWS (Humboldt-Universität zu Berlin/virtuell, SS 2020): *Forschungspraktikum mit Seminar*
- I. V. Hertel, Seminar, 2 SWS (Humboldt-Universität zu Berlin, WS 2020/21): *Forschungspraktikum mit Seminar*
- M. Y. Ivanov, together with T. Bredtmann; Übung, 2 SWS (Humboldt-Universität zu Berlin, WS 2019/20): *Nichtlineare Optik*
- M. Y. Ivanov, together with T. Bredtmann; Vorlesungen und Übungen, 4 SWS (Humboldt-Universität zu Berlin, WS 2020/21): *Nichtlineare Optik*
- A. Perez-Leija, together with K. Busch, and K. Tschernig; Vorlesungen und Übungen, 4 SWS (Humboldt-Universität zu Berlin, WS 2020/21): *Diskrete Quantenoptik*
- O. Smirnova, together with U. Woggon; Vorlesung und Übungen, 4 SWS (Technische Universität Berlin, Institut für Optik und Atomare Physik, WS 2019/20): *Höhere Optik I*
- O. Smirnova, together with U. Woggon; Vorlesung und Übungen, 1,5 SWS (Technische Universität Berlin, Institut für Optik und Atomare Physik, SS 2020): *Höhere Optik II*
- O. Smirnova, Seminar, 2 SWS (Technische Universität Berlin, Institut für Optik und Atomare Physik, SS 2020): *Controlled quantum dynamics in laser fields*
- G. Steinmeyer, Vorlesung und Übung, 4 SWS (Humboldt-Universität zu Berlin, SS 2020): *Physik ultraschneller Prozesse (Kurzzeitspektroskopie)*
- G. Steinmeyer, Vorlesung und Übung, 4 SWS (Humboldt-Universität zu Berlin, WS 2020/21): *Physik III Optik*
- M. J. J. Vrakking, Vorlesung, 2 SWS (Freie Universität Berlin, WS 2019/20): *Ultrafast Laserphysics*
- M. J. J. Vrakking, Vorlesungen und Übungen, 4 SWS (Freie Universität Berlin, WS 2020/21): *Ultrafast Laserphysics*
- M. Woerner, Übung, 2 SWS (Humboldt-Universität zu Berlin, WS 2019/20): *Laserphysik*
- M. Woerner, Übung, 2 SWS (Humboldt-Universität zu Berlin, WS 2020/21): *Laserphysik*
- T. Elsaesser, Vortrag (Einstein-Gymnasium Potsdam, Potsdam, 2020-01): *Die Messung der Zeit - eine physikalische Herausforderung*
- T. Elsaesser, Vortrag (Gymnasium auf den Seelower Höhen, Seelow, 2020-02): *Die Messung der Zeit - eine physikalische Herausforderung*
- T. Elsaesser, Vortrag (Christa-und-Peter-Scherpf-Gymnasium, Prenzlau, 2020-03): *Die Messung der Zeit - eine physikalische Herausforderung*
- T. Elsaesser, Vortrag (Marie-Curie-Gymnasium, Ludwigfelde, 2020-03): *Die Messung der Zeit - eine physikalische Herausforderung*
- T. Elsaesser, Vortrag (Weinberg-Gymnasium, Kleinmachnow, 2020-12): *Die Messung der Zeit - eine physikalische Herausforderung*
- T. Elsaesser, Vortrag (Weinberg-Gymnasium, Kleinmachnow, 2020-12): *Die Messung der Zeit - eine physikalische Herausforderung*
- T. Elsaesser, Vortrag (Von-Saldern-Gymnasium, Brandenburg/Havel, 2020-01): *Was ist Quantentechnologie? Die physikalische Sicht*
- T. Elsaesser, Vortrag (Friedrich-Wilhelm-Gymnasium, Königswusterhausen, 2020-02): *Was ist Quantentechnologie? Die physikalische Sicht*
- T. Elsaesser, Vortrag (Leonardo da Vinci Campus, Nauen, 2020-02): *Was ist Quantentechnologie? Die physikalische Sicht*
- T. Elsaesser, Vortrag (Schiller-Gymnasium Potsdam, Potsdam, 2020-02): *Was ist Quantentechnologie? Die physikalische Sicht*
- T. Elsaesser, Vortrag (Oberstufenzentrum Cottbus, Cottbus, 2020-02): *Was ist Quantentechnologie? Die physikalische Sicht*

### General talks (popular, science politics etc.)

S. Eisebitt, 40. Hybrid Talks, „Transparenz“ (Universität der Künste Berlin, 2020-11): Dreifach Unsichtbares sehen

## Appendix 3

### Ongoing Master, and PhD theses

#### Bachelor theses

L. Tran; Tempern von FeGd-Dünnschichten zur gezielten Beeinflussung der magnetischen Eigenschaften (Supervisor: S. Eisebitt), Technische Universität Berlin

#### Master theses

F. Chahrour; *Origin of thermalization effects in multi-mode nonlinear optical systems* (Supervisor: K. Busch, and A. Perez-Leija), Humboldt-Universität zu Berlin

V. Deinhart; *Ion-patterning of ferrimagnetic FeGd films* (Supervisor: S. Eisebitt), Technische Universität Berlin

L. Glöggler; *First pump-probe NEXAFS experiments using a laser-based plasma source* (Supervisor: B. Kanngießer H. Stiel), Technische Universität Berlin

C. Klose; *Coherent Correlation Imaging* (Supervisor: S. Eisebitt), Technische Universität Berlin

L. Maikowski; *Attosecond XUV Fourier transform spectroscopy* (Supervisor: M. J. J. Vrakking, and T. Witting), Freie Universität Berlin

Z. Wang; *Physical mechanisms of air lasing* (Supervisor: M. Y. Ivanov), Humboldt-Universität zu Berlin

#### PhD theses

V. Bender; *Modeling of nonlinear and active material in interaction with plasmonic nanostructures* (Supervisor: K. Busch and A. Perez-Leija), Humboldt-Universität zu Berlin

U. Bengs; *Generation of isolated attosecond pulses with circular polarization* (Supervisor: M. Ivanov and N. Zhavaronkov), Humboldt-Universität zu Berlin

M. Borchert; *Ultrafast magnetic spectroscopy in the extreme ultraviolet spectral range* (Supervisor: S. Eisebitt), Technische Universität Berlin

F. Branchi; *Ultrafast structural dynamics in molecules by time-resolved photoelectron holography* (Supervisor: M. J. J. Vrakking), Freie Universität Berlin

M.-A. Codescu; *Ultraschnelle Dynamik von photoinduzierten Prozessen* (Supervisor: T. Elsaesser), Humboldt-Universität zu Berlin

P. J. Fürtjes; *Generation and application of ultrashort mid-infrared pulses* (Supervisor: T. Elsaesser), Humboldt-Universität zu Berlin

K. Gerlinger; *X-ray imaging of optically induced spin textures* (Supervisor: S. Eisebitt), Technische Universität Berlin

P. Hessing; *Interferenzbasierte zeitaufgelöste Abbildung und Spektroskopie mit XUV-Strahlung* (Supervisor: S. Eisebitt), Technische Universität Berlin

E. Ikonnikov; *Time-resolved photoelectron spectroscopy of solvated molecules with phase-locked pulse pairs* (Supervisor: M. J. J. Vrakking and K. Heyne), Freie Universität Berlin

T. K. Kalousdian; *Strongfield dissociation of state-selected  $H_2^+$  ( $v, J$ )* (Supervisor: M. J. J. Vrakking and H.-J. Freund), Freie Universität Berlin

L.-M. Kern; *Laser-driven magnetic switching at inhomogeneities and nanostructures* (Supervisor: S. Eisebitt), Technische Universität Berlin

J. Klei; *Attosecond time-resolved molecular electron dynamics* (Supervisor: M. J. J. Vrakking), Freie Universität Berlin

C. Kleine; *Ultraschnelle Spektroskopie von Ladungstransferprozessen untersucht mit weichen Röntgenimpulsen* (Supervisor: T. Elsaesser), Humboldt-Universität zu Berlin

L.-M. Koll; *2D XUV Spectroscopy* (Supervisor: M. J. J. Vrakking and T. Witting), Freie Universität Berlin

B. Langbehn; *X-ray imaging of ultrafast dynamics in single helium nanodroplets* (Supervisor: D. Rupp and T. Möller), Technische Universität Berlin

J. Lebendig-Kuhla; *Role of delocalized states for the excited state dynamics of nucleotide oligomers* (Supervisor: M. J. J. Vrakking and A. Lübcke), Freie Universität Berlin

Q. Li; *Ultra long range effects in ultra fast spin dynamics* (Supervisor: P. Brouwer S. Sharma), Freie Universität Berlin

F. Loth; *Light path engineering in disordered waveguide structures* (Supervisor: K. Busch), Humboldt-Universität zu Berlin

F. Mahler; *Spektroskopische Untersuchungen an III-V Halbleiterstrukturen* (Supervisor: T. Elsaesser), Humboldt-Universität zu Berlin

N. Mayer; *Generation, characterization, and application of chiral attosecond pulses* (Supervisor: M. Ivanov, and O. Kornilov), Humboldt-Universität zu Berlin

M. Osolodkov; Attosecond IR pump probe measurements of small molecules using 3D momentum spectroscopy (Supervisor: M.J.J. Vrakking and T. Witting), Freie Universität Berlin

M. Oßwald; Theoretical description and simulation of non-linear spectroscopic signals of the light induced primary processes in (6-4) photolyase (Supervisor: K. Busch and P. B. Fingerhut), Humboldt-Universität zu Berlin

M. Runge; *Nonlinear terahertz spectroscopy of biomolecules* (Supervisor: T. Elsaesser), Humboldt-Universität zu Berlin

J. Schauss; *Ultrakurzzeitdynamik der Wechselwirkung zwischen Ionen und Biomolekülen* (Supervisor: T. Elsaesser), Humboldt-Universität zu Berlin

B. Senffleben; *Time resolved diffractive imaging with intense attosecond pulses* (Supervisor: S. Eisebitt, and D. Rupp), Technische Universität Berlin

P. Singh; *Ultrafast vibrational probes of electric fields in hydrated molecular systems* (Supervisor: J. Kneipp and T. Elsaesser), Humboldt-Universität zu Berlin

K. Tschernig; Tailoring non-classical states of light for applications in quantum information processing (Supervisor: K. Busch and A. Perez-Leija), Humboldt-Universität zu Berlin

K. Yao; *Ultrafast spin dynamics in heterogeneous magnetic systems* (Supervisor: S. Eisebitt), Technische Universität Berlin

Z. Zhang; Soft x-ray spectroscopy of investigating charge transfer processes in push-pull chromophores (Supervisor: M. J. J. Vrakking), Freie Universität Berlin

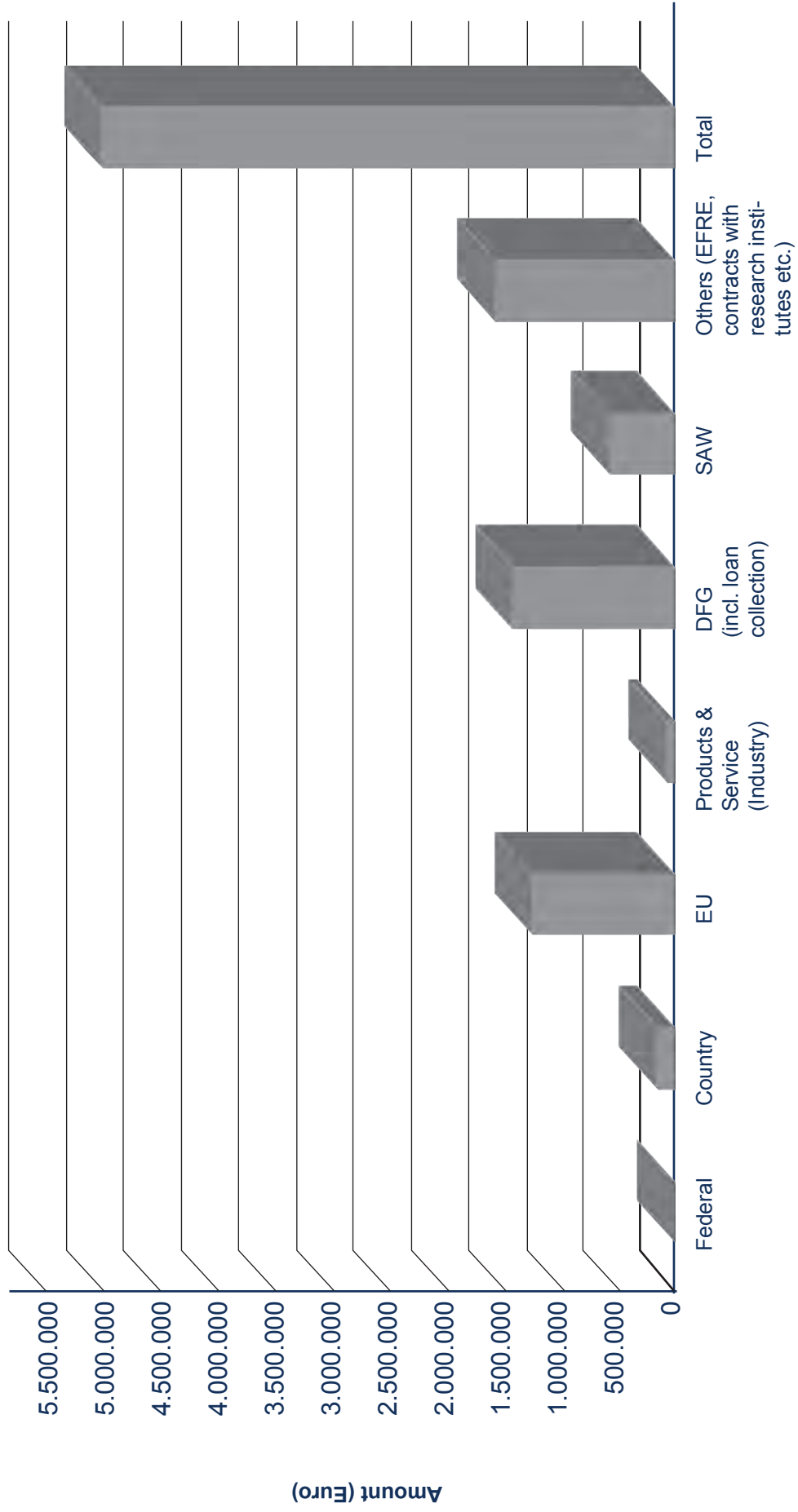
J. Zimmermann; Probing ultrafast electron dynamics in helium nanodroplets with deep learning assisted diffraction imaging (Supervisor: T. Möller and D. Rupp), Technische Universität Berlin

## Appendix 4

### Guest Lectures at the MBI

- D. Karlovets, Tomsk State University, Russia; Seminar C (2020-01-14): *Non-Gaussian matter waves and their potential applications*
- M. Viret, Iramis - Institut Rayonnement Matière de Saclay, CEA, Saclay, France; Seminar B (2020-01-17): *Chiral antiferromagnetic and electric orders at multiferroic domain walls in BiFeO<sub>3</sub> thin films*
- J. van Thor, Imperial College London, UK; MBI Colloquium (2020-01-22): *Ultrafast X-ray crystallography and ultrafast structural optical crystallography of nuclear and electronic protein dynamics*
- H. Koochaki Kelardeh, Max Planck Institute for the Physics of Complex Systems (MPI-PKS), Dresden, Germany; Seminar B (2020-01-24): *Ultrafast kinetics in two-dimensional crystals: topological phenomena*
- A. Polmann, Center for Nanophotonics, AMOLF, Amsterdam, Netherlands; MBI Colloquium (2020-01-29): *Nanoscale (in)coherent optical excitations in the electron microscope*
- M. Bieler, Physikalisch-Technische Bundesanstalt Braunschweig, Germany; Seminar C (2020-01-30): *Generation of ultrafast photocurrents in non-centrosymmetric semiconductors*
- D. Lechner, KIT Karlsruhe Institute of Technology, Karlsruhe, Germany; Seminar A (2020-02-17): *Development of a Shack-Hartmann Sensor based on adaptable diffractive lens arrays for reduction of scintillation effects*
- M. Robinson, University of Potsdam, Germany; Seminar B (2020-02-24): *2-Thiouracil: Determining the features of molecules in the lab and at facilities*
- G. Sansone, Albert-Ludwigs-Universität Freiburg, Germany; MBI Colloquium (2020-02-25): *From attosecond to XUV nonlinear optic*
- O. Johansson, University of Edinburgh, UK; Seminar B (2020-03-02): *Femtosecond charge and spin dynamics in molecular magnets*
- A. P. Dwivedi, University of Wisconsin-Milwaukee, USA; Seminar A (2020-03-12): *Quest for clean energy: From Batteries to Superconductors*
- T. Sidiropoulos, ICFO - The Institute of Photonic Sciences, Barcelona, Spain; Seminar A (2020-06-22): *Transient Attosecond Soft-X-Ray Spectroscopy in Layered Semi-Metals*
- S. Einfeldt, Ferdinand-Braun-Institut, Berlin, Germany; Seminar C (2020-07-16): *Status quo and prospects of UV LEDs*
- S. Wittrock, Unité Mixte de Physique CNRS/Thales, Palaiseau, France; Seminar B (2020-08-21): *From noise & stability to synchronization & complex dynamics in spin torque nano-oscillators*
- K. Amini, ICFO - The Institute of Photonic Sciences, Barcelona, Spain; Seminar A (2020-09-28): *Ultrafast electron diffraction imaging of gas-phase molecules and condensed matter*
- A. Nilsson, Stockholm University, Sweden; MBI Colloquium (2020-10-07): *X-ray Lasers Shed Light on the Mysteries of Water*
- R. Ernstorfer, Fritz-Haber-Institut, Berlin, Germany; MBI Colloquium (2020-10-21): *Ultrafast dynamics of electrons, excitons and phonons in momentum space*
- O. Pronin, Helmut-Schmidt-Universität / Universität der Bundeswehr Hamburg, Germany; Seminar C (2020-10-22): *Ultrafast oscillators around 2  $\mu\text{m}$  & ultra-broadband infrared generation*
- S. Haacke, University of Strasbourg, France; MBI Colloquium (2020-11-04): *Examples for Ultrafast Non-Adiabatic Photo-Reactions: C=C bond isomerisation & Inter-system crossing*
- J. Küpper, Center for Free-Electron Laser Science (CFEL), DESY Hamburg, Germany; MBI Colloquium (2020-10-18): *Unraveling the structure and dynamics of molecules at work*
- P. Hommelhoff, Universität Erlangen, Germany; MBI Colloquium (2020-12-02): *Ultrafast electron control -- Inside of graphene, at the surface of needle tips, and in a nanophotonics-structured vacuum*
- G. G. Brown, Ottawa University, Canada; Seminar A (2020-12-08): *In Situ Measurement and Recombination Effects*
- J. Petrovic, TU Berlin & Vinca Institute of Nuclear Sciences, Belgrade, Serbia; Seminar A (2020-12-09): *Bend-free photonic integrated circuits with the crosstalk as a resource*
- U. Staub, Paul Scherrer Institut, Villigen, Switzerland; MBI Colloquium (2020-12-16): *Ultrafast lattice, electron and spin dynamics through coherent "soft mode driving"*

## Appendix 5 Grants and Contracts



Total amount spent in 2020: 4.973.415 Euro

## Appendix 6

### Activities in Scientific Organizations

#### D. Ayuso

Member, Committee QUTIF-Young Researcher Meeting (Quantum Dynamics in Tailored Intense Fields), Berlin, Germany

#### W. Becker

Member, Editorial Board, Applied Sciences

Member, Editorial Board Laser Physics Letters

Member, Editorial Board ScienceOpen

Member, Advisory and Program Committee, 29th International Laser Physics Workshop - LPHYS'20/21, Lyon, France

Co-chair Seminar 2, Strong Field & Attosecond Physics of the 29th Int. Laser Physics Workshop - LPHYS'20/21, Lyon, France

#### K. Busch

Editor-in-chief, Journal of the Optical Society of America B  
Vice-chairperson, Berlin School of Optical Sciences and Quantum Technologies

#### S. Eisebitt

Chair, Scientific Advisory Committee (SAC) of the European XFEL

Member, Scientific Advisory Council Elettra-Sincrotrone Trieste, Italy

Member, DESY Photon Science Committee

Member, BMBF Gutachterausschuss

Member, Komitee für Forschung mit Synchrotronstrahlung (KFS)

Member, FERMI Proposal Review Panel, Elettra Sincrotrone Trieste, Italy

Member, Extended Governing Board of the Ioffe-Röntgen-Institute (IRI)

Member, Organization Committee Science@FELs 2020 Conference (DESY, Hamburg and European XFEL) Schenefeld, Germany

Member, Advisory Committee for the PM'20 Conference (Physics of Magnetism 2020), Poznan, Poland

Member, Technical Program Committee, General Congress of the International Commission for Optics (ICO-25) and the Conference of International Society on Optics Within Life Sciences (OWLS-16), Dresden, Germany

#### T. Elsaesser

Secretary of the Mathematics and Science Class, Berlin Brandenburg Academy of Sciences

Chair, TELOTA steering group, Berlin Brandenburg Academy of Sciences

Conference Chair, Program Committee, 15th Femtochemistry Conference (FEMTO 15)

Member, IRIS Adlershof, Humboldt-Universität zu Berlin

Member, Kuratorium of the Max Planck Institute for Quantum Optics, Garching, Germany

Member, Standing Committee for the Evaluation of International Max Planck Centers, Max Planck Society, Munich, Germany

Member, Editorial Board, Chem. Phys. Lett.

Member, Advisory Board, Conference Series on Time Resolved Vibrational Spectroscopy

Member, Proposal Review Panel for the LCLS X-ray FEL facility, SLAC, Menlo Park, CA, USA

Associate Editor, Struct. Dyn., AIP

Member, Science Policy Committee, SLAC, Menlo Park, CA, USA

Member, FXE Proposal, Review Panel, Schenefeld, European XFEL

Chair, Physics Group, Gesellschaft Deutscher Naturforscher und Ärzte (GdNÄ)

Member, Advisory Board, Int. Conference on Coherent Multidimensional Spectroscopy

#### F. J. Furch

Member, Program Committee HILAS High-brightness Sources and Light-driven Interactions Congress, Compact (EUV and X-Ray) Light Sources (Washington D.C, USA)

#### U. Griebner

Member, Program Committee, EPS-QEOD Europhoton Conference 2020 (Prague, Czech Republic)

Member, Program Committee, International Conference Laser Optics - ICLO 2020 (St. Petersburg, Russia)

#### R. Grunwald

Member, SPIE Fellows Committee 2020

Member, Editorial Board, Applied Sciences (MDPI)

Member, Editorial Board, Scientific Reports

Member, Programm Committee Photonics West, OPTO, Complex light and optical forces XIV

Member, Programm Committee, International Commission of Optics ICO 2021

#### **M. Ivanov**

Member, Program Committee SPIE Photonics Europe, Advances in Ultrafast Condensed Phase Physics II (Strasbourg, France)

#### **E. T. J. Nibbering**

Member, Scientific Selection Panel, Helmholtz-Zentrum Berlin - BESSY II

Member, Editorial Board, Journal of Photochemistry and Photobiology A

Member, Advisory Board, Conference Series on Time Resolved Vibrational Spectroscopy

Member, Proposal Review Panel, Linac Coherent Light Source LCLS

#### **B. Pfau**

Member, Organizing Committee, 736. WE-Heraeus-Seminar, Magnetism at the Nanoscale: Imaging - Fabrication - Physics, Wilhelm und Else Heraeus-Stiftung, Bad Honnef, Germany

#### **V. Petrov**

Member, Program Committee, SPIE Photonics West 2020: Nonlinear Frequency Generation and Conversion: Materials and Devices XIX (San Francisco, USA)

#### **A. Rouzée**

Editor, Advances in Physics X

#### **O. Smirnova**

Member, Advisory Board of the Max Planck School of Photonics

Member, dynaMENT Mentoring for Women in Natural Sciences, Universität Hamburg and DESY

Member, Scientific Committee International Conference on Attosecond Science and Technology, ATTO

Member, Scientific Committee for Faraday Discussion on Ultrafast dynamics

Member, Scientific Committee, International Conference on Photonic, Electronic and Atomic Collisions, ICPEAC

#### **S. Sharma**

Member, Executive Organising Committee SPIE Photonics Europe, Advances in Ultrafast Condensed Phase Physics II (Strasbourg, France)

#### **G. Steinmeyer**

Member, Editorial Board, Phys. Rev. A

Associate Editor, Optica

Member, Editorial Board, Phys. Lett. A

Member, Program Committee SPIE Photonics West, Real-time Measurements, Rogue Phenomena, and Single-Shot Applications V (San Francisco, USA)

Member, Program Committee Ultrafast Optics 2023, Bariloche, Argentina

#### **H. Stiel**

Member, Scientific Committee, International Conference on X-ray Lasers 2020, Dübendorf, Switzerland

Member, Advisory Board, Institute of Applied Photonics (IAP) e.V.

#### **J. W. Tomm**

Permanent Member, Int. Steering Committee, Int. Conference on Defects - Recognition, Imaging and Physics of Semiconductors, DRIP (Berlin, Germany)

Member Editorial Board, Journal of Electronic Materials (JEMS)

Member Editorial Board, Communications in Physics (CIP)

Member, Programm Committee, ESREF 2020, 31st European Symposium on Reliability of Electron Devices, Failure Physics and Analysis, Athens, IESL/FORTH and AUTH & HNA, Greece

#### **M. J. J. Vrakking**

Editor-in-chief, Journal of Physics B

Member, Panel Chair, ERC Advanced Grant 2020 evaluation (Brussels, Belgium)

Chairman, SAC of the Advanced Research Centre for Nanolithography (Amsterdam, Netherlands)

Chairman, Access Panel of the ARTEMIS user facility at RAL (Oxford, UK)

Member, Proposal review panel of LCLS FEL

Chairman, Physics faculty evaluation panel (Freiburg, Germany), University of Freiburg

Member, Project review panel of FLASH FEL

Conference chair and member of program committee, 15th Femtochemistry Conference FEMTO 15 (Berlin, Germany)

Local organizer/host, QUTIF Annual Meeting (Berlin, Germany)

Member, Management Board, Laserlab Europe V AISBL

## Honors and awards

B. P. Fingerhut: Coblentz Award, Coblentz Society

J. Mikosch: Consolidator Grant, The European Research Council (ERC)

D. Reiche: The Best Poster Award, together with K. Busch, and F. Intravaia, METANANO 2020 ONLINE, V International Conference on Metamaterials and Nanophotonics

A. Rouzee: JCP Editor's Choice Award, Atomic-resolution imaging of carbonyl sulfide by laser-induced electron dif-fraction (Denver, USA)

O. Smirnova: Ahmed Zewail Award in Ultrafast Science & Technology (ACS, San Francisco, CA, USA)



**Max-Born-Institut (MBI)**  
für Nichtlineare Optik und Kurzzeitspektroskopie  
im Forschungsverbund Berlin e. V.

**Mail Address:** Max-Born-Institut  
Max-Born-Straße 2 A  
12489 Berlin  
Germany

**Phone:** (+49 30) 6392 1505  
**Fax:** (+49 30) 6392 1519  
mbi@mbi-berlin.de  
www.mbi-berlin.de

**The Divisions of the Max-Born-Institut**

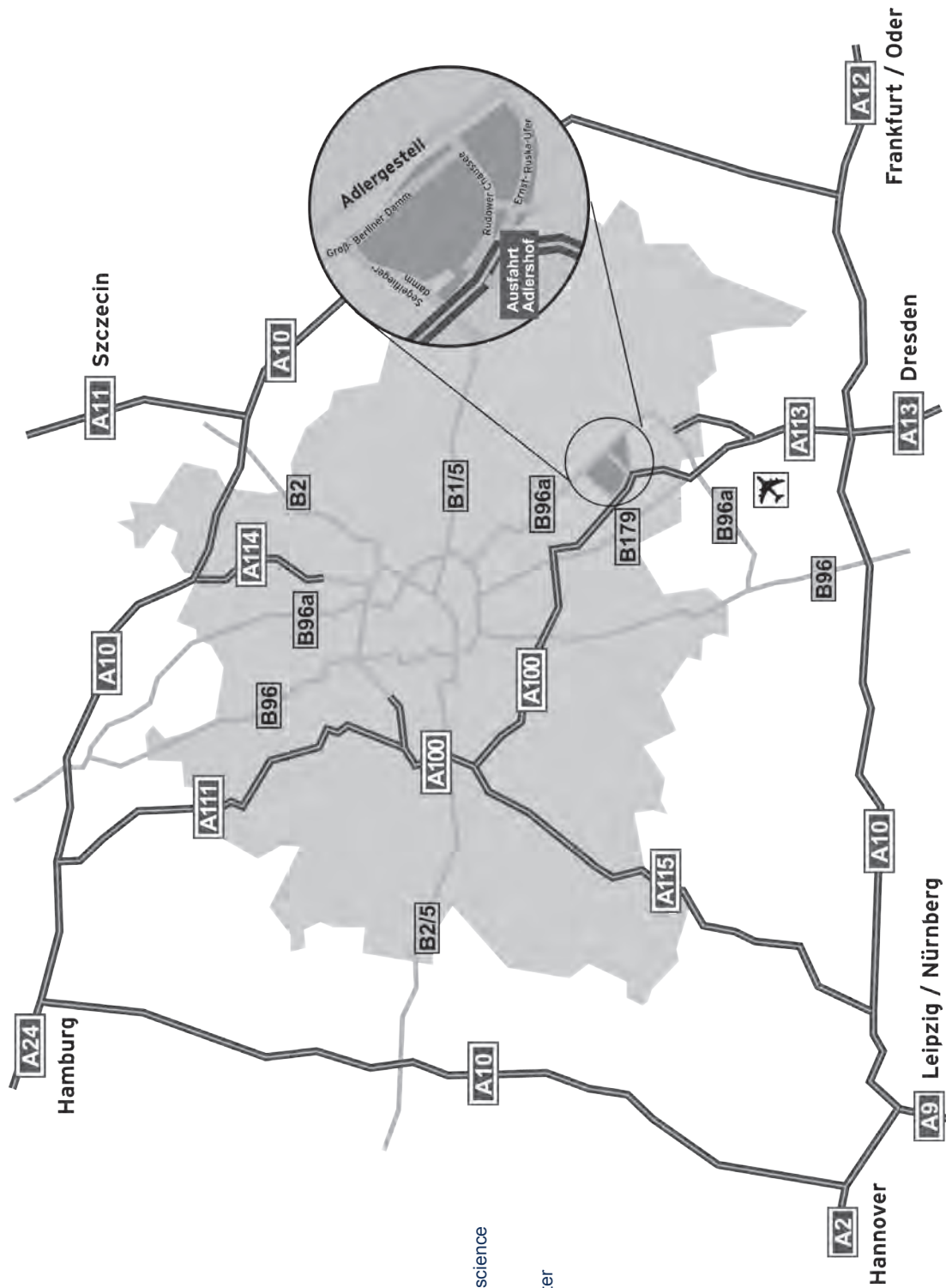
- Division A:** Attosecond Physics  
Prof. Dr. M. J. J. Vrakking
- Division B:** Transient Electronic Structure and Nanoscience  
Prof. Dr. S. Eisebitt
- Division C:** Nonlinear Processes in Condensed Matter  
Prof. Dr. T. Elsaesser

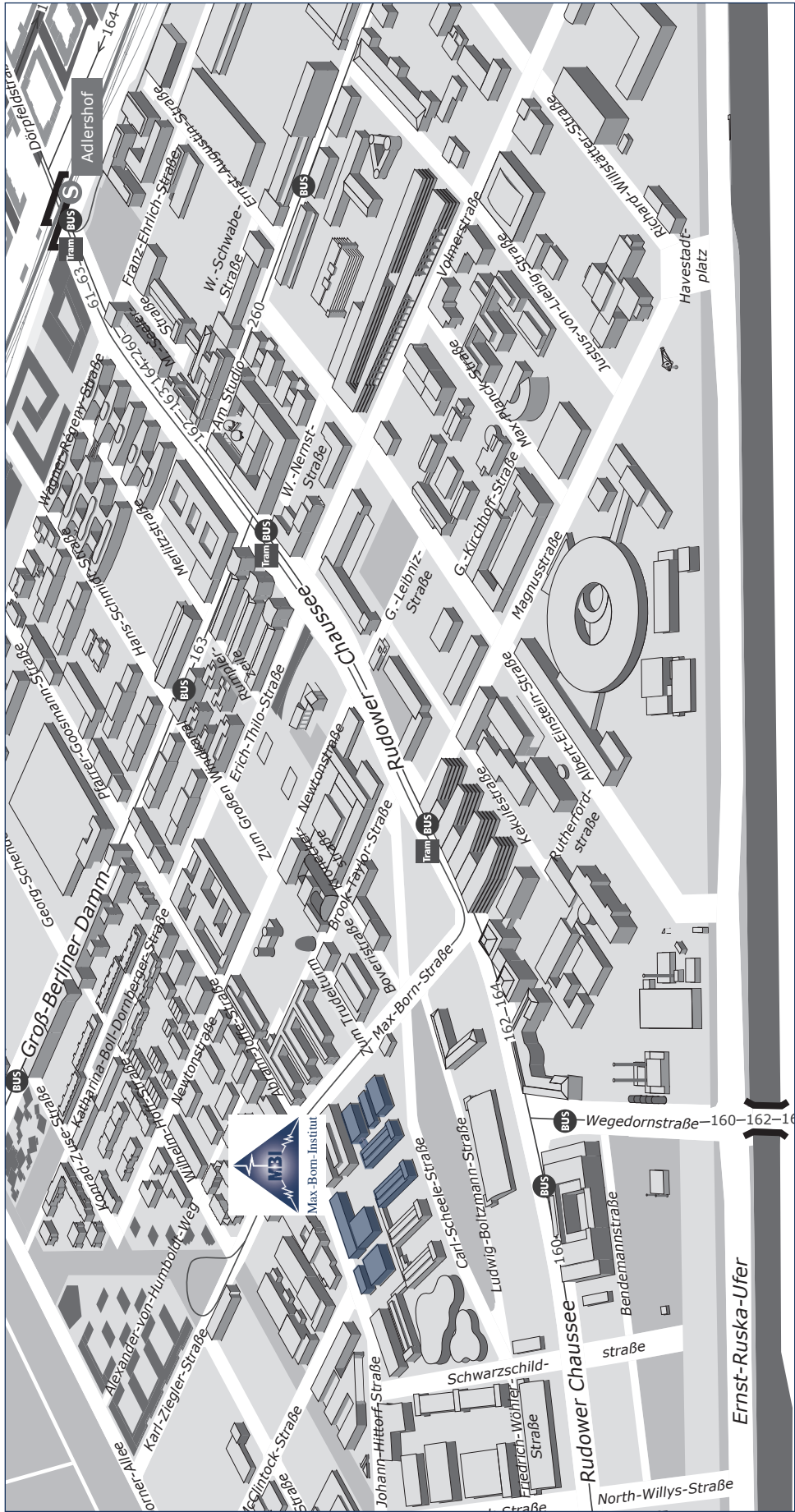
**City district:** Berlin Treptow-Koepenick  
**Subdistrict:** Berlin-Adlershof

**Site:** Berlin-Adlershof  
**Street:** Max-Born-Straße 2 A

**S-Bahn:** S45, S46, S85, S8, and S9  
**Station:** Berlin-Adlershof  
from there:  
Bus 162, 164 to Magnusstraße  
Tram: 61, 63 to Karl-Ziegler-Straße

**Subway:** U7  
**Station:** Rudow  
from there:  
Bus 162 to Magnusstraße











**Max-Born-Institut**  
für Nichtlineare Optik  
und Kurzzeitspektroskopie  
im Forschungsverbund Berlin e.V.

Max-Born-Straße 2 A  
D-12489 Berlin

Phone: (++49 30) 63 92 - 15 05  
Fax: (++49 30) 63 92 - 15 19  
e-mail: [mbi@mbi-berlin.de](mailto:mbi@mbi-berlin.de)  
<http://www.mbi-berlin.de>